
FACULTY
OF MATHEMATICS
AND PHYSICS
Charles University

# DOCTORAL THESIS

Vlastimil Peksa

## Designing and testing of new metal nanosubstrates for biomolecular sensors based on surface-enhanced Raman scattering (SERS) spectroscopy

Institute of Physics of Charles University

Supervisor: doc. RNDr. Marek Procházka, Ph.D.

Study programme: Physics

Specialization: Biophysics, chemical and macromolecular physics

Prague 2017

I declare that I carried out this doctoral thesis independently, and using only the cited sources and references.

I acknowledge the fact that my work relates to rights and obligations under the Act No. 121/2000 Coll., the Copyright Act, as amended, in particular the fact that the Charles University has the right to conclude a license agreement on the use of this work as a school work pursuant to section 60 paragraph 1 of the Copyright Act.

In Prague, 13. 6. 2017 Vlastimil Peksa

I would like to thank my supervisor doc. RNDr. Marek Procházka, Ph. D. for his patience and approach. I would also like to thank the entire Department of Biomolecules for creation of such a hospitable work environment. Funding from Project P205/13/20110S from the Czech Science Foundation is gratefully acknowledged. Last but not least I would like to thank my family and my close ones for their support during the writing of this thesis.

Název práce: Vývoj a testování nových kovových nanosubstrátů pro biomolekulární senzory založené na spektroskopii povrchem zesíleného Ramanova rozptylu (SERS)

Autor: Vlastimil Peksa

Katedra / Ústav: Fyzikální ústav UK

Vedoucí disertační práce: doc. RNDr. Marek Procházka, Ph.D., Fyzikální ústav UK

Abstrakt: Tato experimentální metodická práce byla zaměřena na optimalizaci vybraných zlatých a stříbrných povrchů a práci s nimi při konstrukci biosenzorů založených na SERS spektroskopii, včetně následné praktické aplikace. Za tímto účelem bylo testováno několik typů povrchů vytvářených kombinacemi „bottom-up“ technik na pevných substrátech. Vlastnosti těchto povrchů byly studovány pomocí modelových molekul, jmenovitě methylene blue, porfyrinů a tryptofanu, na konfokálním Ramanově mikrospektrometru. Získané poznatky o vlivech aplikace analytu, fokusování a interního intenzitního standartu byly využity pro optimalizaci měřících postupů s ohledem na citlivost, přesnost a reprodukovatelnost měření. Na základě těchto poznatků byla vyvinuta metoda kvantitativní detekce potravinářského barviva azorubin (E 122) v komerčně dostupných nápojích. Její výsledky ukázaly, že tato aplikace může sloužit jako předběžná testovací metoda pro měření v terénu.

Klíčová slova: Kovové nanopovrchy, biomolekuly, biosenzory, Raman, SERS

Title: Designing and testing of new metal nanosubstrates for biomolecular sensors based on surface-enhanced Raman scattering (SERS) spectroscopy

Author: Vlastimil Peksa

Department: Institute of Physics of Charles University

Supervisor: doc. RNDr. Marek Procházka, Ph.D., Institute of Physics of Charles University

Abstract: This experimental methodical work was aimed at the optimization of selected gold and silver substrates and their use in construction of SERS-based biosensors, including following practical application. Several types of substrates, fabricated via a combination of bottom-up techniques on solid surfaces, were tested. The properties of these substrates were examined with probe molecules, namely methylene blue, porphyrins and tryptophan, on a confocal Raman microspectrometer. Obtained findings about the influence of analyte application, objective focusing and internal intensity standard were exploited for optimization of measurement procedures with regard to sensitivity, accuracy and reproducibility. A method for quantitative detection of food dye azorubine (E 122) in commercially available drinks was developed, based on these findings. Its results have shown its potential as a pre-scan method for field application and preliminary testing.

Keywords: Metal nanosubstrates, biomolecules, biosensors, Raman, SERS

# Content

Content ..... 1
1. Introduction ..... 2
1.1 SERS mechanisms ..... 3
1.2 SERS substrates ..... 4
1.3 Evaluation of SERS measurements ..... 8
1.4 SERS of biomolecules ..... 10
2. Aims of thesis ..... 12
3. Results and Discussion ..... 13
3.1 Experimental conditions and equipment ..... 13
3.2 HCL substrates ..... 13
3.2.1 HCL substrates characterization ..... 13
3.2.2 Optimization of SERS sensor handling ..... 15
3.2.3 Flow cell measurements ..... 19
3.3 OAD substrates and silver island films ..... 22
3.3.1 OAD substrates characterization ..... 22
3.3.2 Silver island film characterization ..... 23
3.3.3 SERS on OAD substrates ..... 24
3.3.4 Silver island film substrates in microfluidics ..... 25
3.4 FON substrates ..... 27
3.4.1 FON substrates characterization ..... 27
3.4.2 Detection of important biomolecules on FON substrates ..... 28
3.4.3 Detection of azorubine in complex matrices ..... 32
4. Conclusions ..... 35
5. References ..... 36
6. List of abbreviations ..... 38
7. List of papers and published conference abstracts ..... 39
8. Supplements ..... 41

# 1. Introduction

The detection and correct identification of molecules is a very important task for numerous biological, biophysical and biochemical applications. A number of detection and analytical methods is currently employed with high precision and sensitivity, such as liquid chromatography, mass spectrometry, nuclear magnetic resonance or capillary electrophoresis, as well as numerous optical methods like absorption spectroscopy. These methods are however often expensive to perform, time-consuming, information-poor, invasive or require large-scale laboratory material, making them difficult to perform in field conditions. It is therefore desired to develop new ways of cheaper, faster and more accurate detection to be employed in future sensors' fabrication and handling. Vibrational optical spectroscopy has proven itself to be a very interesting method for this, as it provides a high degree of information, while being rapid and easy to use. One of the methods of vibrational optical spectroscopy is the Raman spectroscopy, based on inelastic photon scattering (Raman scattering, RS) (Dietzek et al. 2011; Le Ru and Etchegoin 2009; Raman 1928). RS occurs when a photon interacts with a molecule, changing its vibrational state, thus changing the energy of scattered photons. The photons are either red shifted (Stokes shift) or blue shifted (anti-Stokes shift), depending on whether the molecule is excited into a higher vibrational state or lower vibrational state. Under room temperature conditions the majority of molecules are in a ground state and therefore the Stokes shift is much more likely. RS provides a very detailed fingerprint spectral information about the molecular structure; however, the RS effect is rather weak. The RS signal can be vastly enhanced if the molecule is in a close vicinity of a rough metallic surface. This effect was discovered by Fleischmann (Fleischmann et al. 1974), and it is known as the Surface-Enhanced Raman Scattering (SERS).

The SERS effect can be explained by two enhancement mechanisms, electromagnetic and chemical (molecular). An enhancement up to $10^{11}$ can be achieved, and even single molecular detection using SERS was reported (Kneipp et al. 1997; Weiss and Haran 2001). Nowadays, SERS has been used for a large variety of bioanalytical and sensing applications, as it is a method very suitable for detection

of various biomolecules in low concentrations (Etchegoin et al. 2003; Haynes et al. 2005; Procházka 2016; Schlucker 2014; Schlücker 2010).

## *1.1 SERS mechanisms*

The intensity of RS depends on the induced electric dipole $\vec{\mu}$, which is given by Eq. 1

$$\vec{\mu} = \alpha\vec{E} \tag{1}$$

where $\alpha$ is the polarizability of the scattering system and $\vec{E}$ is the intensity of the incident electric field. Both of these values can be enhanced via a different mechanism. For more details of theory of RS and both enhancement mechanisms see (Le Ru and Etchegoin 2009; Procházka 2016; Schrader 1995)

*Electromagnetic mechanism*

The enhancement of incident electric field is associated with localized surface plasmons (LSP). When electric field interacts with a metallic surface the LSP can be excited. The LSP are understood as collective charge density oscillations that are not propagating across the surface. Resonant excitation of LSP results in a strong enhancement of electromagnetic field in a vicinity of the surface. Since the RS (and SERS) have a small difference in energies of incident and scattered photons, the resonant condition is achieved for both fields and a combined enhancement (above $10^6$) can be reached. It is the dominant effect in the overall enhancement of RS.

*Chemical mechanism*

Although the electromagnetic enhancement is definitely the dominant effect, the enhancement (ranging from $10^1$ to $10^2$) from chemical bond with the surface has to be considered. This mechanism is based on increased polarizability of the molecule adsorbed onto the metal surface. It involves formation of new electronic states, charge transfer (CT) between metal and adsorbate due to their bonding interaction and other effects. The most popular model is the CT process when the exciting light is in resonance with a CT transition of adsorbate-surface complex. Due to the interaction between surface and molecule the SERS lines can be shifted compared to a RS spectrum of a free molecule.

## *1.2 SERS substrates*

The SERS substrates are a matter of constant research (Schlucker 2014). Since its discovery a broad variety of substrates have been fabricated and tested for different molecules. Most of the fabrication processes can be divided into two approaches, bottom-up and top-down. Bottom-up approaches represent building up the SERS-active structures from subcomponents, while top-down represent sculpting of the structures from a bulk material via lithography or other methods (Cialla et al. 2012). The bottom-up approaches are generally cheaper, faster and the resulting substrates are mass-producible, while the top-down ones are able to produce more regular substrates and more complex shapes. Both of the approaches can of course be combined in the whole fabrication process. For more details on this see (suppl. III). The most commonly used metals for the fabrication of SERS substrates are gold and silver, and marginally also copper and aluminium (for UV excitation wavelengths).

An ideal SERS substrate should have the following attributes (Natan 2006): (i) It should provide a strong SERS enhancement, (ii) the SERS enhancement should be as uniform as possible across the substrate (ideally with RSD within 20%), (iii) provide good spectral stability and reproducibility, and (iv) be clean enough from stray signals and background fluorescence. The two most important characteristics of SERS substrates are their ability to enhance the RS signal and the regularity of this enhancement and spectral stability over different measurements. The most commonly used SERS substrates are colloids, which provide a very strong RS signal enhancement, but the reproducibility of collected spectra is generally rather poor. It is therefore desirable to develop new solid substrates with ordered nanostructures to overcome the problems associated with colloid aggregation and ageing. Since both the enhancement of the RS signal and the spectral stability are dependent on the examined molecule, the SERS sensors have to be developed for a specific combination of analyte and substrate.

The substrates examined in this thesis were prepared using different methods composed of mainly bottom-up fabrication techniques, and consist of either gold or silver (suppl. III). The first substrate is fabricated using the Hole-mask Colloidal Lithography (HCL), which produces arrays of gold nanoparticles with different

shapes on any given support. In this thesis particles with disc, cone and dimer shapes were examined. The method was first described in (Fredriksson et al. 2007), and it consists of eight fabrication steps, summarized on Fig. 1.2.1. In the first step the support (glass, silicon) is covered via spin-coating with poly(methylemetacrylate) (PMMA) layer. In the second step it is covered by a charged layer of polydiallyldimethyl ammonium (PDDA) via immersion into a solution. Negatively charged polystyrene nanobeads are then dispersed onto the PDDA surface. The surface with beads is covered with a thin layer of protective gold mask. The nanobeads are subsequently stripped away using an adhesive tape, leaving an array of nanoholes in the gold mask. The PMMA at the bottom of the holes is removed by etching in oxygen plasma for 5 minutes for discs and cones, and 10 minutes for dimers. To form an array of final particles gold is deposited onto the resulting nanohole pattern. 50 nm thick gold layer is deposited for the fabrication of discs, 260 nm thick for cones and two 25 nm thick layers from two different angles for dimers.

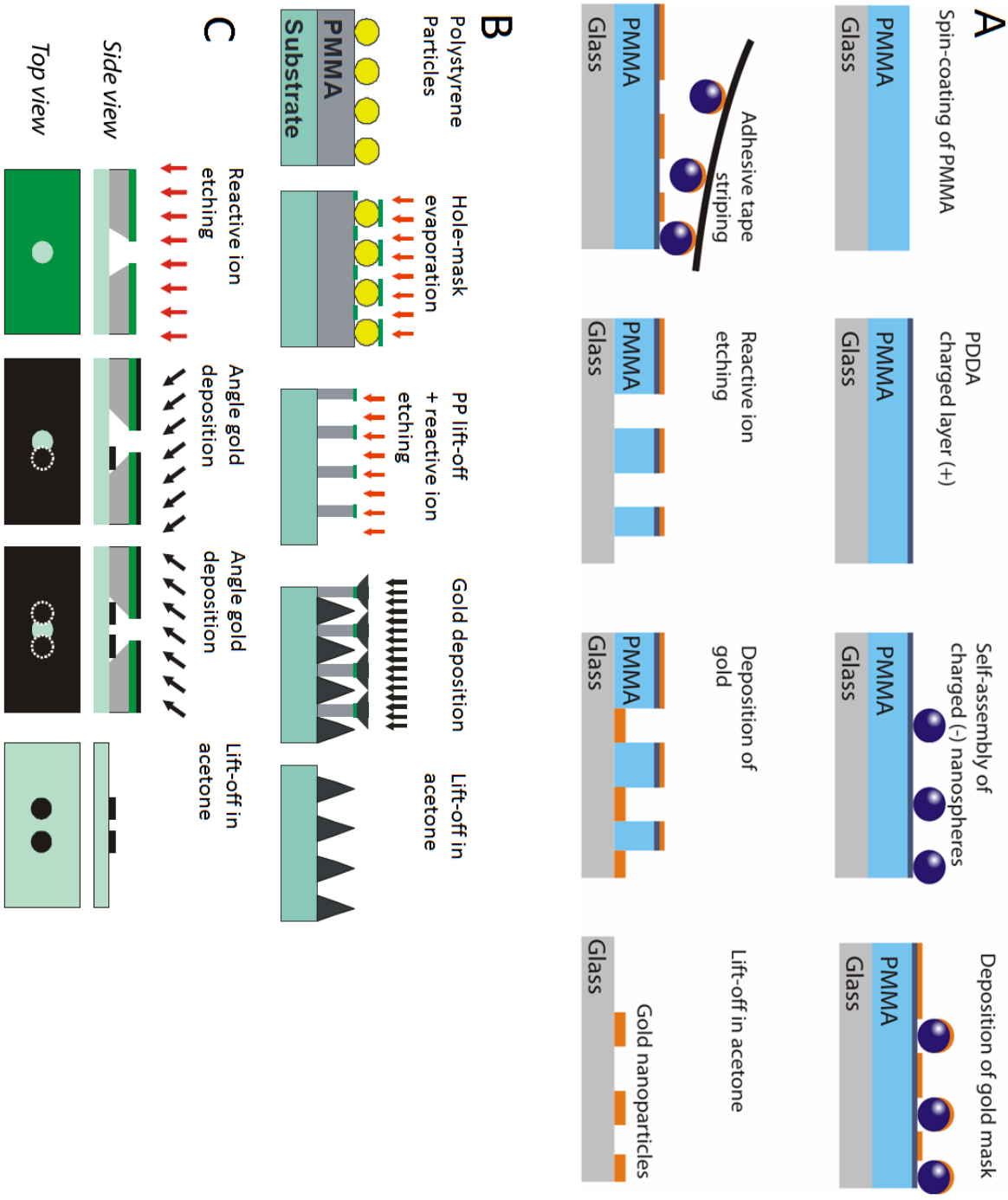


**Fig. 1.2.1:** A – Basic HCL preparation process with 50 nm high gold nanodiscs as a resulting substrate. B – Alteration to the basic process to produce cones, the thickness of layer of deposited gold is 260 nm instead of 50 nm. C – Alteration to the basic process to produce dimers, the reactive ion etching is 10 minutes long instead of 5 minutes, and the gold is then deposited at two different angles.

The second type of substrate is Film Over Nanospheres (FON) (Haynes and Van Duyne 2001). It is fabricated using method described by (Kosiorek et al. 2004; Stolcova et al. 2013). Polystyrene nanobeads (107 nm diameter) are dispersed in water-ethanol solution (1:1) and then deposited onto water surface using a glass pipette. There they form monolayers with hexagonal close-packed patterns, which are transferred to silicon wafer and left to dry. A 20 nm gold layer is then sputtered onto the beads, as depicted on fig. 1.2.2.

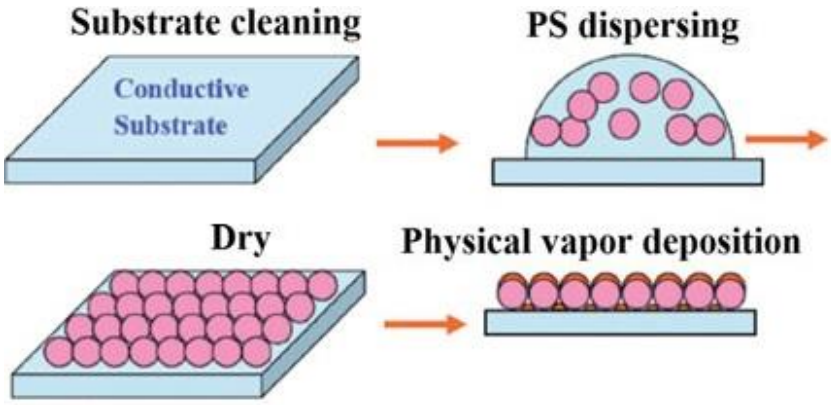


**Fig.1.2.2:** Schematic of FON preparation

The third type of substrates are silver nanorods and silver island films. The nanorods are fabricated via the method of Oblique Angle vapor Deposition (OAD) (Chaney et al. 2005). The OAD utilizes an effect of self-shadowing, which occurs when a collimated flux of vaporized atoms arrives at a substrate at an oblique angle of 85° with respect to the surface normal. The aggregating atoms shadow the area behind them, thus creating individual elongating particles – nanorods. The deposition of metal takes place in a vacuum chamber on a glass slide or silicon wafer via magnetron sputtering.

The silver island films are fabricated in a similar fashion by magnetron sputtering of silver onto a support covered with thin dielectric film composed of magnetron sputtered polytetrafluorethylene (PFTE). The silver sputtering leads to formation of randomly shaped and sized islands. There can be optionally deposited a prior metal (silver) layer beneath the PFTE layer, acting as a mirror and vastly enhancing the signal from such substrates (fig. 1.2.3) (Subr et al. 2015a).

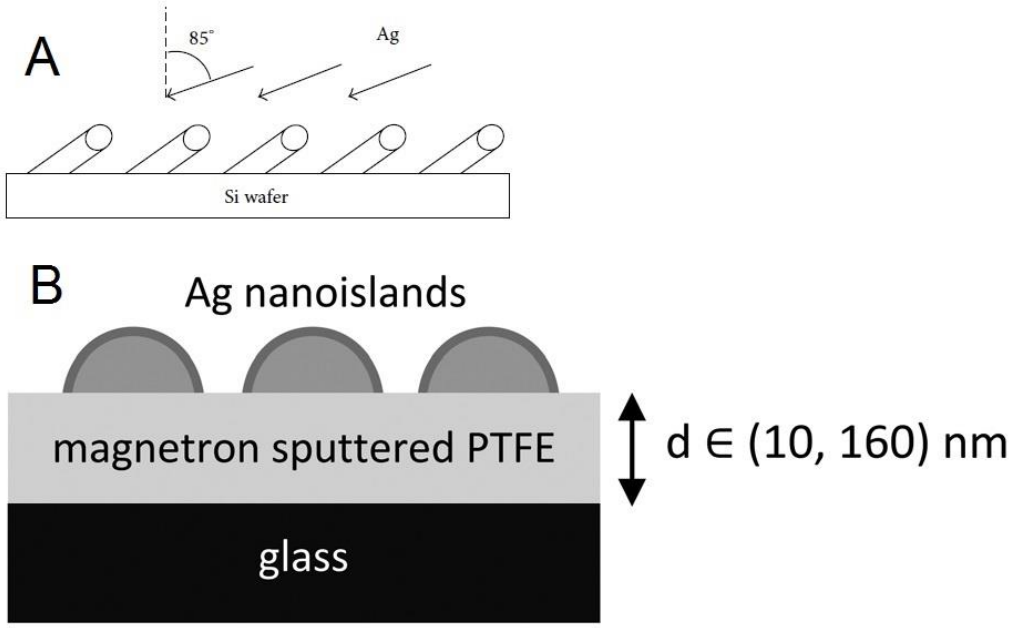


**Fig. 1.2.3:** A – schematic of Ag OAD substrates fabrication. The silver is sputtered at an oblique angle of 85°. B – schematic of Ag nanoislands. The base metal layer can be included or omitted depending on circumstances.

## *1.3 Evaluation of SERS measurements*

The SERS measurement from a single point can be affected by a number of specific local conditions, which can alter the SERS spectrum shape and intensity. It is therefore necessary to map the substrate and measure a statistically significant amount of points. This however creates a large amount of data which need to be correctly interpreted and evaluated. In addition, the measured experimental spectra can have a large fluorescence background signal, which can hamper further analysis, and its correct subtraction is necessary.

Factor analysis (FA) is a statistical method, which enables characterisation of large datasets with several common factors (Malinowski 1991). It can be performed using different methods that yield the same results, such as principal component analysis (PCA) or singular value decomposition (SVD). The SVD algorithm decomposes matrix $A$ of $m \times n$ to a product of multiplication of three matrices

$$A = UWV^T \tag{2}$$

where $U$ is an orthogonal column matrix $m \times n$, $V$ is an orthogonal matrix $n \times n$, and $W$ is a diagonal $n \times n$ matrix with nonnegative values. The $W$ values are called

singular values. This decomposition (2) can be utilized during the spectral processing. Each spectrum is a set of intensity values for corresponding wavenumbers. The number of these values within a single spectrum is *m*, and the number of measured spectra is *n*. The intensity values of each spectrum are written into the columns of the resulting *m*×*n* matrix *A*. The resulting matrix can be expressed as

$$A_i(\tilde{\nu}_k) = \sum_{j=1}^{n} W_j V_{ij} U_j(\tilde{\nu}_k) \quad (3)$$

where $i = 1..n$, $k = 1..m$. $A_i(\tilde{\nu}_k)$ represents the element in the *k*th row and the *i*th column of the matrix *A*, $W_j$ are singular values of diagonal matrix *W*, $V_{ij}$ represent the value in the *i*th row and the *j*th column of *V* matrix and $U_j(\tilde{\nu}_k)$ the value in *k*th row and *j*th column of matrix *U*. The expression (3) serves for the interpretation of the method. A given *i* spectrum can be expressed as a linear combination of *n* subspectra, where each subspectrum is one column vector of matrix *U*. Coefficients of this linear combination are written in the *i*th row of matix *V*. The subspectra from matrix *U* are multiplied by a weight factor $W_j$ (for further procedures we assume the weight factors are arranged in descending order). It was demonstrated that the expression of experimental spectra via the first subspectrum approximates the spectral set by one spectrum in the best possible way in the sense of the least squares method (Palacky et al. 2011). The second subspectrum describes the most significant differences between the spectra in the set, which are not included in the first subspectrum (optimization of the difference between original spectra and spectra expressed using only the first subspectrum by the least squares method). The same approach can further be applied to higher number subspectra. The higher the number of subspectra is considered in the sum in (3), the better are the experimental results approximaned by the FA.

In case of SERS measurements the most spectra are quite similar in their shape, and therefore are represented by the first subspectrum. The absolute intensities however vary based on local enhancement. The distribution of SERS signal intensity is characterised by its mean, relative standard deviation (RSD) and skewness calculated according to the formula

$$S = \frac{n}{(n-1)(n-2)} \sum \left(\frac{x_i - \bar{x}}{\sigma}\right)^3 \quad (4)$$

where $n$ is the number of measured values, $\bar{x}$ is the mean of the distribution and σ is the standard deviation of the distribution. The skewness reflects the asymmetry of the distribution due to presence of strongly enhancing hot-spots or defects on the substrate.

Since the intensity of the peaks in RS spectrum cannot be directly interpreted as concentration due to a multitude of possible factors, a standard is an important part of quantitative evaluation. The standard can be either external or internal, and it relates the strength of a measured signal to a previously established value. Its purpose is to eliminate problems associated with instrumental factors, such as laser power fluctuation, focusing errors and substrate defects. It also enables effective comparison of results between different experimental setups and equipment.

## *1.4 SERS of biomolecules*

A lot of biomolecules provide a sufficiently strong and distinctive SERS spectrum, so their presence, identification, quantification and/or state can be determined directly. Other biomolecules require chemical labels, chemical surface modifications or derivatized chemistry. There is not a single universal method for detection, and each sensing application has to be developed for a combination of the molecule and the substrate.

In this thesis we utilized both probe molecules with high SERS signal, for determination of substrate parameters and their optimization, and molecules which are present in real-life applications. As the primary probe molecule we selected Methylene Blue (MB), which is a molecule commonly used in SERS experiments involving testing of new substrates. It can be detected even in very low concentrations, up to $10^{-12}$ M (Srichan et al. 2016), and it gives a distinct SERS spectrum with a number of peaks, most notably at 1623 $cm^{-1}$.

The tested molecules include

- Tryptophan. Tryptophan is an essential aminoacid.
- Free-base porphyrins. The porphyrins are heterocyclic macrocycles consisting of four pyrrole rings, joined together by four methine groups.

Synthetic porphyrins are often used in medical applications, such as cancer treatment (Hajduková et al. 2008). Specifically we used 5,10,15,20-tetrakis(1-methyl-4-pyridyl)-21H,23H-porphine ($H_2$TMPyP), 5,10,15,20-tetrakis(4-trimethylammoniophenyl)-21H,23H-porphine ($H_2$TMAP), and 5,10,15,20-tetrakis(4-sulfonatophenyl)-21H,23H-porphine ($H_2$TSPP).

- Picloram herbicide. It is widely used for woody plant control, is water soluble, does not adhere to soil and has environmental lifetime of 2-4 months. In water, it is moderately toxic to fish in concentrations from up around 5-20 mg/L.
- Dipicolinic acid, which is considered a bacterial marker for *bacillus* and *clostridium* strains, and as such could be used in detection of, for example, *bacillus anthracis*.
- Benzocaine. Benzocaine is a local anaesthetic, and it is also often used as a drug marker due to its physical and chemical similarity to cocaine.
- 4-Aminothiophenol (*p*-ATP), which is a commonly used SERS probe, especially suitable for gold nanostructures due to its thiol group.
- Thiolated poly adenine, another commonly used SERS probe suitable for gold nanostructures.
- Protoporphyrin IX, a well-known marker in clinical diagnostics of early stages of cancer.
- Azorubine, which is a widely used food and drink additive. Azorubine (Carmoisine, Food red 3 or E 122) was studied for possible effects on human health, due to unavoidable presence of carcinogenic β-napthylamine (Sahu 2014). Its other health effects include inhibition of cholinesterase, skin rash, breathing difficulties and children hyperactivity (McCann et al. 2007). Its presence in food is therefore banned (USA, Japan) or limited in various countries. In EU the limit is set to 50-500 mg/kg depending on food type.

# 2. Aims of thesis

The main goal of this thesis is to explore the properties of SERS substrates, optimize them and develop methods of handling for specific combinations of substrates and analytes. Such discoveries can be applied either in direct sensor development for the specific studied biomolecules, or for further study of chemically and structurally similar molecules (like benzocaine and cocaine). SERS has already been proven to be a very useful tool in a number of similar bioanalytical or forensic applications (Baia et al. 2008; Procházka 2016; Schlucker 2014). The utilized substrates were gold HCL discs, cones and dimers (Institute of Photonics and Electronics, Czech Academy of Sciences), magnetron sputtered silver nanorods and island films (Department of macromolecular physics, Charles University) and gold-coated FON (Faculty of Nuclear Sciences and Physical Engineering, Czech Technical University).

We initially focused on specific properties of SERS substrates and their handling, which are independent of analyte. We used the HCL substrates and silver nanorods with the aim to optimize the process of analyte deposition and to analyse the sources of SERS signal variability. The aim was to optimize the methodics for future use in practical applications.

The experience obtained from these experiments was then used in SERS detection of multiple biologically important molecules, most dominantly food additive azorubine in commercially-available products. The aim was to develop a SERS sensor application comparable with other commonly used methods, both for the detection and quantification of azorubine.

Apart from the development of measurement methods under “dry” conditions, a number of substrates and molecules were tested for use in a flow cell, fabricated at the Institute of Photonics and Electronics, Czech Academy of Sciences. The flow cell advances the possibilities of SERS sensors, as it enables a direct, real-time monitoring of chemical reactions and events.

# 3. Results and Discussion

This chapter summarizes the results from four published papers in international impacted journals. All of them are attached as part of this thesis.

## *3.1 Experimental conditions and equipment*

All experiments were carried out under standard laboratory conditions. Two SERS spectrometers were used, LabRam HR 800 (Horiba Jobin-Yvon) with an integrated CCD detector and two gratings of 300 and 600 g/mm, and WITec micro-Raman spectrometer with a grating of 600g/mm (azorubine study). The collection time was 10×1s for measurements under dry conditions and 6×10s for measurements in microfluidics. The WITec spectrometer enabled continuous mapping with speed of 1s per point in line. The most commonly employed laser line was 632.8 nm from He-Ne lasers on both spectrometers. The laser power was 1mW - 10μW when measuring with LabRam and 1 mW with WITec. Other laser lines include 514.5 nm from $Ar^+$ laser and 785 nm from diode laser. Absorption spectra were measured using Lambda 12 (Perkin-Elmer) UV-Vis spectrometer with 1 nm step.

## *3.2 HCL substrates*

### 3.2.1 HCL substrates characterization

The gold HCL substrates were fabricated at the Institute of Photonics and Electronics, Czech Academy of Sciences. There were three types of substrates, discs, cones and dimers fabricated on glass support as well as silicon wafer. The AFM images of all three types of substrates are shown in fig. 3.2.1.

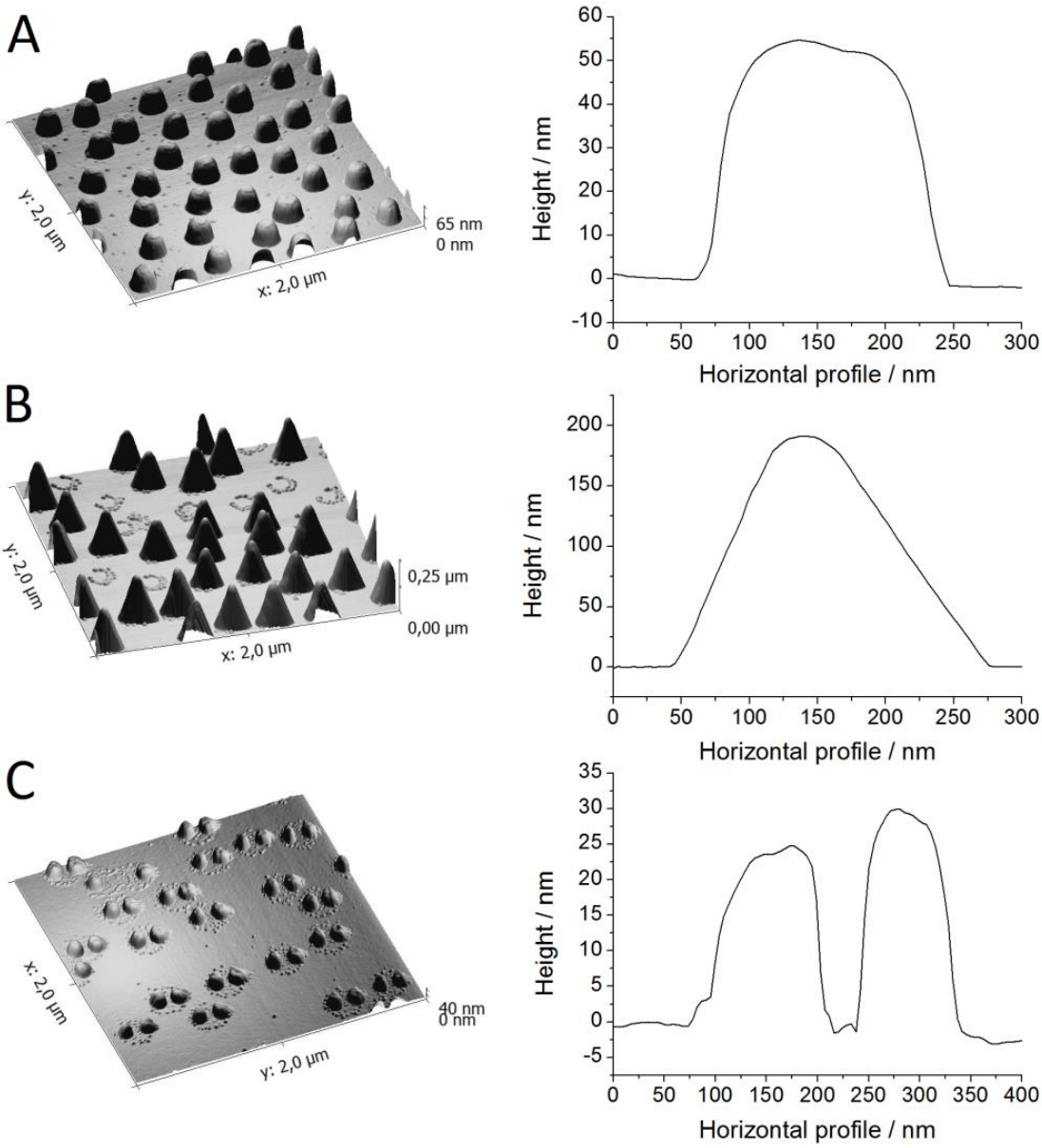


**Fig. 3.2.1:** AFM images of HCL-fabricated gold discs (A), cones (B) and dimers(C). Their average density was 11.1 ± 0.9, 9.6 ± 0.9 and 10.0 ± 0.2 pcs/µm$^2$ respectively. The diameter was 200 nm.

Absorption spectra were collected for substrates fabricated on glass, and the most appropriate laser line of 632.8 nm was selected for further measurements.

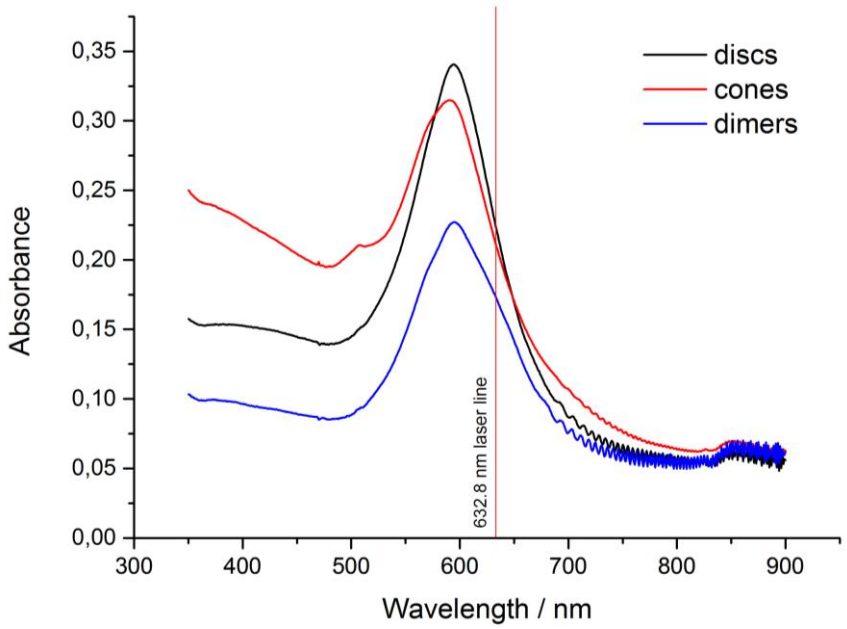


**Fig. 3.2.2:** Absorption spectra of HCL-fabricated substrates on glass in air with indicated laser line. The resonance in longer wavelengths is a product of interreflection inside the thin glass slide.

### 3.2.2 Optimization of SERS sensor handling

Signal enhancement and uniformity of SERS sensors are usually directly associated with the substrate fabrication process and morphology, but the resulting SERS maps can be affected by other experimental factors. The first factor, which influences SERS measurements, is the method of analyte application onto a solid substrate. There are two most widely used methods for this, incubation and droplet deposition and drying. Whilst incubation results in a homogeneous coverage of SERS substrate surface with analyte, some types of analytes do not bind very well to surface and the resulting signal is poor due to low surface concentration of the analyte. Droplet deposition overcomes the binding issues, but the analyte is distributed inhomogeneously on the surface, resulting in higher RSD values.

The first experiments therefore explored different methods of analyte application. HCL-fabricated gold discs substrate was cut into three pieces, and each piece was used for a different analyte application method. First piece was incubated in $10^{-6}$ M MB aqueous solution for 1 hour, and after removal cleaned and dried with

an air stream. On second piece a 5 µl droplet of $10^{-6}$ M MB aqueous solution was deposited and left to evaporate in ambient atmosphere. On third piece a 5 µl droplet of $10^{-6}$ M MB ethanoic solution was deposited and left to evaporate in ambient atmosphere. All three substrates were then used for Raman mapping of three 7x7 points maps, and the area of 1621 $cm^{-1}$ peak of MB was used for plotted together with white field optical microscope images from the substrates (see Fig. 3.2.3 and details in suppl. IV). The results have shown that incubation results in the smallest RSD (19%), due to homogeneous analyte distribution. All future experiments then utilized the incubation method, only with differing analytes, analyte concentrations and incubation times.

Different HCL substrates (discs, cones, dimers) were tested using the incubation in $10^{-6}$ M MB aqueous solution method and subsequent Raman mapping (suppl. IV), using 100 µW laser power on the sample with 50x objective (laser spot diameter 1.4 µm) on LabRam spectrometer. Although there was a correlation between the observed SERS intensity and the level of background fluorescence, the quantitative analysis of averaged spectra showed no direct proportionality between SERS intensity and fluorescence background. While the ratio of SERS intensity for discs, cones and dimers was 1 : 3.3 : 1.5 respectively, the ratio of fluorescence levels was 1 : 3.1 : 2.6. The cones therefore provided the highest enhancement as well as the best signal-to-background ratio. The mapping on clean substrates revealed no stray peaks, with laser power of 100, 10 and 1 µW. The fluorescence background was independent on the deposited analyte, as even freshly fabricated substrates exhibited it, and it was therefore assumed to be intrinsic fluorescence of the gold structures themselves.

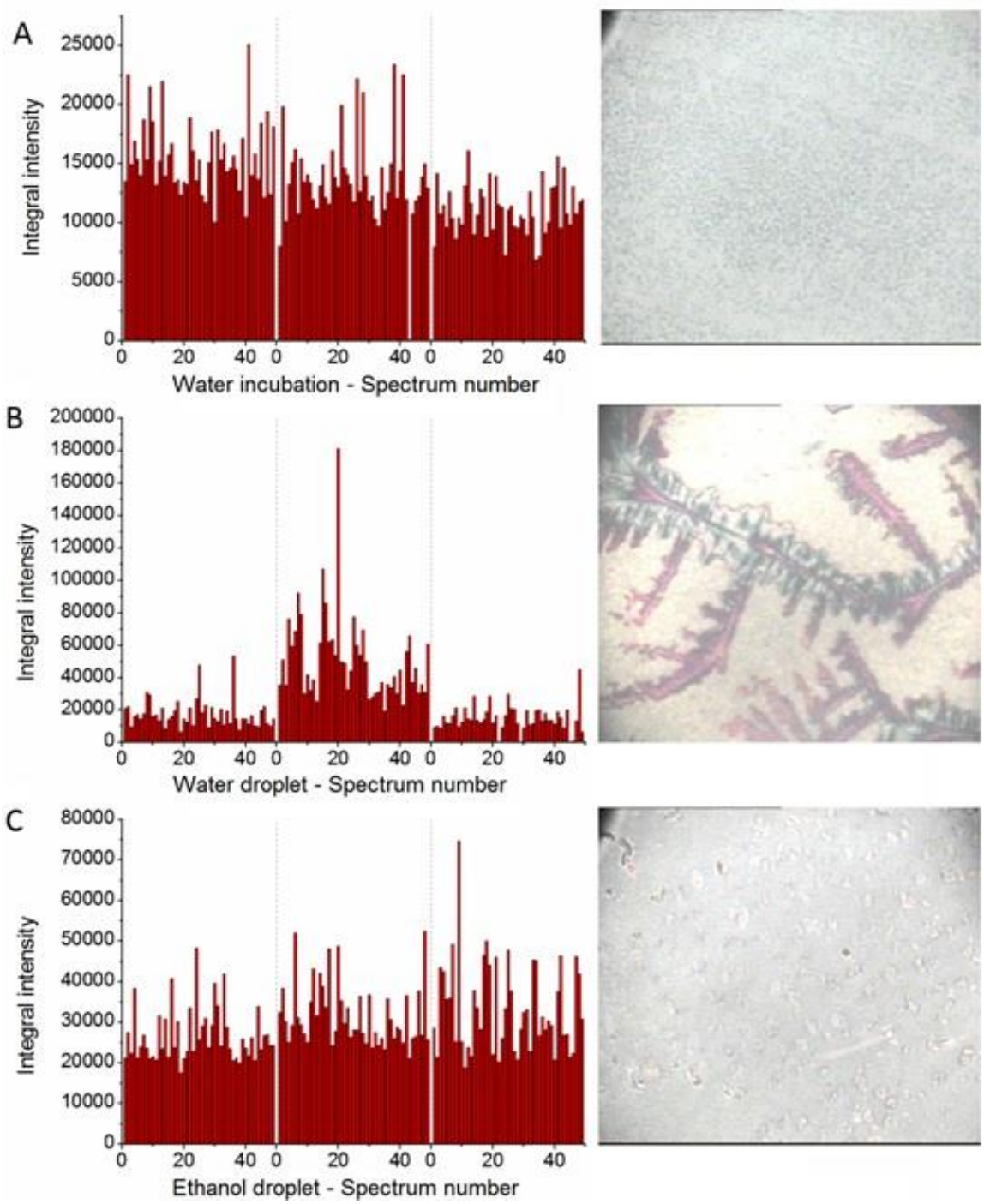


**Fig. 3.2.3:** Left: Variation of the baseline-corrected integrated intensity of the 1620 $cm^{-1}$ peak of MB deposited by different methods (A – incubation in aqueous solution, B – $H_2O$ droplet drying, C – ethanoic droplet drying) over three different mapping areas on the nanodisc substrate. Right: Optical microscopy images of the substrates (100x magnification).

The RSD from all three types of HCL substrates was very similar, 19%, 20% and 20% respectively. The origin of this RSD was however unclear and was a subject

of additional study. The cones substrate was mapped using 100x objective (laser spot diameter 0.86 μm) and 10x objective (laser spot diameter 3.09 μm). The RSD from resulting maps was 29% and 12%, respectively. That indicated the fact that the experimental conditions strongly affect the evaluation of signal reproducibility on a SERS substrate. The RSD, as a function of laser spot diameter ($d_f$) depends on four factors. First is the varying density of individual particles on the substrate ($RSD_{dens}$), which as determined using AFM mapping. Second is the varying amount of randomly-distributed particles present in the laser spot ($RSD_{numb}$). Third is the variation of SERS signal from individual nanoparticles ($RSD_i$) and fourth are the imperfections in measurement process, including laser power stability, spectrometer noise effects and imperfections in the calculation of peak intensity ($RSD_{ap}$). In repeated experiments we found this value to be 3-6%. These factors combined together give the resulting RSD, according to eq. 5.

$$RSD(d_f) = \sqrt{RSD_{dens}^2 + RSD_{numb}^2(d_f) + \frac{RSD_i^2}{N(d_f)} + RSD_{ap}^2} \qquad (5)$$

where $N$ stands for the number of particles within a laser spot. The values of $RSD_{numb}$ were investigated using a computer simulation, using a 20x20 μm area covered with non-overlapping circles of the same size and density as determined from AFM scans. A circle representing the laser spot diameter was then randomly placed to various positions inside the area and the number of particle centres within it was calculated. This was performed both for random and ordered distribution of nanoparticles (the real distribution is semi-regular, due to repulsive forces between the polystyrene nanoparticles during substrate fabrication). The results, summarized in Table 1, demonstrate that the most significant effect for resulting RSD is the variation of SERS signal from a single nanoparticle. The most reproducible nanoparticles were cones, with variation between 51% and 45%; least reproducible were dimers with 69%-46%. Lower, but still significant variations in the SERS signal may be caused by variations in the number of the nanoparticles in the laser spot. In both cases the signal variability can be decreased when the laser spot diameter is increased and/or the measurements are carried out for several laser spot positions and averaged. Maps from all three substrates also exhibited a positive skewness value, indicating the presence of strongly enhancing hot-spots, most notably the dimers.

**Table 1.** Experimental and theoretical evaluation of relative standard deviation (RSD) of SERS intensity on three different types of HCL nanostructures.

| Nano-structure | Density ($\mu m^{-2}$)[a] | $RSD_{dens}$ (%)[a] | Objective | $RSD$ (%)[b] | Skewness[b] | $RSD_{numb}$ (%)[c] | $RSD_i$ (%)[d] |
|---|---|---|---|---|---|---|---|
| discs | 11.1 | 8 | 50× | 19 | 0.41 | 6 , 13 | 62 ; 40 |
| cones | 9.6 | 9 | 10×<br>50×<br>100× | 12<br>20<br>29 | 0.75 | 1.5 , 4<br>7 ; 11<br>17 ,20 | 51 ;<br>45[e] |
| dimers | 10.0 | 2 | 50× | 20 | 0.77 | 7 ; 15[f] | 69 ; 46 |

[a] Average surface density of nanoparticles determined with AFM and its RSD.

[b] RSD and skewness of measured SERS intensity obtained from 7×7-point maps.

[c] Numerically determined RSD due to variable number of nanoparticles in the laser spot. Values for uniform (first number) and random (second number) distribution of nanoparticles are given.

[d] Variation of SERS signal from a single nanoparticle calculated according to Eq. 5. The first number corresponds to $RSD_{numb}$ calculated for uniformly distributed nanoparticles and the second to the random distribution.

[e] $RSD_i$ values for nanocones were obtained by the least square fit (see the Supplementary Material for details).

[f] $RSD_{numb}$ values for nanodisc dimers were estimated considering the nanoparticle density and area of the nanoparticle base

### 3.2.3 Flow cell measurements

The HCL substrates on glass are optically transparent, which is necessary for any setup involving microfluidics. Microfluidics, combined with SERS, presents a potent tool for kinetics studies, as the flow transfers the temporal information spread into spatial, and possible in-situ measurements. A flow cell was constructed with collaboration of the Institute of Photonics and Electronics. The flow cell consisted of three layers. Bottom layer was a 25.4x25.4 mm glass slide covered with HCL-fabricated nanodiscs on the channel side. Middle layer was a PFTE gasket with the channels cut into the gasket. The channels were cut in a H pattern (see fig. 5 right). Top layer was a PDMS block with four screw-threaded holes drilled into it, each leading into one of the vertexes of the H pattern. The flow cell was placed into a steel holder and the layers were tightly pressed together. The optofluidic system was completed with two PEEK tubes with 0.8 mm outer diameter and 0.25 mm inner diameter screwed into two opposing inlets and two PEEK tubes with 0.8 mm outer

diameter and 0.5 mm inner diameter screwed into the remaining two inlets. The tubes with 0.5 mm inner diameter acted as waste outlets and tubes with 0.25 mm inner diameter were connected to high-precision pumps (KD Scientific) used to drive analyte and water/ethanol used as cleaning solvent into the system.

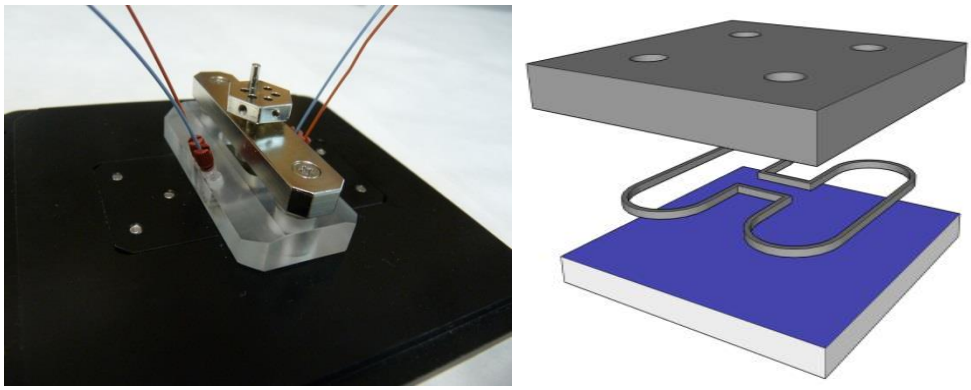

**Fig. 3.2.4:** Left – photo of the flow cell. Right – schematic of layer composition of the flow cell.

In this setup the two diagonally opposing vertexes are used as inlets, one for analyte and one for cleaning solvent. The other two are used as waste outlets. When the analyte is being pumped inside, the waste outlet in the same wing is sealed, forcing the liquid to pass through the middle. When the operating mode is switched to cleaning of the system, the waste outlet is opened and the other is sealed, causing the analyte to avoid the middle point and flow directly into the waste, while the cleaning solvent passes through the middle part. This minimizes the "memory effect" by minimizing the area that needs to be cleaned from sediments attached to channel walls. The washing of these sediments away causes significant delays between switching different analytes, repeating measurements, etc.

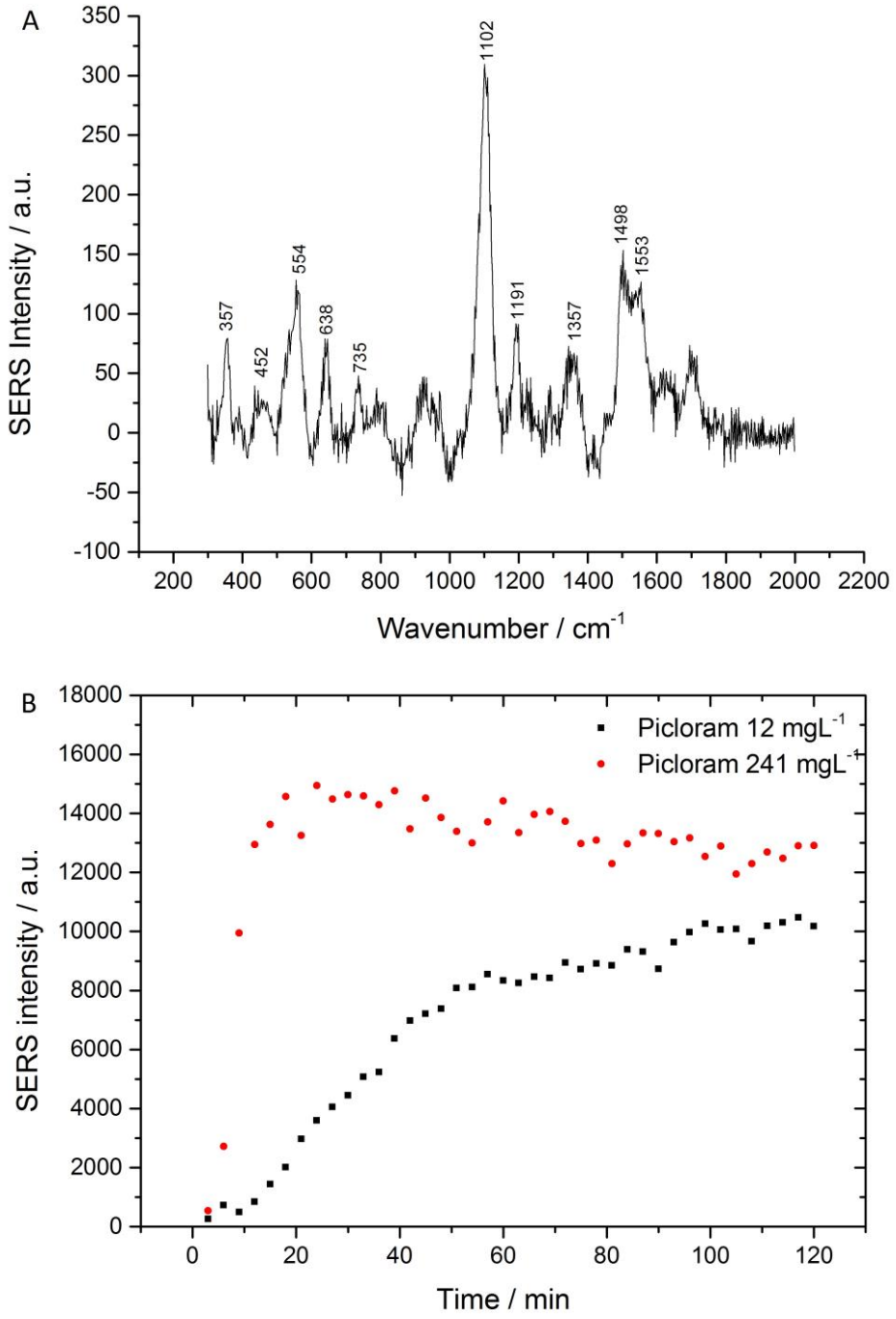


**Fig. 3.2.5:** A – SERS spectrum of 12 $mgL^{-1}$ picloram in flow cell. B - Performance of flow cell with picloram (1102 $cm^{-1}$ peak).

The flow cell utility was tested using picloram herbicide. It has a rich SERS spectrum (Fig. 3.2.5 A), with the most dominant peak at 1102 $cm^{-1}$. The system was injected with several different concentrations of picloram and the intensity of 1102 $cm^{-1}$ peak was monitored. The SERS spectrum was visible in concentrations as low

as 1 $mgL^{-1}$, despite significant background fluorescence. Fig. 3.2.5 B shows the rate of picloram adsorption onto the metal substrate for two different concentrations.

The cleaning of picloram with distilled water took 1 hour, when using ethanol, the SERS signal disappeared within 3 minutes after switching. This shows a clear potential for such gold substrates to be employed in environment monitoring, as such a flow cell device can be easily placed into a water stream and then operate autonomously.

## *3.3 OAD substrates and silver island films*

### 3.3.1 OAD substrates characterization

The OAD substrates were fabricated at the Department of macromolecular physics, Charles University. The silver nanorods were fabricated on a silicon wafer. The resulting substrate (shown on fig. 3.3.1) was not transparent and therefore the absorption spectra could not be obtained. The laser lines of 514.5, 632.8 and 785 nm were tested on LabRam spectrometer, with 632.8 nm line of He-Ne laser was found to provide the best SERS enhancement and signal-to-noise ratio (determined via mapping of the substrate incubated in $10^{-6}$ M MB aqueous solution).

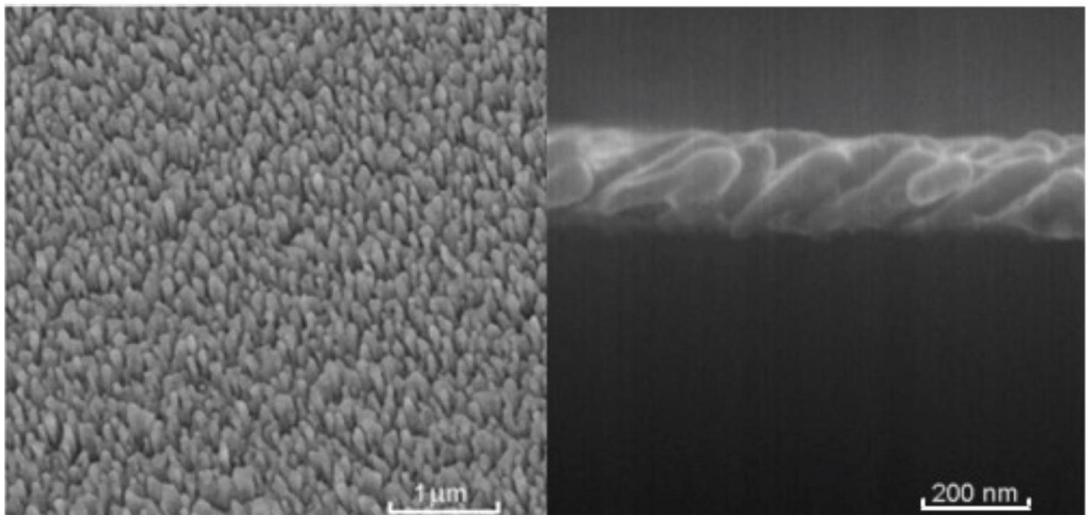


**Fig. 3.3.1:** OAD-fabricated silver nanorods. Left: top view, right: side view.

The reproducibility and SERS signal enhancement of silver nanorods was tested using a similar method as in the case of HCL substrates. A much higher enhancement was expected due to better silver properties, as well as a downgraded stability of the substrate. The substrates were prone to contamination with random

ambient aerial carbonaceous species, whose SERS bands overlapped with the bands of studied molecule. Such issue was previously described (Negri et al. 2011), and the recommended solution was to expose the substrate to $Ar^+$ plasma. It was however reported that this treatment led to a decrease in SERS enhancement by a factor of 2-10. In our case was this issue solved by keeping the substrates in the vacuum right after their fabrication, or by 5-minute ultrasonic treatment. Although the ultrasonic treatment was more effective, the SERS intensity of molecules adsorbed on treated substrates was approximately 4 times worse than on untreated substrates. By extending the time for which the substrates were kept in the vacuum the parasitic bands gradually decreased with no apparent effect on the SERS effectiveness, up to almost complete suppression after overnight storage in vacuum (Subr et al. 2015b) (suppl. II).

### 3.3.2 Silver island film characterization

Silver island films were fabricated at the Department of macromolecular physics, Charles University (Subr, et al. 2015a). The silver metal layer beneath 40 nm PFTE layer was omitted to obtain a transparent substrate, on the expense of further SERS signal enhancement. The transparent Ag island film was deposited on a glass substrate, and its absorption spectra were collected. With extinction maximum at 612 nm the red laser line of 632.8 nm was selected for further measurements. Laser line of 514.5 nm was also tested, as it also matched with the extinction spectra and yielded qualitatively comparable results to 632.8 nm during measurements in ambient atmosphere (both lines are indicated on fig. 3.3.2). Its SERS intensity was however significantly diminished when the substrates were submerged in water and the extinction maximum was red-shifted by about 8 nm into longer wavelengths.

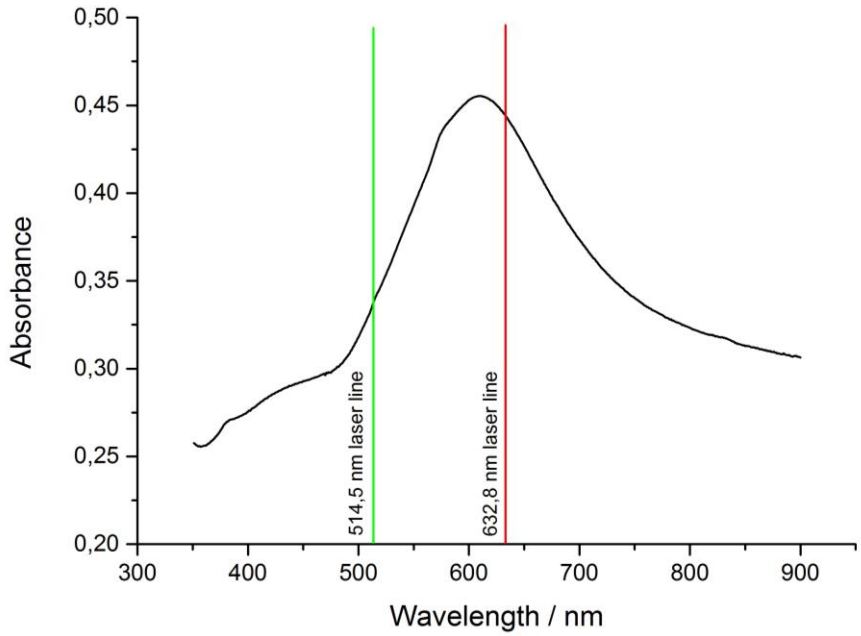


**Fig. 3.3.2:** Absorption spectra of Ag island film on glass in air with possible indicated laser lines.

### 3.3.3 SERS on OAD substrates

The initial tests with MB showed that OAD substrates provided a very strong SERS enhancement, which was even further improved when a silver mirror-like layer was deposited onto the surface prior to OAD deposition. The sensitivity of the substrates was tested using MB and three free-base porphyrins ($H_2$TMPyP, $H_2$TMAP, $H_2$TSPP) and tryptophan, with concentrations down to $3\text{-}5\times10^{-7}$ M for porphyrins and $1\times10^{-5}$ M for tryptophan.

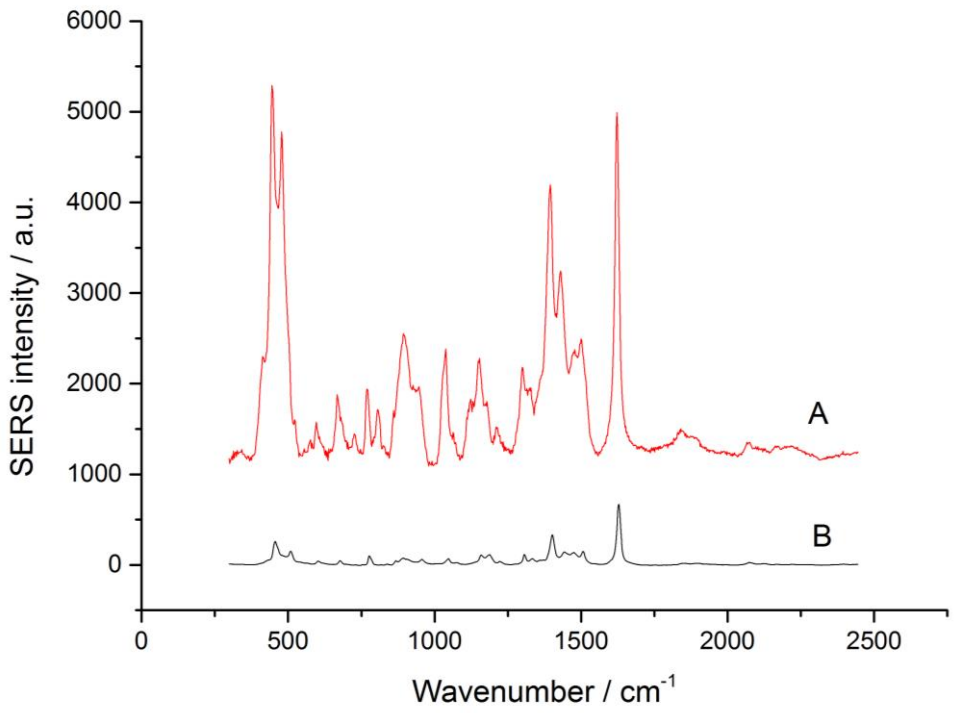


**Fig. 3.3.3:** SERS spectra of $1\times10^{-6}$ M MB on OAD substrates (A) and HCL discs (B) for comparison. The spectra are background-corrected and vertically shifted for clarity.

The most important part of this testing was a shelf-life measurement of the silver substrates. Silver substrates are often prone to degradation and oxidation of the surface, leading to a decrease of SERS signal enhancement and appearance of stray peaks from contaminants. The clean OAD substrates, treated with vacuum after their fabrication, were kept in locker storage at room temperature for one year. The resulting SERS measurement showed only a minimal decrease in SERS intensity, and an increase in fluorescence background.

### 3.3.4 Silver island film substrates in microfluidics

As silver provides a much higher enhancement compared to gold, it seems more suitable for use in a microfluidic flow cell, where the signal loses are far more significant compared to routine microscope measurements. The flow cell was assembled with Ag island film substrates inside and its capabilities were tested using dipicolinic acid.

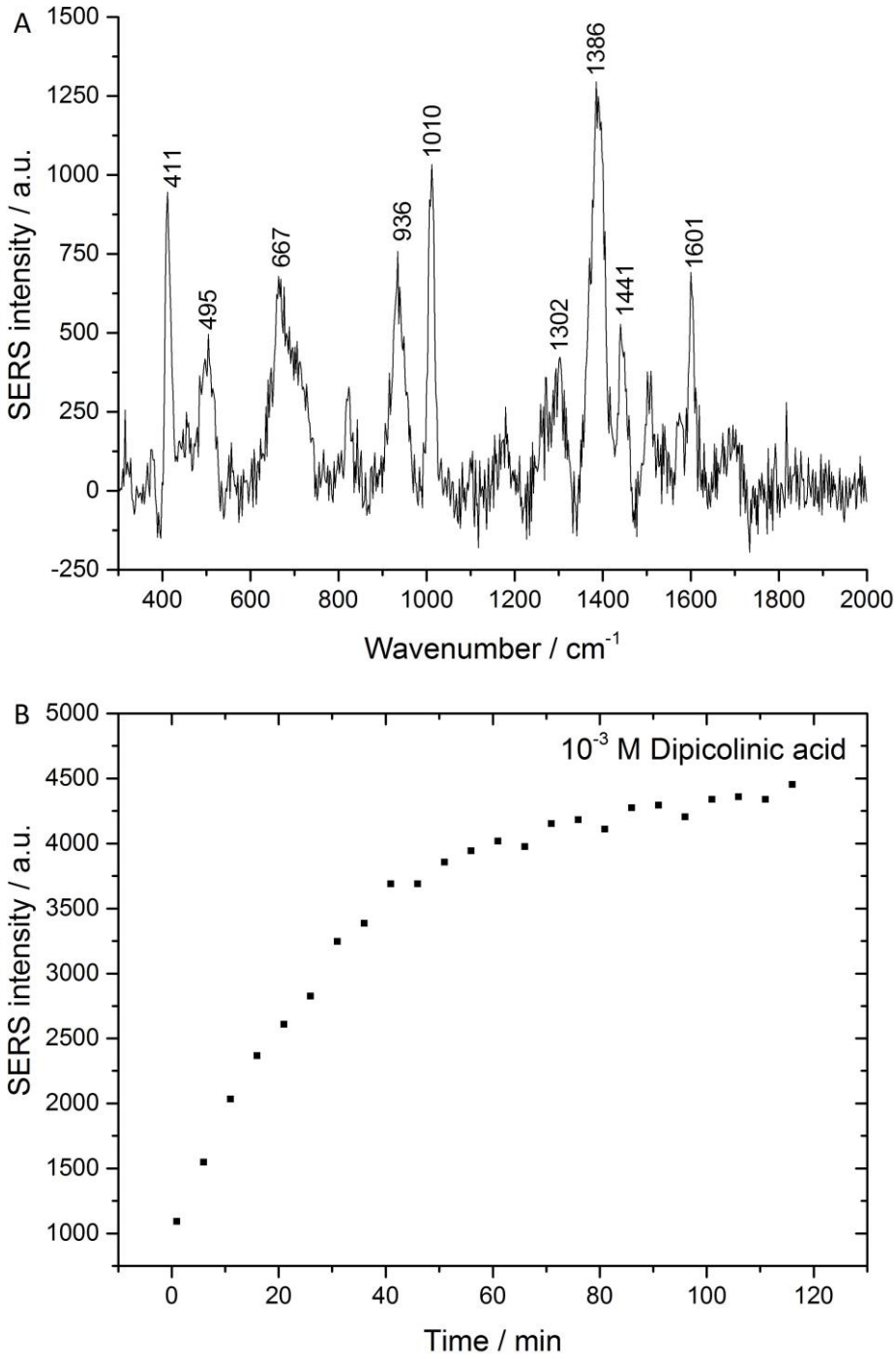


**Fig. 3.3.4:** A – SERS spectrum of $10^{-3}$ M dipicolinic acid on OAD substrates. B – Performance of flow cell with Ag island film substrates and dipicolinic acid.

The initial measurements appeared promising, as a very strong SERS signal from 1010 $cm^{-1}$ peak of dipicolinic acid showed a clear approach into adsorption equilibrium. However, the silver structures were far less stable and robust than the gold structures and washing away of large parts of structures was repeatedly observed. It can be most likely attributed to a significant capillary pressure extended

on the channel walls, which lead to their erosion and breakdown. It was concluded that albeit its strong enhancement this kind of silver structures is not suitable for practical application in a flow cell.

## *3.4 FON substrates*

### 3.4.1 FON substrates characterization

The FON substrates were fabricated at the Faculty of Nuclear Sciences and Physical Engineering, Czech Technical University. The monolayer formed at the water-air surface was homogeneous on a centimetre scale, and easily transferable onto silicon support (Štolcová 2011). The resulting substrate (fig. 3.4.1) was also not transparent and different laser lines had to be tested. Both 632.8 and 785 nm provided good SERS enhancement, and the fluorescence background for 632.8 nm was smoother.

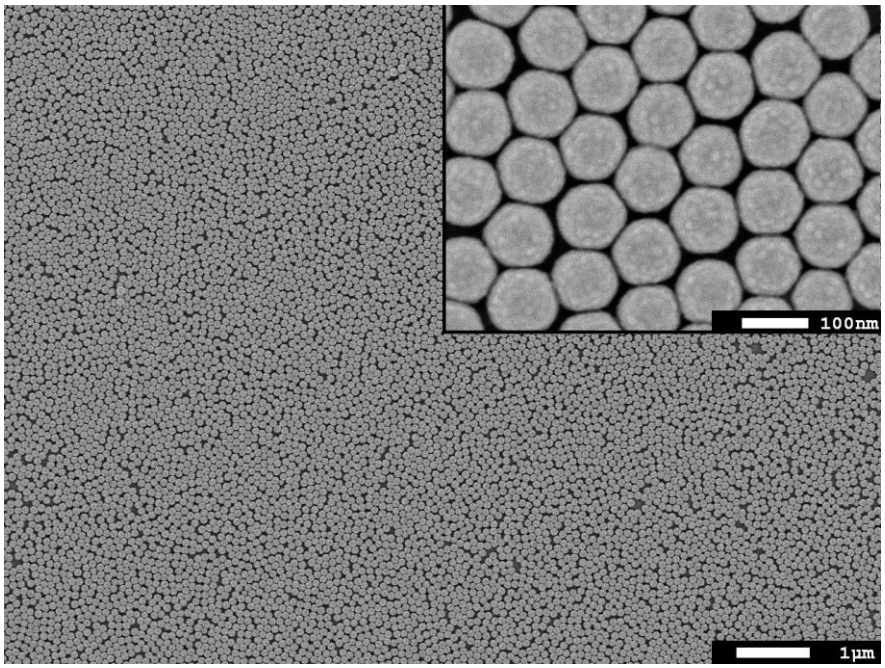


**Fig. 3.4.1:** SEM image of gold FON consisting of 107 nm polystyrene beads covered with 20 nm of sputtered gold. Inset: Detail of the structure.

A significant advantage of this substrate is the presence of 520 $cm^{-1}$ peak of silicon. Raman mapping of the substrate has shown it has a RSD of less than 4% (see fig. 3.4.2). Therefore, the peak can be employed as an internal standard for further measurements.

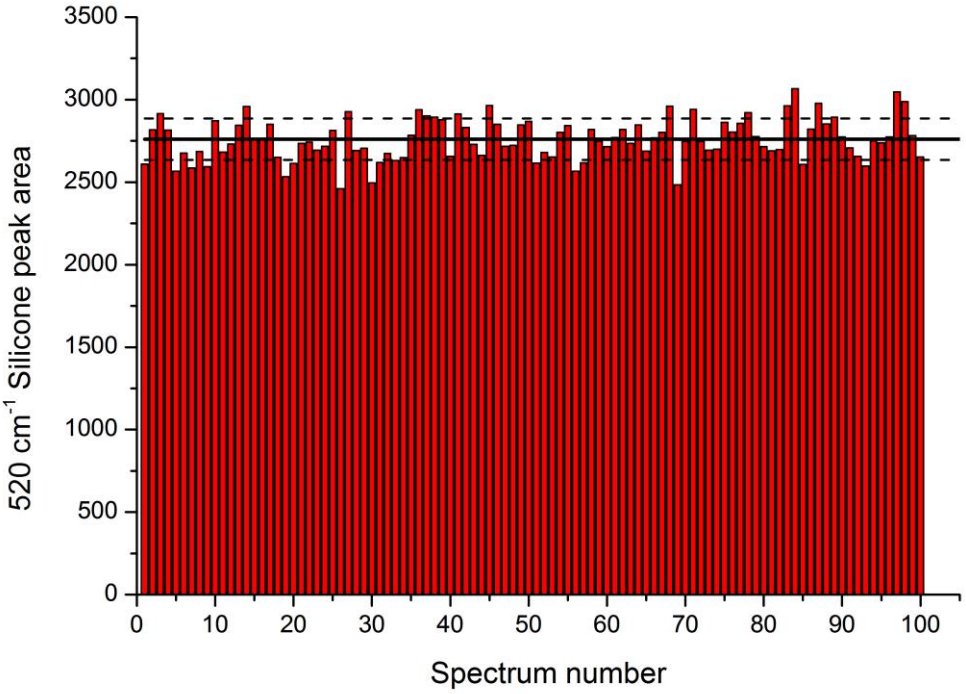


**Fig. 3.4.2:** Stability of the 520 $cm^{-1}$ Si peak on FON substrate, RSD is below 4%.

### 3.4.2 Detection of important biomolecules on FON substrates

The FON structure was found to provide a strong and stable SERS enhancement (suppl. V). The uniformity of the FON substrates was tested using incubation in TMPyP porphyrin under the conditions described in chapter 3.1.2. The resulting RSD of TMPyP was found to be 17-19% in single 10x10 point maps, using a 100x objective, which is far better, compared to RSD of 29% on HCL substrates using the same objective (Fig. 3.4.3). The sensitivity was tested using *p*-ATP as a probe for a comparison with other gold substrates that were previously reported. The lowest detectable concentration of *p*-ATP was $10^{-7}$ M (Fig. 3.4.4 A), compared to previously reported $10^{-3}$ M on bigger PS spheres (Baia et al. 2006; Farcau and Astilean 2010). A number of other biomolecules was detected using gold FON substrates. The FON substrates were incubated in different concentrations of water-dissolved analytes. Background spectrum of FON substrate had to be in some cases subtracted from the resulting spectra to erase stray signals from polystyrene. The measured molecules, together with their respective lowest detected concentrations, are shown in fig. 3.4.4 B and fig. 3.4.5.

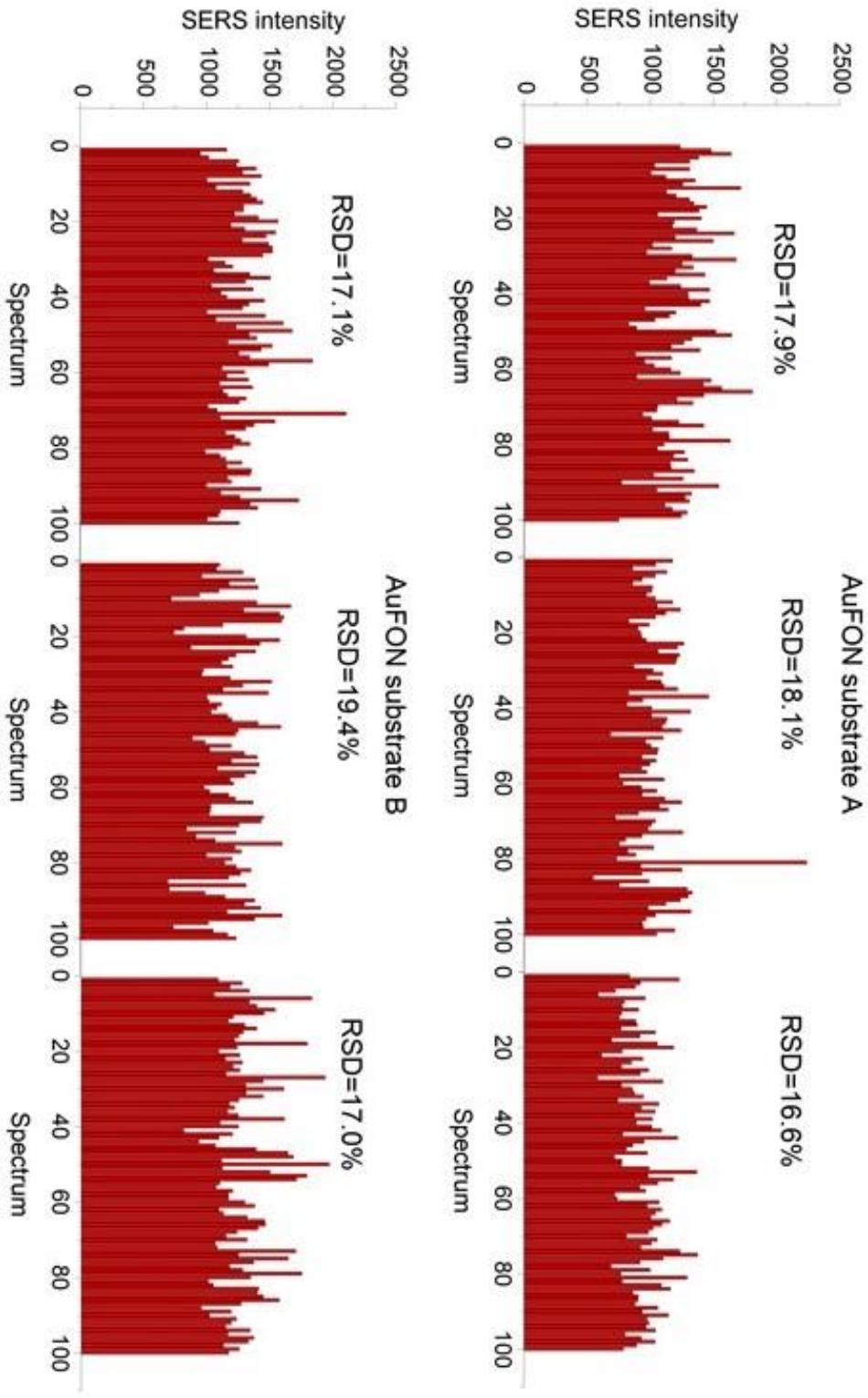


**Fig. 3.4.3:** RSD of $1\times10^{-6}$ M TMPyP peak at 1220 $cm^{-1}$ on gold FON substrates from two different batches.

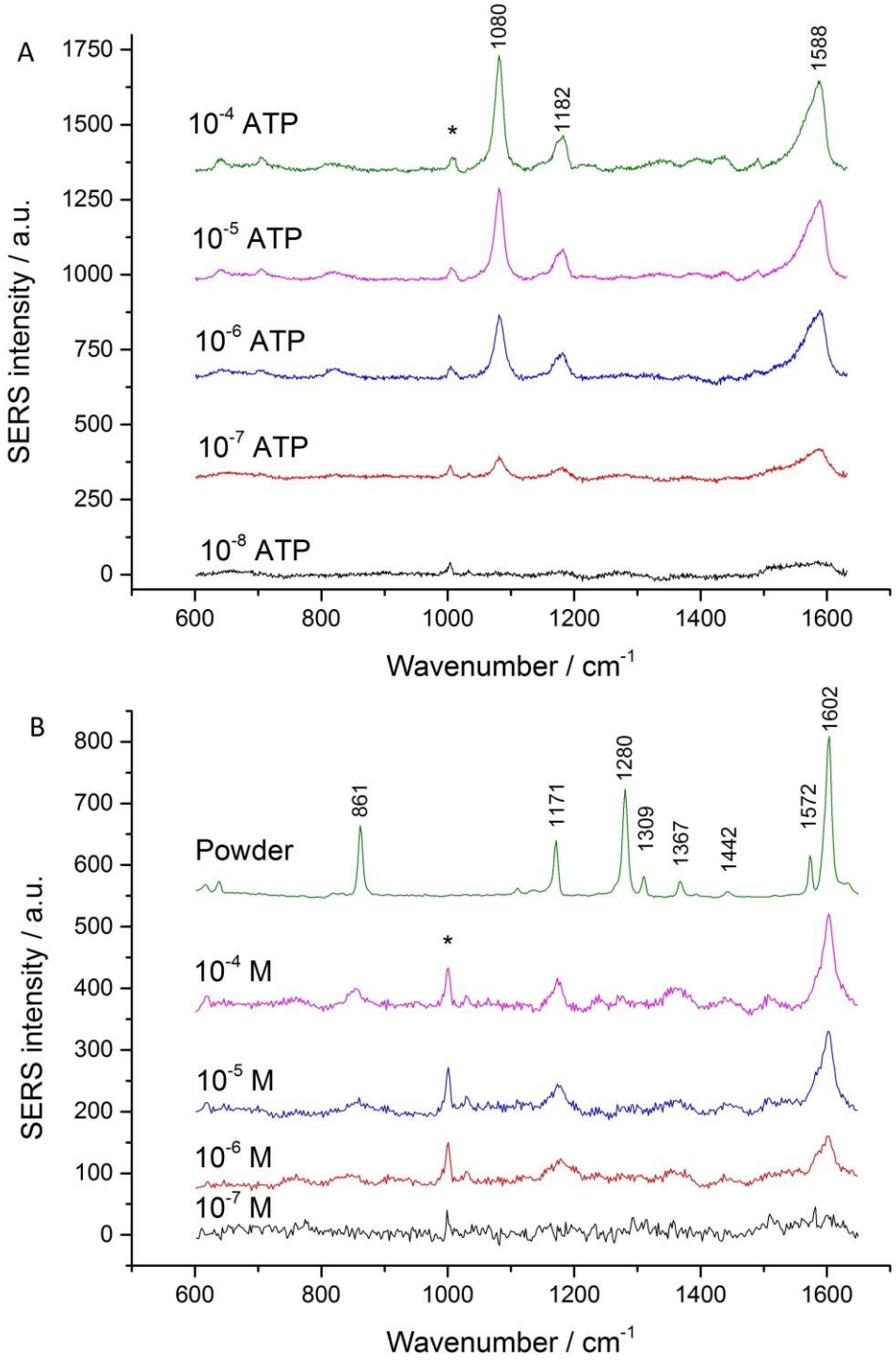


**Fig. 3.4.4:** SERS spectra on gold FON incubated in different concentrations of *p*-ATP (A) and benzocaine (B). Powder spectrum from *p*-ATP was not obtained due to a strong fluorescence background of the powder. Spectra are vertically shifted for clarity. Asterisk (*) denotes Raman signal from PS nanospheres.

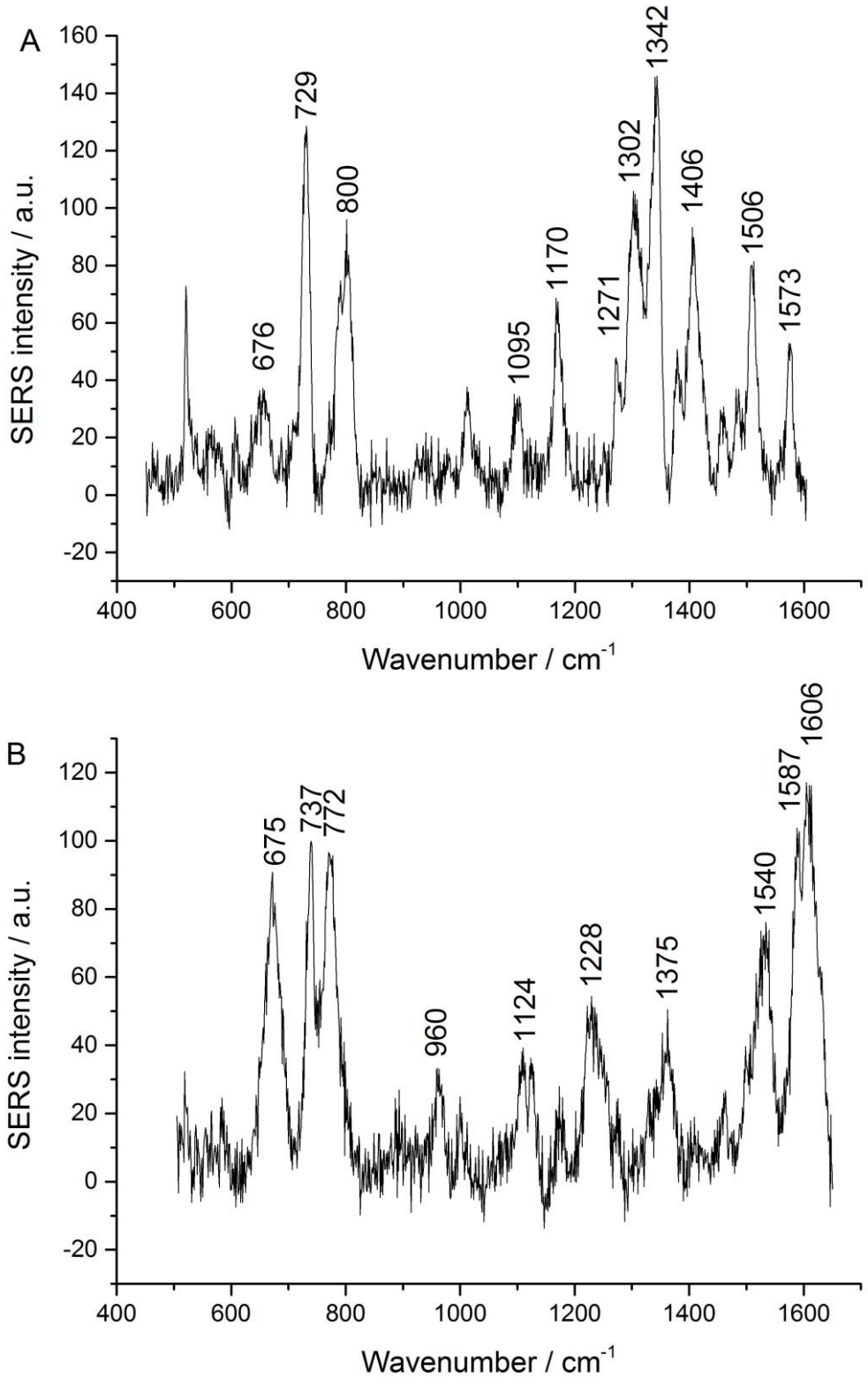


**Fig. 3.4.5** SERS spectra of different biomolecules detected on FON substrates. A - 10-mer thiolated polyA ($8\times10^{-5}$ M concentration in base pairs), B- protoporphyrin IX ($1\times10^{-5}$ M incubation concentration).

### 3.4.3 Detection of azorubine in complex matrices

Food colourants are widely used as additives in both food and drinks to increase their visual attractiveness or to restore their original appearance when it has been lost in production process. Most widely employed methods for their control are high-performance liquid chromatography (HPLC), high-performance ion chromatography or enzyme-linked immunosorbent assay. These approaches are generally time and money-consuming, and require large-scale laboratory equipment. It was therefore desirable to provide a fast and reliable method for detection of small colourant molecules within complex matrices, without the need for extensive laboratory pre-treatment.

Gold FON fabricated on a silicon wafer was selected for task, since it is a structure providing strong SERS signal with very low RSD. In addition the silicon peak was necessary as internal standard for spectral normalization. Seven different sweet drinks were purchased in stores in Czech Republic and Germany, five positive containing azorubine (energy drink, grenadine, strawberry and passion fruit vodka, raspberry lemonade) and two negative controls without azorubine (blood orange lemonade, raspberry syrup). Incubation method in aqueous solutions was used throughout all experiments to avoid unnecessary SERS signal deviations due to varying surface concentration, with 30 minutes incubation time. To find an approach how to determine the content of azorubine in commercial samples SERS spectra of azorubine adsorbed on FON from aqueous solutions in wide concentration range were measured. The SERS spectra were normalized using the 520 $cm^{-1}$ Si peak intensity, and SERS signal strength was monitored from the intensity of 1356 $cm^{-1}$ azorubine peak. The resulting points were fitted with Freundlich adsorption isotherm, which reflects the inhomogeneity of the binding sites on the FON surface, as shown on fig. 3.4.6. (suppl. I)

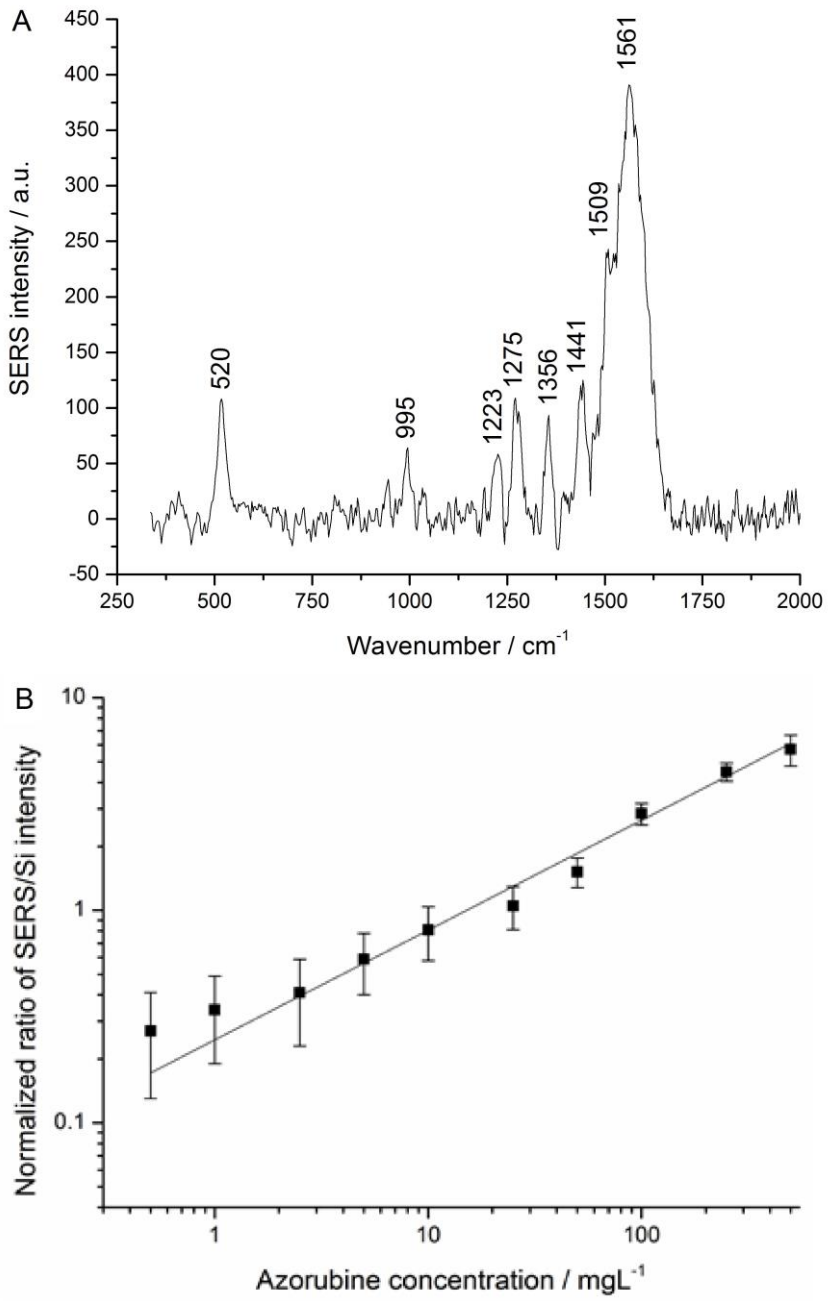


**Fig. 3.4.6:** A – background-corrected SERS spectrum of azorubine on FON. The ratio of azorubine peak at 1356 $cm^{-1}$ and Si peak at 520 $cm^{-1}$ was used for concentration estimation. B - Calibration curve of normalized SERS intensity of azorubine in water versus azorubine concentration.

Each of the sweet drinks had a different composition, with different sweetening agent and its concentration, alcohol content, microparticles etc. All of these factors influence the outcoming SERS signal, and to assess their impact a complete chemical analysis of the drinks would have to be made prior to measuring

azorubine content. The only pre-treatment of the samples was dilution 1:5 with water, to reduce the sugar concentration, since it was the main source of fluorescence and in addition it created large drying patterns across the entire substrate surface. The issue with sugar residues blocking the SERS-active surface was solved using an air stream directly after the substrate removal from solution. Although most of the substrate was covered with sugar stains, the edges were cleaned and it was possible to obtain unhampered SERS signal from them. Raman mapping was performed on the edges using WITec spectrometer to obtain average SERS spectra for all seven sweet drink samples and using the SERS/Si ratio the original azorubine concentration was estimated using the calibration curve in fig. 3.4.6 (estimated concentration multiplied by 5 to account for previous dilution). The samples were also tested using standard HPLC technique for determination azorubine content. The results are compared in table 2.

**Table 2.** Azorubine concentration in different drinks identified by HPLC and SERS.

| Sample | HPLC ($mgL^{-1}$) | SERS ($mgL^{-1}$) |
|---|---|---|
| Energy drink | 26 ± 2.6 | 27 ± 5 |
| Grenadine | 280 ± 28.0 | 355 ± 77 |
| Strawberry vodka | 12 ± 1.2 | 18 ± 4 |
| Passion fruit vodka | 1.7 ± 0.2 | 4.7 ± 1.8 |
| Raspberry lemonade | 4 ± 0.4 | 5.3 ± 1.4 |
| Blood orange | <0.1 | <0.2 |
| Raspberry syrup | <0.1 | <0.2 |

The SERS quantification of azorubine content successfully distinguished positive and negative samples, and the resulting estimates are within the margin of error for all non-alcoholic samples. In case of alcoholic samples, the resulting estimated concentration was significantly higher than the HPLC result. Further tests have shown that the most likely cause for this is the decrease in surface tension, due to the presence of ethanol. The liquid with a lower surface tension had better penetrated into the gaps in FON structure, thus increasing the effective binding area. The resulting errors from this effect are nevertheless much smaller than the established EU regulations, which permit 50 $mgL^{-1}$ of azorubine in non-alcoholic drinks and 200 $mgL^{-1}$ of azorubine in alcoholic drinks.

# 4. Conclusions

Several types of solid SERS substrates were tested in this work, including HCL-fabricated gold discs, cones and dimers, gold FON, OAD-fabricated silver nanorods and silver island films. Different handling techniques were applied and an optimal method of sensor operation and result evaluation was established. That includes the following:

1. Substrate incubation was determined to result in the most homogeneous sample distribution across the SERS-active surface.
2. Objective magnification (and the corresponding laser spot diameter) was distinguished as a crucial factor in RSD evaluation.
3. Third moment of a SERS intensity distribution from Raman mapping was used for hot-spots presence assessment.
4. Silicon support was evaluated and applied as an internal standard for spectral normalization.

Several biologically important molecules were detected using those substrates and handling techniques:

1. Methylene Blue (probe molecule, all types of substrates)
2. Picloram herbicide (1 $mgL^{-1}$ in water in microfluidics, gold discs)
3. Azorubine (4.9 $mgL^{-1}$ in commercial sweet drinks, gold FON)
4. $H_2TMPyP$, $H_2TMAP$ and $H_2TSPP$ porphyrins (~$10^{-7}$ M in water concentrations, silver nanorods)
5. Tryptophan ($10^{-5}$ M in water, silver nanorods)
6. Dipicolinic acid ($10^{-3}$ M in water in microfluidics, silver island films)
7. Benzocaine, *p*-ATP, SH-polyA, protoporphyrin IX, ($10^{-6}$ M, $10^{-7}$ M, $8\times10^{-5}$ M, $10^{-5}$ M, respectively, in water, gold FON)

Overall a number of SERS substrate + analyte systems was successfully tested. The quantitative azorubine detection in commercially available sweet drinks demonstrated the potential of SERS applications, as the results were comparative with commonly used HPLC method.

# 5. References


BAIA, L., M. BAIA, J. POPP AND S. ASTILEAN Gold films deposited over regular arrays of polystyrene nanospheres as highly effective SERS substrates from visible to NIR. Journal of Physical Chemistry B, Nov 2006, 110(47), 23982-23986.

BAIA, M., S. ASTILEAN AND T. ILIESCU *Raman and SERS Investigations of Pharmaceuticals*. Edtion ed. Heidelberg: Springer-Verlag Berlin, 2008.

CIALLA, D., A. MARZ, R. BOHME, F. THEIL, et al. Surface-enhanced Raman spectroscopy (SERS): progress and trends. Analytical and Bioanalytical Chemistry, Apr 2012, 403(1), 27-54.

DIETZEK, B., D. CIALLA, M. SCHMITT AND J. POPP. Introduction to the Fundamentals of Raman Spectroscopy. In T. DIEING, O. HOLLRICHER AND J. TOPORSKI eds. *Confocal Raman Microscopy.* Berlin, Heidelberg: Springer Berlin Heidelberg, 2011, p. 21-42.

ETCHEGOIN, P., R. C. MAHER, L. F. COHEN, H. HARTIGAN, et al. New limits in ultrasensitive trace detection by surface enhanced Raman scattering (SERS). Chemical Physics Letters, Jun 2003, 375(1-2), 84-90.

FARCAU, C. AND S. ASTILEAN Mapping the SERS Efficiency and Hot-Spots Localization on Gold Film over Nanospheres Substrates. Journal of Physical Chemistry C, Jul 2010, 114(27), 11717-11722.

FLEISCHMANN, M., P. J. HENDRA AND A. J. MCQUILLAN Raman spectra of pyridine adsorbed at a silver electrode. Chemical Physics Letters, 1974, 26(2), 163.

FREDRIKSSON, H., Y. ALAVERDYAN, A. DMITRIEV, C. LANGHAMMER, et al. Hole–Mask Colloidal Lithography. Advanced Materials, 2007, 19(23), 4297-4302.

HAJDUKOVÁ, N., M. PROCHÁZKA, P. MOLNÁR AND J. ŠTĚPÁNEK SERRS of free-base porphyrins on immobilized metal gold and silver nanoparticles. Vibrational Spectroscopy, Sep 2008, 48(1), 142-147.

HAYNES, C. L. AND R. P. VAN DUYNE Nanosphere lithography: A versatile nanofabrication tool for studies of size-dependent nanoparticle optics. Journal of Physical Chemistry B, Jun 2001, 105(24), 5599-5611.

HAYNES, C. L., C. R. YONZON, X. Y. ZHANG AND R. P. VAN DUYNE Surface-enhanced Raman sensors: early history and the development of sensors for quantitative biowarfare agent and glucose detection. Journal of Raman Spectroscopy, Jun-Jul 2005, 36(6-7), 471-484.

CHANEY, S. B., S. SHANMUKH, R. A. DLUHY AND Y. P. ZHAO Aligned silver nanorod arrays produce high sensitivity surface-enhanced Raman spectroscopy substrates. Applied Physics Letters, Jul 2005, 87(3), 3.

KNEIPP, K., Y. WANG, H. KNEIPP, L. T. PERELMAN, et al. Single molecule detection using surface-enhanced Raman scattering (SERS). Physical Review Letters, Mar 1997, 78(9), 1667-1670.

KOSIOREK, A., W. KANDULSKI, P. CHUDZINSKI, K. KEMPA, et al. Shadow nanosphere lithography: Simulation and experiment. Nano Letters, Jul 2004, 4(7), 1359-1363.

LE RU, E. C. AND P. G. ETCHEGOIN *Principles of Surface-Enhanced Raman Spectroscopy and Related Plasmonic Effects*. Edtion ed. Amsterdam: Elsevier, 2009. ISBN 978-0-444-52779-0.

MALINOWSKI, E. R. *Factor analysis in chemistry*. Edtion ed. New York: John Wiley and Sons, 1991.

MCCANN, D., A. BARRETT, A. COOPER, D. CRUMPLER, et al. Food additives and hyperactive behaviour in 3-year-old and 8/9-year-old children in the community: a randomised, double-blinded, placebo-controlled trial. Lancet, Nov 2007, 370(9598), 1560-1567.
NATAN, M. J. Concluding remarks - Surface enhanced Raman scattering. Faraday Discussions, 2006, 132, 321-328.
NEGRI, P., N. E. MAROTTA, L. A. BOTTOMLEY AND R. A. DLUHY Removal of Surface Contamination and Self-Assembled Monolayers (SAMs) from Silver (Ag) Nanorod Substrates by Plasma Cleaning with Argon. Applied Spectroscopy, Jan 2011, 65(1), 66-74.
PALACKY, J., P. MOJZES AND J. BOK SVD-based method for intensity normalization, background correction and solvent subtraction in Raman spectroscopy exploiting the properties of water stretching vibrations. Journal of Raman Spectroscopy, Jul 2011, 42(7), 1528-1539.
PROCHÁZKA, M. *Surface-enhanced Raman spectroscopy, Bioanalytical, Biomolecular and Medical Applications*. Edtion ed.: Springer International Publishing Switzerland, 2016.
RAMAN, C. V. A change of wavelength in light scattering (Reprinted from Nature, vol 121, pg 619, 1928). Current Science, Feb 1928, 74(4), 381-382.
SAHU, J. K. *Introduction to Advanced Food Process Engineering*. edited by J.K. SAHU. Edtion ed.: CRC Press, 2014.
SCHLUCKER, S. Surface-Enhanced Raman Spectroscopy: Concepts and Chemical Applications. Angewandte Chemie-International Edition, May 2014, 53(19), 4756-4795.
SCHLÜCKER, S. SERS Microscopy: Nanoparticle Probes and Biomedical Applications. In *Surface Enhanced Raman Spectroscopy*. Wiley-VCH Verlag GmbH & Co. KGaA, 2010, p. 263-283.
SCHRADER, B. *Infrared and Raman spectroscopy: methods and applications*. Edtion ed.: VCH, 1995. ISBN 9783527264469.
SRICHAN, C., M. EKPANYAPONG, M. HORPRATHUM, P. EIAMCHAI, et al. Highly-Sensitive Surface-Enhanced Raman Spectroscopy (SERS)-based Chemical Sensor using 3D Graphene Foam Decorated with Silver Nanoparticles as SERS substrate. Scientific Reports, Mar 2016, 6, 9.
STOLCOVA, L., J. PROSKA AND M. PROCHAZKA RATIONALLY DESIGNED SERS SUBSTRATES FOR THE ULTRASENSITIVE DETECTION OF BIOLOGICALLY IMPORTANT COMPOUNDS. Nanocon 2013, 2013, 659-664.
SUBR, M., M. PETR, O. KYLIAN, J. KRATOCHVIL, et al. Large-scale Ag nanoislands stabilized by a magnetron-sputtered polytetrafluoroethylene film as substrates for highly sensitive and reproducible surface-enhanced Raman scattering (SERS). Journal of Materials Chemistry C, 2015a, 3(43), 11478-11485.
SUBR, M., M. PETR, V. PEKSA, O. KYLIAN, et al. Ag Nanorod Arrays for SERS: Aspects of Spectral Reproducibility, Surface Contamination, and Spectral Sensitivity. Journal of Nanomaterials, 2015b, 7.
ŠTOLCOVÁ, L. Analysis and realization of nanostructures for surface-enhanced Raman scattering. Czech Technical University in Prague, 2011.
WEISS, A. AND G. HARAN Time-dependent single-molecule Raman scattering as a probe of surface dynamics. Journal of Physical Chemistry B, Dec 2001, 105(49), 12348-12354.

# 6. List of abbreviations

| | |
|---|---|
| CT | Charge transfer |
| FA | Factor analysis |
| FON | Film over nanospheres |
| HCL | Hole-mask colloidal lithography |
| HPLC | High-performance liquid chromatography |
| LSP | Localized surface plasmon |
| MB | Methylene Blue |
| OAD | Oblique angle vapour deposition |
| *p*-ATP | 4-Aminothiophenol |
| PDDA | Polydiallyldimethyl ammonium |
| PMMA | Poly(methylemetacrylate) |
| PFTE | Polytetrafluorethylene |
| RS | Raman scattering |
| RSD | Relative standard deviation |
| SERS | Surface-enhanced Raman scattering |

# 7. List of papers and published conference abstracts

**List of papers:**

1. PEKSA, V., JAHN, M., STOLCOVA, L., SCHULZ, V., PROSKA, J., PROCHAZKA, M., WEBER, K., CIALLA-MAY, D., POPP, J., Quantitative SERS Analysis of Azorubine (E 122) in Sweet Drinks. Analytical Chemistry, Mar 2015, 87(5), 2840-2844. IF 5.89, 21 times cited (by 13.6.2017)

   *Author's contribution*: majority of experimental work, data treatment and writing of the paper

2. SUBR, M., PETR, M., PEKSA, V., KYLIAN, O., HANUS, J., PROCHAZKA, M., Ag Nanorod Arrays for SERS: Aspects of Spectral Reproducibility, Surface Contamination, and Spectral Sensitivity. Journal of Nanomaterials, 2015, 729234. IF 1.76, 2 times cited (by 13.6.2017)

   *Author's contribution*: part of experimental work and data treatment

3. JAHN, M., PATZE, S., HIDI, I. J., KNIPPER, R., RADU, A., MUHLIG, A., YUKSEL, S., PEKSA, V., WEBER, K., MAYERHOFER, T., CIALLA-MAY, D., POPP, J., Plasmonic nanostructures for surface enhanced spectroscopic methods. Analyst, 2016, 141(3), 756-793. IF 4.03, 21 times cited (by 13.6.2017)

   *Author's contribution*: part of writing of the paper

4. PEKSA, V., LEBRUSKOVA, P., SIPOVA, H., STEPANEK, J., BOK, J., PROCHAZKA, M., HOMOLA, J., Testing gold nanostructures fabricated by hole-mask colloidal lithography as potential substrates for SERS sensors: sensitivity, signal variability, and the aspect of adsorbate deposition. Physical Chemistry Chemical Physics, Aug 2016, 18(29), 19613-19620. IF 4.45, 1 time cited (by 13.6.2017)

   *Author's contribution*: majority of experimental work, data treatment and writing of the paper

5. STOLCOVA, L., PEKSA, V., PROSKA, J., PROCHÁZKA, M., Gold film over very small (107 nm) spheres as efficient substrate for sensitive and reproducible surface-enhanced Raman scattering (SERS) detection of biologically important molecules. Submitted to Journal of Raman Spectroscopy.

   *Author's contribution*: Part of experimental work, data treatment.

**List of conference abstracts:**

1. PEKSA, V., LEBRUŠKOVÁ, P., PROCHÁZKA, M., ŠÍPOVÁ, H., et al. SERS substrates fabricated by hole-mask colloidal lithography, poster, *XV European Conference on the Spectroscopy of Biological Molecules*, Oxford, Great Britain, 25.-30. August 2013
2. PEKSA, V., ŠTOLCOVÁ, L., PROCHÁZKA, M., PROŠKA, J., et al. Detection and Quantification of Azorubine (E 122) Dye in Real Food Matrices Using Highly Ordered SERS Substrates, poster, *XIV International Conference on Raman Spectroscopy*, Jena, Germany, 10.-15. August 2014
3. PEKSA, V., CHADT, K., LEBRUŠKOVÁ, P., PROCHÁZKA, M., et al. Fluidic system with regular Au nanostructure array for online sensitive and reproducible SERS detection, poster, *XVI European Conference on the Spectroscopy of Biological Molecules*, Bochum, Germany, 6.-11. September 2015
4. PEKSA, V. CHADT, K., LEBRUŠKOVÁ, P., ŠTĚPÁNEK, J., et al. Real time detection of picloram herbicide using a SERS flow cell, poster, *XXXIII European Congress on Molecular Spectroscopy*, Szeged, Hungary, 30. July – 4. August 2016
5. PROCHÁZKA, M., ŠTOLCOVÁ, L., PEKSA, V., PROŠKA, J., Gold film over very small spheres as a substrate for sensitive and reproducible SERS detection of biomolecules, *XVII European Conference on the Spectroscopy of Biological Molecules*, Amsterdam, Netherlands, 11.-14.September 2017

# 8. Supplements

**Supplement [I]**

PEKSA, V., M. JAHN, L. STOLCOVA, V. SCHULZ, J. PROSKA, M. PROCHAZKA, K. WEBER, D. CIALL-MAY, J. POPP, **Quantitative SERS Analysis of Azorubine (E 122) in Sweet Drinks.** Analytical Chemistry, Mar 2015, 87(5), 2840-2844.

analytical chemistry

Article

pubs.acs.org/ac

# Quantitative SERS Analysis of Azorubine (E 122) in Sweet Drinks

Vlastimil Peksa,[†] Martin Jahn,[‡,§] Lucie Štolcová,[∥] Volker Schulz,[⊥] Jan Proška,[∥] Marek Procházka,[†] Karina Weber,[‡,§] Dana Cialla-May,*[,‡,§] and Jürgen Popp[‡,§]

[†]Institute of Physics, Faculty of Mathematics and Physics, Charles University in Prague, Ke Karlovu 5, 121 16 Prague 2, Czech Republic

[‡]Institute of Physical Chemistry and Abbe Center of Photonics, Friedrich-Schiller-University Jena, Helmholtzweg 4, 07743 Jena, Germany

[§]Leibniz Institute of Photonics Technology (IPHT), Albert-Einstein-Strasse 9, 07745, Jena, Germany

[∥]Faculty of Nuclear Sciences and Physical Engineering, Czech Technical University in Prague, Břehová 7, 11519 Praha 1, Czech Republic

[⊥]Food GmbH Jena, Analytik Consulting, Orlaweg 2, 07743, Jena, Germany

Supporting Information

**ABSTRACT:** Considering both the potential effects on human health and the need for knowledge of food composition, quantitative detection of synthetic dyes in foodstuffs and beverages is an important issue. For the first time, we report a fast quantitative analysis of the food and drink colorant azorubine (E 122) in different types of beverages using surface-enhanced Raman scattering (SERS) without any sample preparation. Seven commercially available sweet drinks (including two negative controls) with high levels of complexity (sugar/artificial sweetener, ethanol content, etc.) were tested. Highly uniform Au "film over nanospheres" (FON) substrates together with use of Raman signal from silicon support as internal intensity standard enabled us to quantitatively determine the concentration of azorubine in each drink. SERS spectral analysis provided sufficient sensitivity (0.5−500 mg $L^{-1}$) and determined azorubine concentration closely correlated with those obtained by a standard HPLC technique. The analysis was direct without the need for any pretreatment of the drinks or Au surface. Our SERS approach is a simple and rapid (35 min) prescan method, which can be easily implemented for a field application and for preliminary testing of food samples.

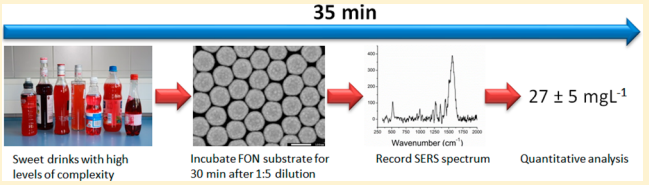


## 1. INTRODUCTION

Food colorants (synthetic or natural) are added to food and drinks to increase their visual attractiveness to consumers and to restore their original appearance when it has been lost during production processes. However, some of the additive colorants represent a potential risk to human health, especially in the case of excessive consumption. For that reason, the presence of synthetic colorants in foods and drinks is rigidly controlled by legislation in many countries. Azorubine (Carmoisine, Food red 3 or E 122 in Europe, disodium 4-hydroxy-3-((4-sulphonatonaphthyl)azo) naphthalenesulfonate, CAS number 3567-69-9), studied here, is widely used as an artificial food and drink additive. It appears as a reddish-maroon powder. Azorubine has been studied for possible effects on human health due to the unavoidable presence of carcinogenic $\beta$-naphthylamine[1] and its influence on human behavior, causing hyperactivity in children.[2] Among its other side effects on human health are the inhibition of cholinesterase,[3] skin rash, and breathing difficulties.[4] Also, a decrease of hemoglobin in the blood or adrenal gland hyperplasia[5] has been reported. Its presence in food is therefore banned (e.g., in the United States and Japan) or limited in many countries. In the European Union, azorubine is a permitted food colorant with a maximum use level up to 50−500 mg/kg, depending on food or drink type, according to Commission Regulations 1129/2011[6] and 232/2012.[7] Specifically, it is allowed in nonalcoholic flavored drinks at levels up to 50 mg $L^{-1}$ and in alcoholic drinks up to 200 mg $L^{-1}$.

From a strictly chemical point of view, drinks are complex mixtures and, as such, must be treated in the process of standardized chemical analysis. Identification and quantification of drink colorants should therefore be preceded by separation of components and their subsequent determination. The most widely employed techniques are high-performance liquid chromatography (HPLC),[8] high-performance ion chromatography,[9] or enzyme-linked immunosorbent assay (ELISA).[10] Such approaches require large-scale laboratory equipment and are costly and time-consuming and, therefore, are not suitable for point-of-care testing.

In the case of mass-produced beverages and alcoholic drinks, ad-hoc methodology based on surface-enhanced Raman scattering (SERS) spectroscopy can be employed for sensitive

**Received:** November 13, 2014
**Accepted:** February 9, 2015
**Published:** February 9, 2015





DOI: 10.1021/ac504254k
*Anal. Chem.* 2015, 87, 2840−2844

sensing of additive colorants.[11] Raman scattering (RS) spectroscopy provides a "spectral fingerprint", a unique molecular spectral patterns by which the molecule can be clearly identified. SERS is based on a giant RS enhancement (above $10^6$) for molecules adsorbed onto a suitable nanostructured metal substrate.[12] SERS thus combines molecular fingerprint specificity and high sensitivity enabling a variety of applications including sensing.[13−18] SERS molecular sensing from complex matrix can be hampered by poor efficiency and selectivity of the SERS surface to capture the target analyte. Functionalization of the metal surface by selective coatings can solve this problem,[13−18] but it introduces another step in the analysis. On the other hand, if the affinity of the target analyte is substantially higher to overcome other components from the mixture, its selective adsorption can be achieved directly. To summarize, the SERS spectrum provides qualitative information about the presence of a particular analyte on the metal surface and gives information about its quantity. To eliminate problems connected with experimental factors, such as laser power fluctuations, focusing, drift in the optical alignment, and positioning of the substrate, an internal intensity standard[19] is implemented in SERS quantitative analysis.

The rational design of metal substrates providing a large and uniform SERS enhancement is necessary for SERS quantitative sensing.[20,21] It can be intrinsically ensured at periodic surfaces fabricated by nanosphere lithography.[22] The metal "film over nanospheres" (FON) is formed from polystyrene or silica micro- or nanospheres self-assembled on a solid support and then sputtered with metal. The shape, size, and spacing of the nanostructures can be controlled by the size of nanospheres and the thickness of deposited metal.[23] Owing to their excellent spectral reproducibility, they were successfully employed in SERS sensing of small molecules such as glucose and biowarfare agents.[22,24]

Within this contribution, a highly reproducible FON surface is applied for the detection of azorubine in different commercially available beverages, regardless of the alcohol content or different sweetening agents (i.e., sugar, artificial sweetener, or monosaccharides). A comparison of the method with HPLC is made, demonstrating the potential of SERS in quantitative food analysis and the negligibility of influence due to the competition of different adsorbates from the beverages' complex matrixes.

## 2. EXPERIMENTAL SECTION

**2.1. FON Fabrication.** Polystyrene spherical beads (107 nm diameter) in aqueous dispersion (microParticles GmbH) were diluted with ethanol (1:1 v/v) and deposited onto water surface using a glass pipet, as described by Kosiorek et al.[25] There, they formed monolayers with hexagonal close-packed ordering, which were then transferred onto cleaned silicon substrates and left to dry. Then, 20 nm of gold was deposited onto the monolayer by magnetron sputtering using a high-resolution sputter coater (Figure 1).

**2.2. SERS Detection.** The pure azorubine SERS measurement was carried out by incubating the Au substrates in azorubine aqueous solution for 30 min; then, they were removed from the solution, and the excess analyte was cleared away with an air stream. Drink specimens were purchased in stores in Germany and Czech Republic. The treatment of the drink samples for SERS measurement included 1:5 dilution with distilled water. The Au substrates were then incubated in the samples for 30 min, and after their removal, the remaining liquid was cleared away using an air stream.

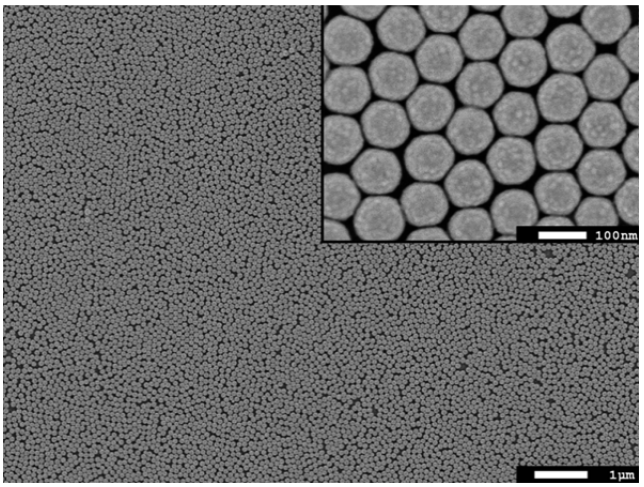


**Figure 1.** Scanning electron microscopy (SEM) image of Au FON prepared by self-assembly of 107 nm polystyrene beads covered with 20 nm gold layer.

SERS spectra were obtained using a WITec micro-Raman spectrometer equipped with a 632.8 nm line of He−Ne laser (1 mW laser power at the substrate) and a 50× objective lens. The SERS spectra were recorded as a set of 1 s scans from three 10 × 10 points square maps with the side of 50 $\mu$m. Two substrates were always used, and thus, data analysis included 600 SERS spectra per sample. The data processing included background subtraction using the method described by Palacký et al.[26] The peaks at 520 and 1356 $cm^{-1}$ were fitted to Lorentz curves, and the area of these curves was determined using the midpoint integration method in OriginPro software. The ratio between these areas was plotted against the respective concentration, and then the OriginPro linear regression routine (weighted for the standard deviation of each of the ratios) was used to obtain the equation of the line. The reproducibility of the signal was calculated as relative standard deviation (RSD) of the ratio. The estimated limit of detection is 0.2 mg $L^{-1}$ (Figure S1, Supporting Information), although the uncertainty in the low concentration range is more than 30%. Normal Raman spectra of azorubine powder (Sigma-Aldrich) were acquired by employing the 785 nm line (0.1 mW laser power at the sample) of a diode laser.

**2.3. HPLC Detection.** The drinks were diluted with purified water and passed through 0.45 $\mu$m syringe filters. Dilutions from 1:1 to 1:100 were prepared to achieve optimal HPLC signals. These solutions were injected directly into the HPLC-System. Calibration standards in purified water ranging from 1.0 to 100 $\mu g mL^{-1}$ were used to calculate sample concentrations. The HPLC system consisted of a Shimadzu LC-20AT binary gradient system with DGU-20A3 degassing unit, SIL-10AF autosampler, CTO-20AC column oven and SPD-M20A diode array detector. The injection volume was 20 $\mu$L and the separation was performed on a 250 × 4.6 mm Vydac 201TP54 column. The mobile phase consisted of purified water (TKA system, solvent A) and acetonitrile (Promochem, solvent B). The total flow was 1.0 mL $min^{-1}$, and the column temperature was adjusted to 30 °C. The gradient program started isocratically with 0% solvent B. After 5 min, a linear gradient was applied up to 80% solvent B (20 min) followed by a constant period (25 min) and finished with


DOI: 10.1021/ac504254k
Anal. Chem. 2015, 87, 2840−2844

the starting conditions (0% B, 35 min). The peaks were evaluated at three different wavelengths from the DAD spectrum; at 500, 519, and 550 nm. Concentrations from all three wavelengths and different dilutions were compared and averaged for the final result. The limit of quantification (LOQ) of this HPLC-DAD method determined with blank samples was 0.1 mg $L^{-1}$.

## 3. RESULTS AND DISCUSSION

In this study, we prepared a set of 34 Au FON substrates consisting of 20 nm thick gold layer sputtered on a self-assembled monolayer of polystyrene spherical beads deposited on a silicon wafer (Figure 1). Polystyrene beads do not reveal a perfect close-packed arrangement. However, packing defects are negligible with regard to the measuring laser spot with a diameter about 1 $\mu$m, whereas the sphere diameter is 107 nm. The substrates are highly uniform, showing RSD of the azorubine SERS intensity up to 15%, and have a shelf lifetime in a time scale of months (Figure 2 top). The normal Raman

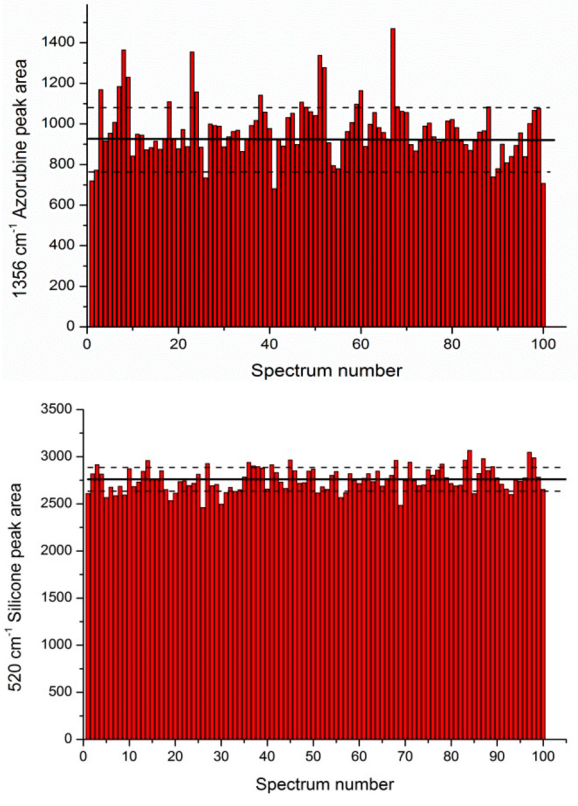


**Figure 2.** (Top) Stability of 1356 $cm^{-1}$ azorubine peak within a single map from a substrate incubated in 2.5 mg $L^{-1}$ azorubine solution. (Bottom) Stability of 520 $cm^{-1}$ Si peak within a single map. The relative standard deviation (RSD) of silicone peak intensity is 4%, RSD of azorubine is 15%.

signal intensity from the silicon peak at 520 $cm^{-1}$ varies by only 4% in single maps (Figure 2 bottom). This therefore ensures a good reliability to use it as the internal intensity standard.[19] Although it cannot assess possible fluctuations in local SERS enhancement, such issues can be effectively countered by mapping of several larger areas.

To plot a calibration curve (SERS intensity versus azorubine concentration), we acquired SERS spectra of azorubine adsorbed on Au FON substrates from 0.5 to 500 mg $L^{-1}$ concentrated aqueous solutions. The comparison with the azorubine powder spectrum (Figure S2, Supporting Information) and literature[27,28] indicates that 1225, 1275, 1356, 1441, and 1507 $cm^{-1}$ bands in SERS spectra (Figure 3 top, spectrum

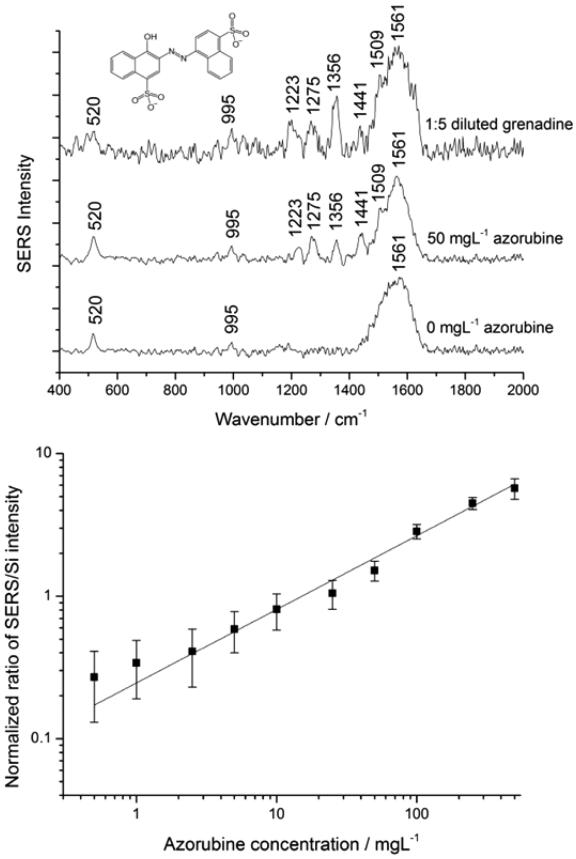


**Figure 3.** (Top) SERS spectra obtained from pure azorubine and grenadine (control experiment, RS spectrum of clean metal substrate). Spectra are shifted vertically for clarity. (Inset) Chemical structure of azorubine. (Bottom) Calibration curve, normalized SERS intensity at 1356 $cm^{-1}$ of azorubine versus concentration.

for 50 mg $L^{-1}$, for example) are assigned to the azorubine dye. The other bands are attributed to the solid support: 520 $cm^{-1}$ to silicon and 995 and 1560 $cm^{-1}$ to polystyrene beads[27] (Figure 3 top, spectrum for 0 mg $L^{-1}$). The SERS spectra were normalized using the silicon Raman band at 520 $cm^{-1}$ and the SERS intensity was determined as the area of the 1356 $cm^{-1}$ azorubine band. The log–log plot of the calibration curve (Figure 3 bottom) exhibits a linear trend indicating the possibility of performing quantitative SERS analysis. In the case of low azorubine content, the signal-to-noise ratio of the SERS spectra is low and the azorubine concentrations were estimated with high uncertainty (about 30%). However, the determination of the azorubine content in the relevant concentration range, determined by the limit of usage set by the EU (50 and 200 mg $L^{-1}$), is possible with sufficient accuracy.[6,7] Further on, traces of azorubine more than 1 order of magnitude lower than these threshold values are still detectable. Hence, the used method provides a good estimation of the azorubine content in the relevant concentration range and can be applied as simple and rapid (35 min) prescan method.

To prove the potential of our approach for azorubine detection in complex matrices, we tested seven commercially


DOI: 10.1021/ac504254k
Anal. Chem. 2015, 87, 2840–2844

available sweet drinks: five with expected positive azorubine contents (energy drink, grenadine, raspberry lemonade, strawberry vodka, and passion fruit vodka) and two red-colored negative controls without azorubine (blood orange lemonade and raspberry syrup). The above-mentioned drinks are characterized by unified composition, regardless of their complexity (sugar/artificial sweetener, ethanol content, etc.). The drinks were diluted 1:5 with water to improve the signal-to-noise ratio and to lower the high background signals caused by sugar, as well as to operate in the concentration range where the substrate is the most sensitive to differences in the azorubine concentration. SERS spectra of all five positive samples clearly show the azorubine Raman bands without any spectral interference from other additives in drink (Figure 4).

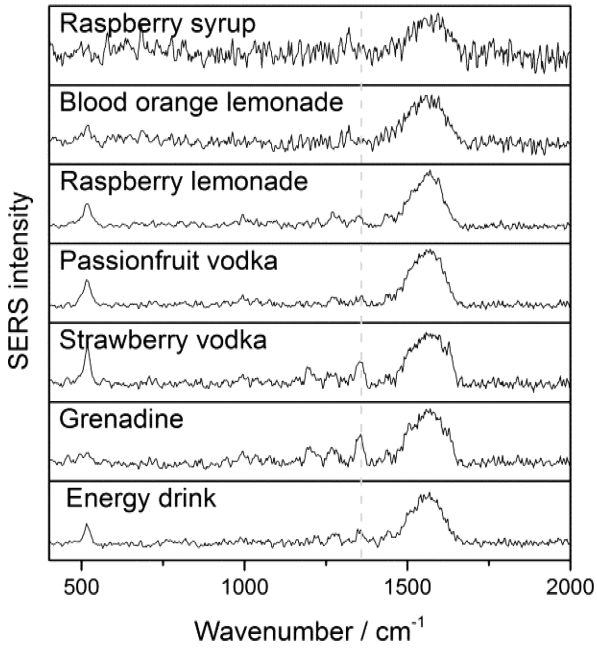


**Figure 4.** Typical SERS spectra of all commercial samples. Gray dashed line indicates the azorubine peak at 1356 $cm^{-1}$ used for determination of azorubine concentration. Full size spectra are available in the Supporting Information.

This indicates that azorubine dye itself has a sufficiently high affinity to the Au surface. The azorubine concentration in each drink was determined by interpolation of the area of normalized 1356 $cm^{-1}$ azorubine band in corresponding SERS spectrum using the calibration curve. The results summarized in Table 1 show close correlation of azorubine concentrations obtained by SERS and standard HPLC technique in all tested drinks. The grenadine, which appeared as thick, dense syrup, was found exceeding the level of azorubine content permitted in the European Union;[6] however, the serving instructions on the bottle label specifically suggested dilution to 1:10 before drinking.

**Table 1. Azorubine Concentration in Different Drinks Identified by HPLC and SERS**

| sample | HPLC (mg $L^{-1}$) | SERS (mg $L^{-1}$) |
|---|---|---|
| energy drink | 26 ± 2.6 | 27 ± 5 |
| grenadine | 280 ± 28.0 | 355 ± 77 |
| strawberry vodka | 12 ± 1.2 | 18 ± 4 |
| passion fruit vodka | 1.7 ± 0.2 | 4.7 ± 1.8 |
| raspberry lemonade | 4 ± 0.4 | 5.3 ± 1.4 |
| blood orange lemonade | <0.1 | <0.2 |
| raspberry syrup | <0.1 | <0.2 |

The higher-than-expected signal from alcoholic samples was attributed to the lower surface tension of the liquids, which led to their penetration into nanoscopic gaps in the FON structure, thus increasing the amount of deposited azorubine. The two negative controls were correctly identified due to the absence of 1356 $cm^{-1}$ azorubine peak in the SERS spectra.

## 4. CONCLUSIONS

In conclusion, the Au FON substrates prepared on silicon wafer represent robust, highly sensitive and reproducible SERS substrates that can be applied for quantitative analysis of azorubine dye in different sweet drinks with minimum effort. The analysis is rapid (35 min) and direct, without the need for any pretreatment of the samples or functionalization of the Au surface. This makes SERS a perfect prescan method, which can be easily implemented for field application employing portable Raman systems in future work and for fast preliminary testing of foods and beverages.

## ■ ASSOCIATED CONTENT

### Supporting Information

Estimation of the limit of detection applying SERS; powder azorubine spectrum together with band assignment; and full-size spectra of commercial samples. This material is available free of charge via the Internet at http://pubs.acs.org.

## ■ AUTHOR INFORMATION

### Corresponding Author

*E-mail: dana.cialla-may@uni-jena.de.

### Author Contributions

The manuscript was written through contributions of all authors. All authors have given approval to the final version of the manuscript.

### Notes

The authors declare no competing financial interest.

## ■ ACKNOWLEDGMENTS

Funding of research projects P205/13/20110S from the Czech Science Foundation and grant No. SVV 260092 from the Charles University in Prague, QuantiSERS (03IPT513A) and JBCI 2.0 (03IPT513Y) within the framework of InnoProfile Transfer—Unternehmen Region of the Federal Ministry of Education and Research, Germany (BMBF) is gratefully acknowledged. The authors thank Bernd Giese (Food GmbH) for critical discussions.

## ■ REFERENCES

(1) Sahu, J. K. *Introduction to Advanced Food Process Engineering*; CRC Press: Boca Raton, FL, 2014.
(2) McCann, D.; Barrett, A.; Cooper, A.; Crumpler, D.; Dalen, L.; Grimshaw, K.; Kitchin, E.; Lok, K.; Porteous, L.; Prince, E.; Sonuga-Barke, E.; Warner, J. O.; Stevenson, J. *Lancet* **2007**, *370*, 1560−1567.
(3) Osman, M. Y.; Sharaf, I. A.; Osman, H. M. Y.; El-Khouly, Z. A.; Ahmed, E. I. *Br. J. Biomed. Sci.* **2004**, *61*, 128−132.
(4) Rowe, K. S. *Aust. Paedr. J.* **1988**, *24*, 143−147.
(5) Groten, J. P.; Butler, W.; Feron, V. J.; Kozianowski, G.; Renwick, A. C.; Walker, R. *Regul. Toxicol. Pharmacol.* **2000**, *31*, 77−91.
(6) The European Commission, Commission Regulation (EU) No 1129/2011 of 11 November 2011 amending Annex II to Regulation


DOI: 10.1021/ac504254k
*Anal. Chem.* 2015, 87, 2840−2844

(EC) No 1333/2008 of the European Parliament and of the Council by establishing a Union list of food additives. *Off. J. Eur. Union*, L295, 1, 12/11/2011.
(7) The European Commission, Commission Regulation (EU) No 232/2012 of 16 March 2012 amending Annex II to Regulation (EC) No 1333/2008 of the European Parliament and of the Council as regards the conditions of use and the use levels for Quinoline Yellow (E 104), Sunset Yellow FCF/Orange Yellow S (E 110) and Ponceau 4R, Cochineal Red A (E 124). *Off. J. Eur. Union*, L78, 1, 17/3/2012.
(8) Minioti, K. S.; Sakellariou, C. F.; Thomaidis, N. S. *Anal. Chim. Acta* **2007**, *583*, 103−110.
(9) Chen, Q. C.; Mou, S. F.; Hou, X. P.; Riviello, J. M.; Ni, Z. M. *J. Chromatogr. A* **1998**, *827*, 73−81.
(10) Wang, Y. Z.; Wei, D. P.; Yang, H.; Yang, Y.; Xing, W. W.; Li, Y.; Deng, A. P. *Talanta* **2009**, *77*, 1783−1789.
(11) Zheng, J. K.; He, L. L. *Comp. Rev. Food Sci. Food Saf.* **2014**, *13*, 317−328.
(12) Le Ru, E. C.; Etchegoin, P. G. *Principles of Surface-Enhanced Raman Spectroscopy and Related Plasmonic Effects*; Elsevier: Amsterdam, 2009.
(13) Bantz, K. C.; Meyer, A. F.; Wittenberg, N. J.; Im, H.; Kurtulus, O.; Lee, S. H.; Lindquist, N. C.; Oh, S. H.; Haynes, C. L. *Phys. Chem. Chem. Phys.* **2011**, *13*, 11551−11567.
(14) Cialla, D.; Marz, A.; Bohme, R.; Theil, F.; Weber, K.; Schmitt, M.; Popp, J. *Anal. Bioanal. Chem.* **2012**, *403*, 27−54.
(15) Procházka, M., Štepánek, J. In *Applications of Raman Spectroscopy to Biology: From Basic Studies to Disease Diagnosis*, Ghomi, M., Ed.; IOS Press: Amsterdam, 2012.
(16) Schlücker, S. In *Surface Enhanced Raman Spectroscopy*; Wiley-VCH Verlag GmbH & Co. KGaA: Weinheim, 2010; pp 263−283.
(17) Schlücker, S. *Angew. Chem., Int. Ed.* **2014**, *53*, 4756−4795.
(18) Negri, P.; Dluhy, R. A. *J. Biophotonics* **2013**, *6*, 20−35.
(19) Bell, S. E. J.; Sirimuthu, N. M. S. *Chem. Soc. Rev.* **2008**, *37*, 1012−1024.
(20) Banholzer, M. J.; Millstone, J. E.; Qin, L. D.; Mirkin, C. A. *Chem. Soc. Rev.* **2008**, *37*, 885−897.
(21) Fan, M. K.; Andrade, G. F. S.; Brolo, A. G. *Anal. Chim. Acta* **2011**, *693*, 7−25.
(22) Zhang, J. H.; Li, Y. F.; Zhang, X. M.; Yang, B. *Adv. Mater.* **2010**, *22*, 4249−4269.
(23) Baia, L.; Baia, M.; Popp, J.; Astilean, S. *J. Phys. Chem. B* **2006**, *110*, 23982−23986.
(24) Haynes, C. L.; Yonzon, C. R.; Zhang, X. Y.; Van Duyne, R. P. *J. Raman Spectrosc.* **2005**, *36*, 471−484.
(25) Kosiorek, A.; Kandulski, W.; Chudzinski, P.; Kempa, K.; Giersig, M. *Nano Lett.* **2004**, *4*, 1359−1363.
(26) Palacký, J.; Mojzeš, P.; Bok, J. *J. Raman Spectrosc.* **2011**, *42*, 1528−1539.
(27) Anema, J. R.; Brolo, A. G.; Felten, A.; Bittencourt, C. *J. Raman Spectrosc.* **2010**, *41*, 745−751.
(28) Snehalatha, M.; Ravikumar, C.; Joe, I. H.; Sekar, N.; Jayakumar, V. S. *Spectrochim. Acta, Part A* **2009**, *72*, 654−662.



DOI: 10.1021/ac504254k
*Anal. Chem.* 2015, 87, 2840−2844

**Supplement [II]**

SUBR, M., M. PETR, V. PEKSA, O. KYLIAN, J. HANUS, M. PROCHAZKA, Ag Nanorod Arrays for SERS: **Aspects of Spectral Reproducibility, Surface Contamination, and Spectral Sensitivity**. Journal of Nanomaterials, 2015, 729234.

Hindawi Publishing Corporation
Journal of Nanomaterials
Volume 2015, Article ID 729231, 7 pages
http://dx.doi.org/10.1155/2015/729231

*Research Article*

# Ag Nanorod Arrays for SERS: Aspects of Spectral Reproducibility, Surface Contamination, and Spectral Sensitivity

**Martin Šubr,[1] Martin Petr,[2] Vlastimil Peksa,[1] Ondřej Kylián,[2] Jan Hanuš,[2] and Marek Procházka[1]**

[1] *Institute of Physics, Faculty of Mathematics and Physics, Charles University in Prague, Ke Karlovu 5, 121 16 Prague, Czech Republic*
[2] *Department of Macromolecular Physics, Faculty of Mathematics and Physics, Charles University in Prague, V Holešovičkách 2, 180 00 Prague, Czech Republic*

Correspondence should be addressed to Marek Procházka; prochaz@karlov.mff.cuni.cz

Received 25 November 2014; Accepted 17 February 2015

Academic Editor: Weihai Ni



Ag nanorod arrays prepared by oblique angle vapor deposition (OAD) represent regular, large area substrates for surface-enhanced Raman scattering (SERS) spectroscopy. We studied uniformity and spectral reproducibility of silver OAD-fabricated substrates (AgOADs) by spectral mapping of methylene blue. The results demonstrate good reproducibility apart from occasional "hot-spot" sites where the intensity is higher. The number of "hot-spots" represents 2%–6% of SERS-active sites of mapping substrate area. We were able to obtain good SERS spectra of testing amino acid tryptophan at $1 \times 10^{-5}$ M concentration and three different free-base porphyrins down to ~$10^{-7}$ M concentration. We found out that keeping the AgOADs in a vacuum chamber overnight prevents the surface from binding any contaminants from the ambient atmosphere, without significant reduction in the SERS enhancement. Such substrates provide stable SERS enhancement even when stored for 1 year after preparation.

## 1. Introduction

Surface-enhanced Raman scattering (SERS) is a spectroscopic technique capable of detecting specific molecules at low concentrations [1, 2]. It yields to enormous enhancement (above $10^5$) of Raman scattering of molecules placed in the vicinity of certain metal nanostructures. It is generally recognized that the dominant contribution to the SERS enhancement is due to the electromagnetic effect. This phenomenon is based on the resonance excitation of localized conduction-electron oscillations at the metal surface, which are termed surface plasmons [3]. The conditions for localized surface plasmon resonance (LSPR) are given by, namely, the size, shape, and degree of the aggregation of metal nanostructures [1, 3]. In bioanalytical, medical, and biosensing applications of SERS (e.g., [2, 4–6]), the most commonly used metals are silver and gold because of their highly effective LSPR in the visible spectral region. The advantage of silver is the strongest enhancement allowing very low concentrations of analytes to be detected. Gold is due to its chemical inactivity more suitable for incorporation inside biological systems and/or designing of bioassay and biosensor platforms.

Roughened metal electrodes, metal island films, and metal colloids have been used in SERS spectroscopy since its discovery in the 70s. In attempts to fabricate more uniform and spectrally reproducible substrates, close attention has been paid to more sophisticated control of substrate morphology in the last 10–15 years. The wide variety of employed preparation methods, including nanoparticle immobilization, nanoimprinting, templating, and nanosphere or nanocolloidal lithography, is reviewed, for example, in [7–9]. Chaney and coworkers developed a nanofabrication technique based on oblique angle vapor deposition (OAD) to obtain a versatile, simple, and inexpensive way of producing regular Ag nanorod arrays for SERS applications [10]. OAD utilizes an effect of self-shadowing

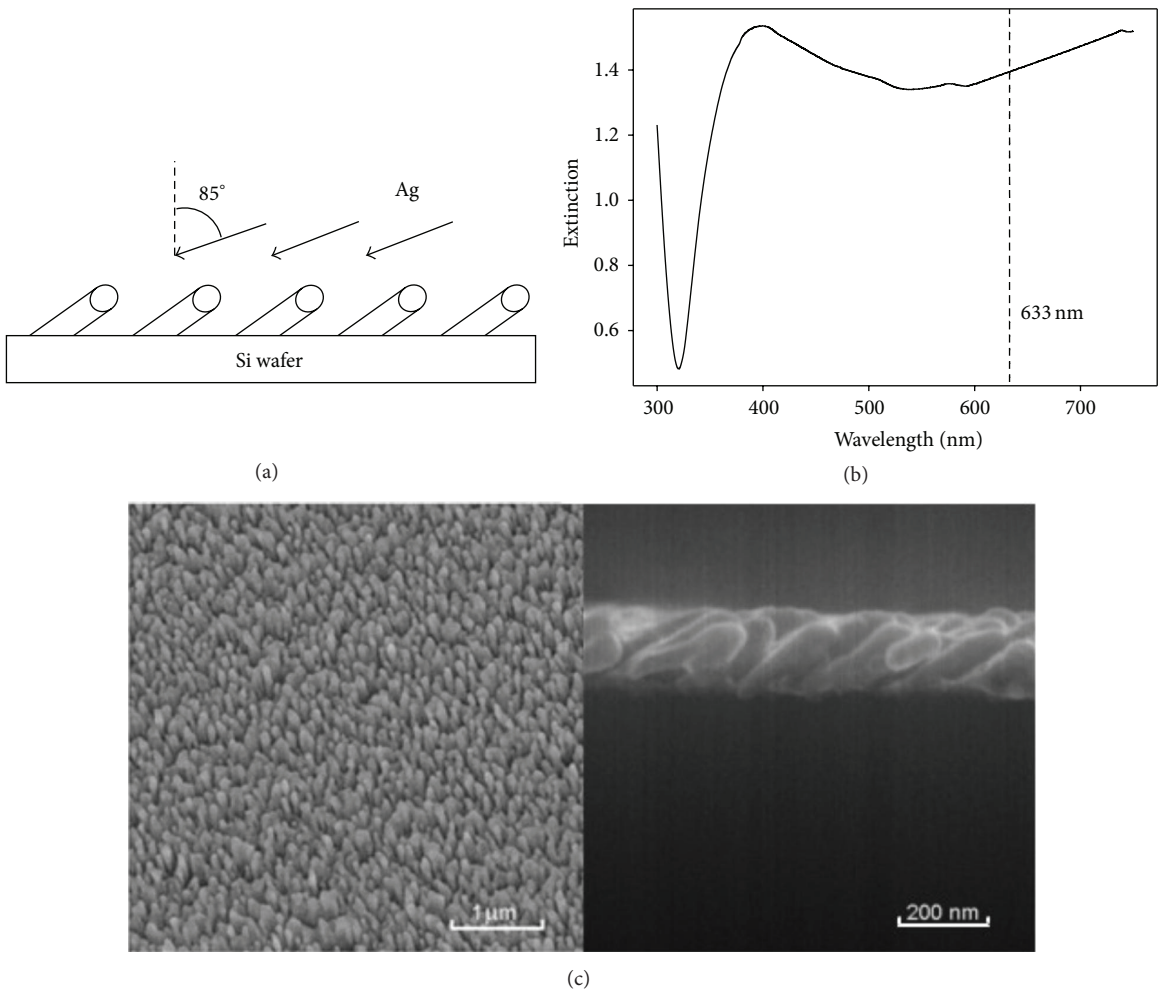


Figure 1: (a) Scheme of the OAD procedure, (b) extinction spectrum of prepared structures with excitation wavelength used for SERS measurements indicated by a dashed line, and (c) SEM images of a typical Ag nanorod array (top and side view).

which occurs when a collimated flux of vaporized atoms arrives at a substrate at an oblique angle with respect to the substrate normal. In this case, the growing nuclei shadow the area opposite to the incoming flux, and therefore the film grows through the formation of columnar structures separated from each other by voids and inclined towards the source of the flux (Figure 1(a)). The main advantage of OAD preparation is its simplicity. It is a one-step, vacuum-based process and, since no chemical substances are required, is also environmentally friendly. It was proved that OAD offers uniform, reproducible, large area SERS-active substrates with high SERS enhancement [11]. Ag nanorod arrays fabricated by OAD have been investigated as SERS-active substrates for the detection of pathogens, including viruses and bacteria, as well as assessing the potential of nucleotide-modified Ag nanorod arrays in a variety of biorecognition and biosensing applications [11].

In spite of recent advances in substrate fabrication suitable for SERS applications, employed metal nanostructures still pose a serious drawback for routine SERS quantitative analysis. In the case of Ag substrates, surface contamination irrespective of the nature of the fabrication method is often observed. It comes either from the preparation procedure or from the ambient atmosphere during storage and involves mainly organic (carbonaceous) species that are adsorbed on Ag surface. In the case of studied molecules with weak affinity to Ag surface, it can make their adsorption on the contaminated surface difficult or even impossible. Moreover, the surface contaminants (or impurities) manifest themselves, even in very small concentrations, by their anomalous SERS bands that overlap the SERS signal of a studied molecule. Such problems were previously reported in the case of both colloidal NPs [12, 13] and solid substrates [9, 14, 15]. Thus, special care must be exercised when analyzing any spectral pattern in an effort to reliably distinguish the bands coming from the analyte from those of the contaminants or, better still, to develop a method for preventing the contamination. There have been numerous ways to clean SERS-active surfaces from contaminants under ambient conditions, including electrochemical [9], plasma [14, 15], or ozone cleaning [16], but none have been uniformly successful [11]. Unfortunately, a side result of some electrochemical desorption

techniques can be the introduction of surface defects where the carbon contamination was present or strong oxidation due to the high chemical reactivity of Ag [16, 17]. In the case of Ag nanorod arrays prepared by the OAD technique, it was demonstrated that under controlled plasma conditions and exposure times (<4 min.) the Ar plasma cleaning procedure essentially eliminated any detectable background organic and carbonaceous contamination from the surface without substantially changing their morphology [14]. Moreover, it was demonstrated that the process of ion etching was able to recover SERS effectiveness of such substrates even after 1-month storage [15].

In this paper, we focused on testing of silver OAD-fabricated nanorod array substrates (AgOADs) for SERS spectroscopy. We studied uniformity and spectral reproducibility of AgOADs by spectral mapping of methylene blue. We were able to obtain SERS spectra of biomolecules tryptophan down to $1 \times 10^{-5}$ M concentration and porphyrins down to ~$10^{-7}$ M. We found out that keeping the substrates in a vacuum chamber overnight prevents it from binding any further contaminants from the ambient air, moreover, without significant reduction in the SERS enhancement.

## 2. Materials and Methods

*2.1. Materials.* Methylene blue (MB), L-tryptophan, 5, 10,15,20-tetrakis(1-methyl-4-pyridyl)-21H,23H-porphine ($H_2$TMPyP), 5,10,15,20-tetrakis(4-trimethylammoniophenyl)-21H,23H-porphine ($H_2$TMAP), and 5,10,15,20-tetrakis(4-sulfonatophenyl)-21H,23H-porphine ($H_2$TSPP) were purchased from Sigma-Aldrich.

*2.2. Preparation and Characterization of AgOADs.* For preparation of the AgOADs, a magnetron sputtering of silver target was used (Figure 1(a)). Depositions were performed in a cylindrical stainless steel vacuum chamber (40 l) pumped by scroll and turbomolecular pumps to base pressure lower than $10^{-3}$ Pa. Films were deposited onto Si wafer support introduced into the deposition chamber by a load-lock system. Ar (purity 99.99%) was used as a working gas. The pressure during deposition was 0.18 Pa, magnetron current was 300 mA, distance between magnetron and substrate was 10 cm, deposition angle was 85°, and deposition time was 15 minutes. Under these conditions the mean diameter of individual Ag nanorods was 60 nm, the mean distance between their centers was 150 nm, and the height of the nanorod array was around 200 nm as can be seen in Figure 1(c) where top and side views of Ag nanorods acquired by scanning electron microscopy (SEM, TESCAN Mira 3, 15 kV accelerating voltage) are presented. For the sake of characterization of the surface plasmon properties of the AgOADs, silver deposition was performed on glass and extinction spectra of structures fabricated in this way were obtained (UV-Vis spectrophotometer Hitachi U-3300). From Figure 1(b) it follows that the AgOADs exhibit plasmon resonance over a very broad range of wavelengths.

*2.3. SERS Measurements.* For spectral reproducibility measurements, the AgOADs (deposited on Si wafer) were cut into ~0.5 cm × 0.5 cm pieces, immersed in $1 \times 10^{-6}$ M stock solution of MB for 1 hour, and then removed and dried with an air stream. For SERS measurements of tryptophan and porphyrins, a small drop of sample was deposited on the Ag surface and left to dry. SERS spectra were collected at room temperature using an integrated confocal Raman microscopic system LabRam HR800 (Horiba Jobin-Yvon), equipped with a diffraction grating with 300 grooves/mm and a liquid nitrogen cooled CCD detector. We tried 514.5 nm, 632.8 nm, and 785 nm excitation wavelengths, but the 632.8 nm one provided the best SERS signal. Thus, He-Ne laser, operating at the wavelength 632.8 nm, was used as an excitation source for all SERS measurements. Laser power at the sample was 0.07 mW, 0.02 mW, and 0.002 mW for MB, tryptophan, and porphyrins, respectively. The laser beam was focused to a spot of about 1 $\mu$m diameter using 100x objective; NA = 0.9. Scattered radiation was collected in a back-scattering geometry and filtered by an edge filter for Rayleigh rejection before focusing it onto the 100 $\mu$m entrance slit of the spectrometer. Acquisition times were 1 s, 10 s, and 60 s for MB, tryptophan, and porphyrins, respectively.

## 3. Results and Discussion

*3.1. Aspects of Spectral Reproducibility.* Uniformity and spectral reproducibility of the prepared AgOADs were evaluated by spectral mapping of MB, which is a well-established SERS probe molecule and a very efficient Raman scatterer (for its chemical structure see Figure 2). We tested different batches of AgOADs by mapping of random places at the samples covering $10 \times 10$ spectral points. Spectral maps were processed by in-house developed software based on factor analysis (FA), using a singular value decomposition (SVD) algorithm [18]. This procedure provides a set of singular values $W_j$, orthonormal subspectra $S_j(t)$, and a unitary matrix of corresponding $V_{ij}$ coefficients. A particular experimental spectrum $Y_i(t)$ within the treated series ($i = 1, \ldots, N$) can be expressed as

$$Y_i(t) = \sum_{j=1}^{m} W_j V_{ij} S_j(t). \quad (1)$$

The factor dimension $m$ can be determined as the number of independent components (subspectra) resolvable in the analyzed spectral set and its value can be derived from the plot of the residual error values against the subspectra numbers. The $W_j$ is a vector representing the relative statistical weight of each subspectrum and the $V_{ij}$ is a unitary matrix representing relative contents of a subspectrum $S_j(t)$ in a particular spectrum $Y_i(t)$. In our case, spectra obtained in different mapping points may vary in intensities but not in the shape of the basic spectral profile (in an ideal case, all spectra in different mapping points are just multiples of one basic spectral profile). That is why we may assume with sufficient preciseness that $m = 1$ with only the first subspectrum $S_1$ being relevant for our further calculations, whereas other subspectra represent only noise or at most slight changes in the background, traces of parasitic signal, and other artifacts. Thus, we used the coefficients $V_{i1}$ to construct spectral maps of MB.

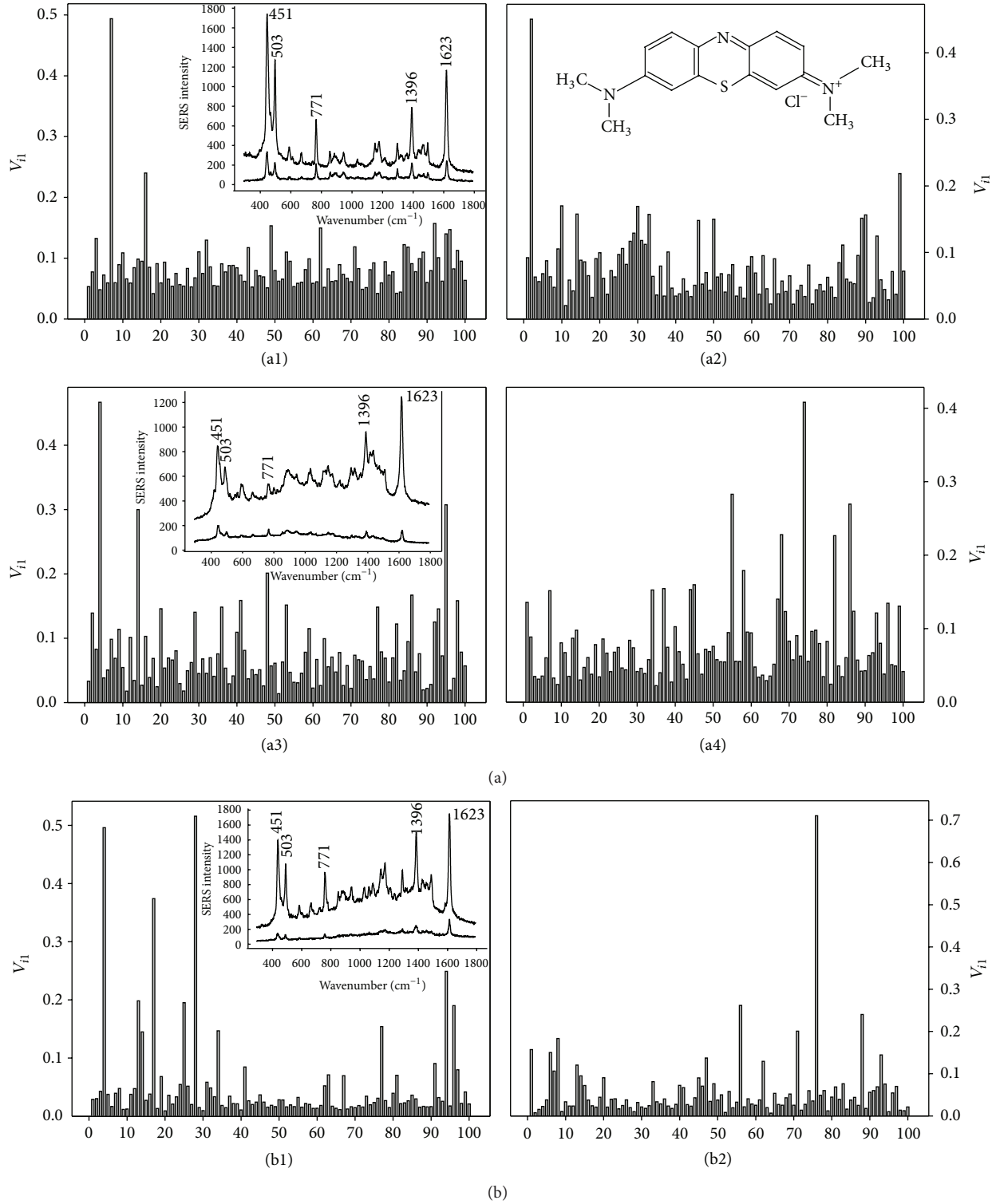


Figure 2: Reproducibility of spectral maps of MB on two different batches of AgOADs ((a) and (b)) in terms of coefficients $V_{i1}$. Steps between mapping points were 5 $\mu$m. Spectral maps on the batch (a) were taken two days after their fabrication ((a1), (a2)) and after 1-year storage ((a3), (a4)). Examples of MB spectra with an average enhancement and spectra obtained from "hot-spot" sites are depicted as insets of graphs (a1), (a3), and (b1). Chemical structure of MB is depicted as inset of graph (a2).

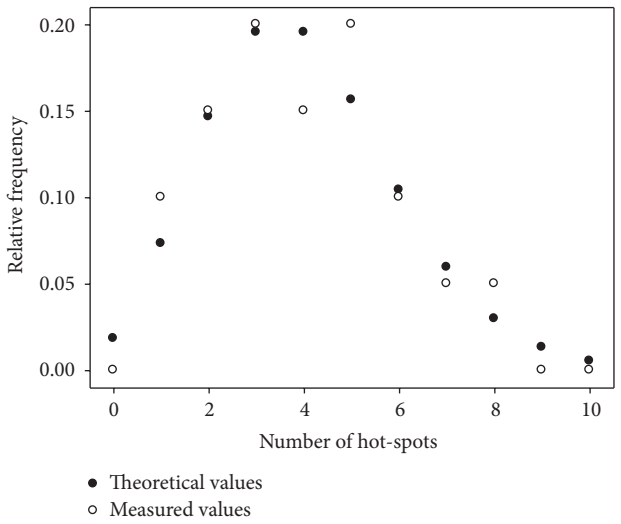


Figure 3: Comparison of the relative frequency of number of "hot-spots" in a given map of 10 × 10 spectral points (out of 20 maps in total) with the values predicted by the Poisson distribution with fixed mean value of 4.

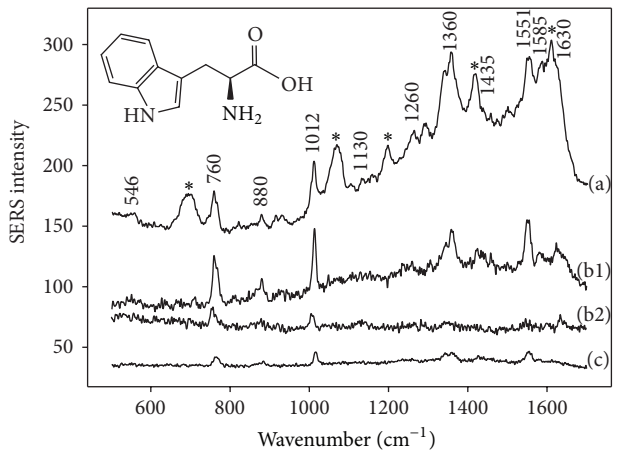


Figure 4: SERS spectra of tryptophan on two different AgOADs and demonstration of the effect of cleaning: (a) $1 \times 10^{-4}$ M tryptophan on contaminated substrate, (b) tryptophan on clean substrate kept in vacuum overnight, $1 \times 10^{-4}$ M (1) and $1 \times 10^{-5}$ M concentration (2), and (c) $1 \times 10^{-4}$ M tryptophan on contaminated substrate after 5 min. ultrasonic cleaning. Positions of main anomalous bands are marked with asterisks. Inset: chemical structure of tryptophan.

Comparison of spectral reproducibility and SERS effectiveness of two different batches of AgOADs ((a), (b)) and after different storage times (2 days and 1 year) on a given batch are depicted in Figure 2. It is clear that both batches as well as 2-day and 1-year aged substrates provide reproducible SERS enhancement, signal variation up to 20% apart from occasional points where the intensity is higher. Higher SERS intensity obviously comes from excitation of "hot-spot" sites, which are sparsely distributed over the surface. Thus, reproducibility of a given spectral map is influenced mainly by the presence of occasional "hot-spots"; however, the actual number of "hot-spots" in a given set of 10 × 10 spectral points fluctuates (see maps (a) and (b) in Figure 2). We determined the relative frequency of number of "hot-spots" in a mapping area (10 × 10 spectral points) using 20 spectral maps of MB, exhibiting the expected Poisson distribution (Figure 3). We assumed that "hot-spot" is a point where the intensity was at least 3 times the average intensity of a given spectral map. The mean number of "hot-spots" in a given set is ~4 and the mean deviation is ~2. Thus, we conclude that the number of "hot-spots" represents 2%–6% of SERS-active sites of the mapping substrate area.

*3.2. Aspects of Surface Contamination and SERS Sensitivity.* In order to evaluate the SERS sensitivity of AgOADs, we tested amino acid tryptophan and porphyrins. They represent biomolecules widely studied by means of SERS. We measured their SERS spectra by depositing a droplet of a stock solution on the AgOADs and left it to dry. This process resulted in rather irregular distribution of molecules on the metal surface, leading to the loss of reproducibility of obtained spectra across different mapping points (in comparison to Figure 2). On the other hand, increased concentration of the analyte in certain regions of the substrate can increase the SERS sensitivity.

As already mentioned, one of the major limitations of exploiting AgOADs for SERS applications is the contamination of their surface by organic contaminants. This problem may be overcome by specific cleaning of the substrate, for example, by Ar plasma [14, 15] or ozone [16] treatment. However, the success of these methods strongly depends on the time of the applied cleaning and may lead to a reduction in SERS effectiveness due to suffered oxidation damage or distortion of the surface nanostructures. In the case of MB measurements no anomalous SERS bands of impurities were observed probably because MB molecules have a high affinity to silver and are able to replace the contaminants from the surface. On the other hand, when tryptophan was measured, we found a strong interference of surface contaminant bands with the tryptophan spectrum. Thus, we tried to find a way of cleaning the Ag surface before deposition of tryptophan. Figure 4 demonstrates the SERS spectra of tryptophan on (a) substrates exposed to the ambient atmosphere immediately after their fabrication, exhibiting anomalous bands marked with asterisks, (b) substrates kept in vacuum overnight, and (c) substrates after a 5 min. ultrasonic treatment.

Although the ultrasonic treatment did in some cases lead to the disappearance of anomalous bands from the spectra, the SERS effectiveness was approximately 4x worse. Keeping the substrates several hours in vacuum immediately after the deposition managed to reduce the spectra of contaminants significantly without a significant decrease in the SERS enhancement. By extending the time for which the substrates were kept in a vacuum after the deposition, SERS intensity of anomalous bands was gradually decreasing with almost complete suppression of a parasitic signal after overnight storage in a vacuum. We suggest that keeping the substrates in a vacuum chamber for at least 16 hours prevents it from binding any further contaminants in the ambient air. Such

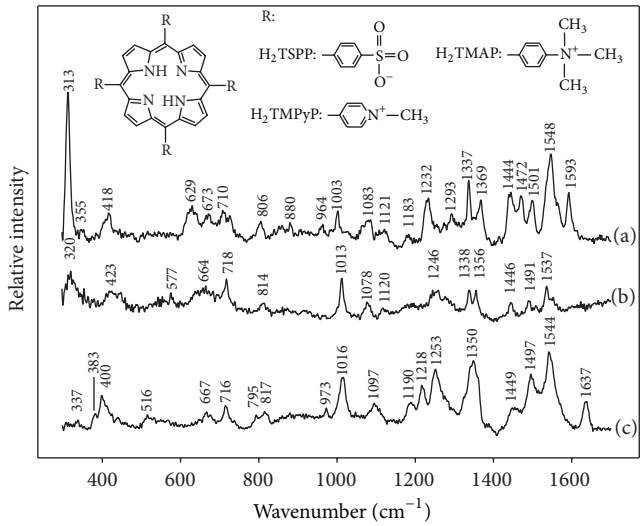


Figure 5: SERS spectra of three free-base porphyrins on AgOADs: (a) $H_2$TSPP, $3 \times 10^{-7}$ M, (b) $H_2$TMAP, $3 \times 10^{-7}$ M, and (c) $H_2$TMPyP, $5 \times 10^{-7}$ M concentrations. Spectra are baseline corrected and shifted in vertical scale for the sake of clarity. Inset: chemical structure of porphyrins.

substrates provide stable enhancement even 3 months after their fabrication. We consider this method of keeping the substrates in a vacuum immediately after the deposition convenient due to the possibility of not using any other chemicals or further cleaning procedures whose influence on the surface morphology may be arguable.

The SERS spectra of tryptophan are dominated by two intense bands around 760 and 1012 $cm^{-1}$ (Figure 4), which are assigned to the ring-breathing vibrations of the indole ring [19]. These two bands remain obvious down to $1 \times 10^{-5}$ M concentration. Our tryptophan spectra are analogous to those reported previously using Ag nanoparticles [19, 20].

The final step of this study was testing of capability of fabricated clean AgOADs, that is, substrates that were kept 16 hours in vacuum after their deposition, to detect different porphyrins. The chemical structures of studied free-base porphyrins are depicted as inset of Figure 5. Two porphyrins ($H_2$TMPyP and $H_2$TMAP) are positively charged and one is charged negatively ($H_2$TSPP). SERS spectra of these three porphyrins of the order of $10^{-7}$ M concentration were obtained from clean AgOADs (Figure 5). Our SERS spectra have a very good signal-to-noise ratio and positions of bands correspond very well with the spectra obtained previously using Ag nanoparticles [21, 22]. No anomalous bands of surface contaminants were observed.

## 4. Conclusions

We studied uniformity and spectral reproducibility of Ag nanorod arrays prepared by an oblique angle vapor deposition (OAD) technique. SERS spectra of methylene blue were used for spectral mapping through the AgOADs. The results demonstrated good reproducibility apart from occasional "hot-spot" sites where the intensity is higher. The number of "hot-spots" represents 2%–6% of SERS-active sites of mapping substrate area. Freshly prepared substrates exhibited strong anomalous bands from surface contaminants, often overlapping SERS spectra of the studied molecules. We found out that keeping the substrates in a vacuum chamber overnight after the preparation is a simple way to avoid this effect without a significant reduction in the SERS enhancement. Such substrates provide stable enhancement even after 1-year storage. We demonstrate that, by such substrate treatment, appropriate choice of laser power with respect to a given molecule, and reduced time of exposure to the laser beam, we were able to obtain SERS spectra of tryptophan at $1 \times 10^{-5}$ M concentration and as low as ~$10^{-7}$ M for porphyrins.

## Conflict of Interests

The authors declare that there is no conflict of interests regarding the publication of this paper.

## Acknowledgments

Funding of research Projects P205/13/20110S from the Czech Science Foundation and no. SVV 260092 from the Charles University in Prague is gratefully acknowledged.

## References

[1] E. C. Le Ru and P. G. Etchegoin, *Principles of Surface-Enhanced Raman Spectroscopy and Related Plasmonic Effects*, Elsevier, Amsterdam, The Netherlands, 2009.

[2] S. Schlücker, "Surface-enhanced Raman spectroscopy: concepts and chemical applications," *Angewandte Chemie International Edition*, vol. 53, no. 19, pp. 4756–4795, 2014.

[3] M. Moskovits, "Surface-enhanced spectroscopy," *Reviews of Modern Physics*, vol. 57, no. 3, pp. 783–826, 1985.

[4] K. C. Bantz, A. F. Meyer, N. J. Wittenberg et al., "Recent progress in SERS biosensing," *Physical Chemistry Chemical Physics*, vol. 13, no. 24, pp. 11551–11567, 2011.

[5] D. Cialla, A. März, R. Böhme et al., "Surface-enhanced Raman spectroscopy (SERS): progress and trends," *Analytical and Bioanalytical Chemistry*, vol. 403, no. 1, pp. 27–54, 2012.

[6] M. Procházka and J. Štěpánek, "Surface-enhanced Raman scattering (SERS) and its application to biomolecular and cellular investigation," in *Applications of Raman Spectroscopy to Biology—From Basic Studies to Disease Diagnosis*, M. Ghomi, Ed., IOS Press, Amsterdam, The Netherlands, 2012.

[7] M. J. Banholzer, J. E. Millstone, L. D. Qin, and C. A. Mirkin, "Rationally designed nanostructures for surface-enhanced Raman spectroscopy," *Chemical Society Reviews*, vol. 37, no. 5, pp. 885–897, 2008.

[8] M. Fan, G. F. S. Andrade, and A. G. Brolo, "A review on the fabrication of substrates for surface enhanced Raman spectroscopy and their applications in analytical chemistry," *Analytica Chimica Acta*, vol. 693, no. 1-2, pp. 7–25, 2011.

[9] X.-M. Lin, Y. Cui, Y.-H. Xu, B. Ren, and Z.-Q. Tian, "Surface-enhanced Raman spectroscopy: substrate-related issues," *Analytical and Bioanalytical Chemistry*, vol. 394, no. 7, pp. 1729–1745, 2009.

[10] S. B. Chaney, S. Shanmukh, R. A. Dluhy, and Y.-P. Zhao, "Aligned silver nanorod arrays produce high sensitivity surface-enhanced Raman spectroscopy substrates," *Applied Physics Letters*, vol. 87, no. 3, Article ID 031908, 2005.

[11] P. Negri and R. A. Dluhy, "Ag nanorod based surface-enhanced Raman spectroscopy applied to bioanalytical sensing," *Journal of Biophotonics*, vol. 6, no. 1, pp. 20–35, 2013.

[12] S. Sánchez-Cortés and J. V. García-Ramos, "Anomalous Raman bands appearing in surface-enhanced Raman spectra," *Journal of Raman Spectroscopy*, vol. 29, no. 5, pp. 365–371, 1998.

[13] N. R. Yaffe and E. W. Blanch, "Effects and anomalies that can occur in SERS spectra of biological molecules when using a wide range of aggregating agents for hydroxylamine-reduced and citrate-reduced silver colloids," *Vibrational Spectroscopy*, vol. 48, no. 2, pp. 196–201, 2008.

[14] P. Negri, N. E. Marotta, L. A. Bottomley, and R. A. Dluhy, "Removal of surface contamination and self-assembled monolayers (SAMs) from silver (Ag) nanorod substrates by plasma cleaning with argon," *Applied Spectroscopy*, vol. 65, no. 1, pp. 66–74, 2011.

[15] N. Nuntawong, P. Eiamchai, B. Wong-Ek et al., "Shelf time effect on SERS effectiveness of silver nanorod prepared by OAD technique," *Vacuum*, vol. 88, no. 1, pp. 23–27, 2013.

[16] K. L. Norrod and K. L. Rowlen, "Removal of carbonaceous contamination from SERS-active silver by self-assembly of decanethiol," *Analytical Chemistry*, vol. 70, no. 19, pp. 4218–4221, 1998.

[17] S. Z. Zou, Y. X. Chen, B. W. Mao, B. Ren, and Z. Q. Tian, "SERS studies on electrode/electrolyte interfacial water I. Ion effects in the negative potential region," *Journal of Electroanalytical Chemistry*, vol. 424, no. 1-2, pp. 19–24, 1997.

[18] J. Hanzlíková, M. Procházka, J. Štěpánek, J. Bok, V. Baumruk, and P. Anzenbacher Jr., "Metalation of 5,10,15,20-tetrakis(1-methyl-4-pyridyl)porphyrin in silver colloids studied via time dependence of surface-enhanced resonance Raman spectra," *Journal of Raman Spectroscopy*, vol. 29, no. 7, pp. 575–584, 1998.

[19] C.-H. Chuang and Y.-T. Chen, "Raman scattering of L-tryptophan enhanced by surface plasmon of silver nanoparticles: vibrational assignment and structural determination," *Journal of Raman Spectroscopy*, vol. 40, no. 2, pp. 150–156, 2009.

[20] P. Šimáková, M. Procházka, and E. Kočišová, "SERS microspectroscopy of biomolecules on dried Ag colloidal drops," *Spectroscopy*, vol. 27, no. 5-6, pp. 449–453, 2012.

[21] M. Procházka, J. Hanzliková, J. Štěpánek, and V. Baumruk, "Metalation of positively charged water soluble mesoporphyrins studied via time-resolved SERRS spectroscopy," *Journal of Molecular Structure*, vol. 410-411, pp. 77–79, 1997.

[22] M. Itabashi, K. Kato, and K. Itoh, "Electrochemical processes of meso-tetrakis (4-sulfonatophenyl) porphine at a silver electrode studied by surface-enhanced resonance Raman spectroscopy," *Chemical Physics Letters*, vol. 97, no. 6, pp. 528–532, 1983.

**Supplement [III]**

JAHN, M., S. PATZE, I. J. HIDI, R. KNIPPER, A. RADU, A. MUHLIG, S YUKSEL, V. PEKSA, K. WEBER, T. MAYERHOFER, D. CIALLA-MAY, J. POPP, **Plasmonic nanostructures for surface enhanced spectroscopic methods**. Analyst, 2016, 141(3), 756-793.

Analyst

CRITICAL REVIEW

View Article Online
View Journal | View Issue



Cite this: *Analyst*, 2016, **141**, 756

# Plasmonic nanostructures for surface enhanced spectroscopic methods

Martin Jahn,[a,b] Sophie Patze,[a,b] Izabella J. Hidi,[a,b] Richard Knipper,[a,b] Andreea I. Radu,[a,b] Anna Mühlig,[a,b] Sezin Yüksel,[a,b] Vlastimil Peksa,[c] Karina Weber,[a,b] Thomas Mayerhöfer,[a,b] Dana Cialla-May*[a,b] and Jürgen Popp[a,b]

A comprehensive review of theoretical approaches to simulate plasmonic-active metallic nano-arrangements is given. Further, various fabrication methods based on bottom-up, self-organization and top-down techniques are introduced. Here, analytical approaches are discussed to investigate the optical properties of isotropic and non-magnetic spherical or spheroidal particles. Furthermore, numerical methods are introduced to research complex shaped structures. A huge variety of fabrication methods are reviewed, *e.g.* bottom-up preparation strategies for plasmonic nanostructures to generate metal colloids and core–shell particles as well as complex-shaped structures, self-organization as well as template-based methods and finally, top-down processes, *e.g.* electron beam lithography and its variants as well as nanoimprinting. The review article is aimed at beginners in the field of surface enhanced spectroscopy (SES) techniques and readers who have a general interest in theoretical modelling of plasmonic substrates for SES applications as well as in the fabrication of the desired structures based on methods of the current state of the art.

Received 6th October 2015,
Accepted 23rd December 2015

DOI: 10.1039/c5an02057c

www.rsc.org/analyst

[a]*Institute of Physical Chemistry and Abbe Center of Photonics, Friedrich Schiller University Jena, Helmholtzweg 4, 07743 Jena, Germany. E-mail: dana.cialla-may@uni-jena.de*
[b]*Leibniz Institute of Photonics Technology (IPHT), Albert-Einstein-Strasse 9, 07745 Jena, Germany*
[c]*Institute of Physics, Charles University in Prague, Ke Karlovu 5, 121 16 Prague 2, Czech Republic*

## 1. Introduction

Metallic nanostructures are known to show interesting optical properties within the electromagnetic spectrum from UV to the MIR spectral region. As an example, they are utilized to enhance the optical signal in fluorescence, Raman and IR

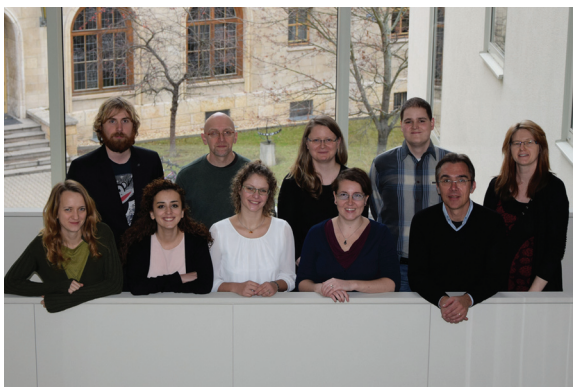

**From left to right: Andreea I. Radu, Richard Knipper, Sezin Yüksel, Thomas Mayerhöfer, Sophie Patze, Dana Cialla-May, Izabella Hidi, Martin Jahn, Jürgen Popp, Karina Weber**

*The research group Jena Biochip initiative (JBCI), embedded within the research group of Prof. Dr Jürgen Popp, is headed by Dr Karina Weber and Dr Dana Cialla-May. The objective of JBCI is the research and establishment of novel chip-based detection methods for biomolecules and pathogens that are based on specific metal deposition reactions as well as the application of innovative plasmonic active metallic nanostructures in bioanalytics. As an example, surface enhanced spectroscopic methods such as SERS are in focus. The JBCI group works on the fabrication and characterization of powerful SERS substrates achieved by bottom-up and top-down methods. By combining SERS with microfluidics, SERS measurements in high throughput and under reproducible conditions are performed by JBCI addressing analytical questions in therapeutic drug monitoring, pathogen diagnostics and the detection of ecological harmful substances. Additionally, SERS is applied in food and environmentally relevant detection schemes by the group. Moreover, the research group deals with the simulation, fabrication and characterization of SEIRA substrates. Finally, the sample preparation is an important research topic of JBCI* e.g. *extraction and amplification. Thus, the entire analysis chain is covered by JBCI to address the needs of modern bioanalytics.*

spectroscopies. In the Late Antiquity period the optical properties of gold nanoparticles were employed for coloring glass and artworks, evidently without knowledge about the physical phenomenon arising from nanometer-scaled metallic particles. The Late Roman Lycurgus Cup, which appears red when illuminated from behind and, in contrast, green when illuminated from the front, is one of the most prominent representatives of the optical effect of gold nanoparticles in artworks.[1,2]

In the 19th century, Michael Faraday described for the first time the preparation of gold nanoparticles as well as their intense red-violet color as a function of the particles.[3,4] Today, it is commonly known that the underlying phenomenon is attributed to the excitation of localized surface plasmon resonances based on the collective oscillation of the electron cloud within the metal nanoparticle.[5] An analytical solution of Maxwell's equations for the scattering of an electromagnetic wave by a metallic sphere was presented in 1908 by Gustav Mie.[2,6] These findings provided the basis for the research on plasmonic effects of metallic nanoparticles as well as their applications in a variety of application fields *e.g.* chemical analysis and catalysis,[7–9] detection of biomolecules,[10–12] medicine (diagnosis, imaging and therapy),[7,9,13,14] detection of pollution and heavy metal ions,[15] small inorganic compounds,[16] food analysis investigating food additives and contaminations[17] and, as recently summarized, ultrafast optical processes.[18]

In section 2, the interaction of light with metallic nanostructures based on the excitation of surface plasmon polariton modes, field enhancement as well as various types of surface enhanced spectroscopic (SES) techniques will be introduced. The focus of this review article is the optical simulation and fabrication of nanostructures which are utilized in SES techniques. Therefore, in section 3, the simulation of the optical properties of metallic nanostructures is described in detail. Here, a variety of nanoparticle structures and arrangements of nanostructures are introduced. To prepare the exceptionally designed nanostructures as well as arrays, various bottom-up, top-down and self-organization methods are available. Thus, in sections 4, 5 and 6, we introduce these fabrication methods in the order of increasing complexity. As a consequence, the interested reader will get a comprehensive overview of the fabrication routines of plasmonic nanostructures to accomplish the desired optical concept.

## 2. Theoretical background

Due to the interaction of light with metallic nanoparticles, surface plasmon resonances are excited and, as a consequence, a strong electromagnetic field is induced on the metallic surface. This resonant excitation composed of the oscillation of electrons in metallic nanoparticles and their related local field enhancement is known as localized surface plasmon polariton (LSPP).[5] Its physical concept is depicted in Fig. 1A. Here, the metal nanoparticle acts as a dipole antenna and emits light according to the characteristic of a Hertzian dipole. The spectral position of the plasmon resonance is defined by

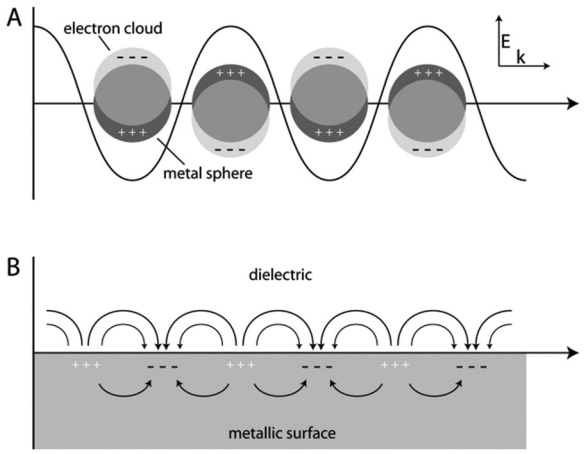


**Fig. 1** Schematic illustration of (A) localized and (B) propagating surface plasmon polaritons. *E* depicts the electric field vector and *k* the wave vector.

the plasmon resonance condition ($\mathrm{Re}(\varepsilon_i) \approx -2\varepsilon_a$; $\mathrm{Im}(\varepsilon_i) \ll 1$; $\mathrm{Re}(\varepsilon_i)$ – real part of the dielectric constant of the metal; $\mathrm{Im}(\varepsilon_a)$ – imaginary part of the dielectric constant of the surrounding medium).[19] It is tunable by changing the surrounding medium as well as the size, shape and material of the nanoparticles.[20,21] In the case of planar metal surfaces, propagating surface plasmon polariton (PSPP) modes are found at boundaries between the dielectric and metal conductors.[5] This is illustrated in Fig. 1B. However, an excitation of the PSPP mode at a smooth metallic surface is only possible if the *k* vector of the incoming light is parallel to the surface.[22] Thus, the so-called Kretschmann or Otto configurations, which are based on the concept of the attenuated total reflection, have to be applied. The strong dependency of the surface plasmon resonance on changes of the refractive index in the close vicinity of a planar metal surface is used in bioanalytics by SPR sensors.[23,24] Micro- and nanostructuring of the metallic surface enable the excitation of PSPP modes by electromagnetic waves with the *k* vector with a non-parallel orientation to the surface.[22] Here, the spectral position of the PSPP mode is defined by the incidence angle of light and the grating constant of the periodically structured surface (grating coupling). The patterning of metallic surfaces enables PSPP modes, which are accompanied by near-field enhancements of the electric field *E*.

By using these effects, various application fields in ultrasensitive analytics open up. Accordingly, the electromagnetic field enhancement is applied for enhancing the Raman cross-section (surface enhanced Raman spectroscopy, SERS),[25–27] fluorescence (surface enhanced fluorescence, SEF),[28–31] as well as the IR absorption (surface enhanced infra-red absorption, SEIRA).[32,33]

### 2.1 Surface-enhanced Raman spectroscopy (SERS)

The SERS effect was first discovered in the 70s of the last century when the Raman signal of the pyridine adsorbed on roughened silver electrodes was investigated.[34–36] Due to the

high sensitivity and molecular specificity, the SERS technique became a powerful tool in chemical, biochemical and biological application fields.[10,37,38] SERS is applied as a diagnostic and imaging tool in medicine, *e.g.* immuno assays employing SERS tags, for research on the interaction of metallic nanoparticles with cells,[7,9,13,14,39] for the investigation of catalytic reactions at plasmonic active surfaces,[7–9] to detect environmental pollution[15,40] and to investigate food additives and contaminations.[17] By combining SERS with microfluidic devices, high throughput measurements under reproducible conditions are available.[41–43] In order to describe the enhancing mechanism in SERS, two contributions are discussed: the electromagnetic as well as the chemical enhancement. The main contribution to the SERS signal is based on the electromagnetic mechanism, which is described in the following paragraphs.

Surface plasmon polaritons can be excited in nanostructured metallic surfaces or metallic nanoparticles if the wavelength of the incident light meets the plasmon resonance condition.[19] As a result, a strong electromagnetic field with an evanescent character is induced on the metallic nanostructure. Since the plasmon resonance has to overlap with the excitation wavelength applied in the SERS experiment, silver, gold and copper are preferentially used in the visible and NIR spectral ranges, and aluminum, ruthenium, rhodium, palladium and platinum in the UV region.[44,45] As a consequence, the Raman modes of a molecule which is located in close vicinity to the nanostructure are enhanced since the Raman intensity is proportional to the squared incident electromagnetic field intensity. Based on the characteristics of a Hertzian dipole, the Raman scattered light is emitted – summarized over all orientations of the molecule – in all spatial directions. It is collected and detected according to the aperture of the microscope objective. In addition, the Raman scattered light undergoes a further enhancement if the Raman mode also overlaps with the plasmon resonance. In the literature, this phenomenon is named emission enhancement or the second part of the electromagnetic mechanism and has been investigated theoretically[46,47] as well as experimentally.[48–50] As a consequence, Raman modes next to the plasmon resonance are the most intense.

The overall electromagnetic enhancement factor $G$ shows a fourth-power dependency and is defined as follows:[48,50–52]

$$G = M_{\mathrm{Loc}}(\omega_{\mathrm{L}})M_{\mathrm{Loc}}(\omega_{\mathrm{R}}) = \frac{|E_{\mathrm{Loc}}(\omega_{\mathrm{L}})|^2}{|E_0(\omega_{\mathrm{L}})|^2}\frac{|E_{\mathrm{Loc}}(\omega_{\mathrm{R}})|^2}{|E_0(\omega_{\mathrm{R}})|^2} \approx \frac{|E_{\mathrm{Loc}}(\omega_{\mathrm{L}})|^2|E_{\mathrm{Loc}}(\omega_{\mathrm{R}})|^2}{|E_0|^4} \quad (2.1.1)$$

with $M_{\mathrm{Loc}}$ being the local field enhancement at the laser excitation frequency ($\omega_{\mathrm{L}}$) and the frequency of the Raman mode ($\omega_{\mathrm{R}}$). Moreover, $E_{\mathrm{Loc}}$ is defined as a locally enhanced electromagnetic field and $E_0$ is the electromagnetic field of the incident laser light. Based on theoretical considerations, the influences of shape, size, material and interparticle distances of nanoparticles on the SERS enhancement factor are investigated.[53] Here, the maximum electromagnetic enhancement factor under SERS conditions is theoretically estimated to be $10^{11}$.

The chemical mechanism, which contributes to the overall SERS enhancement by a factor of $10^1$ to $10^3$, is understood as the sum of various contributions: (1) signal enhancement based on chemical interactions between a molecule and a nanoparticle in the ground state, (2) SERS enhancement due to resonant excitation of charge transfer processes between a nanoparticle and a molecule and (3) resonance Raman enhancement based on the excitation of an electronic transfer within the molecule.[54]

When comparing SERS and Raman spectra, spectroscopically forbidden Raman modes are observable under SERS conditions. In 1988, the variation in spectroscopic selection rules based on field gradients in optical tweezers had already been discussed; however, without giving an experimental proof.[55] As already mentioned, the electromagnetic field, which is induced on the surface of the metallic nanoparticle, shows an evanescent character and, thus, the molecules of interest in the close vicinity of the surface are strongly affected by the field gradient. This leads to a breakdown of the conventional selection rules applied for Raman spectroscopy.[56] Observations of spectroscopically forbidden Raman modes within the SERS spectrum under near-field conditions are established and referred to as the field gradient Raman effect.[57] Moreover, forbidden electronic transitions, induced by the field gradient effect, are observable in the form of resonance Raman bands in the SERS spectra of carbon nanotubes.[58]

The changes in Raman intensities of various modes within the SERS spectrum are discussed based on surface selection rules.[59–61] A molecule is characterized by its Raman tensor and the orientation relative to the metallic surface. The enhancement of various Raman active modes is dependent on field components parallel and perpendicular relative to the surface. Due to the dominance of the Raman tensor diagonal component over the Cartesian coordinate parallel to the surface normal, only vibrations with a dynamic dipole perpendicular to the surface will be observed. Raman modes, which are oriented parallel to the metal surface, are – if at all – detected with very weak intensity.

Another important parameter with respect to the interaction of plasmon modes with molecular excitonic resonances is the so-called coupling rate. This depends on the oscillator strength of the molecular resonance and the mode volume of the confined fields. If the coupling rate approaches the dephasing rate of the two resonances the approximation of weak coupling, in which both resonances are treated independently, is no longer valid. This means, energy is coherently exchanged between the plasmon and the exciton and, hence, hybridized resonances are formed. This transition from the weak- to the strong-coupling regime can be observed experimentally in the form of the so-called Rabi splitting and Fano-like resonances in the scattering spectrum.[56]

### 2.2 Surface-enhanced fluorescence (SEF)

The detection of fluorescence is one of the most common techniques for assays utilized in drug detection, high-throughput screening or cellular imaging. The sensitivity of fluorescence

 

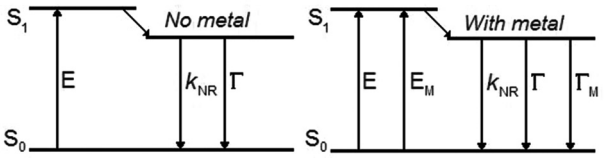


Fig. 2 Jablonski diagram for inclusion of metal–fluorophore interactions (modified from Hao *et al.*[73]).

to the local environment due to chemical interactions can be used to monitor for example pH changes, viscosity or local polarity. In order to increase the intensity of fluorescence, the most fundamental property of a fluorophore, its radiative decay rate, has to be changed. This rate can be changed by modifying the photonic mode density around the fluorophore by positioning it in the proximity of a metal surface or particle. A 1000-fold fluorescence enhancement near a metal particle had been theoretically predicted already in 1981,[62] which was later experimentally confirmed.[63,64] In several studies, the application of SEF in (bio)analytics is introduced. As an example, dual-mode SERS-fluorescence nanoparticle arrangements are employed among others for the detection of markers on cells.[65] Further on, SEF is a promising detection tool in immunoassays[66] to detect the toxin microcystin-LR[67] or the tumor marker carcinoembryonic antigen.[68] SEF is additionally applied to detect mercury ions relevant in environmental science.[69] Finally, the potential of the SEF method is illustrated by an antenna-in-box device, which can be utilized for single-molecule experiments at physiologically relevant concentrations.[70]

To understand the fluorescence enhancement in close proximity to metal surfaces, first the processes related to fluorescence will be briefly described. Fig. 2 shows the basic excitation and emission processes in molecules. A molecule is excited by absorbing a photon ($E$). Then the molecule swiftly relaxes to the excited state $S_1$, from which it drops back to the ground state $S_0$ either by radiating a photon ($\Gamma$) or by any form of non-radiative process ($k_{NR}$). The average time a molecule stays in the excited state is described as its lifetime $\tau_0$.

$$\tau_0 = \frac{1}{\Gamma + k_{NR}} \quad (2.2.1)$$

The fluorescence quantum yield $Q_0$ is defined in general as the ratio between radiative decay and total decay, or, in other words, the ratio between the number of emitted and absorbed photons.

$$Q_0 = \frac{\Gamma}{\Gamma + k_{NR}} \quad (2.2.2)$$

Both the lifetime and quantum yield can be strongly affected by the surrounding environment. A very significant change occurs in the proximity of a metal surface. One effect is the enhancement of the local field ($E_M$) by the interaction with the surface plasmons. Another effect is the increase of the radiative decay rate by including the metal-induced radiative rate $\Gamma_M$. This leads to the following modifications of eqn (2.2.1) and (2.2.2) for the lifetime $\tau_M$ and quantum yield $Q_M$:

$$\tau_M = \frac{1}{\Gamma + \Gamma_M + k_{NR}} \quad (2.2.3)$$

$$Q_M = \frac{\Gamma + \Gamma_M}{\Gamma + \Gamma_M + k_{NR}} \quad (2.2.4)$$

A more detailed theoretical description is given in the literature.[31] With an increase of $\Gamma_M$ the lifetime decreases and the quantum yield increases. Since the maximum number of photons per second emitted by a molecule is roughly proportional to the inverse of the lifetime, a shorter lifetime leads to a higher photon flux, especially with a higher illumination intensity. Additionally, the reduced lifetime of the excited state increases the fluorophore photostability. In order to achieve the maximum possible enhancement it is desirable to achieve an overlap between the fluorophore emission wavelength and the surface plasmon resonance of the metallic structure.

Moreover, the interspace between a fluorophore and the metal surface is very important. In the case of very small gaps (<2–3 nm), the fluorescence is quenched due to energy transfer to the metal surface. The optimal distance for fluorophores from a surface is still a subject of discussion, but it generally ranges between 5 nm (ref. 71) and 20 nm,[72] with most of the research studies agreeing on a displacement of around 10 nm.[28,30,73,74] However, the surface enhancement of fluorescence has already been reported for silver nanoparticle aggregates with an interparticle distance of only 1–2 nm.[64] In such narrow gap regions the local electromagnetic fields seem to be strong enough in order to enhance the fluorescence signal despite the quenching processes. The spacing between a metal surface and a fluorophore is usually achieved by a non-conductive layer with a defined thickness, *e.g.* composed of $Al_2O_3$,[73] $SiO_2$ [72] or DNA strands.[28] Another important effect, which influences the total fluorescence enhancement, is the possibility of non-radiative emission directly into the metal.[64] This additional decay pathway, in combination with the increased radiative decay rate, can lead to the breakdown of the general molecular electronic dynamics.[56] When the total enhanced decay rate equals the vibrational relaxation rate, or exceeds it, direct emission from the excited vibrational states in $S_1$ cannot be neglected anymore. The nature of this emission, again, can be radiative as well as non-radiative. In the latter case, an anomalous ratio between the intensities of SERS and SEF signals is observable. If the radiative decay is dominating, the shape of the fluorescence spectrum is changed and it becomes blue-shifted relative to the spectrum of a free space molecule. A comprehensive overview of this so-called fast-dynamics SEF can be found elsewhere.[56]

Further on, metal surfaces are also utilized for studying the Förster Resonance Energy Transfer (FRET) between molecules. This is based on a dipole–dipole interaction between a donor and an acceptor molecule. This interaction is strongly dependent on the distance between the molecules, and it has been proven that the presence of metallic surfaces can increase the

strength of donor–acceptor interactions, and therefore increase the Förster distance, which is defined as the distance at which the FRET is 50% effective, by up to 75%.[75]

### 2.3 Surface-enhanced infrared absorption (SEIRA)

SEIRA and SERS share the same mechanism of an electromagnetic enhancement model. Therefore, SEIRA also depends on analyte–surface structure interactions to couple incident light into plasmon resonances, as it is described for the SERS mechanism. The enhancement of absorption bands between 2850 $cm^{-1}$ and 2960 $cm^{-1}$ was demonstrated first by Hartstein *et al.*[76] in a metal-on-analyte-setup and also in an analyte-on-metal-configuration, called the metal under/overlayer geometry, and later proved by Hatta *et al.*[77] Results and advances in the emerging field of SEIRA are comprehensively reviewed.[78,79] Recently, several studies reported on SEIRA application fields, *e.g.* the detection of protein monolayers,[80] an investigation of the chemical interaction between recognition proteins with target antibodies[81] as well as research on few nm thick organic layers.[82–84] Moreover, biolabels based on SEIRA active fluorophore–antibody nanoconjugates are described as promising tools in fast, reliable and multiplexed screening.[85]

A significant difference of SEIRA in contrast to SERS is the different frequency range, and thus the application of different metals as an enhancing medium. In SERS, silver, gold and copper for the visible and NIR spectral regions and aluminum, rhodium, ruthenium, palladium and platinum for the UV region are preferentially used as plasmonic materials. For the infrared range of SEIRA, the plasmon resonance condition ($|\mathrm{Re}(e)| \gg \mathrm{Im}(e)$), and with this the excitation of plasmon polariton modes, is fulfilled additionally for the metals indium, protactinium, nickel and lead. However, since copper, indium and aluminum tarnish fast and feature low enhancement, not much attention has been paid to these materials.

Relying on the same surface enhancement effect as SERS, the surface selection rules already known are applied as well. Namely, away from the plasmon frequency only dipole changes normal to the surface result in enhanced absorption bands. The short-ranged enhancement model was also proven for SEIRA,[86–88] where Langmuir Blodgett spacer films support the distance relationship for the enhancement to be

$$|E_{\mathrm{loc}}|^2 = \frac{4p^2}{d^6} \tag{2.3.1}$$

with $p = \alpha VE$ being the dipole moment [$\alpha$ = polarizability; $V$ = volume of the metal island] and $d$ = distance from the metal surface. Again, as for SERS, a chemical contribution is also present for SEIRA as molecules can be oriented by chemisorption with a particular axis perpendicular to the surface, leading to a stronger absorption of the dipole changes along this axis. Furthermore, charge-transfer processes boosting the absorption-cross-section are also present but are nearly negligible.

In 2012, Alonso-Gonzalez *et al.*[89] further improved and solidified the SEIRA theory by shedding light on the electromagnetic mechanism of scattering in surface enhanced processes. Briefly, not only the $f^2$ dependent infrared absorption

$$f^2 = \frac{|E_{\mathrm{loc}}|^2}{|E_{\mathrm{in}}|^2} \tag{2.3.2}$$

has to be taken into account, but also the $f^4$ dependent structure-mediated scattering. The scattering effect by the metal antenna-like structures, whether metal-island or artificial, is considered to be small. But regarding the fourth power dependency, it may be an important contributor in SEIRA as well as in comparison to the case of SERS.

## 3. Simulation of plasmonic nanostructures

Knowing how electromagnetic waves interact with metallic nanoparticles and nanostructured metallic surfaces is crucial to exploit and optimize them for specific applications. A variety of theoretical approaches have been developed to get further insight into the physics of these plasmonic structures.[90,91] For predicting the light scattering behavior of isotropic and non-magnetic spherical or spheroidal particles the analytical approach of the Mie theory can be used.[92] In this theory, the fields in the Maxwell equations are expressed as spherical harmonics. It is also possible to extend this theory to predict the plasmonic properties of core–shell nanoparticles.[93,94] By introducing the electrostatic approximation, also known as quasi-static or long-wavelength approximation, the problem of solving the Maxwell equations is reduced to the solution of Poisson's equation for an electrostatic field.[95,96] In this simplified picture, the electromagnetic wave is treated as a uniform electric field whose field vector oscillates up and down with the frequency $\omega$. Therefore, it is obvious that the approximation is only valid in cases where the important dimensions are sufficiently smaller than the wavelength. Even though the maximum dimension is limited to $\frac{\lambda}{20}$, the electrostatic approximation is often applied for larger particles because of their simplicity.[95]

For the description of the optical properties of more complex shaped structures a variety of numerical methods like the discrete dipole approximation (DDA),[97] the dyadic Green's tensor method,[98] the boundary elements method (BEM),[99] the finite elements method (FEM)[100] and the finite difference time domain (FTDT) or frequency domain (FDFD) method[101] with their numerous variants are applied. These methods are based on solving the Maxwell equations either in the frequency domain (DDA, BEM, FEM and FDFD) or in the time domain (FDTD). In the case of the DDA the particles are assumed to consist of small dipoles which reduces the problem to the investigation of electromagnetic interactions of coupled dipoles.[90] The Green's tensor method is based on the volume integral equation for scattering, whereby the Green's dyad gets introduced to compute the total electric field.[98,102] To avoid

 

convergence difficulties and singularities at the mesh center it is also possible to transform the equation into its surface integral expression.[103] Furthermore, both methods, DDA and Green's tensor method, are extendable to cover thermal effects and calculate the temperature profiles of plasmonic structures.[104] In BEM the surface integral formulation of the Maxwell equations is used to solve the problem by discretization.[91] The concept of discretization is also used in FEM and FDTD. For FEM the Helmholtz equations are discretized in space and are solved numerically. Thereby, the aim is to find solutions which fulfill the boundary conditions. In FDTD the discretization is used in space as well as in time. The differential equations are expressed in terms of difference quotients and get solved for every space element in each time step. A detailed explanation of these numerical techniques is beyond the scope of this work and can be found elsewhere.[90,91] The FDTD method has the benefit of a comparably simple implementation and provides in contrast to FEM, spectral broad-band information on a single run.[105,106] On the other hand, FDTD is based on a rectangular grid which causes inaccuracies while computing curved or highly dynamic surfaces. In FEM modelling triangular or tetrahedral meshes are used. Thus, this technique handles the modeling of round shaped structures more efficiently. Regarding the computational performance, FDTD is more limited by the speed and number of processors, whereas, FEM is more memory demanding.

An important phenomenon is the coupling of particle plasmons which happens when nanoparticles are in close vicinity to each other. Thereby an increase in field strength by several orders of magnitude can be observed. In addition to numerical methods, an alternative approach for the investigation of this coupling behavior was developed: the so-called plasmon hybridization method.[107–109] In analogy to the hybridization of atomic orbitals in the molecular orbital theory the plasmon modes of coupled nanoparticles can be seen as "hybridized" plasmon modes resulting from the interaction of the plasmons of the involved nanoparticles. These interactions result in low energy "bonding" and high energy "anti-bonding" plasmon modes which correspond to the symmetric and antisymmetric coupling of the modes. Aside from a qualitative understanding, the plasmon hybridization method also delivers quantitative results in good agreement with the Mie theory and numerical approaches.[107,108,110] For investigating the plasmonic response of more complex shaped nanoparticles this model is also applicable. Here, the particle is assumed as being decomposed into simple-shaped parts. The plasmon resonances from the particle can then be treated as the result of the hybridization of the plasmon modes from these artificial parts. In the case of a nanoshell, for example, the plasmon modes follow from the assumed interaction of the plasmons from a sphere and a spherical cavity (see Fig. 3).

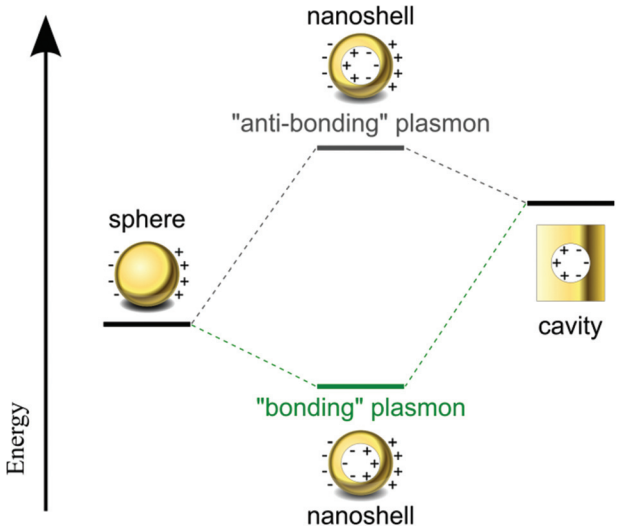


Fig. 3 Energy level diagram to depict the principle of the plasmon hybridization model at the example of a metal nanoshell. The resulting anti-symmetrically ("anti-bonding") and symmetrically (bonding) coupled plasmon modes of the nanoshell originate from the imagined interaction between the plasmons of a sphere and a cavity (modified from Prodan *et al.*[107]).

### 3.1 Coupled nanoparticles

Adjusting the spectral position of plasmon resonances to the desired working wavelength is vital for designing and optimizing plasmonic substrates for spectroscopic applications. The optical response of metallic nanoparticles can be tuned by changing their size, shape, material as well as the surrounding medium.[5,94,111–114] An additional approach is to couple them with nearby placed nanoparticles by means of their electromagnetic near-fields. This coupling of plasmon modes leads also to the formation of volumes between the particles with strongly enhanced electromagnetic fields, the so-called "hot-spots".[115–119] Nowadays, there are several established fabrication techniques for the production of nanostructures with well-defined design parameters for tailoring the interaction between the plasmon resonances. A widely used group of approaches is self-organizing processes by which dimers or larger aggregates of identical as well as diverse particles can be realized.[120–123] For the generation of nanostructures on plain substrates by bottom-up techniques the phenomenon of self-organization plays a prominent role.[124] On the other hand nanofabrication techniques like nanosphere lithography, electron beam lithography (EBL) or focused ion beam milling (FIB) can be applied for producing arbitrary structures with high reproducibility.[25,125–127]

Independently of the fabrication technique, the gap size is a crucial parameter for the design of plasmonic structures as it has a remarkably influence on the coupling strength and thus on the resonance frequency. In order to calculate the extinction efficiency spectrum of nanoparticle dimers and trimers the DDA method can be employed.[128] Earlier, a universal scaling rule for the coupling of the plasmon modes of nanosphere pairs was found.[129] According to that, the spectral position of the plasmons only depends on the distance between the particles in length units normalized to the particle dimensions in spectral regions with a low variance of optical con-

stants. Within the study this scaling behavior is proven to be also valid for pairs of spheroids, cylinders and rods as well as for nanosphere trimers. The resonance frequency of the bonding plasmon mode shows an exponential decay (red-shift) with a decreasing interparticle distance, whereas the near-field enhancement is increasing. Thereby, the relative red-shift is dependent only on the ratio of the gap size and a characteristic size parameter of the structure. Parameters like the particle shape, material (considering low variances in optical constants) and the surrounding medium do not affect this scaling rule. Furthermore, the authors forecast that this scaling behavior is a general phenomenon which should be valid for the three-dimensional case as well. For tuning the resonances of nanoparticle arrangements to the desired wavelength this scaling rule can be very helpful.

However, for a given gap size the influence of the particle shape in the gap region cannot be neglected. Especially in the case of nanoparticle pairs with small gap sizes, their shape has a remarkable effect on the coupling behavior of plasmon modes. To get further insight, silver nanocube dimers with gap widths in the lower nanometer range of about 1–2 nm were investigated by means of spatial modulation spectroscopy.[131] In this study, the resulting optical extinction spectra were compared with DDA and FEM calculations to clarify the origin of the observed spectral features. It is shown that the local surface plasmon resonance splits into two modes in dependence on the curvature of the cube corners. This proves that small changes in the particle shape, especially for the case of small gap sizes, have a strong influence on the plasmonic properties. Thus, the exact particle shape in the close proximity regime should be taken into account for designing and tailoring plasmonic substrates.

Aside from particles with a spherical or a cubical geometry often nanorods are used as building blocks for nanoparticle dimers. A lot of attention is also paid to triangular shaped structures the corners of which show strongly enhanced local fields due to the lightning rod effect. Based on calculations carried out using the DDA method it can be concluded that the extinction spectra of triangular nanoprisms are independent from the polarization of the incident light while the distribution of the local electric fields is remarkably dependent on it.[130] The strongest near-fields caused by the main plasmon resonance occur at the two corners of the edge which is parallel to the electric field vector. A study for investigating the local field distribution of quasi two-dimensional crystalline metallic nanoprisms came to the same result.[132] By using interferometric tip-scattering scanning near-field optical microscopy (s-SNOM) to probe the evanescent fields and the DDA method to determine the origin of the measured plasmon resonances it was shown that in addition to dipole quadrupole and higher order modes are also excitable. Normally these modes get dampened as a result of the interaction in the bulk material, but not in this case due to the small thickness of the nanoprisms, which is in the range of the skin depth. Nevertheless, it has to be taken into account that the radiation into the far-field of higher order modes is of in general a rather low intensity because of their weak coupling to dipolar modes. In addition, it was found that the highest local field enhancement in the case of multipole modes is, counter intuitively, not necessarily located at the tips of such structures. According to the authors, attention should be paid to these facts for tailoring the optical properties of nanoprisms for spectroscopic applications. In the more complex case of hollow triangular shaped structures (see Fig. 4) the local electric field distribution at the outer sides is the same as for solid prisms. The differences occur inside the structure, where additional hot spots arise.[130] The strongest local field is thereby located at the inner corner opposite to the edge the corners of which are the hot-spots in the case of solid triangles. Furthermore, the main plasmon peak of solid prisms splits up into two prominent features in the extinction spectrum of the hollow triangles. These bands are both red shifted with respect to the solid triangular structures. Besides adjusting their optical response by increasing the edge length, which leads to a further red shift, hollow triangles can be tuned by changing the size of the inner triangle. Hence, the adjustability as well as the number of effective hot spot areas per structure can be increased by using hollow nanotriangles instead of solid ones. However, the greater technical effort for realizing these structures should also be kept in mind.

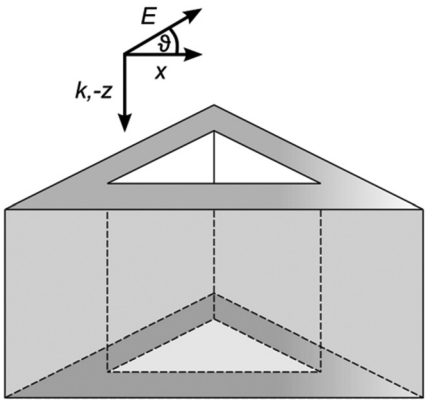


Fig. 4 Schematic illustration of a hollow triangular nanoprism and the polarization of the incident light. The simulation was performed for different angles $\vartheta$ in the range between 0 and 60 degrees (modified from Zhang *et al.*[130]).

As mentioned earlier, triangular particles are also often used as building blocks for dimers, which will thus be described as bowtie antennas. In a study based on the Green's tensor technique the optical properties of nanorod pairs and bowtie antennas were compared (see Fig. 5a and b).[133] Both structures show a strong field enhancement in the gap region. In all simulated cases nanorod pairs which are aligned along their long axes achieve a higher field enhancement. In the case of nanorod pairs the plasmon resonances also depend much more strongly on the gap width than for bowtie antennas. Besides this, the spectral position of the plasmon resonances can, independently from the type of the structure, be controlled by the length of the two coupled antennas. In con-

 

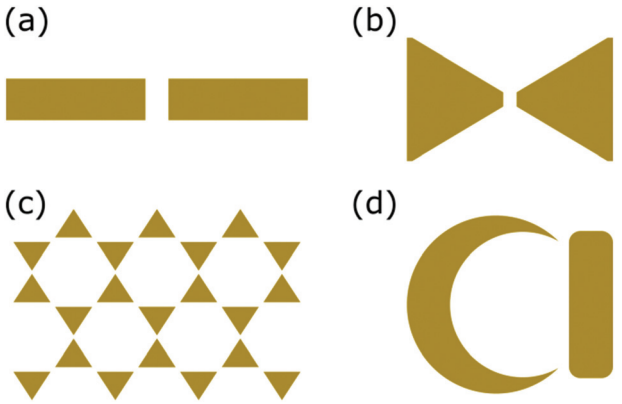


Fig. 5 Geometry of different simulated metal nanostructures: (a) nanorod pair, (b) bowtie antenna (modified from Fischer *et al.*[133]), (c) Fischer pattern (modified from Galarreta *et al.*[134]) and (d) nanocrescent coupled to a nanostrip antenna (modified from Kumar *et al.*[135]).

clusion, nanorod pairs seem to be more convenient for applications in which the near-field enhancement plays a more crucial role than bowtie structures. Otherwise, the plasmon resonances of bowtie antennas are more sensitive to refractive index changes compared to those of coupled nanorods. This is the reason why the former are a more suitable choice as platforms for surface plasmon sensing. Another often used SERS substrate which also relies on coupled triangular shaped nanostructures is the so-called Fischer pattern (see Fig. 5c), which is fabricated by means of nanosphere lithography. In contrast to Bowtie antennas the triangles are arranged in this case in a hexagonal grid. By FDTD simulations a clear dependency of the electric field distribution on the wavelength and the polarization of the incident light was found.[134] Another crucial parameter which determines the plasmon resonance frequency is the edge length of the triangles. Furthermore, it is shown that the highest field enhancement occurs at the gaps between the corners of the triangular structures for parallel to the connection axes polarized light. However, the authors conclude from their results that Fischer patterns in view of near-field enhancement per unit area are not necessarily optimal structures. For increasing the number of hot-spots maybe the use of hollow triangles as building blocks could be a suitable solution.

Nanocrescents are promising structures for surface enhanced spectroscopy because of their strong field-enhancement at both sharp ends. The ability of tuning the optical properties of metallic nanocrescents by changing their geometry was shown in various studies.[136–138] An alternative approach for altering the plasmon resonances and near-field enhancement of such structures is the coupling to another metallic nanoparticle (see Fig. 5d).[135] In this numerical study, based on a 2D FEM approach, a gold nanostrip antenna is brought into the close vicinity of gold nanocrescents. The coupling of the plasmon modes causes a red-shift of the nanocrescents' dipolar-resonance. The spectral position of this mode as well as its near-field enhancement depends on the length of the nanostrip as well as on its distance to the crescent. Hence, there are new degrees of freedom for tailoring the resonance frequency of the nanocrescents' dipolar mode without changing the shape of the structure itself. Furthermore, the field enhancement in the hot-spot of the coupled structures has an anisotropic behavior and can therefore be tuned by the angle of the incident light.

Another suitable platform for SERS applications with strongly enhanced local fields is two-dimensional subwavelength nanohole arrays.[139] In a comparative study the transmittance and SERS intensity of shallow and deep nanohole arrays with different diameters and edge-to-edge distances were investigated.[140] Based on three-dimensional FDTD calculations and SERS measurements it was shown that deep nanohole structures deliver the highest signal intensities. An explanation for this behavior is given by the coupling strength between the cavity plasmon modes of the top gold layer and the modes of the gold disks at the bottom of the cavities. In the case of shallow nanocavities there is a strong coupling, which leads to a weakening of the local electromagnetic fields and reduces in this way the SERS intensity. In contrast to this, the weakly coupled plasmon modes in deep nanohole structures result in strongly enhanced local electromagnetic fields and cause strong SERS signals. For this reason, avoiding a strong coupling between the two gold layers seems to be beneficial in such cavity structures to achieve high signal intensities.

Due to their strong and reproducible signal networks of corrugated silver nanowires and also nanowires with attached nanoparticles have attracted attention in the last few years as SERS substrates. Simulations for five different model structures were carried out to get a deeper insight into the enhancement mechanisms of these structures.[141] For the calculation of the electric field distribution a three-dimensional FDTD method was used. It is seen that corrugated nanowires provide higher field enhancements compared to smooth nanowires. Therefore, the density of the wires also plays a crucial role. With increasing density the number of gaps between the nanowires also increases but the gap size decreases. This results in more and brighter hot spots for a dense nanowire network in comparison with one of a lower density. The most homogeneous SERS signals were achieved with asymmetrically ordered nanowires. Such highly asymmetric substrates cause a depolarization of the incident light which leads to a higher uniformity of the gained signals. Furthermore, the attached nanoparticles enhance the local electric fields additionally by the interaction of their localized plasmon modes with the plasmon resonances of the nanowire.

The principle applicability of large aperiodic structures for surface enhanced spectroscopy derived from mathematical algorithms was investigated in a study based on the generalized Ohm's law approach.[142] Different structures like Fibonacci and the Rudin–Shapiro pattern as well as the random walk method generated cluster–cluster aggregates are part of this study. In addition an algorithm for generating random deterministic structures is applied. The authors found evidence for an inversely proportional relation between the density of hot spots and the maximal obtainable field enhancement in such

deterministic structures. The design parameters for optimizing the average signal enhancement can be estimated on the basis of the degree of disorder in the pattern. Such deterministic aperiodic structures, which can in principle be produced by EBL, could be applicable for surface enhanced sensing techniques. In addition, these results could lead to a more detailed understanding of the optical properties of planar, poorly ordered nanoparticle assemblies.

The coupling of plasmon modes in close spaced arrangements of metallic nanoparticles results in the formation of new modes, which can be described *via* using the plasmon hybridization method.[107,108] Because of symmetry reasons the excitation of anti-bonding modes by normally incident light is forbidden.[144] Furthermore, out-of-phase modes in symmetric nanoparticle dimers are "dark" as well because of their vanishing resulting dipole moment.[145] For this reason special illumination strategies or asymmetric plasmonic structures are needed to investigate these modes in experiment. One approach is the excitation and direct observation of anti-bonding modes *via* two-photon excited photoluminescence (TPPL).[146] In combination with FDTD calculations the near-field enhancement depending on the gap size between two rod-shaped nanoantennas and their aspect ratios was investigated. Aside from the increasing near-field enhancement with a decreasing gap-size smaller gaps lead to strong coupling which enables the selective excitation of the anti-bonding modes. These show a lower enhancement factor accompanied with a higher quality factor, which is defined as the ratio of the spectral peak position and its full width half maximum. On account of this, anti-bonding modes might be more interesting for near-field engineering and surface plasmon sensing than for surface enhanced spectroscopy.

This conclusion can be supported by a study based on a 3D FEM model for the calculation of the extinction spectra of asymmetric double split ring nanostructures (see Fig. 6).[143] Several electromagnetic resonances are found which originate from the coupling of the dipole with dipole modes as well as the dipole with multipole modes. Their spectral position is thereby clearly dependent on the degree of asymmetry. With respect to applications where the field enhancement is crucial it is shown that the dipole–dipole as well as the dipole–quadrupole bonding modes deliver a higher near-field enhancement in the two gap regions than the anti-bonding modes. The spectral position of the bonding modes is thereby located in the near-infrared region.

As seen before, breaking the structures' symmetry is another approach for the excitation of normally dark modes. By doing this, in-phase and out-of-phase modes should be visible simultaneously. Easily viable structures for investigating this effect are asymmetric dimers which can be realized by using particles which differ in size or material. Based on polarized scattering spectroscopy symmetric and asymmetric pairs of silver and gold nanospheres were investigated.[145] The measured spectra were corroborated with data gained by applying a coupled dipole–dipole model in the electrostatic approximation as well as the DDA method. For homodimers as well as size-asymmetric heterodimers the observed modes and their spectral position are explicable using the plasmon hybridization model while taking the asymmetry into account. In contrast to this, there is an unexpected red shift of the anti-bonding mode observed for asymmetric couples of silver and gold nanospheres. The origin of this effect is the coupling of interband absorption processes in the gold nanoparticles with the silver plasmon mode. Because of this, the plasmon hybridization model, in which normally the approximation of free electrons is used, needs to be expanded by considering interband transitions. Furthermore, due to the interaction of the partners in asymmetric heterodimers a couple of interesting effects like avoided crossing of plasmon modes, Fano resonances and an asymmetric scattering behavior can arise.[147] These effects have been studied extensively for dimers consisting of differently sized gold nanospheres and –shells (see Fig. 7) by FTDT calculations and the use of the plasmon hybridization method. In addition angle dependent dark-field spectroscopy at single heterodimers was carried out to prove and support the theoretical findings. Because of the fact that such a variety of effects appears in the case of an asymmetric couple of spheres it is pointed out that for more complex structures a virtually similar behavior is expected.

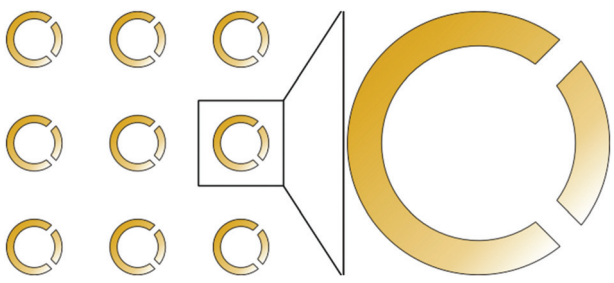

Fig. 6 Scheme of an array of asymmetric double split ring nanostructures (modified from Ding *et al.*[143]).

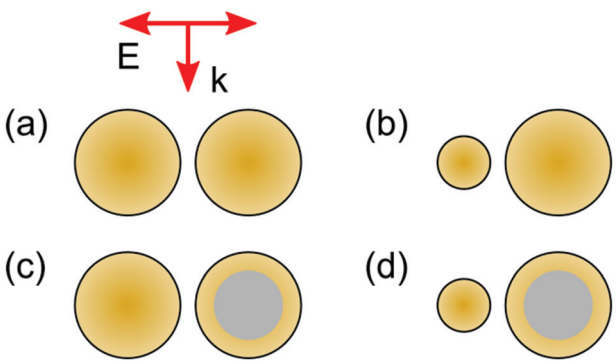


Fig. 7 Scheme of the simulated dimer structures: (a) gold nanosphere homo- and (b) heterodimers as well as (c) same and (d) different sized gold nanosphere/nanoshell heterodimers. The red arrows depict the polarization and direction of the incident light (modified from Brown *et al.*[147]).

 

In an earlier FDTD study it has already been shown that symmetry breaking has a remarkable effect on the optical response of nanoparticle assemblies and Fano resonances can appear.[148] As an example, metallic rings with a disk of the same material placed in their center were chosen. For symmetric arrangements two modes are observable which are formed by the interaction of the resonances of the ring and the disk: a subradiant bonding and a superradiant antibonding mode. In contrast, Fano-resonances arise in non-symmetric structures due to the interaction between the quadrupolar mode of the ring and the dipolar disk resonance. Due to the high sensitivity of such structures to a change of the refractive index of the material between the disk and the ring they are well suited as platforms for surface plasmon resonance sensing.

The central issue in the research studies reviewed before is the effect of coupling between closely arranged nanoparticles on their optical properties. Another question of interest for designing plasmonic structures is the influence of the substrate material on nearby placed nanoparticles. In a combined experimental and theoretical study this subject was investigated for the case of dielectric substrates.[149] For spherical bulk and core–shell nanoparticles a splitting of the dipolar mode into two dipolar modes polarized parallel and perpendicular to the surface was found. For a qualitative understanding of this behavior the simplified picture of image charges can be used. According to this, the spectral splitting is dependent on the dielectric constants of the substrate material, the distance between the particle and the substrate and the polarization of the incoming electromagnetic wave. The spectral shift between the two differently polarized plasmon modes increases thereby linearly with an increasing dielectric constant. Additionally, the highest influence is observed for bulk material gold nanospheres. From this study follows that the influence of the substrate material on the plasmon modes of nanoparticles cannot be simply neglected and should be taken into account for simulations as well as for experimental studies.

Also related to this topic is the interaction between nanoparticles and a thin metallic film. Based on single-particle dark-field spectroscopy the scattering spectra of spherical gold nanoparticles on top of a thin gold film as well as partly inserted into a gold film were recorded.[150] To reveal the origin of the observed optical resonances the electric field distribution was calculated by using the FDTD method. In the case of particles on top of the gold film the prominent spectral features arise from highly confined gap modes with azimuthal angular momenta. In contrast to this, strong dipole moments perpendicular and parallel to the film are responsible for the discovered scattering maxima of partly embedded particles. In both cases the resulting scattering spectra depend strongly on the polarization of the incident light. Additionally, a strong polarization dependency of the radiation pattern for particles on top of the gold film is observed.

For calculating the resulting electric fields in the more complex case of the interaction between the plasmon modes of a plain metallic layer and a nearby placed single metallic nanowire or grid the dyadic Green's tensor method was applied.[151] In order to get the optical response the authors employed additionally a scattering matrix based formalism. The interaction between the wire and the film leads to a red shift of the localized surface plasmon of the wire. This mode depends mainly on the layer-wire distance whereas the layer thickness itself has only a weak influence on the observed shift. In the case of the grid a contrasting behavior was observed. Now the localized resonance of the wire can be tuned by changing the thickness of the metallic film. For the design of substrates, in which a dielectric spacer layer separates the structure from a plain metallic film,[152] it should be important to consider these findings.

Another interesting question, regarding SEF, is the interaction of a spontaneous optical emitter like a fluorescent molecule with a metallic nanorod dimer. A model based on the Green's theorem surface integral equations was used for the description of the electromagnetic fields involved in this problem.[153] From it, the influence of the position and the orientation of the molecule on the radiative and non-radiative decay rates was investigated. For molecules in the center of the gap with a dipole moment parallel to the dimer axis the largest enhancement of the radiative decay rate was found which is attended by an increase of the quantum efficiency of the emitter. Furthermore, the molecule position and orientation of the dipole has also a strong influence on the near- and far-field pattern of the emitted light.

The resonance fluorescence of single molecules in the vicinity of a plasmonic nanostructure was investigated by applying Green's tensor technique.[154] Therewith, the near-field of these nanostructures, which consists of four nanostrip antennas, was determined. Based on this the fluorescence spectrum of a nearby placed dibenzanthanthrene molecule was calculated for different molecule positions. The resulting spectra show additional sidebands which can be explained by the splitting of the two-level system into a four-level system. Hereby, two competing effects play an essential role: the near-field enhancement and the modification of the decay rate. Both effects show a clearly visible dependency on the position of the molecule with respect to the four nanostripes. Positions with a high near-field enhancement combined with a low influence on the decay rate are optimal for recording resonance fluorescence spectra. Additionally, the spectral position of the plasmon modes should be tuned to match with the molecules resonances. By careful balancing of the aforementioned effects it is possible to realize conditions for observing phenomena like the Mollow triplet and photon antibunching of molecular fluorescence.

### 3.2 Core–shell nanoparticles

Core–shell nanoparticles open up more design options by combining advantages of different materials. Hence, particles are realizable which not only have the desired optical but also chemical properties for a certain application. Moreover, due to the fact that they consist of materials with different optical properties there are more parameters available for tailoring

their plasmonic behavior. A general guideline for optimizing the absorption and scattering properties of coated metal nanoparticles consisting of four basic steps was presented in the case of spherical core–shell nanospheres.[155] Because of their spherical geometry the method of choice for calculating the electromagnetic fields is the Mie theory. According to the proposed scheme the starting point is the definition of realistic boundaries for the optimization parameters. The next step involves preliminary calculations of the scattering energy to select the parameter range for the simulation on the basis of a certain threshold. Afterwards, the selection of the material takes place followed by optimization of the particle geometry. From this, it is possible to deduce from the calculations additionally the tolerances of the design parameters and with it the critical parameters for optimizing the particles. Moreover, this method of design is not limited to tuning the optical response of spherical particles. It can be as well adapted to other geometries by using for example FEM for the field computation.

Bimetallic multilayer nanoparticles with a dielectric or metallic core combine the stronger plasmon resonances of silver with the stability of gold nanoparticles.[156] Furthermore, an outer gold layer is also beneficial for biomedical applications. By numerical calculations based on the Mie theory it is found that the extinction efficiency of nanoparticles with a silver core or an inner shell and an outer shell of gold is higher than that for pure gold core–shell and multilayer nanoparticles. Besides the particle size, the crucial parameters for tuning the optical response of the nanoshells are the thicknesses of the dielectric layers and the outer shell. In accordance with the aforementioned study it was shown that a thin gold layer on silver nanoshells with a dielectric core (see Fig. 8) is beneficial with respect to the near-field enhancement which is stronger than that for pure silver shell nanoparticles.[157] It was found that the charges which are induced by the interaction of the conduction electrons with the incoming electromagnetic wave at the inner and outer surfaces of each layer have an opposite sign for the silver and gold layers (compare Fig. 8). A variation of the layer thickness of either the silver or the gold layer results in two competing effects. In a thicker layer more conduction electrons exist which contribute to the induced charge and this leads to a stronger near-field enhancement. On the other hand, a thicker layer causes a more pronounced separation between the inner and outer surfaces of the layer which reduces the effect of one of the surfaces on the other layer. Due to this the near-field enhancement is reduced. Therefore, the interplay of both effects has to be taken into account for designing and optimizing double layered core–shell nanoparticles.

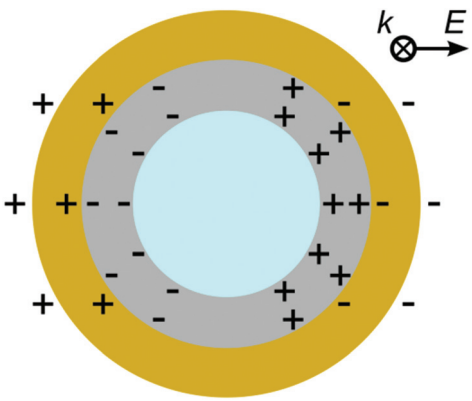


Fig. 8 Schematic illustration of the hybridization of the dipolar plasmon mode in silica–silver–gold nanoshell particles (modified from Wu *et al.*[157]).

Aside from using bilayer particles to combine the benefits of different metals, nanoshells made of a bimetallic alloy have also attracted interest in the last few years. The optical response of bimetallic nanoshells can not only be tuned by varying the shell thickness but also by a change of the material composition.[158] In the hybridization model the plasmon modes of the nanoshells result from the coupling between the solid sphere and inner wall cavity modes. The hybridization strength depends thereby remarkably on the dielectric constants and the wall thickness. Because of this dependence an increasing gold content as well as a decrease in shell thickness leads to a red shift of the LSPR. The highest achievable field enhancement, which is also dependent on these two parameters, was found to be located for lower gold content particles in the near-infrared region. Because of the transparent window of biological tissues in this spectral region and their better biocompatibility in comparison to pure silver nanoshells such alloy core–shell nanoparticles are promising for biomedical applications.

The transition from spherical to spheroidal shaped nanoshells yields a higher tuning ability and local field enhancement.[159] In a study based on DDA it was pointed out that the origin of this behavior is the dependency of the LSPR hybridization strength on the aspect ratio of the nanoshell structure. The hybridization strength corresponds to the polarizibility which is greater for the long axes of elongated structures than for a sphere. Hence, the higher the aspect ratio of a particle is, the stronger is the coupling between the LSPR of the inner and outer sides of the shell. This results in a higher sensitivity of the plasmon resonance spectral position to a change in shell thickness. In addition, because of the larger near-field enhancement they are also more suitable for surface enhanced spectroscopy compared to spherical particles.

Also in the case of nanoshells the influence of a broken symmetry on their plasmon resonances is of interest. Breaking the symmetry of spherical core–shell nanoparticles by displacing the dielectric core from the center (see Fig. 9) allows the hybridization of multipolar sphere and cavity modes.[160] This leads to a couple of excitable plasmon resonances which can be tuned by varying the offset of the core. The maximum field enhancement of these structures called nanoeggs is located nearby the thinnest part of the shell. With an increase of the core offset the plasmon resonances corresponding to the maximum field enhancement get red shifted until the core

 

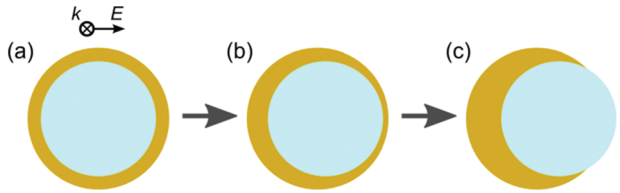


Fig. 9 Depiction of different structures realized by displacing the dielectric core of core–shell nanoparticles relative to their center: (a) symmetric core–shell (without offset), (b) nanoegg and (c) nanocup particles (modified from Knight *et al.*[160]).

drives through the shell surface ending up with a nanocup structure. An increase in the core offset will further lead to a blue shift of the observed modes. By knowing this, the optical properties like field confinement and the relation between scattering and absorption can be tailored for the specific task by changing the particle size, core displacement as well as selecting a plasmon resonance which should be excited.

A further promising concept to increase the near-field enhancement is the use of core–shell nanoparticles designed for nanolasing applications.[161] Such particles consist of a noble metal core surrounded by a dielectric coating which contains a gain material. As a gain material covalently bonded fluorophores whose emitting frequency matches with the lasing wavelength were used. By applying the Mie theory the lasing frequencies as well as the thresholds of such nanostructures were calculated. Silver is, due to its smaller ohmic losses in comparison to gold, the more suitable core material. Besides silica dielectrics also with a higher (lower) refractive index are usable as coating materials which result in a longer (shorter) lasing wavelength. The calculations of the electric fields in proximity to these nanoparticles suggest stronger enhanced fields for particles with a gain compared to ones without. The closer is the gain to the threshold for lasing the higher is the resulting enhancement.

In summary, a wide range of plasmonic nanostructures has been investigated by simulations for applications in surface enhanced spectroscopic techniques. Within this section, metallic nanostructures ranging from single and isolated particles up to complex shaped architectures were in the focus. For further application schemes, the here described particles are suitable to be applied for detection under wet conditions (for example metal colloids) as well as arranged on substrate materials for chip-based applications. The fabrication routines for the preparation of the here described and simulated nanostructures will be introduced within the following sections reviewing bottom-up, self-organized, template-based as well as top-down methods for substrates suitable for surface enhanced spectroscopic techniques.

### 3.3 Complex shaped nanoparticles

Most of the articles discussed in section 3.1 were focused on the coupling of unconnected nanoparticles caused by their electromagnetic near-field. Two important results of this coupling are the strong modification of their plasmon modes due to hybridization and the formation of hot-spots. A promising approach to further increase the near-field volume between two parallel arranged nanorods is to connect them on one side with an additional bar which results in a planar U-shaped structure.[162] By using the DDA method it was shown that in a couple of parallel arranged nanorods only transversal plasmon modes can be excited whereas in U-shaped nanostructures longitudinal dipole and multipole resonances are also excitable. The reason therefore is the direct coupling of the electrons in the two parallel rods of the U-shaped structure by the connecting bottom rod which is perpendicularly aligned. Additionally it was found that the frequency of the plasmon modes in such an arrangement is dependent exponentially on the radii of the rods and shows a linear dependency on the distance between the two parallel rods. Besides the high tunability of U-shaped nanostructures they provide more hot-spots in comparison to parallelly arranged nanorods. Hence, a pattern made of such structures seems to be well suited as the substrate for surface enhanced spectroscopic methods. The same is true for split-ring resonators which are very similar in shape. A smaller gap at their opening provides an additional hot-spot. Nanorods in which a small gap is cut also show strongly enhanced fields but this enhancement goes hand in hand with a decrease in the quality factor due to dipole radiation losses.[163] The local field distribution of straight nanorod antennas was compared to that of different strength bent ones ending up eventually in split-ring structures. According to the presented results it is possible to reduce the losses by scattering nearly completely by taking split-ring structures with a gap-width of 10 nm. This reduction of radiation losses is caused by a decrease in the electric-dipole moment. Hence, the quality factor is increased accompanied by a high field enhancement which makes these structures promising candidates as substrates for surface enhanced spectroscopy techniques.

Instead of preparing positive structures on a substrate it is also possible to use cavities in the metal layer of the same shape. According to the generalized Babinet theorem, the transmission and reflection spectra of the positive and negative structures show the same behavior but are interchanged under irradiance with complementarily linear polarized light (see Fig. 10).[164] Additionally, the electric field distribution of the positive structure is qualitatively similar to the magnetic field distribution of the inverted one. Hence, the plasmonic eigenmodes of both types of structures can be denoted in the same way. Furthermore, a complementary behavior of the effective material parameters was found. In spite of the lack of perfect conductivity and the finite film thickness of these structures,[164,165] the qualitative validity of this theorem was shown for several shapes like nanorod antennas,[166] U-shaped structures[167] and split-ring resonators.[164] By means of dark field microscopy and FEM simulations the advantages of using inverse structures were also demonstrated for nanocrescents.[165] Crescent-shaped nanoholes combine the high tunability of their plasmon resonances by changing the geometric

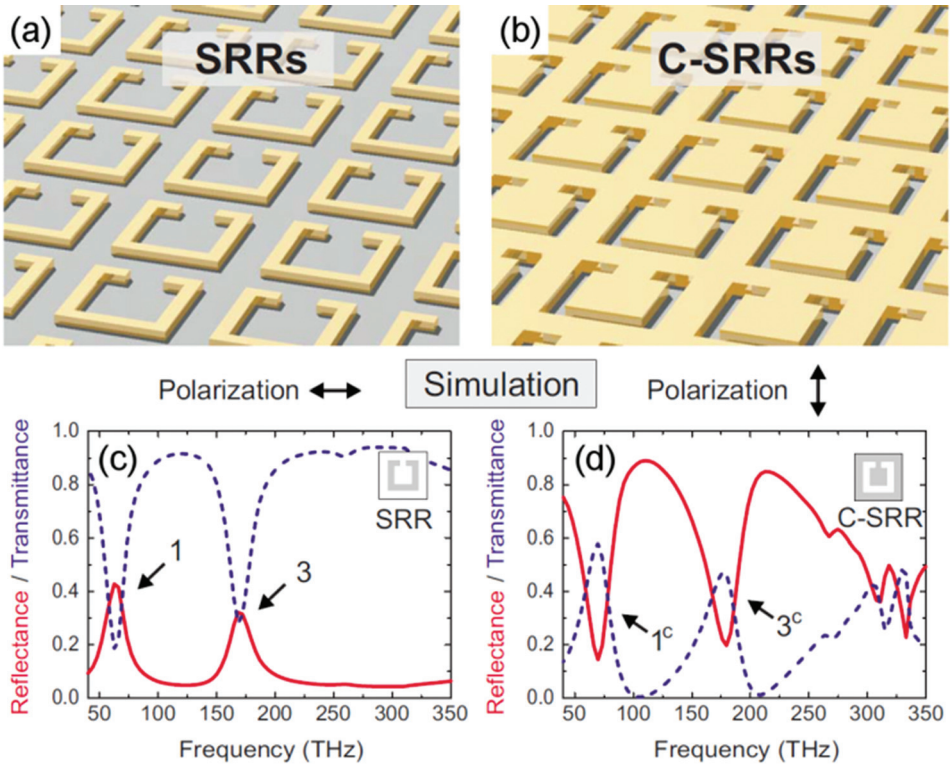


**Fig. 10** Schematic illustration of (a) positive and (b) negative split-ring resonator structures. Transmittance (blue, dotted) and reflectance (red, solid) curves calculated for (c) positive and (d) negative structures illuminated with complementary linear polarized light. The numbers mark the first- and third-order eigenmodes of the split-ring resonators (adapted with permission from T. Zentgraf, T. P. Meyrath, A. Seidel, S. Kaiser, H. Giessen, C. Rockstuhl and F. Lederer, *Phys. Rev. B: Condens. Matter*, 2007, **76**, 033407,[164] copyrighted by the American Physical Society ©2007).

parameters with the possibility of fabricating sharper tips in comparison with positive crescents. This results in a higher local field enhancement for the nanohole type of crescent structure. In addition, analyte molecules can be caught more effectively inside the cavities.

As already shown, the plasmon hybridization model is a powerful approach for analyzing qualitatively and quantitatively the optical properties of coupled nanoparticles. Moreover, it was shown that this model is also applicable for investigating the optical properties of more complex shaped nanoparticles. An example of this is a study on metallic tori with different aspect ratios.[168] The aspect ratio is herein defined as the ratio of the tube to the torus radius. For incident light which is polarized parallel to the torus plane an intense low energy feature, assigned to a dipolar in plane plasmon mode, and a high energy feature, corresponding to several overlapping higher order excitations, were found in the absorption spectrum. The dipolar mode is strongly dependent on the aspect ratio and, hence, highly tunable. In the case of weak hybridization, which is fulfilled for aspect ratios smaller than 0.8, this mode can be described as a plasmon of an infinite cylinder. The spectral position of this mode is thereby dependent on the circumference of the torus. In contrast, for perpendicular polarized light two spectrally less separated features arise in the spectrum. These peaks can be interpreted as bonding and antibonding combinations of two different infinite cylinder plasmons. Both resulting resonances show only a slight dependence on the aspect ratio. Because of the good agreement of these results compared to those obtained *via* using FDTD calculations the usability of the plasmon hybridization method for complex shapes like a toroidal geometry is proven. Furthermore, it should be as well possible to treat toroidal core–shell nanoparticles within this framework. Even the plasmon resonances of symmetry broken structures like nanobowls, open nanocages and open nanoeggshells can be well described by the plasmon hybrization model.[169] While using the FDTD method the height dependence of the dipolar and quadrupolar plasmon modes existing in such structures was investigated. These modes are the result of the interaction between the dipolar nanohole plasmon resonances, which appear at the opening of these structures, and the dipolar as well as quadrupolar plasmon modes of the non-symmetry broken closed shell structures. By cutting the full shell structure a red shift of the dipolar bonding mode is caused. Furthermore, a hyperbolic dependency of this mode on the height of the structure exists for all simulated shapes. From the viewpoint of using the envisaged structures as platforms for surface enhanced spectroscopy methods they show promising highly enhanced local fields close to the corners and edges.

 

Another technique for treating complex shaped structures is based on the Coulomb interaction of the surface charges at the walls of the particles.[170] In order to get the distribution of the surface charges the intensity of the local electric fields and their direction contours was calculated *via* the DDA method. From this, it was possible to investigate the surface plasmon resonances of metallic nanotubes. The optical properties of the nanotubes are tunable by changing their aspect ratio as well as their wall thickness. Hence, they combine the tunability of shell nanoparticles and nanorods with the additional benefit that analyte molecules can bind outside and inside the nanotube. This makes them promising candidates for surface plasmon sensing as well as surface enhanced spectroscopies. Furthermore, the herein presented approach is also extendable to the investigation of the plasmon coupling of other complex shaped metallic nanoparticles.

By considering metal nanorods as resonators for PSPPs it is possible to develop a model based on Fabry–Pérot interferences to calculate the local electric fields and the associated field enhancement.[171] The partial reflection of PSPPs at the end of the antennas results in interferences which cause the local field enhancement. The amplitude and the phase of the reflected part of the propagating mode are estimated using a simple Fresnel reflection model as well as by full field FDFD simulations. By comparing the calculated electric fields with the field maps resulting from the FDFD model the usability of the Fabry–Pérot model was validated. The good accordance between both models shows that metallic structures with dimensions on the wavelength scale indeed behave as resonators for propagating plasmon modes. In principle this model should be adaptable for treating particles of different shapes as well. Hence, it is a helpful tool for tailoring and optimizing metallic nanostructures for plasmonic applications.

Designing plasmonic devices can also be performed on the basis of transformation optics which was shown for structures with broadband light-harvesting capabilities.[172] By applying a conformal transformation an infinite plasmonic structure with a broadband absorption spectrum can be transferred into a finite structure which shows the same absorption behavior (see Fig. 11). In doing so, a non-realizable structure with the desired optical properties is convertible into a viable one. Starting from two semi-infinite structures, a metallic thin film and a sandwich structure consisting of two metallic slabs separated by a dielectric layer, the authors end up with two promising structures by using this technique: a crescent shaped cylinder and two attached cylinders. Besides their capability of broadband light-harvesting these structures deliver strong field enhancements. This opens another analytical path for designing nanostructures for surface enhanced spectroscopy methods.

In the last few years a lot of research effort was put in the exploration of fabrication techniques for plasmonic nanostructures. However, structures which are produced at the limits of technical feasibility often differ in shape from the idealized structures used for modeling the optical parameters. Therefore, an important question for designing plasmonic

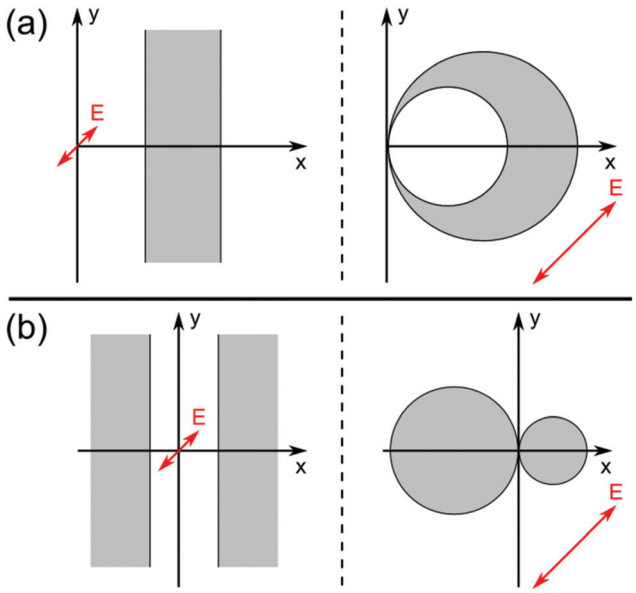


**Fig. 11** Semi-infinite structures (left) and *via* conformal transformation resulting plasmonic nanostructures. Two examples are depicted: (a) a crescent shaped cylinder obtained from a thin metal layer and (b) a heterodimer of two touching cylinders resulting from two metallic slices separated by a dielectric layer (modified from Aubry *et al.*[172]).

nanostructures based on simulation results is the effect of shape imperfections and also the surface roughness on their optical properties. For the ring-like plasmon resonances in gold nanoring–disk nanostructures a considerable deviation between the calculated and measured spectral positions was discovered.[173] To get a deeper insight into this phenomenon structures with rounded edges were simulated by applying BEM. This leads to a significant red shift of the ring-like plasmon wherefore the calculated extinction spectra matches very well with the measured one. The explanation for this effect is given by the variation of the mean wall thickness due to the rounding of the ring edges. Hence, there is a stronger inter-wall interaction which results in an observed spectral shift of about 25% for a change in the mean wall thickness of 10%. Additionally, the surface roughness seems to have also a slight influence on the position of the spectral features. In contrast to these findings, the disk-like plasmon shows a minor dependency on the sharpness of the disk edges. A reasonable explanation for this behavior is that the deformation of the structure is small in comparison to its size.

The question concerning the necessity of taking the irregular shape of non-ideal nanostructures into account was also considered in a study on the emission behavior of molecules nearby these structures.[174] To simulate the excitation and re-emission enhancement of molecules close to a pair of metallic nanostripes BEM was applied as well. For comparison, the calculations were carried out for an ideally as well as for a non-ideally shaped nanostripe pair. The parameters for the shape of an experimentally realized non-ideal pair of nanoantennas were therefore extracted from a scanning electron microscopy

(SEM) image. In the far-field no difference in comparison with the ideal structure is visible, whereas the near-field depends notably on irregularities of the structures. Hence, the irregular shape of fabricated nanostructures should be taken into account if the particle localization is crucial for the investigation.

## 4. Bottom-up preparation strategies of plasmonic nanostructures

Plasmonic nanostructures can be fabricated by a variety of methods. This section will highlight the progress in the field of bottom-up fabrication within the last few years. Reported metal nanostructures as plasmonic materials range from classical metal colloids, to core–shell nanoparticles and structures as well as complex-shaped nanoparticles prepared by seed mediated growth.

### 4.1 The classical approach – metal colloids

Metallic nanoparticles suspended in an aqueous environment are one of the most frequently applied SERS substrates in the last few years. Classically, the nanoparticles are prepared by simple and easy-to-follow wet chemical processes. The most commonly used method to produce silver nanoparticles is based on the reduction by citrate, a protocol published by Lee and Meisel.[175] Following this procedure, a solution of citrate buffer is added dropwise to a boiling solution of silver nitrate. A change in color to turbid grey-yellow indicates the successful generation of silver nanoparticles. For the application as a SERS substrate, the signal intensity can be increased dramatically by adding salts *e.g.* KCl, NaCl or $MgSO_4$ due to the formation of aggregates.[176] Hot spots are generated by means of nano-sized gaps between silver nanoparticles which are known as one of the most commonly applied substrates in SERS. As an example, single silver nanostructures produced by the Lee–Meisel protocol have been used for a fundamental investigation of the electromagnetic enhancement of the SERRS mechanism.[177] Moreover, these nanostructures are applied in surface enhanced hyper Raman scattering (SEHRS).[178] They can be also used in combination with further bioanalytical techniques, *e.g.* microfluidic lab-on-a-chip devices.[179–183] Liu *et al.* employed citrate-reduced AgNPs in a microdroplet PDMS detector for trace level crystal violet detection with a LoD of 3.6 nM.[184] A SEF-based immunoassay employing silver NPs produced by the Lee–Meisel protocol was presented by Zhang *et al.*[185] Within this investigation a glass slide with several polyelectrical layers was covered with BSA (bovine serum albumin) and antigens before binding silver-antibody nanoconjugates (SANC).

The citrate reduction was also adapted for the production of gold nanoparticles. To do so, trisodium citrate was injected into a boiling solution of $HAuCl_4$. Finally, a suspension of AuNPs results, wherein the particle size can be manipulated by changing the amount of added trisodium citrate.[186] These AuNPs have been used recently to detect melamine in milk with a detection limit of 0.017 mg $l^{-1}$.[187] Kämmer *et al.* compared the UV-SERS enhancement potential of citrate reduced gold nanoparticles with the enhancement of palladium, platin and silver colloids as well as Au–Ag and Ag–Au core–shell structures, using melamine as a test molecule.[188] Within this study, gold nanoparticles with a diameter of 120 nm activated with KBr were identified to be the best combination of nanoparticles and activation agents to detect melamine by UV-SERS at an excitation wavelength of 244 nm.

In conclusion, a rather high number of studies about citrate reduced metal nanoparticles can be found in the literature; however, only a limited number of them could be covered within this review. The combination of metal NPs with other techniques *e.g.* microfluidics is a very promising field, although the question of time stability and reproducibility remains.

Besides the Lee–Meisel protocol, the reduction of silver nitrate can be performed by using sodium borohydrate as a reduction agent.[189] As an example, borhydrate reduced silver nanoparticles have been employed as adenosine detectors based on the fluorescence enhancement of a label molecule.[190] Additionally, borohydate reduced copper NPs are employed in SERS applications.[191] A further approach for generating plasmonic nanostructures for SEF is the usage of silver nanoprisms. These metallic nanostructures were produced by irradiation of borohydride reduced silver nanospheres, whereas nanoprisms with a high yield were obtained after 70 h.[192] Munechika *et al.* characterized nanoprisms as a SEF substrate by illustrating the enhancement of the photoluminescence of quantum dots.[193]

In 2003 Leopold and Lendl published a fast preparation protocol for SERS active silver colloids at room temperature by reducing silver nitrate with hydroxylamine hydrochloride.[194] Hydroxylamine reduced silver NPs are very promising because of a minimal spectral background when applied as SERS substrates combined with an easy preparation protocol.[195] To illustrate the potential as a SERS substrate, several analyte substances have been investigated, *e.g.* zidovudine, melamine,[196] paroxetine,[197] and amoxicillin.[198] Additionally SEF experiments for the detection of quinacridone were performed by using Leopold–Lendl colloids.[199] The protocol has been adapted to an immobile device for the detection of pathogens causing urinary tract infections.[200] The bacteria sample was applied on a positively charged glass surface, followed by a two-step synthesis of the SERS-active substrate. A silver nitrate solution was added and allowed to adhere (1 h), and subsequently a hydroxylamine hydrochloride reducing agent was added (1 h reaction time). The generated silver islands were applied as SERS substrates to discriminate *Escherichia coli* and *Proteus mirabilis* bacteria. Additionally, the Leopold–Lendl silver colloid can also be prepared *in situ* on the bacteria cell wall for SERS-based detection of pathogens.[201]

In addition to the well-established protocols for citrate, borhydrate and hydroxylamine reduced metallic nanoparticles, further bottom-up strategies are developed. As an example, ethylenediaminetetraacetic acid (EDTA) was employed as a

 

reducing agent,[202] detecting dye-labelled DNA.[203] A one-step synthesis of star-like gold nanoparticles, using hydroquinone solution in water as a reducing agent, was presented by Morasso *et al.*[204] For an electrochemical etching process a reduced graphene oxide (RGO)-covered Si wafer was immersed into a mixed solution of HF and $AgNO_3$.[205] The AgNP-decorated RGO film on Si was utilized as a SERS substrate. As an alternative, RGO was heated to 60 °C under stirring and an aqueous $AgNO_3$ solution was added.[206] After 48 h a RGO–AgNP product was obtained. The as-prepared RGO–AgNPs have been successfully combined with folic acid to yield a promising hybrid material with good biocompatibility and targeting ability, as well as applicability in Raman-based detection of live cancer cells. As a further strategy, the reduction of a silver ammonia complex with glucose to pure silver nanoparticles is reported, whereas the size of the particles is tuned by the amount of added ammonia.[207] Photo-induced silver reduction in a flow cell was presented by Herman *et al.*[208] Here, aqueous solutions of silver nitrate and NaOH/hydroxylamine hydrochloride were pumped into a flow cell and illuminated with a laser for 30 s. Thus, SERS-active silver substrates were produced inside the channel system. Further, by heating liquids in a microfluidic channel, gaseous bubbles and, at their interface, gold nanoparticle aggregates are generated.[209] After drying, a highly SERS active ring is formed. Dimer and trimer gold nanoantennas were prepared on glass slides by aggregating commercially available colloidal suspensions of monodisperse, citrate stabilized gold nanoparticles.[210] The angular distribution of the experimentally measured SERS enhancement of these gold nanoantennas shows that most of the light is emitted at angles exceeding the critical angle of the air–glass interface. This finding was supported by theoretical considerations.

In conclusion, numerous strategies for bottom-up nanoparticle production protocols have been reported, whereas mostly silver and gold were used as plasmonic materials. In addition to the optimization of established protocols, new procedures have been designed. Thus, a wide range of applications, *e.g.* surface enhanced spectroscopy in life science, can give access to metallic colloidal nanoparticles.

### 4.2 Core–shell nanoparticles and structures

The usage of aqueous metallic colloidal suspensions has a number of advantages regarding the fast and simple production. However, the reproducibility of the results may be affected by spontaneous agglomeration of the nanoparticles,[179,211] or surface passivation occurring during the transfer of the nanoparticles to different media.[212] Therefore, attention was directed towards combining the plasmon resonance of a metal nanoparticle with the stability of another material by creating a core–shell structure. Depending on the preparation protocol, the obtained core–shell structure may consist of a dielectric shell which encapsulates a single nanoparticle of a desired dimension or an aggregation of a small number of nanoparticles.

Gold nanoparticles with a silica shell have a broad plasmon resonance band between 500 nm and 800 nm, depending on the number of cores and their arrangement in the silica shell.[40,213–215] They are synthesized according to protocols consisting of mainly two steps. First, colloidal gold nanoparticles are prepared.[186,216] Second, the colloidal Au particles are mixed with pH-activated sodium silicate.[217,218] At this step, Raman reporter molecules could be optionally added to the mixture, creating SERS labels.[37,217,219] The silica shell growth is performed with tetraethylorthosilicate (TEOS) and ammonia and continues until the desired shell thickness is obtained.[217] In order to separate the core–shell structures with different clustering degrees (*i.e.* monomers, dimers *etc.*) and to have narrow plasmon peaks, the nanoparticle suspension can be centrifuged in surfactant-free aqueous iodixanol with a linear density gradient.[220] In the case of the particles produced by Tyler *et al.*,[220] the highest SERS enhancement was observed for the trimer structure. Instead of Raman reporter molecules, fluorescence dyes can be integrated in the same type of gold–silica core–shell structure.[221,222] As a result, enhanced fluorescence can be observed if the plasmon peak of the gold nanoparticle overlaps with the emission peak of the fluorescent dye.[221]

Besides gold, other metals also such as silver or a combination of different gold and silver nanoparticles together with iron oxide can be used as the core material.[223–229] In the case of silver, the plasmonic absorption range can be tuned from 400 nm (VIS) to 900 nm (NIR) depending on the dimensions and shapes of the nanoparticles.[212,223,230] Moreover, according to Gole *et al.*[223] silver–silica core–shell nanoparticles can be used for bio-medical applications, because of their diminished cytotoxicity. In order to enhance the medical applicability, iron oxide nanoparticles were synthesized with a silver–silica shell, creating nanoparticles with magnetic properties.[223] As an example, nanoprobes for cancer cell separation are prepared by decorating magnetic nanobeads with SERS-active Au core–Ag shell nanorods.[231] These composites are coated with a silica layer, wherein CdTe quantum dots – the fluorescent agent – are immobilized. Thus, SERS-fluorescent joint spectral encoding (SFJSE) was realized. Furthermore, by employing single-DNA-tethered heterodimeric gold–silver core–shell nanodumbbells (GSND) the gap between two nanoparticles and the analyte can be tuned based on the applied DNA sequences (see Fig. 12).[214] The obtained particles are very specific and sensitive SERS substrates.

As a further strategy, silver nanoparticles are prepared by employing metal seeds.[224,227] As an example, Au seeds with a size of 12 nm are synthesized by a modified Lee–Meisel protocol[175] and $AgNO_3$ is reduced on its surface employing ascorbic acid. In a next step, the obtained nanostructures are encapsulated in a silica shell. The resulting Au-seed Ag-growth nanoparticles with a silica shell had uniform dimensions. To realize bimetallic core–shell nanostructures, palladium hexagonal nanoplates were also applied as seeds.[227] Depending on the $AgNO_3$/Pd ratio, the plasmon resonance could be tuned between 477 and 971 nm.

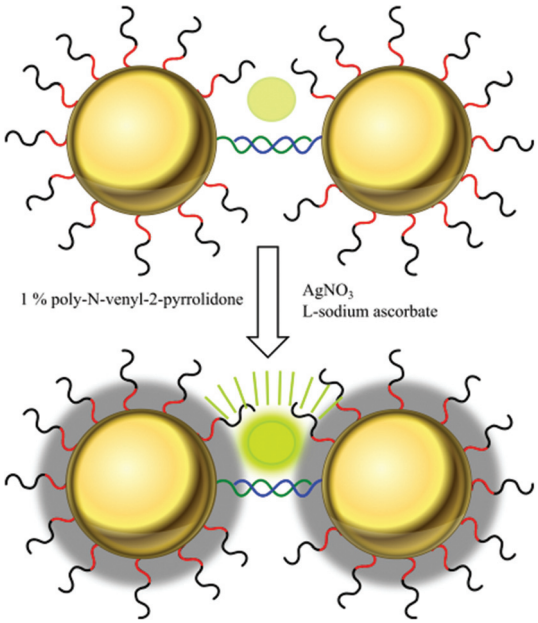


Fig. 12 Nanometer-scale silver–shell growth-based gap-engineering in the formation of the SERS-active GSND (modified from Lim *et al.*[214]).

Various other combinations of bimetallic nanostructures have been developed for specific applications. For instance, Guo *et al.*[232] employed different ratios of gold ions for the core and platinum ions for the shell in order to achieve a plasmon resonance between 500 nm and 600 nm. Because of the low amount of different chemicals and the reaction at room temperature, the proposed fabrication is relatively easy. Also, dielectric materials *e.g.* $NaYF_4$:Yb,Er[233] or $BaTiO_3$ [234] were used as core materials for AuNPs. Further, structures consisting of a liquid core containing fluorescent organic dyes and a gold shell were produced by miniemulsion techniques.[235] Another example is realized by embedding small quantum dots in a gold shell. This is done by immobilizing gold ions into their surrounding layer and reducing these ions to metallic gold.[215] Moreover, the distance between quantum dots and their gold coat can be tuned by varying the thickness of the surrounding polyelectrolyte bilayer. These particles show a stable fluorescence intensity. Moreover, because of the reduced toxicity they can be used in biological systems.

Besides the core–shell structures, particle-in-a cavity or yolk–shell nanostructures also possess interesting optical properties. By tuning the core particle and the cavity's size, shape and material, the obtained nanostructures can be applied for the study of plasmon hybridization, optical trapping, the Fano-like resonance effect, SERS-based biosensing, and the magneto-optical effect.[226] Preparation protocols have been developed for silica cavities with Au cores[226,236] and further core-materials as $Fe_2O_3$.[226] They were prepared using chemical bottom up methods and also top down techniques like ion milling. Gold particles in the ring structure can have their resonance in the NIR region and are considered as substrates for SERS-based molecule detection.

In addition to the most commonly used core–shell nanostructures with a silica exterior shell, various other materials have been used for encapsulation depending on the application field. Tian *et al.*[218,237,238] developed protocols for preparing silver and gold nanoparticles with $Al_2O_3$,[218] $MnO_3$ [237,238] and $Ag_2S$[238] shells. Wang *et al.*[225] synthesized metal–carbon core–shell nanospheres and Zhang *et al.*[239] prepared silver and gold cores with $Cu_2O$ shells. Gold nanoparticles with a silver shell were applied in a SERS-based immunochromatographic assay (ICA) to detect phenylethanolamine as an illegal food additive.[240] For combined SERS and SEF experiments, a fluorescence dye is implemented in a polymer layer between a gold core and a silver shell.[241] Mesoporous shells with a high potential for drug delivery were developed by Ran *et al.*[228]

Core–shell particles have been applied in shell-isolated nanoparticle-enhanced Raman spectroscopy (SHINERS).[40] Here, the signal enhancement is due to gold nanoparticles with an ultrathin silica or alumina shell. A monolayer of core–shell nanoparticles was spread over the surface to be probed. Thus, the chemical composition of any surface is detectable by SHINERS. Recently, SHINERS particles have been applied as noninvasive glucose sensors.[242] If the dielectric shell around a metal particle is thicker than the critical distance for minimum fluorescence quenching by the metal, these particles can be used for SEF and SERS experiments.[243] Moreover, core–shell particles were immobilized on a substrate.[211,244,245] The most commonly used immobilization technique implies at least two steps. In the first step, the substrate is cleaned and functionalized in order to be able to attach the nanoparticles. In the second step, the as-prepared substrate is immersed in a colloidal solution for different periods of time and then rinsed with water or alcohol.[211,245] If needed, the obtained substrate can be further functionalized.

In conclusion, a wide range of preparation strategies for the synthesis of core–shell particles are available. Due to their increased stability combined with excellent enhancement properties, core–shell particles are promising tools in SES applications.

### 4.3 Complex-shaped nanostructures by means of seed mediated growth

The uniformity of the surface reactivity of the metallic nanoparticles plays a critical role when exploiting them in a particular application. One approach to achieve this is to synthesize nanostructures by the seed-mediated growth mechanism. Usually, small metallic particles used as seeds are added to a growth solution containing metal salts and a suitable reducing agent. The surface of the seeds has the role of catalyzing the reduction of the metal salts, a process that occurs more readily at the surface than in the bulk solution. Therefore, control over the final morphology is possible, resulting in particles with a high size monodispersity.[126,246] Additionally, the aspect ratio and the shape of the resulting structures can be easily

 

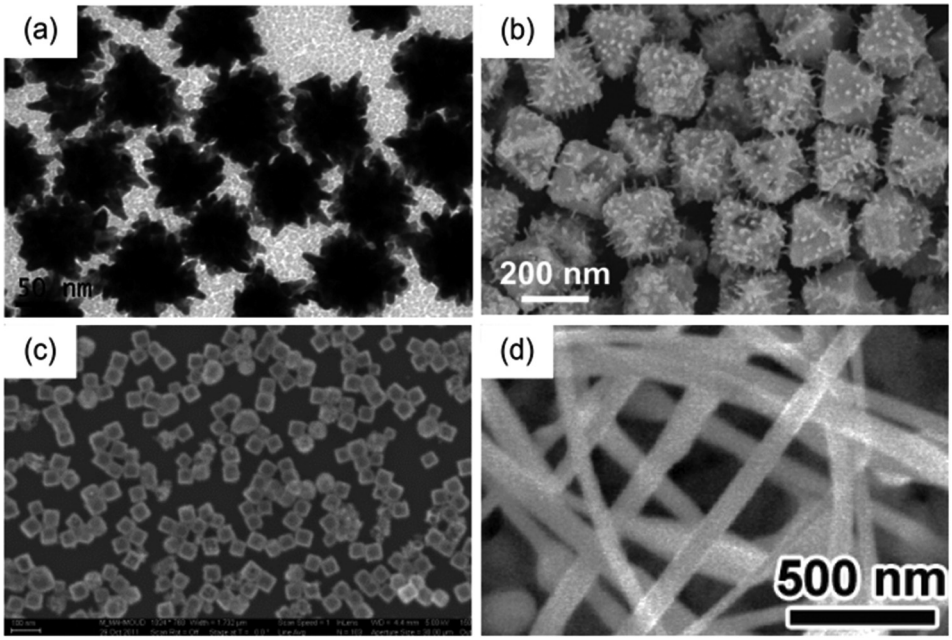


**Fig. 13** SEM image of (a) gold nanostars (adapted with permission from S. Barbosa, A. Agrawal, L. Rodriguez-Lorenzo, I. Pastoriza-Santos, R. A. Alvarez-Puebla, A. Kornowski, H. Weller and L. M. Liz-Marzan, *Langmuir*, 2010, **26**, 14943–14950,[247] copyright 2010 American Chemical Society). (b) Ag–Au spiky nanoparticles (adapted with permission from S. Pedireddy, A. Li, M. Bosman, I. Y. Phang, S. Li and X. Y. Ling, *J. Phys. Chem. C*, 2013, **117**, 16640–16649,[255] copyright 2013 American Chemical Society). (c) SEM image of AuPt nanocages (adapted with permission from M. A. Mahmoud, *Langmuir*, 2013, **29**, 6253–6261,[248] copyright 2013 American Chemical Society). (d) SEM image of Au nanowires (adapted with permission from Y.-C. Yang, T.-K. Huang, Y.-L. Chen, J.-Y. Mevellec, S. Lefrant, C.-Y. Lee and H.-T. Chiu, *J. Phys. Chem. C*, 2011, **115**, 1932–1939,[254] copyright 2011 American Chemical Society).

manipulated. As a result, colloidal solutions of nanostars,[247] nanocages,[248] nanoplates[249,250] and nanorods,[251,252] can be obtained. Moreover, nanowires[253] and nanothorns[254] grown on substrates can also be synthesized either by electrochemical reactions or by chemical bath deposition. In Fig. 13, SEM images of selected complex-shaped nanostructures are illustrated.

Homogeneous as well as heterogeneous spiky nanostructures are mostly preferred when a high overall plasmonic excitation cross section is required. They gain their characteristics due to the hybridization of plasmons localized at the core and the tips of the nanoparticles. In order to obtain such kinds of structures, seeds with different shapes can be used.

Homogeneous structures, such as nanostars obtained by Barbosa *et al.*,[247] are based on spherical Au nanoparticles and *N*,*N*-dimethylformamide (DMF) as the solvent for the growth solution. More specifically, seeds were prepared either by adding $HAuCl_4$ to a poly(vinylpyrrolidone) (PVP) solution in a DMF/$H_2O$ mixture and reducing Au with $NaBH_4$, or by the standard citrate reduction method. As a subsequent step in the case of the second method, Au nanoparticles were transferred into ethanol through PVP modification. The as-prepared gold particles were used as seeds for another reduction process of chloroauric acid in DMF in the presence of PVP. The plasmon resonance in the visible region could be tuned by changing the ratio of $Au^{3+}$/seed, temperature, size of the seeds and controlled pre-reduction from Au(III) to Au(I). Therefore, when the optical enhancing properties of different nanostars were assessed for the detection of 1-naphthalenethiol, it was shown that structures with sharper tips yield higher intensities. A similar synthesis method was also employed to obtain colloidal suspensions of nanowires covered with sharp tips with a high SERS activity.[256] In this case, ultrathin gold nanowires were used as seeds. They were prepared by reduction of chloroauric acid with oleylamine and with tri-isopropylsilane as the surfactant. *Via* thiol bridges, the analyte molecule-tainted nanowires were bound to a smooth gold film, giving an enhanced Raman signal. Gold nano-crosses prepared by a seed-growth reaction method and decorated with the dye Cy5 are applied as the SEF label in an immunosensor for the detection of microcystin-LR.[67]

Furthermore, in order to obtain spiky heterogeneous nanostructures, Pedireddy *et al.*[255] employed morphologically controlled Ag cores as seeds and high molecular weight PVP for the growth process. First, Ag octahedral nanoparticles were obtained by a polyol method[257] while in the second step PVP (MW = 360 kg $mol^{-1}$) and $HAuCl_4$ were dropwise added to the seed solution. The anisotropic growth was attributed to a galvanic replacement mechanism,[258] where the difference in standard reduction potentials for Ag and Au plays a major role.[259] The length of the gold nanospikes could be varied from 10 to 130 nm by changing the amount of the gold precursor added and the injection rates. Field enhancements of up to $10^4$ were obtained in the case of 130 nm spikes. As another example for

an efficient SERS-active substrate, spiky nanourchin structures are prepared employing roughened and aminosilane-functionalized silica cores.[260] Here, gold nanoseeds are immobilized on the surface of the silica cores and grow due to reduction processes into long wires.

The same galvanic replacement method can be also used to obtain gold nanoframes,[261] and gold–palladium and gold–platinum double-shell hollow nanoparticles[248] starting from silver nanocubes. The seeds were prepared by reduction of silver nitrate by sodium sulfide in the presence of PVP in ethylene glycol. Chloroauric acid was added to the boiling seed solution and the gold frames were formed by galvanic replacement. The wall thickness of the frames could be tuned by varying the ratio of the added gold salt, whereas thinner walls brought a red shift in the plasmon resonance. In the case of double-shell hollow particles, the gold frames were further used as seeds. The palladium and platinum shells have been obtained by adding $Na_2PdCl_4$ or $K_2PtCl_4$ solution to the seeds. The experimental and theoretical calculations illustrated that the particles containing transition metals show SERS enhancement one factor less than the single shell ones.

One of the strategies to enhance the fluorescent emission of quantum dots (QD) is to conjugate them with silica coated gold nanorods (AuNR).[251] Due to surface plasmonic effects of the attached AuNR the excitation intensity and spontaneous emission of QDs is modified. In order to prepare the AuNRs, Li *et al.*[251] synthesized gold nanoparticle seeds by reducing chloroauric acid with sodium borohydrate in the presence of cetyltrimethylammonium bromide (CTAB). The as-prepared seeds were drop-wise added to the growth solution prepared by mixing aqueous silver nitrate, CTAB and chloroauric acid. The addition of tetraethylorthosilicate (TEOS) under alkaline conditions produced a silica coating on the AuNRs. Finally, QDs were mixed with the silica coated gold nanorods.

The seed mediated growth process can also be employed to obtain silver nanostructures.[249,262–265] The easiest way is to prepare the seeds by a modified Lee–Meisel protocol, where silver nitrate was reduced not only by sodium citrate but also with sodium borohydrate. The growth solution was made by mixing CTAB, silver nitrate and ascorbic acid. Depending on the ratio of seed/growth media amount, silver nanoplates with varying diameters can be synthesized. The silver nanoplates were stabilized with a positively charged thiol layer. After functionalization with a carboxyl group containing mercapto-linker, the bioconjugation to a green fluorescence protein is possible and results in a 5.6 times brighter fluorescence based immunoassay than without metal activation.[249]

The previously presented synthesis methods resulted in colloidal suspensions of differently structured plasmonic nanoparticles. However, nanostructures immobilized on solid substrates have several advantages over the conventional ones. Concerning seed-mediated growth two approaches to prepare these types of structures are available: (1) to synthesize the metallic colloids and afterwards link those to a solid substrate and (2) to grow the nanostructures directly on the substrate. Gold nanorods obtained by seed-mediated growth were immobilized on multiple substrates, such as electrospun polymer nanofibers,[266] mesostructured silica films,[222] conductive indium tin oxide (ITO)-coated glass substrates,[267] or gold film coated substrates. Additionally, as already mentioned, colloidal suspensions of nanowires covered with sharp tips can be immobilized *via* thiol bridges to a gold film. Furthermore, in order to obtain 3D SERS substrates 3D templates were decorated with plasmonic nanostructures. For this, a rough Au layer deposited by thermal evaporation on a large area silicon substrate served as the seed for the growth of ZnO nanowires (see Fig. 14).[253] Subsequently, Au nanorods obtained by seed mediated growth were deposited on the poly(2-vinyl pyridine) (P2VP) modified ZnO nanowires. A SERS enhancement factor of $1.85 \times 10^{14}$ was achieved for the analyte molecule 1,4-benzenedithiol.

In the second approach, gold seeds with a high monodispersity and homogeneous morphology can be easily formed on the surface of a bare ITO electrode by applying a short-term high overpotential.[268] Then, due to the preferential deposition and reduction of $AuCl_4^-$ anions on the existing Au seeds, the size of the gold nanoparticles will consequently become larger. By utilizing cyclic voltammetry, the gaps between adjacent nanoparticles can be controlled. The as-prepared substrates proved to have a high reproducibility, stability and an enhancement factor of $\sim 1.3 \times 10^6$ for the SERS signal. Furthermore, Yang *et al.*[254] reduced and deposited $AuCl_4^-$ on an ITO cathode coated sequentially with a layer of sputtered Ti and a layer of sputtered Au. The Au layer served as a seeding layer for Au nucleation. By controlling the growth parameters, a series of nanostructures was obtained, including nanoparticles, nanothorns and nanowires.

In conclusion, seed-mediated growth offers researchers a complete toolbox to obtain differently structured nanoparticles either in colloidal suspensions or on solid substrates. Additionally, these structures proved to offer high enhancements for both Raman scattering and fluorescence emission,

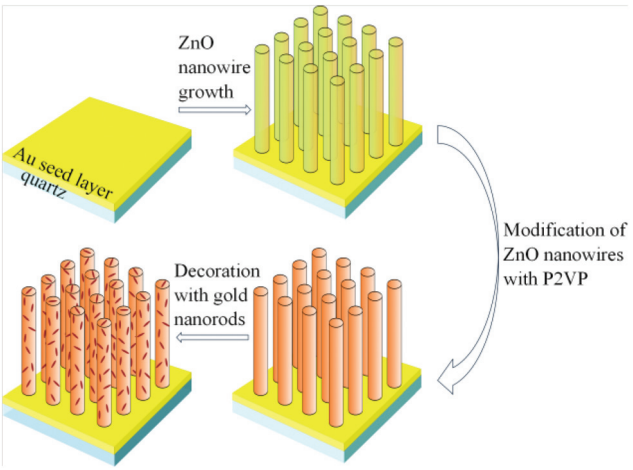


Fig. 14 3D SERS-active substrate based on the seed-mediated growth of ZnO nanowires (modified from Kattumenu *et al.*[253]).

 

having the additional advantage of being highly monodisperse.

## 5. Self-organization processes for the fabrication of assemblies and arrays

In the previous section, bottom-up fabrication strategies to produce metallic colloids, core–shell architectures and complex structures by seed mediated growth were reviewed. The following section focuses on the controlled assembly of bottom-up produced nanoparticles, the formation of clusters and the immobilization of nanoparticles on a substrate. Furthermore, self-organizing processes play an enormous role in template-based methods. For some preparation strategies, a clear classification of template-based or self-assembling processes is not possible since both approaches are applied for the production. Thus, we did the classification in the following section based on the structure-defining step.

### 5.1 Self-assembled nanoparticles, clusters and arrays

One of the easiest ways to create plasmonic substrates is the self-assembly of bottom-up nanoparticles from colloidal solutions. The methods are easy to handle, cost-efficient and the structures can be fabricated on non-planar substrates, or even on liquid/liquid interfaces.[269] The nanoparticles can form different patterns with various degrees of complexity, from one-dimensional arrays to three-dimensional clusters. This self-assembly occurs as a result of reaching the minimal energy state due to electrostatic interactions or (bio)chemical conjugations, or because of an applied external electric field.[270]

The electrostatic interaction that occurs between the nanoparticles themselves and also between the nanoparticles and the substrate is well known; however, it is difficult to tune or alter the properties of such structures.[272] Two principle strategies are available to create controllable nanosized gaps between nanoparticles: with small molecular weight substances like alkanethiols,[273] or with high molecular weight substances like two compatible DNA strands,[64] proteins[271] or special macrocycles.[274] A well-known and very strong bioconjugation is the streptavidin–biotin interaction.[271] By coating citrate-reduced gold nanoparticles with biotin the nanoparticles are conjugated at a distance of 8 nm with streptavidin as the linker molecule (see Fig. 15). The assembly of nanoparticles by biotin interactions only leads to a reduced gap size. With a defined distance of 5 nm between two gold nanoparticles, the analytical SERS enhancement factor is estimated to be $10^7$. Gold nanoparticles can also be assembled by utilizing cucurbit[*n*]uril, an organic macrocycle based on glycouril monomers.[274] Here, the number of glycouril monomers defines the distance within the conjugate. Employing cucurbit[5]uril, distances of 0.9 nm between the gold nanoparticles with a plasmon resonance in the visible region could be created.

The assembly of nanoparticles in one dimension results in the arrangement of worm-like chains. These structures can be prepared by electrostatic interactions on a grooved surface (see Fig. 16),[275] *via* covalent binding applying CTAB and thiol-terminated polystyrene,[276,277] by side specific ligand exchange,

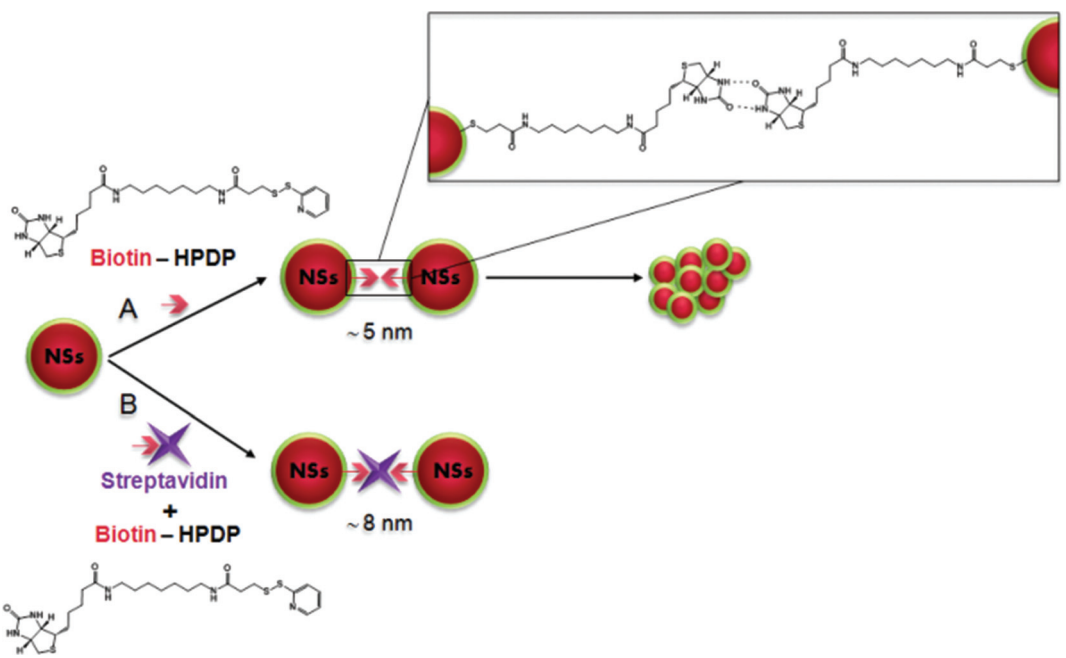


**Fig. 15** Bioconjugation between functionalized nanoparticles using the biotin–streptavidin bonding (reprinted with permission from J. C. Fraire, L. A. Pérez, E. A. Coronado, *ACS Nano*, 2012, **6**(4), 3441–3452,[271] copyright 2012 American Chemical Society).

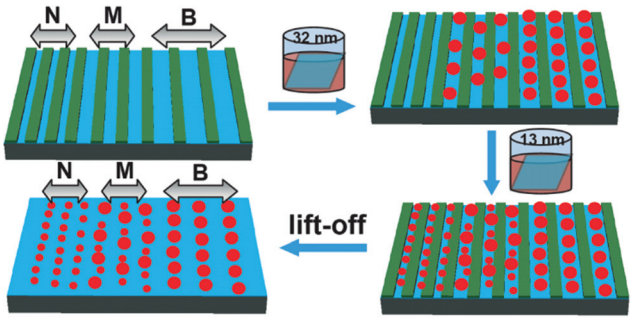


Fig. 16 Fabrication of multiplexed 1D nanoparticle arrays on a grooved surface (reprinted with permission from L. Jiang, Y. Sun, C. Nowak, A. Kibrom, C. Zou, J. Ma, H. Fuchs, S. Li, L. Chi and X. Chen, *ACS Nano*, 2011, **5**(10), 8288–8294,[275] copyright 2011 American Chemical Society).

by application of an external electromagnetic field[278] or by AFM based techniques.[279] These structures are applied for the development of theoretical models and basic research. However, the SERS-active substrate area is relatively small, decreasing the cost-efficiency of the fabrication process and, thus, making such substrates unattractive for life-science applications.

The fabrication of two-dimensional arrays is much easier in comparison with worm-like arrangements. The production of regular arrays based on self-assembly strategies is, in most cases, based on a combination of top-down and bottom-up techniques. The most common techniques used in the fabrication of such substrates include the dispersion of polystyrene beads on a surface, dispersion of metallic particles, deposition of metallic layers, functionalization of the surface, wet or plasma etching or e-beam lithography (EBL). By functionalizing the surface using various thiols, silanes or polymers, followed by the attachment of metallic nanoparticles from a solution, a very high signal enhancement can be obtained.[280] This procedure can be repeated to form a multi-layered array, tuning its properties and sensitivity up to the detection of tens of molecules, or varying the distance between the layers by alterations of pH or salt concentration.[281] This approach allows for the fabrication of easily controllable SEF substrates.[282] Another common approach uses charged polystyrene nanospheres (nanotemplating), which tend to disperse on the glass surface, thus forming an even distribution pattern.[283] A layer of metal is deposited onto the nanospheres,[284] forming a temporarily stable substrate with both uniform enhancement areas and hot-spots.[285,286] These substrates, known as film over nanospheres (FON), are compatible with mass production methods.

Furthermore, arrays can be created from nanoholes or nanovoids ordered in a regular pattern. Nanohole arrays can be prepared with conventional EBL or by using self-assembling of polystyrene nanospheres combined with wet etching processes for size reduction.[287,288] These arrays are coated with evaporated silver,[289,290] and gold[287] or decorated by electroplating of Ni/Au.[288] Finally, the polystyrene spheres are removed.

EBL nanohole arrays can be filled with nanoparticles by dipping the wafer in a colloidal solution and drying.[121] In Fig. 17, such a fabrication procedure is introduced. The resulting arrays are very regular with tunable shapes of the holes, their periodicity and diameter. Gold arrays produced by the same routine are used for surface enhanced coherent anti-Stokes Raman spectroscopy (SECARS) experiments showing an enhancement of the coherent anti-Stokes Raman spectroscopy (CARS) spectrum by $10^9$.[287] To prepare a regular pattern of nanovoids, gold nanoparticles are prepared on and in an inverse opal structure of $TiO_2$.[291] Here, $TiO_2$ sol is infiltrated over self-assembled monodisperse polymer microspheres. After calcinations and removing the polymer beads, the gold nanoparticles are sputtered in the array. The DNA detection of the human immunodeficiency (HI) and the severe acute respiratory syndrome (SARS) virus are performed based on the enhanced fluorescence.

By patterning of silicon wafers with an array of lines utilizing EBL and reactive ion etching (RIE), silver nanoparticle suprastructures with a controllable size, morphology and position can be prepared.[292] Following this approach, a silver–amino acid complex is reduced *in situ* to pure silver particles, which self-assemble to form metal supraspheres. By applying this substrate in SERS, 4-aminothiophenol can be detected down to a concentration of $10^{-10}$ mol $L^{-1}$. Instead of positioning metal nanoparticles in a nanohole array, the inverse form of nanoantennas[293] or nanopyramids[294] are prepared on a substrate. The pyramids are prepared by self-assembling of the pretreated colloidal silver solution (citrate reduced) on a pure semitransparent silver mirror. A 1000-fold fluorescence enhancement was observed. Furthermore, the combination of bottom-up and top-down techniques is used for the production of different shapes of nanoantennas.[293,295] First, pillars were prepared on a Si wafer by nanoimprint and RIE. The evaporation of gold leads to a self-assembling of small gold dots at the side of the pillar, showing a high SERS activity. This procedure is precise, simple, cost efficient and can create large areas of a regular pattern (in this case on a 4″ wafer).

Ordered arrays of nanoparticles can also be prepared based on the production of nanocones of a silicon–germanium mixture.[296] In this case, a silicon–germanium layer was placed and plasma was etched on a silicon wafer. As a result, a regular and homogeneous layer of nanocones was formed. The assembly of gold nanoparticles results in a SERS substrate with an enhancement factor of $2 \times 10^8$, in this case used for the investigation of the analyte 1,2-bi-(4-pyridyl)ethylene.

Metallic nanoparticles can also be self-assembled in non-periodical arrangements. As an example, Lee *et al.*[297] developed a "plasmonic paper", starting from a filter paper on which seed-mediated grown gold nanorods were adsorbed. By using this flexible plasmonic substrate, an enhancement factor of $\sim 5 \times 10^6$ for the SERS signal of a non-resonant analyte was found. Another flexible substrate was developed by using natural rubber and assembling gold nanoparticles.[298] Here, a thin rubber film is dipped in a solution of gold(III) chloride solution. The reduction is triggered by the reducing agents

 

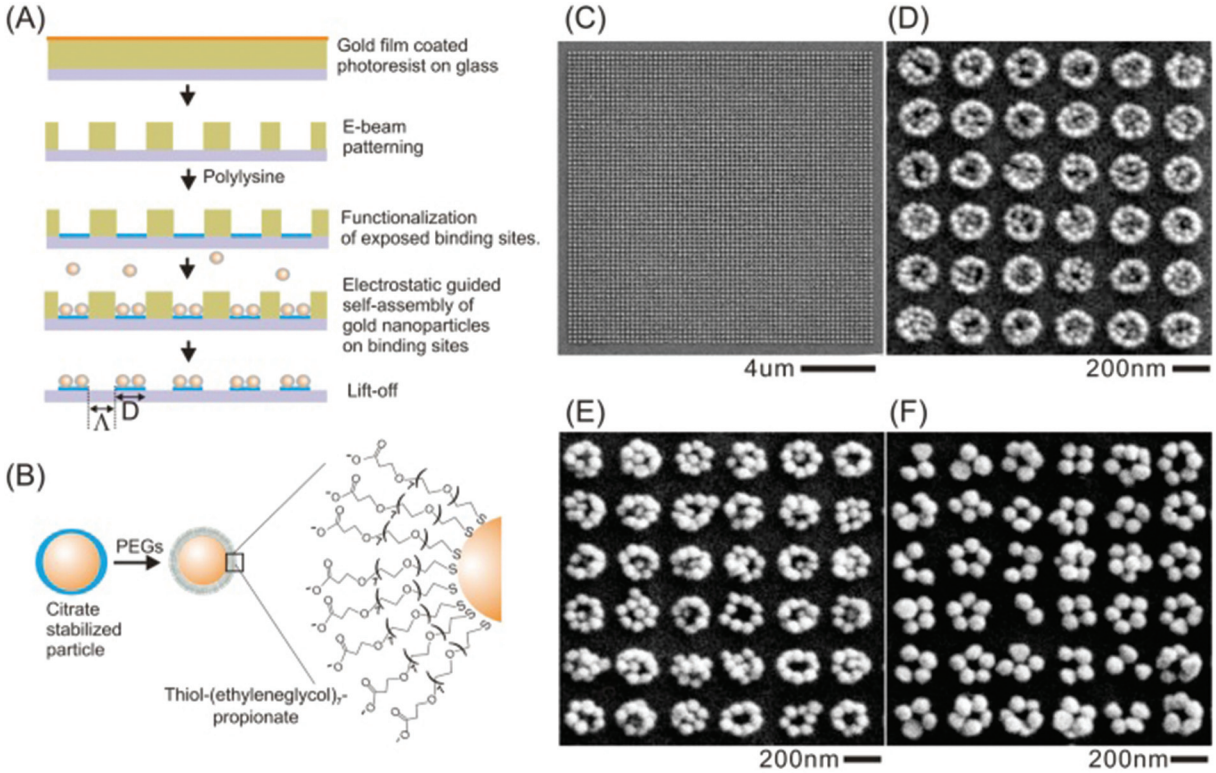


**Fig. 17** Self-assembly of different gold particle patterns based on their size. (A) Fabrication scheme for the production of nanoparticle cluster arrays (NCA). (B) Functionalization of the nanoparticles with short PEG molecules. (C) SEM image of NCA and SEM images of NCAs with a gold nanoparticle diameter of (D) 40 nm, (E) 60 nm and (F) 80 nm (reprinted with permission from B. Yan, S. V. Boriskina and B. M. Reinhard, *J. Phys. Chem. C*, 2011, **115**(50), 24437–24453,[121] copyright 2011 American Chemical Society.)

comprised in natural rubber. Moreover, spraying of silver nanocubes dispersed in chloroform and their assembling on quartz surfaces was reported.[299] In the next step, a fluorescent conjugated polymer was assembled on this nanoparticle surface by using a Langmuir–Blodgett technique. Also, nanoparticles with a rosette-like structure are reproducibly created based on the self-assembly of enzymes on a surface.[300–302] Here, silver nitrate is reduced by the enzymatic activity of the horseradish peroxidase. The self-assembling of plasmonic active particles in swellable polymers is done by preparing silver fibers and functionalizing them with gold nanorods embedded into reactive polyacrylic acid.[303] The pre-prepared positively charged gold nanorods attach to the negatively charged silver nanowires in a simple wet chemical reaction. By varying the pH value, the distance between gold nanoparticles and the silver wire can be tuned due to the swelling of the reactive PAA layer, which also changes the plasmonic resonance wavelength. In order to increase the homogeneity of the physical properties of citrate-reduced gold nanorods, they can be functionalized by a layer-by-layer assembly of thin films. Here, positively charged rods are functionalized by positively charged thiol molecules.[304,305] Other procedures can also be used for the functionalization of the structures in order to obtain certain application-related properties.[306–308] For example, self-organization of gold nanoparticles in a solution of *N*-methyl-*N*-hexadecylmorpholinium bromide (C16MMB) during crystallization leads to a plasmonic nanoparticle material which can be used for SERS experiments.[309] Also, by heat treatment of an $Ag^+$/polymer composite film on quartz glass, a large-area plasmonic active substrate can be prepared by a simple and cost-efficient protocol.[310]

Three-dimensional substrates, whose complexity exceeds that of simple multi-layered arrays, can be fabricated directly in solvents. A more advanced building material for such clusters is amphiphilic micelle-like nanoparticles,[269,311] which are composed of gold nanoparticles and amphiphilic block copolymers. Depending on nanoparticle sizes, solvent or copolymers length, they can be crafted into a variety of higher level structures. These structures are not fixed on any solid surface and can be used directly in solutions or *in vivo*. In Fig. 18, a scheme and SEM images of these amphiphilic micelle-like nanoparticles are depicted.

If particles without residual chemicals are needed, surfactant-free gold nanoparticles can be produced *via* laser ablation.[312] Ultra-short laser pulses excite a submersed metal target causing it to eject nanoparticles into the surrounding medium, for example purified water. The advantage of this method is the absence of additional chemicals. Thus, no background contribution due to the stabilizer molecules is expected. The size of the nanoparticles is very homogeneous

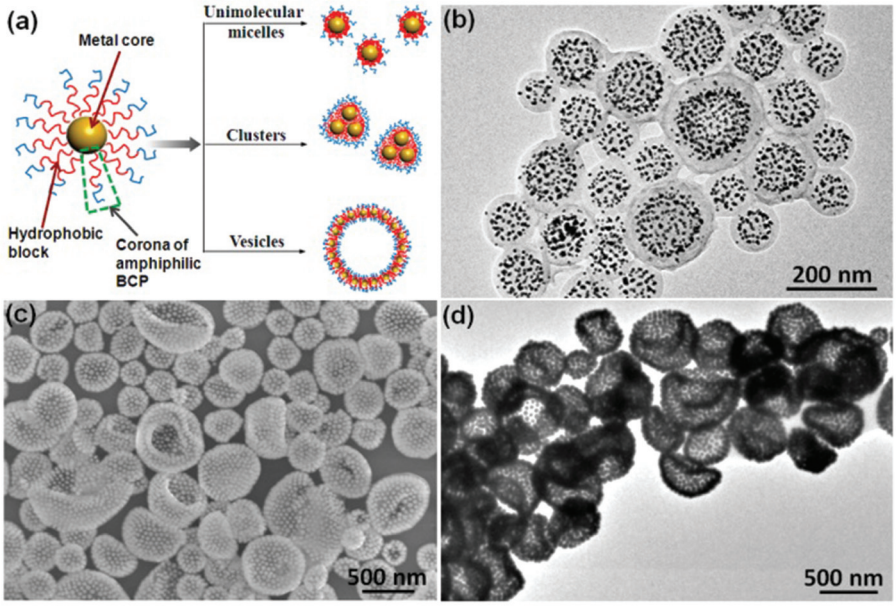


**Fig. 18** Amphiphilic nanoparticles' structure (APMNS) and their vesicular assemblies. (a) Shows the production scheme for APMN, (b–d) show the TEM (b, d) or SEM (c) images for AMNPS with a polystyrol mass-weight of 34 000 and a gold-core diameter of 5 nm (b) or 40 nm (c, d) (reprinted with permission from J. He, X. Huang, Y.-C. Li, Y. Liu, T. Babu, M. A. Aronova, S. Wang, Z. Lu, X. Chen and Z. Nie, *J. Am. Chem. Soc.*, 2013, **135**(21), 7974–7984,[311] copyright 2013 American Chemical Society).

and the size as well as the plasmonic active range can be tuned by the laser power and ablation time. With laser ablation processes also Au–Fe-alloys can be prepared which can be used as SERS substrates whereas the plasmonic range can be easily tuned by the amount of iron in the alloy.[313]

In summary, the main advantage of self-assembly methods is their cost efficiency and the simplicity of preparation, allowing the fabrication of large plasmonic active areas. Although the resulting substrates may not be as uniform as top-down fabricated substrates, they provide high enhancement at a low cost, making them ideal for mass applications.

### 5.2 Template based methods

Another method to create complex plasmonic structures and arrays is based on the usage of template structures. Such template structures are prefabricated nanostructures with a specific orientation at the surfaces for preparing arrays of metal nanoparticles. These substrates allow the fabrication of large surface areas with a well-ordered, nanostructured architecture. Template based substrates are promising not only due to their plasmonic properties but also because of their smaller manufacturing effort and their high efficiency across a large area.

Another critical issue of plasmonic substrates is their storage lifetime which is affected by environmental conditions. Metals are the key element for surface enhanced spectroscopic techniques; however, if they lack stability, the SES performance is decreased, thus leading to a reduced shelf life. To overcome these issues, template based plasmonic structures are perfect candidates as SES substrates. They can be stored easily until needed and then coated with a metal for the respective chemical or biochemical application. Within the last few years, many research activities have been focused on template based plasmonic structures. In this section, we will summarize surface mask templates, biological templates, porous templates and sheet templates. For more comprehensive details about template based techniques, the reader is referred to the literature.[314]

Most commonly, regular arrays of gold or silver nanostructures are prepared by employing polystyrene (PS), and other polymeric or silica spheres as templates which is known as nanosphere lithography (NSL).[11,21,315–324] Here, monolayers of self-assembled nanospheres are arranged on a substrate by, for example, a spin coating process or self-assembly strategies. In the next step, the metal is deposited on the nanosphere layer. Finally, the nanospheres are removed and only nanostructures representing the holes in the lattice remain (see Fig. 19). In the last decade, the NSL procedure was widely used for the production of plasmonic arrays applied in bioanalytical detection schemes. Similar strategies based on the NSL concept are applied for assembling $SiO_2$ nanospheres and depositing carbon quantum dots into this geometry, building two-dimensional (2D) and three-dimensional (3D) honeycomb structures (see Fig. 20).[325] First, a single layer of colloidal $SiO_2$ is assembled on a flat surface by using the Langmuir–Blodget (LB) technique.[326] In the next step, electrochemical deposition is applied to generate carbon quantum dots in the surface mask. In doing so, carbon quantum dots are deposited onto $SiO_2$ nanospheres under an applied voltage of 5 V, creating the structure of the honeycomb. Finally, the $SiO_2$ cores were removed by etching. Thus, these $SiO_2$ templates are often

 

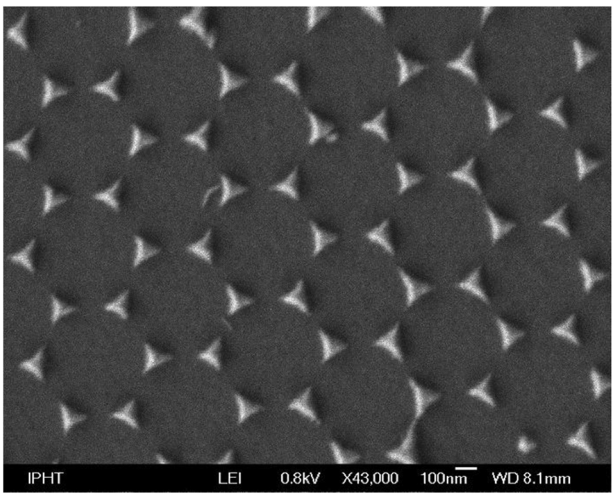


Fig. 19 SEM image of hexagonal arranged gold triangles prepared by nanosphere lithography (NSL).

called sacrificial templates creating new nanostructures which are made from other materials. In addition, 3D honeycomb structures are available by using a 3D colloidal $SiO_2$ nanosphere template. To apply these structures as SERS substrates, 40 nm of gold is deposited by sputtering. Moreover, to produce ZnO hollow nanosphere (HNS) arrays decorated with silver nanoparticles, PS nanosphere templating on silicon substrates is employed.[327] Here, a self-assembled PS nanosphere monolayer on a silicon substrate is used for generating ZnO HNS arrays. Within the production process, oxygen plasma is applied to control the size of the PS nanoparticles, followed by the deposition of a thin ZnO film onto the nanospheres. Finally, the top of the substrate is covered with silver. By this technique, the electrical field is concentrated in hot spots, which is good agreement with FDTD simulations. A further example for surface mask templates is vertically aligned 3D ZnO nanorods having plasmonic nanogaps sputtered with silver.[328] Furthermore, atomic layer deposition (ALD) is used to apply $TiO_2$ onto semi-shell nanospheres in combination with gold. The most important property of these nanostructures is the self-cleaning function by UV photocatalytic degradation of the target molecules. Analogous to the previous fabrication routines, thin films of bowl shaped silver cavities are prepared by using PS sphere templates and electrochemical deposition.[329] The plasmonic properties of these substrates are tunable by changing the silver thickness of the dips. As a SERS-based application of these silver cavities, a sandwich structure is introduced by applying the second layer of silver in order to identify the labeled proteins. The detection limit of TRIT and the Atto610 labeled protein is reported to be 50 and 5 pg $mL^{-1}$, respectively. Similar to bowl or honeycomb-like architectures are hollow-like nanostructures, which are of interest for fields like sensing and biomedical applications. Several strategies for generating hollow nanostructures

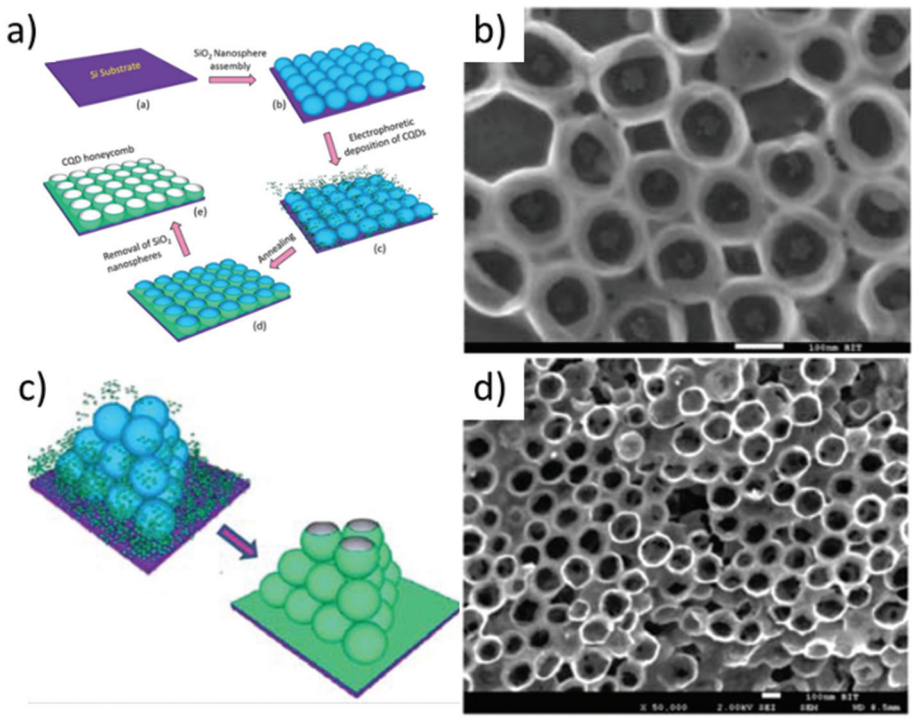


Fig. 20 Fabrication process for the formation of a 2D (a) and a 3D (c) honeycomb structure of carbon quantum dots and the related SEM images of the 2D (b) and 3D (d) structure (reproduced from Y. Fan, H. Cheng, C. Zhou, X. Xie, Y. Liu, L. Dai, J. Zhang and L. Qu, *Nanoscale*, 2012, **4**, 1776–1781,[325] with permission from The Royal Society of Chemistry).

working as sacrificial templates exist.[330] Instead of producing hollow nanosphere structures, creating silver hollow micro cubes by using $Cu_2O$ cubes as a chemical template is reported.[331] Thus, hollow micro cubes decorated with elementary silver are formed by chemical reactions between $AgNO_3$ and $Cu_2O$. With this highly porous shell structure, the detection sensitivity of SERS is as low as $10^{-14}$ M for rhodamine 6G.

Instead of using polymer or silica spheres as the template, porous $Al_2O_3$ produced by different anodizing techniques can be applied.[332–334] These nanoporous templates are versatile platforms for sensing, storage and separation applications and are created by a two-step anodization of a thin aluminum film on the surface of silicon substrates (anodic aluminum oxide, AAO). The porous size and depths are controlled by the anodic oxidation. On this porous substrate template gold nanospheres[333] or silver or gold nanorods[335] can be immobilized. Finally, the entire array can be coated with an evaporated thin gold layer.[334] Furthermore, CdSe nanotubes are used as a template for structuring an aluminum oxide membrane, followed by an immobilization of gold nanoparticles.[336] Thus, arrays of gold nanotubes with tunable sizes are created, providing a SERS enhancement of approximately 4 orders of magnitude. Alternatively, the periodic AAO structure can be loaded with self-assembled gold nanoparticles, creating high hydrophobic AAO channels.[337] Instead of using porous AAO templates, other materials are available for creating nano- or microporous structures. For example, gold nanoparticles, embedded in dried poly(vinyl alcohol) gel, have a great stability and sensitivity detecting crystal violet down to $10^{-12}$ M.[338] Similarly, block copolymer nanostructures demonstrate a strategy for an imprinting mold with sub 100 nm diameter holes.[339] This technique results in arrays of micro-porous cylinders with accommodating gold nanoparticles.

Applying sheet templates is advantageous in sensing, catalysis and biological applications which benefit from the material's good thermal and electrical conductivity, their catalytic activity, durability and porosity.[340] Briefly, these functional materials are used for immobilization of metallic nanoparticles on the surface. In recent years the importance of graphene as a template substrate has increased, since this promising material shows excellent thermal and optical properties.[341] As an example, graphene is applied as a sacrificial template to produce monolithic macroporous gold films by a simple annealing process. The porosity of these metal substrates is controlled by the graphene/gold weight ratio. Moreover, thin multilayer polymer films are used as a template to attached gold nanoparticle arrays with calcination.[342] This template shows a good thermal and chemical stability and will allow applications in sensing, catalysis and optoelectronics.

Furthermore, template printing is described as an efficient and easy-to-perform technique.[343] A PDMS template is evaporated with a thin gold layer. In an organic vapor the polymer swells and the gold cracks into small pieces. In the next step, the PDMS stamp is brought into contact with a self-assembled monolayer of thiols to peel the gold nanoparticles from the PDMS to the final substrate. Silicon wafers can also be employed as a template material.[344] Here, the silicon is structured with lithographic methods or a focused ion beam (FIB). Subsequently it is coated with a metal, which is then printed on a suitable substrate. These substrates show a plasmonic resonance in the green and red spectral regions and were used as SERS substrates with an enhancement factor of $1.4 \times 10^7$. Furthermore, nanohole arrays[345] and gold micro arrays produced by electron beam lithography[346] are discussed as template structures. Since these templates are fabricated by top-down techniques, the reader is referred to the next section for more details.

In addition to the previously described surface-mask templates, nature provides flawless 3D structures with a high conformity as templates for SES substrates. Microorganisms like viruses and bacteria are applied as templates for assembling the nanoparticles.[314,347] As an example, *Coscinodiscus asteromphalus* diatom frustules are used in combination with a wet chemical coating process, mimicking free standing gold nanostructures.[348] This 3D hexagonal hole pattern allows for extraordinary optical transmission studies.

In conclusion, template based techniques have the advantage of better controlled geometries combined with an easy and large-scale fabrication of plasmonic substrates. However, because feature defects from the template can be converted to the final substrate, a high quality and robust template is crucial for the reproducibility of these substrates.

## 6. Top-down techniques for the preparation of highly reproducible plasmonic structures and arrays

In the previous sections, bottom-up and self-organization processes were discussed to produce plasmonic structures and arrays with different complexities. However, such techniques are limited to plasmonic architectures which resemble the specific geometry given by the respective chemical, biochemical or electrochemical reaction. A direct transfer of new and interesting optical characteristics obtained by numerical simulations of artificial patterns might be impossible because previously described fabrication strategies fail to reproduce the desired array. Within this section, the third main group of fabrication strategies for SES substrates, top-down routines, will be discussed. These strategies are the basis of the creation of artificially shaped plasmonic nanostructures with a high reproducibility and structural homogeneity.

In Fig. 21, a selection of possible nanostructures by means of top-down techniques is given. The SEM images illustrate the broad capabilities of electron beam lithography and related techniques. Within the following sections, the various top-down methods are illustrated in detail.

### 6.1 Template preparation by means of electron beam lithography

Electron beam lithography (EBL) is one of the most prominent techniques in creating periodic nanostructures for plasmonic

 

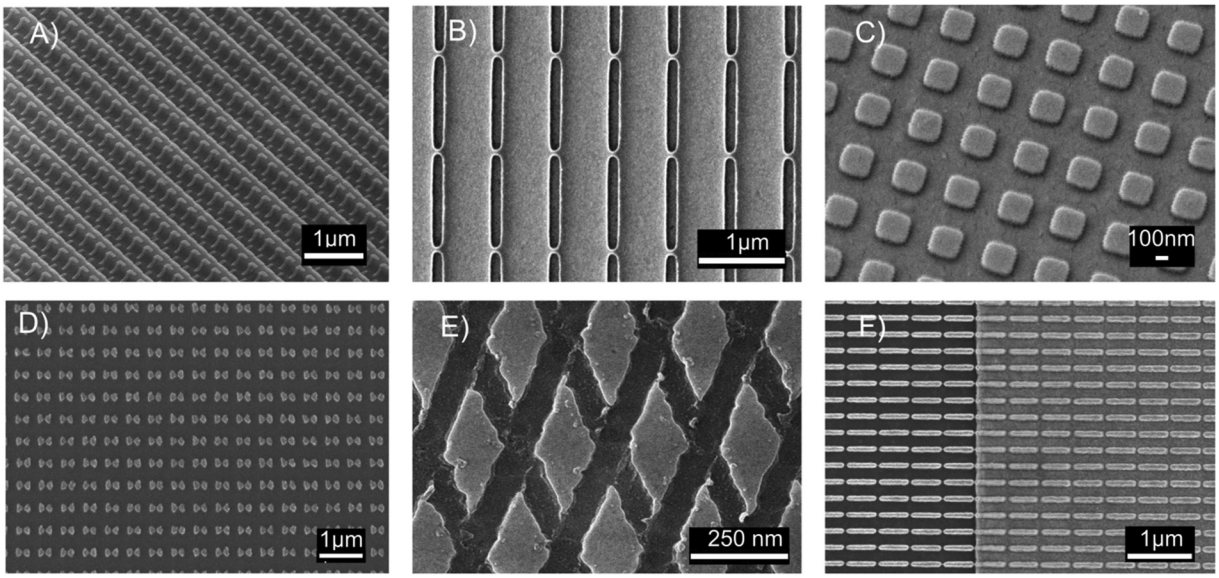


**Fig. 21** SEM images of plasmonic arrays prepared by top down techniques illustrating the spectrum of achievable geometries: (A) chiral plasmonic structures prepared by a multilayer EBL process,[349] (B) plasmonic gaps for enhanced sensing in the MIR region, combining the EBL and ICE-RIE processes, (C) SERS-active silver nano squares produced by EBL,[350] (D) Bowtie antennas as the SERS substrate, (E) gold nanorhombs produced by EBL and RIE etching processes,[50,351] (F) SEIRA structures produced by lift-off EBL.

applications.[352] Here, an electron beam is scanned over a positive resist, *e.g.* PMMA and ZEP520,[353] or a negative resist *e.g.* Calixarenes and Su8,[354] thus changing the solubility of the resist layer by a photochemical process. In the case of positive resist layers, the solubility of the illuminated area is increased due to degeneration of covalent bonds within the polymer. In negative resists, the illumination decreases the solubility, which is attributed to the forming of covalent bonds within the resist layer. After exposure, the intended structure is obtained by removing molecules with a higher solubility utilizing a suitable solvent like aceton.

Due to the diffraction limit, optical lithography is only feasible up to a lateral resolution of around 500 nm, although performance enhancing methods like immersion lithography become available.[355] Since electrons have a much shorter wavelength, EBL structures below 10 nm are possible.[356] Since the scanning operation is an integral part of the process, nearly perfect control of the electron dose and with this, precise control of the structural size is possible. However, the structural features are limited to 10 nm due to the beam broadening and the proximity effect.[357] High costs for EBL are mostly attributed to the laborious devices used and/or slow speed of writing, but recent advances drastically reduce the processing time for periodic arrays of relatively simple shapes like squares and rods applying character projection.[358,359]

A direct approach to generate periodically arranged plasmonic arrays is to apply an EBL structured template and cover or functionalize the layer directly. As an example, quasi 3D SERS substrates were generated by EBL on reflective substrates like silicon or ITO, or on homogeneous dielectric media as *e.g.* PDMS, and finally coated with gold.[139,360] Based on the resulting SERS spectra of 4-mercaptopyridine, an enhancement factor of roughly $10^9$ was estimated. Furthermore, these structures were used to detect microorganisms and to separate between Gram-positive and Gram-negative bacteria strains with SERS spectroscopy. Ring resonators could be produced by EBL forming concentric silver rings which have the same periodicity but a different width.[361] A SERS spectrum of R6G on this substrate had a much better signal-to-noise ratio with lower laser intensity (15 µW) than a comparable SERS spectrum recorded on a silver film with a higher laser intensity (1.5 mW). Such split ring resonators are well described in theory and experiment.[362] Plasmon resonances of the EBL processed and silver-coated split ring resonators were detected in the visible and infrared spectral region, depending on the polarization of the *E*-field of the incident light. The enhancement factors for SERS measurement of 2-mercaptopyridine were calculated to be $10^3$. To detect myoglobin on a SERS substrate, nanograins on a gold–chromium substrate were prepared by means of electro-plating and EBL. Here, EBL-generated holes in a resist layer were subsequently filled *via* an electroplating process. After removal of the resist, individual Au-nanograins remained.[363] By employing these substrates for SERS, reliable spectra of myoglobine were recorded. Finally, silver nano-squares prepared with EBL showed the dependency of the intensity of SERS signals on the thickness of the respective silver layer.[350]

These results demonstrate both the versatility and potential of EBL generated templates. Due to ongoing technical improvements, much of the limitations of EBL, *e.g.* poor speed and high costs, are resolved. Modern techniques such as character projection and high throughput setups significantly

decreased writing, in some cases, *e.g.* for regular patterns such as gratings, by several orders of magnitude. Finally, the masks created by EBL are essential for lift-off processes, which will be highlighted within the next paragraph.

### 6.2 Lift-off processes as part of lithographic methods

An alternative technique to prepare reproducible plasmonic arrays is based on employing templates for lift-off processes or as an etching mask. In a lift-off process, a structured resist layer (see above) is covered with a metal layer. Subsequently, the package is immersed in a solvent,[364] which removes the resist and with that the metal on top of the resist. Only metallic nanostructures remain, which have been deposited through the openings of the resist layer onto the underlying substrate. The quality of the structures created crucially depends on the successful removal of unwanted patterns, requiring resist sidewalls accessible by the solvent. This excludes sophisticated deposition techniques such as atomic layer deposition, because its high surface conformity would cover all sidewalls, preventing the solvent to remove the resist.

The most common technique to produce nanoscale discs with small gap sizes between them is EBL-based lift-off.[366] Two gold discs, one positioned over the other, are separated by a dielectric layer and finally covered with a fluorescent dye. The diameters of the discs and the thickness of the spacer between them vary and influence the plasmonic behavior. The variation of structural parameters can increase the fluorescence intensity up to 30 times. Moreover, pillar structures are available as plasmonic active substrates *via* lift-off processes in EBL. Two different types were defined: pillars with a metal cap standing on a dielectric (like $SiO_2$)[367] and pillars with a metal cap standing on metallic films.[368,369] Comparing the SERS enhancement factors, silicon pillars with a gold cap standing on a gold surface showed a, by two orders of magnitude, increased SERS enhancement over silicon pillars with a gold cap on a silicon surface.[367] Depending on the diameter of one pillar and the gap between two pillars, the enhancement factor for benzenethiol could be calculated to be $1.2 \times 10^8$.[369] A quasi 3D gold nanostructure was fabricated based on applying an EBL-produced master-die, whereon a template was deposited. After removing the master it was coated with gold.[370] Following a similar routine, the group prepared 2D nanohole arrays by coating the EBL structure aforementioned with gold and then lifting off the nanopillars with the help of a PDMS layer, resulting in gold nanoholes on silicon. Both structures were then tested as SERS substrates. The template stripping method can be further combined with other techniques. As an example, bottom up large scale fabricated hemispherical shell noble metal structures was applied as a template for the template stripping process.[371,372] The template was formed by a porous $Al_2O_3$ film on aluminum *via* an anodization technique. A thin metal film was deposited onto the porous $Al_2O_3$ surface. The following steps were performed as in the classical template stripping process. With this method, the radii of the hemispherical cells were tuned and with this tuning the optical characteristics became possible. Template stripping is not only restricted to nanoholes or void structures; also Bull's eye, pyramidal,[373] groove, square-shaped bump, cylinder, hexagonal arrays[374–376] and other structures could be produced by this method. These structures have much smoother surfaces in comparison to reactive-ion etched structures. Moreover, template-stripped structures could be maintained for Ag, Au or Cu metals, thus making integrated multilayer architectures possible.[373] Finally, pyramidal structures could be utilized as tips for near-field spectroscopy techniques, *e.g.* tip-enhanced Raman spectroscopy (TERS). Such tips can be produced massively parallely with a high yield, high reproducibility and high durability (see Fig. 22).[365]

To conclude, lift-off processes in lithographic methods guarantee for a high diversity of plasmonic substrates. However, the resistivity against etching and the achievable aspect ratio of the resist layer might limit the application of these approaches for the fabrication of nanostructure arrays.

### 6.3 Ion etching and ion beam etching in EBL-based processes

Template stripping methods as discussed in the previous section are limited with respect to the thickness of the metal layer and the deposition temperature. Ion etching (IE), as well as its directed form ion beam etching (IBE),[377] are further options to process EBL templates. Moreover, IE as a purely physical process can be combined with a reactive gas like $CF_4$ or $SF_6$, resulting in reactive ion etching (RIE) or its directed form, reactive ion beam etching (RIBE). By depositing the functional layer and afterwards applying an EBL template (structured resist layer), the template acts as a protective layer where non-covered areas of the functional layer are removed.

As an example, gold nanorhombs were prepared by combining IBE with EBL. Here, a resist layer was deposited on a gold coated fused silica substrate.[50,351] The resist layer was structured by EBL, followed by an argon ion beam etching to transfer the layout into the metal layer. A technique of ion implementation was created as a modification of IBE. Here, an aluminum layer was structured with a silver ion beam, resulting in a bimetallic Al–Ag-island film.[378] The substrate showed a broad plasmonic range from UV to VIS for fluorescence enhancing experiments.

Whereas IBE and RIBE are directed but non-focused processes, in focused ion beam (FIB) milling, a focused beam is used to directly structure a functional or sacrificial metal layer, or even to modify resists comparable to EBL.[379,380] FIB milling offers nearly perfect control over the size and shape of the structure, yet it is a rather time-consuming process. Thus, FIB milling can serve as a very good tool for scientific uses but is of little use for industrial production or high volume applications. Nevertheless, FIB milling has become an innovative tool in those cases where single antennas or small arrays suffice.[381,382] Based on FIB milling and EBL, a noble metal nanoantenna centered in an area of photonic crystal cavities was prepared.[383] Here, nanostructured tips, prepared by FIB, were coated with the metal applying chemical vapor deposition. In the next step, the plasmonic active tip was then

 

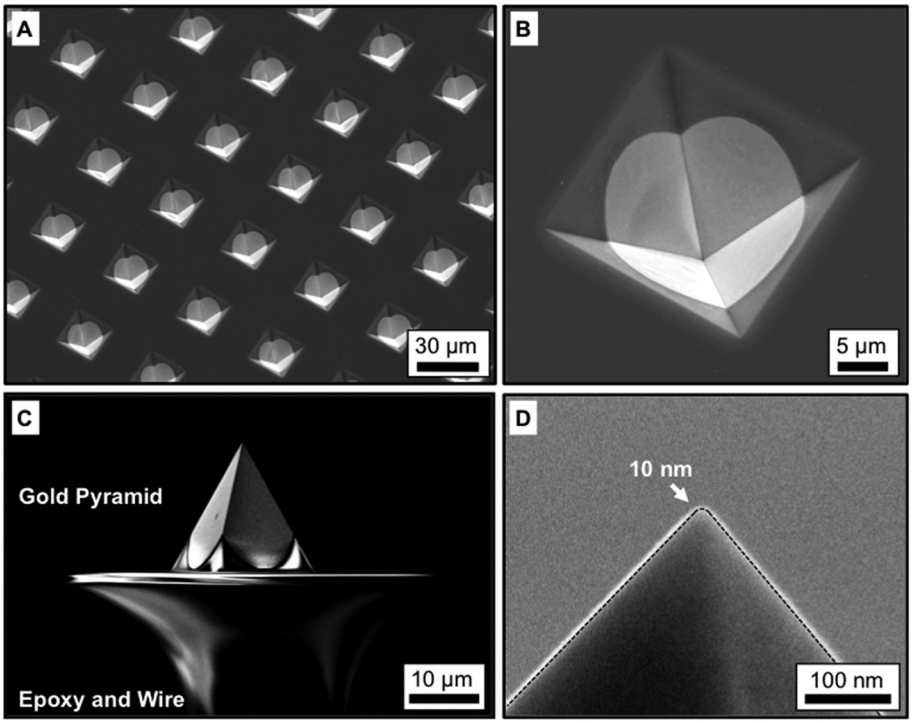


Fig. 22 SEM images of nanopyramides fabricated with the help of a lift-off process. (A) Overview image in order to demonstrate the reproducibility of the applied technique. (B) Gold covered pyramid after performing the lift-off process. (C) Pyramid after template stripping and connection with a tungsten wire. (D) Close-up image of the pyramid apex. Its diameter is about 10 nm which makes it suitable for use as a TERS tip (adapted with permission from T. W. Johnson, Z. J. Lapin, R. Beams, N. C. Lindquist, S. G. Rodrigo, L. Novotny and S.-H. Oh, *ACS Nano*, 2012, **6**, 9168–9174, copyright 2012 American Chemical Society[365]).

covered with silica. To characterize the enhancing properties, quantum dots of CdSe or a monolayer of organic compounds was arranged on the surface of the nanoantennas. The system could also be used in combination with atomic force microscopy (AFM) and allowed for reproducible signals of single molecules with a sub-wavelength resolution as well as in a far-field configuration. Further, ring resonators have been prepared with the FIB method.[384] Gold rings with a decreasing diameter were arranged on a gold surface coated with chromium. By applying the fluorescent dye Alexa 647 on the surface of this structure, a fluorescence enhancement up to 120 was detected.

RIE processes can also produce impressive results if a high order of the surface structure is not aspired, *e.g.* for decorated silicon needles which have been demonstrated to show a strong signal enhancement. For example, a chrome layer for background reduction was introduced in combination with silver as a plasmonic metal.[385] This process is only limited by the size of the device for RIE etching and produces substrates which are commercially available.

IE, RIE, IBE and RIBE as the most common etching techniques play a vital role for all micro- and nanostructure applications. By carefully modifying and adapting these processes to the demands of plasmonics, creative and effective solutions have been found for problems like scaleability and performance. Nevertheless, more cost-efficient techniques are still aspired. Amongst them nanoimprint lithography, which will be introduced in the next section, has the potential to become a standard procedure in nanoscale technology within the next decade.

### 6.4 Nanoimprint lithography (NIL) for high-throughput preparation

Nanoimprint lithography (NIL) combines a fast pattern transfer with a high scalability in size and throughput.[386,387] Instead of repeated illuminations by EBL, one master is prepared by applying the techniques explained in the previous section. This negative master is further used to "stamp" a softened or uncured resist layer. Thus, the pattern transfer only takes some minutes structuring wafers up to 6″ diameter. Moreover, even roll-to-roll methods can be applied.[388] After acquiring a master die, this technique offers the easiest access to high volume substrates, scaling price and effort according to the amount of chips produced. As an example, SEM images of a master mold, the corresponding resist imprint and the obtained gold nanostructure are shown in Fig. 23.[389]

To fabricate aluminum nanovoid substrates for application as SERS substrates in the UV range, the NIL technique was combined with electron beam evaporation.[390] Thus, biological molecules with an absorption in the UV region could be investigated under resonant conditions. Employing a soft nanoimprint lithography protocol, the fabrication of plasmonic

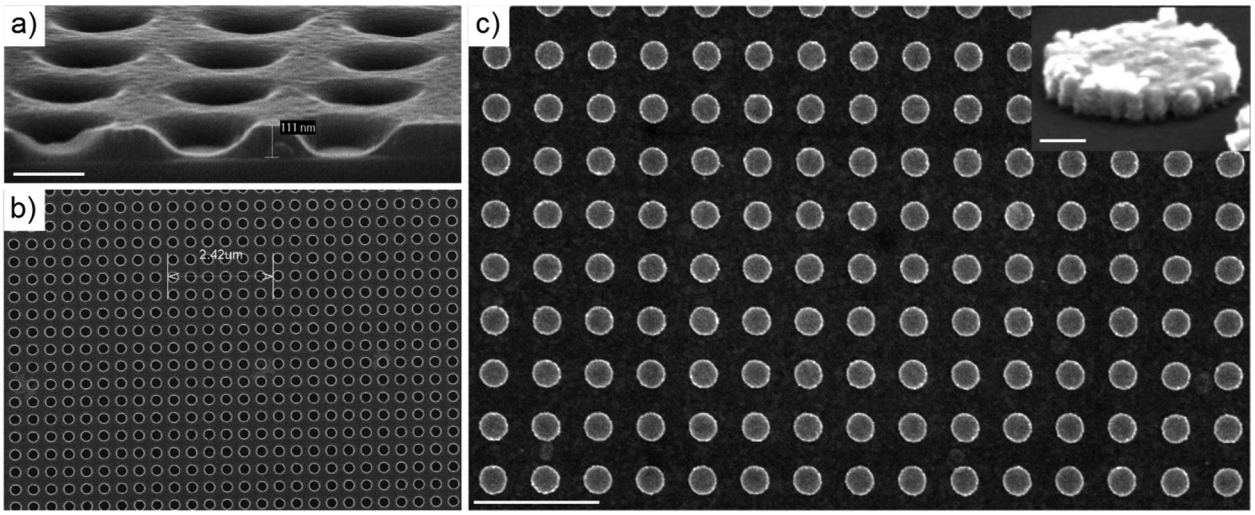


Fig. 23 SEM images of the nanoimprint process steps: (a) the master made by EBL on a silicon substrate, (b) the structure imprinted in a polymer (scale bar: 200 nm) and (c) the resulting gold structure after lifting the resist (scale bar: 1 μm). The inset in (c) represents an example of a nanodisk in detail (scale bar: 50 nm) (adopted from Cottat *et al.*[389]).

crystals was feasible.[391] Here, structured soft PDMS stamps were prepared to texture a polymer surface and coat it with a thin gold film. By doing so, a uniform hole array resulted in plasmonic resonances in the (near) infrared region. The SERS activity is characterized by applying benzenethiol as a model analyte. The enhancement factor was estimated to be $10^5$. A quasi-three-dimensional plasmonic crystal with a plasmonic response in the visible and NIR spectral regions showed comparable SERS enhancement properties for benzenethiol.[392] Here, the SERS enhancement depended on the diameter of the circular nanostructures and the periodicity of the array prepared by means of NIL. Employing NIL, a suspended nanohole array membrane was also prepared for applications in surface tension-driven flow-through SERS.[393]

Furthermore, filled hole arrays were created by NIL. To do so, a structure of petri-dish-shaped $SiO_2$, with an inner core consisting of a silver disc, was fabricated as a SERS substrate.[394] Because of the undercut resist layer (PMGI) and the oblique angle at which the $SiO_2$ was deposited, structures with sub-lithographic dimensions could be produced. Employing these structures as SERS substrates, rhodamine 6G was detected down to nanomolar concentrations. To fabricate ring structures (split rings *etc.*), a four-step procedure was developed.[395] In the first step, an array of epoxy piles was formed by applying soft lithography. Secondly, thin metallic films were deposited on the piles, and, thirdly, the entire structure was embedded in an epoxy cube to prepare thin planes of 80 nm by employing an ultramicrotome ("nanoskiving"). In the final step, the epoxy material was etched. Depending on the structure, the plasmon resonance could be tuned from UV, VIS to IR based on the diameters of the rings and their periodicity. Moreover, metallic cavities (*e.g.* Ag nanoparticles) have been embedded in a dielectric medium ($SiO_2$) by using ion implantation based on a stencil made by soft lithography.[282] The Raman signal of pyridine was strongly enhanced by employing this 3D approach, compared with the spectra of pyridine recorded on silver nanoparticles that were not implanted.

Finally, the NIL technique was combined with other methods to prepare complex plasmonic arrays. Gold substrates with a dielectric core of chitosan were prepared by molding the chitosan-hydrogel on glass substrates with nanoimprint lithography, followed by RIE and deposition of a thin gold film by seed mediated electroless plating.[396]

These advances demonstrate that NIL has become a suitable tool for plasmonics fabrication, promising cost-efficient, fast and large-scale solutions. It can be used both in combination with etching and template stripping, providing a well-tuned process with drastically reduced and high availability.

### 6.5 Template-stripping as a tool for the fabrication of ultra-smooth surfaces

Template-stripping nanofabrication is a technique supplying homogeneous, ultra-smooth surfaces with well-organized two-dimensional patterns over large areas. It is based on metals with low adhesion to the template surface. First, the metal is deposited onto the template surface (*e.g.* silicon template with Au or Ag). After that, an adhesion layer is added in order to attach a supporting glass wafer. In the final step, the glass-template sandwich is separated mechanically. Since the separation will occur between the layers with the weakest adhesion, the metal layer will stick to the glass wafer.[397] For the fabrication of the template, techniques mentioned in the previous paragraphs can be applied.

As an example, the bottom-up large scale fabrication of hemispherical shell noble metal structures as a template for the stripping process was reported.[372,398] By employing top down techniques it was possible to create nearly every 2D single structure element. Well-defined single particles like tri-

 

angles, donuts, equilateral-triangle plasmonic cavities, as well as bowtie antenna were prepared by a combination of the template stripping method and EBL structuring of a template. A metal (*e.g.* silver) layer was deposited on PMMA and glued to another substrate (*e.g.* silicon wafer) surface for transfer and cleaning which resulted in tunable plasmonic substrates for the VIS and IR spectral regions.

Template-stripping is an established technique, but far from a widespread application. This is due to challenges regarding the handling during the transfer process and the sensitivity for incomplete or faulty pattern transfers which hinder its incorporation into standard processes.

In conclusion, the advantages of applying top-down techniques to fabricate plasmonic arrays and structures are attributed to their very high homogeneity and reproducibility. However, these techniques are by far more expensive than bottom-up or self-organization processes. As production costs are high for most top-down techniques, the fabricated substrates should allow for reusability *e.g.* of the template structure. Due to the discussed issues in preparing such structures, however, they are mostly not applied for analytical tools with a high throughput. On the other hand, due to the more precise theoretical foundation, they are often chosen for fundamental research. Great efforts have been put into combining the high reliability of EBL with more cost-efficient and faster techniques to reduce costs and circumvent size limitations. Most prominently, NIL will gain importance for generating regular patterned substrates for analytical application scenarios, as it displays all advantages of EBL. Only, the flexibility in changing the nanostructure's shape and arrangement remains as an issue due to the application of a master die.

## 7. Conclusions

Within this comprehensive review on plasmonic nanostructures for surface enhanced spectroscopic methods, the interested reader has received an overview about the theoretical approaches to simulate plasmonic-active metallic nanoarrangements. In order to investigate the optical behavior of isotropic and non-magnetic spherical or spheroidal particles analytical techniques are applied. However, in the case of more complex shaped structures, numerical methods *e.g.* DDA, BEM, FEM, FTDT and FDFD come into operation. By means of these techniques, a high diversity of nanostructures and their arrays with varying complexities are accessible.

Further on, various fabrication methods based on bottom-up, self-organization and top-down methods are introduced. In order to fabricate the desired nanoparticles, a great variety of methods are available, *e.g.* bottom-up preparation strategies of plasmonic nanostructures to generate metal colloids, core–shell particles and complex-shaped structures employing seed-mediated growth. Moreover, to fabricate nanoparticle clusters and arrays, self-organization as well as template-based methods are applied. Finally, top-down processes, *e.g.* EBL and its variants as well as NIL, guarantee for an improved homogeneity and reproducible character of the plasmonic devices applied in SES. Thus, the interested reader will identify the best-suited method to generate the desired plasmonic structure. By intelligent combination of bottom-up, self-organized or top-down techniques, innovative SES substrates with new optical behaviors might be achievable. However, the conspectus of the fabrication strategies within this review article cannot be complete, due to the enormous number of publications within this field.

In future work, the research on plasmonic substrates applied for SES techniques might focus on different directions depending on the read-out method. In the case of SERS, a huge number of plasmonic structures are described in the literature as well as their application towards (bio)analytics. Thus, the research might point to the direction of transferring innovative SERS substrates in relevant application fields *e.g.* clinical, food and environmental analytical schemes. Further on, SEF substrates show promising results in employing immunoassays as well as in combination with SERS as powerful labels in cell analysis. Thus, the generation of stable and reliable SEF substrates will be of great importance. Finally, the research on powerful SEIRA substrates might lead to tunable plasmonic arrays with optical properties that can be varied by simple structural changes to adjust different frequency ranges.

## Acknowledgements

Funding of the research projects BioInter (13022-715) and FastTB (2013 FE 9058, 2013 VF 0019) by the Development Bank of Thuringia and the European Union (EFRE) as well as InfectoGnostics (13GW0096F) and JCBI 2.0 (03IPT513Y) by the Federal Ministry of Education and Research (BMBF), Germany is gratefully acknowledged. Moreover, we would like to thank the Czech Science Foundation P205/12/G118 for supporting the work of V. Peksa. Finally, funding of the PhD project of I. J. Hidi within the framework "Carl-Zeiss-Strukturmaßnahme" is gratefully acknowledged. Special thanks go to Torsten May for proof reading and many helpful discussions.

## References

1 S. Becht, S. Ernst, R. Bappert and C. Feldmann, *Chem. Unserer Zeit*, 2010, **44**, 14–23.
2 S. A. Love, B. J. Marquis and C. L. Haynes, *Appl. Spectrosc.*, 2008, **62**, 346a–362a.
3 M. Faraday, *Philos. Trans. R. Soc. London*, 1857, **147**, 145–181.
4 P. P. Edwards and J. M. Thomas, *Angew. Chem., Int. Ed.*, 2007, **46**, 5480–5486.
5 K. A. Willets and R. P. Van Duyne, *Annu. Rev. Phys. Chem.*, 2007, **58**, 267–297.
6 G. Mie, *Ann. Phys.*, 1908, **330**, 377–445.
7 W. Xie and S. Schlücker, *Rep. Prog. Phys.*, 2014, **77**, 116502.

8 X.-J. Chen, G. Cabello, D.-Y. Wu and Z.-Q. Tian, *J. Photochem. Photobiol., C*, 2014, **21**, 54–80.
9 S. Schlücker, *Angew. Chem., Int. Ed.*, 2014, **53**, 4756–4795.
10 D. Cialla, S. Pollok, C. Steinbrücker, K. Weber and J. Popp, *Nanophotonics*, 2014, **3**, 383–411.
11 J. N. Anker, W. P. Hall, O. Lyandres, N. C. Shah, J. Zhao and R. P. Van Duyne, *Nat. Mater.*, 2008, **7**, 442–453.
12 W. Ma, H. Kuang, L. Xu, L. Ding, C. Xu, L. Wang and N. A. Kotov, *Nat. Commun.*, 2013, 4.
13 S. McAughtrie, K. Faulds and D. Graham, *J. Photochem. Photobiol., C*, 2014, **21**, 40–53.
14 T. Vo-Dinh, Y. Liu, A. M. Fales, H. Ngo, H.-N. Wang, J. K. Register, H. Yuan, S. J. Norton and G. D. Griffin, *Wiley Interdiscip. Rev.: Nanomed. Nanobiotechnol.*, 2015, **7**, 17–33.
15 D.-W. Li, W.-L. Zhai, Y.-T. Li and Y.-T. Long, *Microchim. Acta*, 2014, **181**, 23–43.
16 R. A. Alvarez-Puebla and L. M. Liz-Marzán, *Angew. Chem., Int. Ed.*, 2012, **51**, 11214–11223.
17 J. Zheng and L. He, *Compr. Rev. Food Sci. Food Saf.*, 2014, **13**, 317–328.
18 E. L. Keller, N. C. Brandt, A. A. Cassabaum and R. R. Frontiera, *Analyst*, 2015, **140**, 4922–4931.
19 J. M. Chalmers and P. R. Griffiths, *Handbook of vibrational spectroscopy*, J. Wiley, 2002.
20 Y. N. Xia and N. J. Halas, *MRS Bull.*, 2005, **30**, 338–344.
21 A. J. Haes, C. L. Haynes, A. D. McFarland, G. C. Schatz, R. P. Van Duyne and S. Zou, *MRS Bull.*, 2005, **30**, 368–375.
22 S. A. Maier, *Plasmonics: Fundamentals and Applications: Fundamentals and Applications*, Springer, 2007.
23 S. A. Kim, K. M. Byun, J. Lee, J. H. Kim, D. G. A. Kim, H. Baac, M. L. Shuler and S. J. Kim, *Opt. Lett.*, 2008, **33**, 914–916.
24 C. Lausted, Z. Y. Hu, L. Hood and C. T. Campbell, *Comb. Chem. High Throughput Screening*, 2009, **12**, 741–751.
25 D. Cialla, A. März, R. Böhme, F. Theil, K. Weber, M. Schmitt and J. Popp, *Anal. Bioanal. Chem.*, 2012, **403**, 27–54.
26 S. Pahlow, A. März, B. Seise, K. Hartmann, I. Freitag, E. Kämmer, R. Böhme, V. Deckert, K. Weber, D. Cialla and J. Popp, *Eng. Life Sci.*, 2012, **12**, 131–143.
27 S. L. Kleinman, R. R. Frontiera, A.-I. Henry, J. A. Dieringer and R. P. Van Duyne, *Phys. Chem. Chem. Phys.*, 2013, **15**, 21–36.
28 J. R. Lakowicz, C. D. Geddes, I. Gryczynski, J. Malicka, Z. Gryczynski, K. Aslan, J. Lukomska, E. Matveeva, J. A. Zhang, R. Badugu and J. Huang, *J. Fluoresc.*, 2004, **14**, 425–441.
29 W. Knoll, F. Yu, T. Neumann, L. Niu and E. L. Schmid, in *Radiative Decay Engineering*, ed. C. D. Geddes and J. R. Lakowicz, Springer, US, 2005, pp. 305–332.
30 Y. Chen, K. Munechika and D. S. Ginger, *Nano Lett.*, 2007, **7**, 690–696.
31 E. Fort and S. Grésillon, *J. Phys. D: Appl. Phys.*, 2008, **41**, 013001.
32 K. Ataka and J. Heberle, *Anal. Bioanal. Chem.*, 2007, **388**, 47–54.
33 J. Kundu, F. Le, P. Nordlander and N. J. Halas, *Chem. Phys. Lett.*, 2008, **452**, 115–119.
34 M. Fleischmann, P. J. Hendra and A. J. McQuillan, *Chem. Phys. Lett.*, 1974, **26**, 163–166.
35 M. G. Albrecht and J. A. Creighton, *J. Am. Chem. Soc.*, 1977, **99**, 5215–5217.
36 W. Ahn and D. K. Roper, *ACS Nano*, 2010, **4**, 4181–4189.
37 Y. Wang and S. Schlucker, *Analyst*, 2013, **138**, 2224–2238.
38 W. Xie and S. Schlucker, *Phys. Chem. Chem. Phys.*, 2013, **15**, 5329–5344.
39 E. A. Vitol, Z. Orynbayeva, G. Friedman and Y. Gogotsi, *J. Raman Spectrosc.*, 2012, **43**, 817–827.
40 J. F. Li, Y. F. Huang, Y. Ding, Z. L. Yang, S. B. Li, X. S. Zhou, F. R. Fan, W. Zhang, Z. Y. Zhou, Y. Wu de, B. Ren, Z. L. Wang and Z. Q. Tian, *Nature*, 2010, **464**, 392–395.
41 A. Marz, T. Henkel, D. Cialla, M. Schmitt and J. Popp, *Lab Chip*, 2011, **11**, 3584–3592.
42 J. Sun, Y. Xianyu and X. Jiang, *Chem. Soc. Rev.*, 2014, **43**, 6239–6253.
43 W. Chao and Y. Chenxu, *Nanotechnology*, 2015, **26**, 092001.
44 Z.-Q. Tian, Z.-L. Yang, B. Ren, J.-F. Li, Y. Zhang, X.-F. Lin, J.-W. Hu and D.-Y. Wu, *Faraday Discuss.*, 2006, **132**, 159–170.
45 B. Ren, G.-K. Liu, X.-B. Lian, Z.-L. Yang and Z.-Q. Tian, *Anal. Bioanal. Chem.*, 2007, **388**, 29–45.
46 M. Kerker, D. S. Wang and H. Chew, *Appl. Opt.*, 1980, **19**, 4159–4174.
47 J. Gersten and A. Nitzan, *J. Chem. Phys.*, 1980, **73**, 3023–3037.
48 T. Itoh, K. Yoshida, V. Biju, Y. Kikkawa, M. Ishikawa and Y. Ozaki, *Phys. Rev. B: Condens. Matter*, 2007, **76**, 085405.
49 W. H. Zhang, H. Fischer, T. Schmid, R. Zenobi and O. J. F. Martin, *J. Phys. Chem. C*, 2009, **113**, 14672–14675.
50 D. Cialla, J. Petschulat, U. Hübner, H. Schneidewind, M. Zeisberger, R. Mattheis, T. Pertsch, M. Schmitt, R. Möller and J. Popp, *ChemPhysChem*, 2010, **11**, 1918–1924.
51 E. C. Le Ru and P. G. Etchegoin, *Chem. Phys. Lett.*, 2006, **423**, 63–66.
52 E. C. Le Ru, M. Meyer, E. Blackie and P. G. Etchegoin, *J. Raman Spectrosc.*, 2008, **39**, 1127–1134.
53 H. X. Xu, J. Aizpurua, M. Kall and P. Apell, *Phys. Rev. E: Stat. Phys., Plasmas, Fluids, Relat. Interdiscip. Top.*, 2000, **62**, 4318–4324.
54 L. Jensen, C. M. Aikens and G. C. Schatz, *Chem. Soc. Rev.*, 2008, **37**, 1061–1073.
55 P. Knoll, M. Marchl and W. Kiefer, *Indian J. Pure Appl. Phys.*, 1988, **26**, 268–277.
56 Y. S. Yamamoto, Y. Ozaki and T. Itoh, *J. Photochem. Photobiol., C*, 2014, **21**, 81–104.
57 E. J. Ayars, H. D. Hallen and C. L. Jahncke, *Phys. Rev. Lett.*, 2000, **85**, 4180–4183.
58 C. M. Aikens, L. R. Madison and G. C. Schatz, *Nat. Photonics*, 2013, **7**, 508–510.

 

59 A. Otto, I. Mrozek, H. Grabhorn and W. Akemann, *J. Phys.: Condens. Matter*, 1992, **4**, 1143–1212.
60 X. P. Gao, J. P. Davies and M. J. Weaver, *J. Phys. Chem.*, 1990, **94**, 6858–6864.
61 M. Moskovits and J. S. Suh, *J. Phys. Chem.*, 1984, **88**, 5526–5530.
62 J. Gersten and A. Nitzan, *J. Chem. Phys.*, 1981, **75**, 1139–1152.
63 A. Kinkhabwala, Z. F. Yu, S. H. Fan, Y. Avlasevich, K. Mullen and W. E. Moerner, *Nat. Photonics*, 2009, **3**, 654–657.
64 R. Gill and E. C. Le Ru, *Phys. Chem. Chem. Phys.*, 2011, **13**, 16366–16372.
65 P.-P. Fang, X. Lu, H. Liu and Y. Tong, *TrAC, Trends Anal. Chem.*, 2015, **66**, 103–117.
66 R. Zhang, Z. Wang, C. Song, J. Yang and Y. Cui, *J. Fluoresc.*, 2013, **23**, 551–559.
67 Y. Li, J. Sun, L. Wu, J. Ji, X. Sun and Y. Qian, *Biosens. Bioelectron.*, 2014, **62**, 255–260.
68 X. Yang, Y. Zhuo, S. Zhu, Y. Luo, Y. Feng and Y. Xu, *Biosens. Bioelectron.*, 2015, **64**, 345–351.
69 G. Zheng, J. Wang, L. Kong, H. Cheng and J. Liu, *Plasmonics*, 2012, **7**, 487–494.
70 D. Punj, M. Mivelle, S. B. Moparthi, T. S. van Zanten, H. Rigneault, N. F. van Hulst, M. F. Garcia-Parajo and J. Wenger, *Nat. Nano*, 2013, **8**, 512–516.
71 P. Anger, P. Bharadwaj and L. Novotny, *Phys. Rev. Lett.*, 2006, 96.
72 N. I. Cade, T. Ritman-Meer, K. A. Kwakwa and D. Richards, *Nanotechnology*, 2009, 20.
73 Q. Hao, T. Qiu and P. K. Chu, *Prog. Surf. Sci.*, 2012, **87**, 23–45.
74 X. F. Zhang, X. M. Kong, Z. P. Lv, S. W. Zhou and X. Z. Du, *J. Mater. Chem. B*, 2013, **1**, 2198–2204.
75 J. Zhang, Y. Fu and J. R. Lakowicz, *J. Phys. Chem. C*, 2007, **111**, 50–56.
76 A. Hartstein, J. R. Kirtley and J. C. Tsang, *Phys. Rev. Lett.*, 1980, **45**, 201–204.
77 A. Hatta, T. Ohshima and W. Suëtaka, *Appl. Phys. A*, 1982, **29**, 71–75.
78 W. Suëtaka, *Surface Infrared and Raman Spectroscopy: Methods and Applications*, Springer, 1995.
79 M. Osawa, *Bull. Chem. Soc. Jpn.*, 1997, **70**, 2861–2880.
80 K. B. Alici, *IEEE Trans. Nanotechnol.*, 2014, **13**, 216–221.
81 C. H. Wu, A. B. Khanikaev, R. Adato, N. Arju, A. A. Yanik, H. Altug and G. Shvets, *Nat. Mater.*, 2012, **11**, 69–75.
82 S. Bagheri, K. Weber, T. Gissibl, T. Weiss, F. Neubrech and H. Giessen, *ACS Photonics*, 2015, **2**, 779–786.
83 C. Huck, F. Neubrech, J. Vogt, A. Toma, D. Gerbert, J. Katzmann, T. Härtling and A. Pucci, *ACS Nano*, 2014, **8**, 4908–4914.
84 K. Chen, R. Adato and H. Altug, *ACS Nano*, 2012, **6**, 7998–8006.
85 A. Hornemann, D. Eichert, S. Flemig, G. Ulm and B. Beckhoff, *Phys. Chem. Chem. Phys.*, 2015, **17**, 9471–9479.
86 T. Kamata, A. Kato, J. Umemura and T. Takenaka, *Langmuir*, 1987, **3**, 1150–1154.
87 K. Itoh, K. Hayashi, Y. Hamanaka, M. Yamamoto, T. Araki and K. Iriyama, *Langmuir*, 1992, **8**, 140–147.
88 E. Johnson and R. Aroca, *J. Phys. Chem.*, 1995, **99**, 9325–9330.
89 P. Alonso-Gonzalez, P. Albella, M. Schnell, J. Chen, F. Huth, A. Garcia-Etxarri, F. Casanova, F. Golmar, L. Arzubiaga, L. E. Hueso, J. Aizpurua and R. Hillenbrand, *Nat. Commun.*, 2012, **3**, 684.
90 J. Parsons, C. P. Burrows, J. R. Sambles and W. L. Barnes, *J. Mod. Optic.*, 2010, **57**, 356–365.
91 F. D. Sala and S. D'Agostino, *Handbook of Molecular Plasmonics*, CRC Press, 2013.
92 C. F. Bohren and D. R. Huffman, *Absorption and scattering of light by small particles*, Wiley, 1983.
93 A. L. Aden and M. Kerker, *J. Appl. Phys.*, 1951, **22**, 1242–1246.
94 P. K. Jain, K. S. Lee, I. H. El-Sayed and M. A. El-Sayed, *J. Phys. Chem. B*, 2006, **110**, 7238–7248.
95 E. L. Ru and P. Etchegoin, *Principles of Surface-Enhanced Raman Spectroscopy: And Related Plasmonic Effects*, Elsevier Science, 2008.
96 S. Schlücker, *Surface Enhanced Raman Spectroscopy: Analytical, Biophysical and Life Science Applications*, Wiley, 2011.
97 M. A. Yurkin, D. de Kanter and A. G. Hoekstra, *J. Nanophotonics*, 2010, **4**, 041585.
98 O. J. F. Martin and N. B. Piller, *Phys. Rev. E: Stat. Phys., Plasmas, Fluids, Relat. Interdiscip. Top.*, 1998, **58**, 3909–3915.
99 V. Myroshnychenko, E. Carbó-Argibay, I. Pastoriza-Santos, J. Pérez-Juste, L. M. Liz-Marzán and F. J. García de Abajo, *Adv. Mater.*, 2008, **20**, 4288–4293.
100 J.-M. Jin, *The Finite Element Method in Electromagnetics*, Wiley, 2002.
101 A. F. Oskooi, D. Roundy, M. Ibanescu, P. Bermel, J. D. Joannopoulos and S. G. Johnson, *Comput. Phys. Commun.*, 2010, **181**, 687–702.
102 M. Paulus, P. Gay-Balmaz and O. J. F. Martin, *Phys. Rev. E: Stat. Phys., Plasmas, Fluids, Relat. Interdiscip. Top.*, 2000, **62**, 5797–5807.
103 Y. O. Agha, O. Demichel, C. Girard, A. Bouhelier and G. C. des Francs, *Prog. Electromagn. Res.*, 2014, **146**, 77–88.
104 G. Baffou, R. Quidant and C. Girard, *Phys. Rev. B: Condens. Matter*, 2010, **82**, 165424.
105 K. Diest, *Numerical Methods for Metamaterial Design*, Springer, 2013.
106 A. V. Lavrinenko, J. Lægsgaard, N. Gregersen, F. Schmidt and T. Søndergaard, *Numerical Methods in Photonics*, CRC Press, 2014.
107 E. Prodan, C. Radloff, N. J. Halas and P. Nordlander, *Science*, 2003, **302**, 419–422.
108 E. Prodan and P. Nordlander, *J. Chem. Phys.*, 2004, **120**, 5444–5454.
109 S. Lal, N. K. Grady, J. Kundu, C. S. Levin, J. B. Lassiter and N. J. Halas, *Chem. Soc. Rev.*, 2008, **37**, 898–898.

110 K. Bao, H. Sobhani and P. Nordlander, *Chin. Sci. Bull.*, 2010, **55**, 2629–2634.
111 K. L. Kelly, E. Coronado, L. L. Zhao and G. C. Schatz, *J. Phys. Chem. B*, 2003, **107**, 668–677.
112 K.-S. Lee and M. A. El-Sayed, *J. Phys. Chem. B*, 2006, **110**, 19220–19225.
113 C. Noguez, *J. Phys. Chem. C*, 2007, **111**, 3806–3819.
114 Y. Xia, Y. Xiong, B. Lim and S. E. Skrabalak, *Angew. Chem., Int. Ed.*, 2009, **48**, 60–103.
115 P. K. Aravind, A. Nitzan and H. Metiu, *Surf. Sci.*, 1981, **110**, 189–204.
116 N. Liver, A. Nitzan and J. I. Gersten, *Chem. Phys. Lett.*, 1984, **111**, 449–454.
117 J. M. McMahon, A.-I. Henry, K. L. Wustholz, M. J. Natan, R. G. Freeman, R. P. V. Duyne and G. C. Schatz, *Anal. Bioanal. Chem.*, 2009, **394**, 1819–1825.
118 N. J. Halas, S. Lal, W.-S. Chang, S. Link and P. Nordlander, *Chem. Rev.*, 2011, **111**, 3913–3961.
119 J. M. McMahon, S. Li, L. K. Ausman and G. C. Schatz, *J. Phys. Chem. C*, 2012, **116**, 1627–1637.
120 N. Ma, F. Tang, X. Y. Wang, F. He and L. D. Li, *Macromol. Rapid Commun.*, 2011, **32**, 587–592.
121 B. Yan, S. V. Boriskina and B. M. Reinhard, *J. Phys. Chem. C*, 2011, **115**, 24437–24453.
122 J. M. Romo-Herrera, R. A. Alvarez-Puebla and L. M. Liz-Marzán, *Nanoscale*, 2011, **3**, 1304–1315.
123 S. J. Barrow, A. M. Funston, X. Wei and P. Mulvaney, *Nano Today*, 2013, **8**, 138–167.
124 D. Mott, J. Lee, N. T. B. Thuy, Y. Aoki, P. Singh and S. Maenosono, *Jpn. J. Appl. Phys.*, 2011, **50**, 065004.
125 J. Henzie, J. Lee, M. H. Lee, W. Hasan and T. W. Odom, *Annu. Rev. Phys. Chem.*, 2009, **60**, 147–165.
126 M. Rycenga, C. M. Cobley, J. Zeng, W. Li, C. H. Moran, Q. Zhang, D. Qin and Y. Xia, *Chem. Rev.*, 2011, **111**, 3669–3712.
127 M. Fan, G. F. S. Andrade and A. G. Brolo, *Anal. Chim. Acta*, 2011, **693**, 7–25.
128 P. K. Jain and M. A. El-Sayed, *J. Phys. Chem. C*, 2008, **112**, 4954–4960.
129 P. K. Jain, W. Y. Huang and M. A. El-Sayed, *Nano Lett.*, 2007, **7**, 2080–2088.
130 Z. Zhang, S. Zhang and Z. Xiong, *Plasmonics*, 2010, **5**, 411–416.
131 N. Grillet, D. Manchon, F. Bertorelle, C. Bonnet, M. Broyer, E. Cottancin, J. Lerme, M. Hillenkamp and M. Pellarin, *ACS Nano*, 2011, **5**, 9450–9462.
132 M. Rang, A. C. Jones, F. Zhou, Z.-Y. Li, B. J. Wiley, Y. Xia and M. B. Raschke, *Nano Lett.*, 2008, **8**, 3357–3363.
133 H. Fischer and O. J. F. Martin, *Opt. Express*, 2008, **16**, 9144–9154.
134 B. C. Galarreta, P. R. Norton and F. o. Lagugné-Labarthet, *J. Phys. Chem. C*, 2010, **114**, 19952–19957.
135 G. V. P. Kumar, *J. Opt. Soc. Am. B*, 2012, **29**, 594–599.
136 R. Bukasov and J. S. Shumaker-Parry, *Nano Lett.*, 2007, **7**, 1113–1118.
137 R. Bukasov, T. A. Ali, P. Nordlander and J. S. Shumaker-Parry, *ACS Nano*, 2010, **4**, 6639–6650.
138 J. Fischer, N. Vogel, R. Mohammadi, H. J. Butt, K. Landfester, C. K. Weiss and M. Kreiter, *Nanoscale*, 2011, **3**, 4788–4797.
139 J. Xu, L. Zhang, H. Gong, J. í. Homola and Q. Yu, *Small*, 2011, **7**, 371–376.
140 J. J. Xu, P. Guan, P. Kvasnicka, H. Gong, J. Homola and Q. M. Yu, *J. Phys. Chem. C*, 2011, **115**, 10996–11002.
141 C. F. Tian, C. H. Ding, S. Y. Liu, S. C. Yang, X. P. Song, B. J. Ding, Z. Y. Li and J. X. Fang, *ACS Nano*, 2011, **5**, 9442–9449.
142 R. Shugayev, *Opt. Express*, 2010, **18**, 24946–24960.
143 P. Ding, E. J. Liang, W. Q. Hu, G. W. Cai and Q. Z. Xue, *Photonics Nanostruct.*, 2011, **9**, 42–48.
144 A. M. Funston, C. Novo, T. J. Davis and P. Mulvaney, *Nano Lett.*, 2009, **9**, 1651–1658.
145 S. Sheikholeslami, Y.-w. Jun, P. K. Jain and A. P. Alivisatos, *Nano Lett.*, 2010, **10**, 2655–2660.
146 J. S. Huang, J. Kern, P. Geisler, P. Weinmann, M. Kamp, A. Forchel, P. Biagioni and B. Hecht, *Nano Lett.*, 2010, **10**, 2105–2110.
147 L. V. Brown, H. Sobhani, J. B. Lassiter, P. Nordlander and N. J. Halas, *ACS Nano*, 2010, **4**, 819–832.
148 F. Hao, Y. Sonnefraud, P. V. Dorpe, S. A. Maier, N. J. Halas and P. Nordlander, *Nano Lett.*, 2008, **8**, 3983–3988.
149 M. W. Knight, Y. Wu, J. B. Lassiter, P. Nordlander and N. J. Halas, *Nano Lett.*, 2009, **9**, 2188–2192.
150 D. Y. Lei, A. I. Fernandez-Dominguez, Y. Sonnefraud, K. Appavoo, R. F. Haglund, J. B. Pendry and S. A. Maier, *ACS Nano*, 2012, **6**, 1380–1386.
151 A. Christ, G. Lévêque, O. J. F. Martin, T. Zentgraf, J. Kuhl, C. Bauer, H. Giessen and S. G. Tikhodeev, *J. Microsc.*, 2008, **229**, 344–353.
152 C. M. Watts, X. Liu and W. J. Padilla, *Adv. Mater.*, 2012, **24**, OP98–OP120.
153 V. Giannini, J. A. Sanchez-Gil, O. L. Muskens and J. G. Rivas, *J. Opt. Soc. Am. B*, 2009, **26**, 1569–1577.
154 Y. Gu, L. Huang, O. J. F. Martin and Q. Gong, *Phys. Rev. B: Condens. Matter*, 2010, **81**, 193103.
155 T. Grosges, D. Barchiesi, T. Toury and G. Grehan, *Opt. Lett.*, 2008, **33**, 2812–2814.
156 O. Peña-Rodríguez and U. Pal, *Nanoscale Res. Lett.*, 2011, **6**, 279–279.
157 D. J. Wu and X. J. Liu, *Appl. Phys. Lett.*, 2010, **96**, 151912.
158 D. Wu and X. Liu, *Appl. Phys. Lett.*, 2010, **97**, 061904.
159 N. Hooshmand, P. K. Jain and M. A. El-Sayed, *J. Phys. Chem. Lett.*, 2011, **2**, 374–378.
160 M. W. Knight and N. J. Halas, *New J. Phys.*, 2008, **10**, 105006–105006.
161 N. Calander, D. Jin and E. M. Goldys, *J. Phys. Chem. C*, 2012, **116**, 7546–7551.
162 Z. Zhang and Y. Zhao, *J. Phys.: Condens. Matter*, 2008, **20**, 345223–345223.
163 A. Pors, M. Willatzen, O. Albrektsen and S. I. Bozhevolnyi, *J. Opt. Soc. Am. B*, 2010, **27**, 1680–1687.

 

164 T. Zentgraf, T. P. Meyrath, A. Seidel, S. Kaiser, H. Giessen, C. Rockstuhl and F. Lederer, *Phys. Rev. B: Condens. Matter*, 2007, **76**, 033407.
165 L. Y. Wu, B. M. Ross and L. P. Lee, *Nano Lett.*, 2009, **9**, 1956–1961.
166 D. Rossouw and G. A. Botton, *Opt. Express*, 2012, **20**, 6968–6973.
167 F. von Cube, S. Irsen, J. Niegemann, C. Matyssek, W. Hergert, K. Busch and S. Linden, *Opt. Mater. Express*, 2011, **1**, 1009–1018.
168 C. M. Dutta, T. A. Ali, D. W. Brandl, T. H. Park and P. Nordlander, *J. Chem. Phys.*, 2008, **129**, 084706.
169 J. Ye, L. Lagae, G. Maes, G. Borghs and P. Van Dorpe, *Opt. Express*, 2009, **17**, 23765–23771.
170 J. Zhu and F. K. Li, *Eur. Phys. J. B*, 2011, **80**, 83–87.
171 E. S. Barnard, J. S. White, A. Chandran and M. L. Brongersma, *Opt. Express*, 2008, **16**, 16529–16537.
172 A. Aubry, D. Y. Lei, A. I. Fernández-Domínguez, Y. Sonnefraud, S. A. Maier and J. B. Pendry, *Nano Lett.*, 2010, **10**, 2574–2579.
173 N. Large, J. Aizpurua, V. K. Lin, S. L. Teo, R. Marty, S. Tripathy and A. Mlayah, *Opt. Express*, 2011, **19**, 5587–5595.
174 A. M. Kern and O. J. F. Martin, *Nano Lett.*, 2011, **11**, 482–487.
175 P. C. Lee and D. Meisel, *J. Phys. Chem.*, 1982, **86**, 3391–3395.
176 S. Kruszewski and M. Cyrankiewicz, *Acta Phys. Pol., A*, 2012, **121**, A68–A74.
177 K. Yoshida, T. Itoh, H. Tamaru, V. Biju, M. Ishikawa and Y. Ozaki, *Phys. Rev. B: Condens. Matter*, 2010, 81.
178 T. Itoh, H. Yoshikawa, K. Yoshida, V. Biju and M. Ishikawa, *J. Chem. Phys.*, 2009, **130**, 214706.
179 A. Walter, A. Marz, W. Schumacher, P. Rosch and J. Popp, *Lab Chip*, 2011, **11**, 1013–1021.
180 A. März, S. Trupp, P. Rösch, G. Mohr and J. Popp, *Anal. Bioanal. Chem.*, 2012, **402**, 2625–2631.
181 A. März, K. R. Ackermann, D. Malsch, T. Bocklitz, T. Henkel and J. Popp, *J. Biophotonics*, 2009, **2**, 232–242.
182 I. J. Hidi, A. Muhlig, M. Jahn, F. Liebold, D. Cialla, K. Weber and J. Popp, *Anal. Methods*, 2014, **6**, 3943–3947.
183 I. J. Hidi, M. Jahn, K. Weber, D. Cialla-May and J. Popp, *Phys. Chem. Chem. Phys.*, 2015, **17**, 21236–21242.
184 B. Liu, W. Jiang, H. Wang, X. Yang, S. Zhang, Y. Yuan, T. Wu and Y. Du, *Microchim. Acta*, 2013, **180**, 997–1004.
185 R. Zhang, Z. Wang, C. Song, J. Yang, A. Sadaf and Y. Cui, *J. Fluoresc.*, 2013, **23**, 71–77.
186 G. Frens, *Nat. Phys. Sci.*, 1973, **241**, 20–22.
187 A. M. Giovannozzi, F. Rolle, M. Sega, M. C. Abete, D. Marchis and A. M. Rossi, *Food Chem.*, 2014, **159**, 250–256.
188 E. Kämmer, T. Dörfer, A. Csáki, W. Schumacher, P. A. Da Costa Filho, N. Tarcea, W. Fritzsche, P. Rösch, M. Schmitt and J. Popp, *J. Phys. Chem. C*, 2012, **116**, 6083–6091.
189 J. A. Creighton, C. G. Blatchford and M. G. Albrecht, *J. Chem. Soc., Faraday Trans. 2*, 1979, **75**, 790–798.
190 Y. Wang, Z. H. Li, H. Li, M. Vuki, D. K. Xu and H. Y. Chen, *Biosens. Bioelectron.*, 2012, **32**, 76–81.
191 M. Dendisová-Vyškovská, V. Prokopec, M. Člupek and P. Matějka, *J. Raman Spectrosc.*, 2012, **43**, 181–186.
192 R. Jin, Y. Cao, C. A. Mirkin, K. L. Kelly, G. C. Schatz and J. G. Zheng, *Science*, 2001, **294**, 1901–1903.
193 K. Munechika, Y. Chen, A. F. Tillack, A. P. Kulkarni, I. J.-L. Plante, A. M. Munro and D. S. Ginger, *Nano Lett.*, 2010, **10**, 2598–2603.
194 N. Leopold and B. Lendl, *J. Phys. Chem. B*, 2003, **107**, 5723–5727.
195 I. A. Larmour, K. Faulds and D. Graham, *J. Raman Spectrosc.*, 2012, **43**, 202–206.
196 N. E. Mircescu, M. Oltean, V. Chiș and N. Leopold, *Vib. Spectrosc.*, 2012, **62**, 165–171.
197 I. B. Cozar, L. Szabó, D. Mare, N. Leopold, L. David and V. Chiș, *J. Mol. Struct.*, 2011, **993**, 243–248.
198 A. Bebu, L. Szabó, N. Leopold, C. Berindean and L. David, *J. Mol. Struct.*, 2011, **993**, 52–56.
199 E. del Puerto, C. Domingo, J. V. Garcia Ramos and S. Sanchez-Cortes, *Langmuir*, 2014, **30**, 753–761.
200 N. Mircescu, H. Zhou, N. Leopold, V. Chiș, N. Ivleva, R. Niessner, A. Wieser and C. Haisch, *Anal. Bioanal. Chem.*, 2014, **406**, 3051–3058.
201 H. Zhou, D. Yang, N. P. Ivleva, N. E. Mircescu, R. Niessner and C. Haisch, *Anal. Chem.*, 2014, **86**, 1525–1533.
202 V. Shautsova, V. Zhuravkov, O. Korolik, A. Novikau, G. Shevchenko and P. Gaiduk, *Plasmonics*, 2014, **9**, 993–999.
203 M. M. Harper, J. A. Dougan, N. C. Shand, D. Graham and K. Faulds, *Analyst*, 2012, **137**, 2063–2068.
204 C. Morasso, D. Mehn, R. Vanna, M. Bedoni, E. Forvi, M. Colombo, D. Prosperi and F. Gramatica, *Mater. Chem. Phys.*, 2014, **143**, 1215–1221.
205 G. Lu, H. Li, C. Liusman, Z. Yin, S. Wu and H. Zhang, *Chem. Sci.*, 2011, **2**, 1817–1821.
206 C. Hu, Y. Liu, J. Qin, G. Nie, B. Lei, Y. Xiao, M. Zheng and J. Rong, *ACS Appl. Mater. Interfaces*, 2013, **5**, 4760–4768.
207 R. Prucek, V. Ranc, O. Balzerová, A. Panáček, R. Zbořil and L. Kvítek, *Mater. Res. Bull.*, 2014, **50**, 63–67.
208 K. Herman, L. Szabó, L. Leopold, V. Chiș and N. Leopold, *Anal. Bioanal. Chem.*, 2011, **400**, 815–820.
209 Z. W. Liu, W. H. Hung, M. Aykol, D. Valley and S. B. Cronin, *Nanotechnology*, 2010, 21.
210 T. Shegai, B. Brian, V. D. Miljkovic and M. Kall, *ACS Nano*, 2011, **5**, 2036–2041.
211 N. Hajduková, M. Procházka, J. Štěpánek and M. Špírková, *Colloids Surf., A*, 2007, **301**, 264–270.
212 M. Potara, A.-M. Gabudean and S. Astilean, *J. Mater. Chem.*, 2011, **21**, 3625–3625.
213 K. L. Wustholz, A.-I. Henry, J. M. McMahon, R. G. Freeman, N. Valley, M. E. Piotti, M. J. Natan, G. C. Schatz and R. P. V. Duyne, *J. Am. Chem. Soc.*, 2010, **132**, 10903–10910.
214 D.-K. Lim, K.-S. Jeon, H. M. Kim, J.-M. Nam and Y. D. Suh, *Nat. Mater.*, 2010, **9**, 60–67.

215 Y. D. Jin and X. H. Gao, *Nat. Nanotechnol.*, 2009, **4**, 571–576.
216 K. C. Grabar, R. G. Freeman, M. B. Hommer and M. J. Natan, *Anal. Chem.*, 1995, **67**, 735–743.
217 S. P. Mulvaney, M. D. Musick, C. D. Keating and M. J. Natan, *Langmuir*, 2003, **19**, 4784–4790.
218 J. F. Li, X. D. Tian, S. B. Li, J. R. Anema, Z. L. Yang, Y. Ding, Y. F. Wu, Y. M. Zeng, Q. Z. Chen, B. Ren, Z. L. Wang and Z. Q. Tian, *Nat. Protoc.*, 2013, **8**, 52–65.
219 B. Küstner, M. Gellner, M. Schütz, F. Schöppler, A. Marx, P. Ströbel, P. Adam, C. Schmuck and S. Schlücker, *Angew. Chem., Int. Ed.*, 2009, **48**, 1950–1953.
220 T. P. Tyler, A.-I. Henry, R. P. Van Duyne and M. C. Hersam, *J. Phys. Chem. Lett.*, 2011, **2**, 218–222.
221 A. De Luca, M. Ferrie, S. Ravaine, M. La Deda, M. Infusino, A. R. Rashed, A. Veltri, A. Aradian, N. Scaramuzza and G. Strangi, *J. Mater. Chem.*, 2012, **22**, 8846.
222 L. Zhao, T. Ming, H. Chen, Y. Liang and J. Wang, *Nanoscale*, 2011, **3**, 3849–3849.
223 A. Gole, N. Agarwal, P. Nagaria, M. D. Wyatt and C. J. Murphy, *Chem. Commun.*, 2008, 6140–6140.
224 V. Uzayisenga, X. D. Lin, L. M. Li, J. R. Anema, Z. L. Yang, Y. F. Huang, H. X. Lin, S. B. Li, J. F. Li and Z. Q. Tian, *Langmuir*, 2012, **28**, 9140–9146.
225 H. Wang, Q. Jin, L. Yang and Y. Liu, *J. Nanopart. Res.*, 2013, **15**, 1803.
226 J. Ye, L. Lagae, G. Maes and P. Van Dorpe, *J. Mater. Chem.*, 2011, **21**, 14394–14394.
227 X. Q. Huang, S. H. Tang, B. J. Liu, B. Ren and N. F. Zheng, *Adv. Mater.*, 2011, **23**, 3420–3425.
228 Z. Ran, Y. Sun, B. Chang, Q. Ren and W. Yang, *J. Colloid Interface Sci.*, 2013, **410**, 94–101.
229 N. Yin, Y. Liu, L. Liu, J. Lei, T. Jiang, H. Wang, L. Zhu and X. Xu, *J. Alloys Compd.*, 2013, **581**, 6–10.
230 W. Deng, D. Jin, K. Drozdowicz-Tomsia, J. Yuan, J. Wu and E. M. Goldys, *Adv. Mater.*, 2011, **23**, 4649–4654.
231 Z. Wang, S. Zong, H. Chen, C. Wang, S. Xu and Y. Cui, *Adv. Healthcare Mater.*, 2014, **3**, 1889–1897.
232 S. J. Guo, J. Li, S. J. Dong and E. K. Wang, *J. Phys. Chem. C*, 2010, **114**, 15337–15342.
233 W. Deng, L. Sudheendra, J. Zhao, J. Fu, D. Jin, I. M. Kennedy and E. M. Goldys, *Nanotechnology*, 2011, **22**, 325604.
234 Y. Pu, R. Grange, C.-L. Hsieh and D. Psaltis, *Phys. Rev. Lett.*, 2010, **104**, 207402.
235 S. Zaiba, F. Lerouge, A. M. Gabudean, M. Focsan, J. Lerme, T. Gallavardin, O. Maury, C. Andraud, S. Parola and P. L. Baldeck, *Nano Lett.*, 2011, **11**, 2043–2047.
236 R. Liu, F. Qu, Y. Guo, N. Yao and R. D. Priestley, *Chem. Commun.*, 2013, **50**, 478–480.
237 X.-D. Lin, V. Uzayisenga, J.-F. Li, P.-P. Fang, D.-Y. Wu, B. Ren and Z.-Q. Tian, *J. Raman Spectrosc.*, 2012, **43**, 40–45.
238 X.-D. Lin, J.-F. Li, Y.-F. Huang, X.-D. Tian, V. Uzayisenga, S.-B. Li, B. Ren and Z.-Q. Tian, *J. Electroanal. Chem.*, 2013, **688**, 5–11.
239 L. Zhang, D. A. Blom and H. Wang, *Chem. Mater.*, 2011, **23**, 4587–4598.
240 M. Li, H. Yang, S. Li, K. Zhao, J. Li, D. Jiang, L. Sun and A. Deng, *J. Agric. Food Chem.*, 2014, **62**, 10896–10902.
241 Y. Zhou and P. Zhang, *Phys. Chem. Chem. Phys.*, 2014, **16**, 8791–8794.
242 I. Al-Ogaidi, H. Gou, A. K. A. Al-kazaz, Z. P. Aguilar, A. K. Melconian, P. Zheng and N. Wu, *Anal. Chim. Acta*, 2014, **811**, 76–80.
243 I. O. Osorio-Román, A. R. Guerrero, P. Albella and R. F. Aroca, *Anal. Chem.*, 2014, **86**, 10246–10251.
244 M. Procházka, P. Šimáková and N. Hajduková-Šmídová, *Colloids Surf., A*, 2012, **402**, 24–28.
245 R. A. Alvarez-Puebla, J. P. Bravo-Vasquez, P. Cheben, D.-X. Xu, P. Waldron and H. Fenniri, *J. Colloid Interface Sci.*, 2009, **333**, 237–241.
246 K. L. McGilvray, C. Fasciani, C. J. Bueno-Alejo, R. Schwartz-Narbonne and J. C. Scaiano, *Langmuir*, 2012, **28**, 16148–16155.
247 S. Barbosa, A. Agrawal, L. Rodriguez-Lorenzo, I. Pastoriza-Santos, R. A. Alvarez-Puebla, A. Kornowski, H. Weller and L. M. Liz-Marzan, *Langmuir*, 2010, **26**, 14943–14950.
248 M. A. Mahmoud, *Langmuir*, 2013, **29**, 6253–6261.
249 X. Le Guevel, F. Y. Wang, O. Stranik, R. Nooney, V. Gubala, C. McDonagh and B. D. MacCraith, *J. Phys. Chem. C*, 2009, **113**, 16380–16386.
250 J. Roh, J. Yi and Y. Kim, *Langmuir*, 2010, **26**, 11621–11623.
251 X. Li, F.-J. Kao, C.-C. Chuang and S. He, *Opt. Express*, 2010, **18**, 11335–11346.
252 X. Ye, L. Jin, H. Caglayan, J. Chen, G. Xing, C. Zheng, V. Doan-Nguyen, Y. Kang, N. Engheta, C. R. Kagan and C. B. Murray, *ACS Nano*, 2012, **6**, 2804–2817.
253 R. Kattumenu, C. H. Lee, L. Tian, M. E. McConney and S. Singamaneni, *J. Mater. Chem.*, 2011, **21**, 15218.
254 Y.-C. Yang, T.-K. Huang, Y.-L. Chen, J.-Y. Mevellec, S. Lefrant, C.-Y. Lee and H.-T. Chiu, *J. Phys. Chem. C*, 2011, **115**, 1932–1939.
255 S. Pedireddy, A. Li, M. Bosman, I. Y. Phang, S. Li and X. Y. Ling, *J. Phys. Chem. C*, 2013, **117**, 16640–16649.
256 N. Pazos-Pérez, S. Barbosa, L. Rodríguez-Lorenzo, P. Aldeanueva-Potel, J. Pérez-Juste, I. Pastoriza-Santos, R. A. Alvarez-Puebla and L. M. Liz-Marzán, *J. Phys. Chem. Lett.*, 2009, **1**, 24–27.
257 A. Tao, P. Sinsermsuksakul and P. Yang, *Angew. Chem., Int. Ed.*, 2006, **45**, 4597–4601.
258 J. Chen, J. M. McLellan, A. Siekkinen, Y. Xiong, Z.-Y. Li and Y. Xia, *J. Am. Chem. Soc.*, 2006, **128**, 14776–14777.
259 J. C. Kotz, P. M. Treichel and G. C. Weaver, *Chemistry and Chemical Reactivity*, Cengage Learning, 2006.
260 V. Sebastian, S.-K. Lee and K. F. Jensen, *Nanoscale*, 2014, **6**, 13228–13235.
261 M. A. Mahmoud and M. A. El-Sayed, *J. Am. Chem. Soc.*, 2010, **132**, 12704–12710.
262 S. H. Han, J. Y. Cheon, S. H. Joo and J.-S. Lee, *Mater. Res. Bull.*, 2013, **48**, 2333–2339.

 

263 H. Lu, H. Zhang, X. Yu, S. Zeng, K.-T. Yong and H.-P. Ho, *Plasmonics*, 2011, **7**, 167–173.
264 M. A. Mahmoud, M. A. El-Sayed, J. Gao and U. Landman, *Nano Lett.*, 2013, **13**, 4739–4745.
265 Q. Zhang, Y. Yang, J. Li, R. Iurilli, S. Xie and D. Qin, *ACS Appl. Mater. Interfaces*, 2013, **5**, 6333–6345.
266 H. L. Chang, T. Limei, A. Abdennour, K. Ramesh and S. Srikanth, *Nanotechnology*, 2011, **22**, 275311.
267 L. Shao, K. C. Woo, H. Chen, Z. Jin, J. Wang and H.-Q. Lin, *ACS Nano*, 2010, **4**, 3053–3062.
268 J. Wang, X. Cao, L. Li, T. Li and R. Wang, *J. Phys. Chem. C*, 2013, **117**, 15817–15828.
269 M. P. Cecchini, V. A. Turek, J. Paget, A. A. Kornyshev and J. B. Edel, *Nat. Mater.*, 2013, **12**, 165–171.
270 Y. Kang, M. Si, Y. Zhu, L. Miao and G. Xu, *Spectrochim. Acta, Part A*, 2013, **108**, 177–180.
271 J. C. Fraire, L. A. Pérez and E. A. Coronado, *ACS Nano*, 2012, **6**, 3441–3452.
272 L. Motte, F. Billoudet and M. P. Pileni, *J. Phys. Chem.*, 1995, **99**, 16425–16429.
273 H. Chen, L. Shao, Q. Li and J. Wang, *Chem. Soc. Rev.*, 2013, **42**, 2679–2724.
274 R. W. Taylor, T.-C. Lee, O. A. Scherman, R. Esteban, J. Aizpurua, F. M. Huang, J. J. Baumberg and S. Mahajan, *ACS Nano*, 2011, **5**, 3878–3887.
275 L. Jiang, Y. Sun, C. Nowak, A. Kibrom, C. Zou, J. Ma, H. Fuchs, S. Li, L. Chi and X. Chen, *ACS Nano*, 2011, **5**, 8288–8294.
276 A. Lee, G. F. S. Andrade, A. Ahmed, M. L. Souza, N. Coombs, E. Tumarkin, K. Liu, R. Gordon, A. G. Brolo and E. Kumacheva, *J. Am. Chem. Soc.*, 2011, **133**, 7563–7570.
277 C. Lee, E. A. Josephs, J. Shao and T. Ye, *J. Phys. Chem. C*, 2012, **116**, 17625–17632.
278 H.-n. Xie, I. A. Larmour, V. Tileli, A. L. Koh, D. W. McComb, K. Faulds and D. Graham, *J. Phys. Chem. C*, 2011, **115**, 20515–20522.
279 P. Moutet, N. M. Sangeetha, L. Ressier, N. Vilar-Vidal, M. Comesana-Hermo, S. Ravaine, R. A. L. Vallee, A. M. Gabudean, S. Astilean and C. Farcau, *Nanoscale*, 2015, **7**, 2009–2022.
280 R. G. Freeman, K. C. Grabar, K. J. Allison, R. M. Bright, J. A. Davis, A. P. Guthrie, M. B. Hommer, M. A. Jackson, P. C. Smith, D. G. Walter and M. J. Natan, *Science*, 1995, **267**, 1629–1632.
281 M. Fan and A. G. Brolo, *Phys. Chem. Chem. Phys.*, 2009, **11**, 7381–7389.
282 R. Carles, C. Farcau, C. Bonafos, G. Benassayag, M. Bayle, P. Benzo, J. Groenen and A. Zwick, *ACS Nano*, 2011, **5**, 8774–8782.
283 Y. Xia, B. Gates, Y. Yin and Y. Lu, *Adv. Mater.*, 2000, **12**, 693–713.
284 L. A. Dick, A. D. McFarland, C. L. Haynes and R. P. Van Duyne, *J. Phys. Chem. B*, 2002, **106**, 853–860.
285 C. Farcau and S. Astilean, *J. Phys. Chem. C*, 2010, **114**, 11717–11722.
286 V. Peksa, M. Jahn, L. Štolcová, V. Schulz, J. Proška, M. Procházka, K. Weber, D. Cialla-May and J. Popp, *Anal. Chem.*, 2015, **87**, 2840–2844.
287 C. Steuwe, C. F. Kaminski, J. J. Baumberg and S. Mahajan, *Nano Lett.*, 2011, **11**, 5339–5343.
288 R. M. Cole, S. Mahajan, P. N. Bartlett and J. J. Baumberg, *Opt. Express*, 2009, **17**, 13298–13308.
289 S. H. Lee, K. C. Bantz, N. C. Lindquist, S. H. Oh and C. L. Haynes, *Langmuir*, 2009, **25**, 13685–13693.
290 H. Im, K. C. Bantz, S. H. Lee, T. W. Johnson, C. L. Haynes and S.-H. Oh, *Adv. Mater.*, 2013, **25**, 2678–2685.
291 W. Z. Shen, M. Z. Li, B. L. Wang, J. Liu, Z. Y. Li, L. Jiang and Y. L. Song, *J. Mater. Chem.*, 2012, **22**, 8127–8133.
292 C. Li, Z. Y. Tang and L. Jiang, *J. Mater. Chem.*, 2010, **20**, 9608–9612.
293 W. D. Li, F. Ding, J. Hu and S. Y. Chou, *Opt. Express*, 2011, **19**, 3925–3936.
294 R. Luchowski, N. Calander, T. Shtoyko, E. Apicella, J. Borejdo, Z. Gryczynski and I. Gryczynski, *J. Nanophotonics*, 2010, **4**, 043516.
295 H. Fredriksson, Y. Alaverdyan, A. Dmitriev, C. Langhammer, D. S. Sutherland, M. Zäch and B. Kasemo, *Adv. Mater.*, 2007, **19**, 4297–4302.
296 Y. S. Hu, J. Jeon, T. J. Seok, S. Lee, J. H. Hafner, R. A. Drezek and H. Choo, *ACS Nano*, 2010, **4**, 5721–5730.
297 C. H. Lee, M. E. Hankus, L. Tian, P. M. Pellegrino and S. Singamaneni, *Anal. Chem.*, 2011, **83**, 8953–8958.
298 F. C. Cabrera, P. H. B. Aoki, R. F. Aroca, C. J. L. Constantino, D. S. dos Santos and A. E. Job, *J. Raman Spectrosc.*, 2012, **43**, 474–477.
299 M. A. Mahmoud, A. J. Poncheri, R. L. Phillips and M. A. El-Sayed, *J. Am. Chem. Soc.*, 2010, **132**, 2633–2641.
300 K. K. Hering, R. Moller, W. Fritzsche and J. Popp, *ChemPhysChem*, 2008, **9**, 867–872.
301 K. K. Strelau, T. Schüler, R. Möller, W. Fritzsche and J. Popp, *ChemPhysChem*, 2010, **11**, 394–398.
302 S. Yüksel, M. Ziegler, S. Goerke, U. Hübner, K. Pollok, F. Langenhorst, K. Weber, D. Cialla-May and J. Popp, *J. Phys. Chem. C*, 2015, **119**, 13791–13798.
303 M. K. Gupta, S. Chang, S. Singamaneni, L. F. Drummy, R. Gunawidjaja, R. R. Naik and V. V. Tsukruk, *Small*, 2011, **7**, 1192–1198.
304 Y. Bao, L. Vigderman, E. R. Zubarev and C. Y. Jiang, *Langmuir*, 2012, **28**, 923–930.
305 Z. Y. Bao, D. Y. Lei, J. Dai and Y. Wu, *Appl. Surf. Sci.*, 2013, **287**, 404–410.
306 J. Casas, M. Venkataramasubramani, Y. Wang and L. Tang, *Biosens. Bioelectron.*, 2013, **49**, 525–530.
307 Y.-J. Guo, G.-M. Sun, L. Zhang, Y.-J. Tang, J.-J. Luo and P.-H. Yang, *Sens. Actuators, B*, 2014, **191**, 741–749.
308 W. Tang, D. B. Chase and J. F. Rabolt, *Anal. Chem.*, 2013, **85**, 10702–10709.
309 D. Huang, J. Cui and X. Chen, *Colloids Surf., A*, 2014, **456**, 100–107.
310 Z. Yi, J. Luo, Y. Yi, X. Xu, P. Wu, X. Jiang, Y. Yi and Y. Tang, *RSC Adv.*, 2014, **4**, 23670–23678.

311 J. He, X. Huang, Y.-C. Li, Y. Liu, T. Babu, M. A. Aronova, S. Wang, Z. Lu, X. Chen and Z. Nie, *J. Am. Chem. Soc.*, 2013, **135**, 7974–7984.
312 E. V. Barmina, G. A. Shafeev, P. G. Kuzmin, A. A. Serkov, A. V. Simakin and N. N. Melnik, *Appl. Phys. A*, 2014, **115**, 747–752.
313 V. Amendola, S. Scaramuzza, S. Agnoli, S. Polizzi and M. Meneghetti, *Nanoscale*, 2014, **6**, 1423–1433.
314 M. R. Jones, K. D. Osberg, R. J. Macfarlane, M. R. Langille and C. A. Mirkin, *Chem. Rev.*, 2011, **111**, 3736–3827.
315 J. C. Hulteen and R. P. Van Duyne, *J. Vac. Sci. Technol., A*, 1995, **13**, 1553–1558.
316 J. C. Hulteen, D. A. Treichel, M. T. Smith, M. L. Duval, T. R. Jensen and R. P. Van Duyne, *J. Phys. Chem. B*, 1999, **103**, 3854–3863.
317 T. R. Jensen, M. L. Duval, K. L. Kelly, A. A. Lazarides, G. C. Schatz and R. P. Van Duyne, *J. Phys. Chem. B*, 1999, **103**, 9846–9853.
318 M. Baia, L. Baia and S. Astilean, *Chem. Phys. Lett.*, 2005, **404**, 3–8.
319 L. Baia, M. Baia, J. Popp and S. Astilean, *J. Phys. Chem. B*, 2006, **110**, 23982–23986.
320 L. J. Sherry, R. Jin, C. A. Mirkin, G. C. Schatz and R. P. Van Duyne, *Nano Lett.*, 2006, **6**, 2060–2065.
321 A. J. Haes, S. Zou, J. Zhao, G. C. Schatz and R. P. Van Duyne, *J. Am. Chem. Soc.*, 2006, **128**, 10905–10914.
322 A. V. Whitney, J. W. Elam, S. Zou, A. V. Zinovev, P. C. Stair, G. C. Schatz and R. P. Van Duyne, *J. Phys. Chem. B*, 2005, **109**, 20522–20528.
323 G. Liu, W. Cai, L. Kong, G. Duan, Y. Li, J. Wang, G. Zuo and Z. Cheng, *J. Mater. Chem.*, 2012, **22**, 3177–3184.
324 G. Liu, W. Cai, L. Kong, G. Duan, Y. Li, J. Wang and Z. Cheng, *J. Hazard. Mater.*, 2013, **248–249**, 435–441.
325 Y. Fan, H. Cheng, C. Zhou, X. Xie, Y. Liu, L. Dai, J. Zhang and L. Qu, *Nanoscale*, 2012, **4**, 1776–1781.
326 Y. Li, Y. Hu, Y. Zhao, G. Shi, L. Deng, Y. Hou and L. Qu, *Adv. Mater.*, 2011, **23**, 776–780.
327 J. Yin, Y. Zang, C. Yue, Z. Wu, S. Wu, J. Li and Z. Wu, *J. Mater. Chem.*, 2012, **22**, 7902.
328 M. N. Liu, X. L. Li, S. K. Karuturi, A. I. Y. Tok and H. J. Fan, *Nanoscale*, 2012, **4**, 1522–1528.
329 S. Tian, Q. Zhou, Z. Gu, X. Gu and J. Zheng, *Analyst*, 2013, **138**, 2604–2612.
330 X. W. Lou, L. A. Archer and Z. Yang, *Adv. Mater.*, 2008, **20**, 3987–4019.
331 Y. Wang, T. Gao, K. Wang, X. Wu, X. Shi, Y. Liu, S. Lou and S. Zhou, *Nanoscale*, 2012, **4**, 7121–7126.
332 C. T. Kresge, M. E. Leonowicz, W. J. Roth, J. C. Vartuli and J. S. Beck, *Nature*, 1992, **359**, 710–712.
333 K. D. Jernshoj, S. Hassing, R. S. Hansen and P. Krohne-Nielsen, *J. Chem. Phys.*, 2011, **135**, 124514.
334 X. Lang, T. Qiu, W. Zhang, Y. Yin and P. K. Chu, *J. Phys. Chem. C*, 2011, **115**, 24328–24333.
335 S. Habouti, M. Mátéfi-Tempfli, C.-H. Solterbeck, M. Es-Souni, S. Mátéfi-Tempfli and M. Es-Souni, *J. Mater. Chem.*, 2011, **21**, 6269–6269.
336 H. Zhu, H. Chen, J. Wang and Q. Li, *Nanoscale*, 2013, **5**, 3742–3746.
337 X. Wang, S. Xu, H. Li, J. Tao, B. Zhao and W. Xu, *J. Raman Spectrosc.*, 2012, **43**, 459–463.
338 S. Yao, C. Zhou and D. Chen, *Chem. Commun.*, 2013, **49**, 6409–6411.
339 S. Y. Lee, S.-H. Kim, M. P. Kim, H. C. Jeon, H. Kang, H. J. Kim, B. J. Kim and S.-M. Yang, *Chem. Mater.*, 2013, **25**, 2421–2426.
340 J. Erlebacher and R. Seshadri, *MRS Bull.*, 2009, **34**, 561–568.
341 S. Sun and P. Wu, *ACS Appl. Mater. Interfaces*, 2013, **5**, 3481–3486.
342 W. Yuan, Z. Lu, H. Wang and C. M. Li, *Phys. Chem. Chem. Phys*, 2013, **15**, 15499–15507.
343 J. Zhu, M. Q. Xue, D. Zhao, M. N. Zhang, L. Duan, Y. Qiu and T. B. Cao, *Angew. Chem., Int. Ed.*, 2011, **50**, 12478–12482.
344 P. Nagpal, N. C. Lindquist, S.-H. Oh and D. J. Norris, *Science*, 2009, **325**, 594–597.
345 M. Coluccio, F. Gentile, M. Francardi, G. Perozziello, N. Malara, P. Candeloro and E. Di Fabrizio, *Sensors*, 2014, **14**, 6056.
346 K. Ju-Hyun, K. Taejoon, Y. Seung Min, L. Sang Yup, K. Bongsoo and C. Yang-Kyu, *Nanotechnology*, 2009, **20**, 235302.
347 Z. Li, S.-W. Chung, J.-M. Nam, D. S. Ginger and C. A. Mirkin, *Angew. Chem., Int. Ed.*, 2003, **42**, 2306–2309.
348 Y. Fang, V. W. Chen, Y. Cai, J. D. Berrigan, S. R. Marder, J. W. Perry and K. H. Sandhage, *Adv. Funct. Mater.*, 2012, **22**, 2550–2559.
349 K. Dietrich, D. Lehr, C. Helgert, A. Tünnermann and E.-B. Kley, *Adv. Mater.*, 2012, **24**, OP321–OP325.
350 U. Huebner, K. Weber, D. Cialla, H. Schneidewind, M. Zeisberger, H. G. Meyer and J. Popp, *Microelectron. Eng.*, 2011, **88**, 1761–1763.
351 D. Cialla, K. Weber, R. Böhme, U. Hübner, H. Schneidewind, M. Zeisberger, R. Mattheis, R. Möller and J. Popp, *Beilstein J. Nanotechnol.*, 2011, **2**, 501–508.
352 P. Rai-Choudhury, *Handbook of Microlithography, Micromachining, and Microfabrication: Microlithography*, SPIE Optical Engineering Press, 1997.
353 A. E. Grigorescu and C. W. Hagen, *Nanotechnology*, 2009, **20**, 292001.
354 B. Bilenberg, M. Schøler, P. Shi, M. S. Schmidt, P. Bøggild, M. Fink, C. Schuster, F. Reuther, C. Gruetzner and A. Kristensen, *J. Vac. Sci. Technol., A*, 2006, **24**, 1776–1779.
355 M. Switkes and M. Rothschild, *J. Vac. Sci. Technol., A*, 2001, **19**, 2353–2356.
356 W. Chen and H. Ahmed, *J. Vac. Sci. Technol., A*, 1993, **11**, 2519–2523.
357 T. H. P. Chang, *J. Vac. Sci. Technol., A*, 1975, **12**, 1271–1275.
358 U. Huebner, E. Pshenay-Severin, R. Alaee, C. Menzel, M. Ziegler, C. Rockstuhl, F. Lederer, T. Pertsch,

 

H.-G. Meyer and J. Popp, *Microelectron. Eng.*, 2013, **111**, 110–113.
359 G. Wiederrecht, *Handbook of Nanofabrication*, Elsevier Science, 2010.
360 E. Sheremet, R. D. Rodriguez, D. R. T. Zahn, A. G. Milekhin, E. E. Rodyakina and A. V. Latyshev, *J. Vac. Sci. Technol., A*, 2014, **32**, 04E110.
361 Y. Hou, J. Xu, P. Wang and D. Yu, *Appl. Phys. Lett.*, 2010, **96**, 203107.
362 A. W. Clark, A. Glidle, D. R. S. Cumming and J. M. Cooper, *Appl. Phys. Lett.*, 2008, 93.
363 G. Das, F. Mecarini, F. De Angelis, M. Prasciolu, C. Liberale, M. Patrini and E. Di Fabrizio, *Microelectron. Eng.*, 2008, **85**, 1282–1285.
364 A. A. Tseng, C. Kuan, C. D. Chen and K. J. Ma, *IEEE Trans. Electron. Packag. Manuf.*, 2003, **26**, 141–149.
365 T. W. Johnson, Z. J. Lapin, R. Beams, N. C. Lindquist, S. G. Rodrigo, L. Novotny and S.-H. Oh, *ACS Nano*, 2012, **6**, 9168–9174.
366 V. G. Kravets, G. Zoriniants, C. P. Burrows, F. Schedin, A. K. Geim, W. L. Barnes and A. N. Grigorenko, *Nano Lett.*, 2010, **10**, 874–879.
367 F. J. Bezares, J. D. Caldwell, O. Glembocki, R. W. Rendell, M. Feygelson, M. Ukaegbu, R. Kasica, L. Shirey, N. D. Bassim and C. Hosten, *Plasmonics*, 2012, **7**, 143–150.
368 H.-Y. Wu and B. T. Cunningham, *Appl. Phys. Lett.*, 2011, **98**, 153103.
369 J. D. Caldwell, O. Glembocki, F. J. Bezares, N. D. Bassim, R. W. Rendell, M. Feygelson, M. Ukaegbu, R. Kasica, L. Shirey and C. Hosten, *ACS Nano*, 2011, **5**, 4046–4055.
370 Q. Yu, S. Braswell, B. Christin, J. Xu, P. M. Wallace, H. Gong and D. Kaminsky, *Nanotechnology*, 2010, **21**, 355301.
371 P. Krohne-Nielsen, S. M. Novikov, J. Beermann, P. Morgen, S. I. Bozhevolnyi and O. Albrektsen, *J. Raman Spectrosc.*, 2012, **43**, 834–341.
372 P. Nielsen, P. Morgen, A. C. Simonsen and O. Albrektsen, *J. Phys. Chem. C*, 2011, **115**, 5552–5560.
373 J. H. Park, P. Nagpal, K. M. McPeak, N. C. Lindquist, S. H. Oh and D. J. Norris, *ACS Appl. Mater. Interfaces*, 2013, **5**, 9701–9708.
374 J. Jose, L. R. Jordan, T. W. Johnson, S. H. Lee, N. J. Wittenberg and S.-H. Oh, *Adv. Funct. Mater.*, 2013, **23**, 2812–2820.
375 N. C. Lindquist, T. W. Johnson, J. Jose, L. M. Otto and S. H. Oh, *Ann. Phys.*, 2012, **524**, 687–696.
376 X. Zhu, Y. Zhang, J. Zhang, J. Xu, Y. Ma, Z. Li and D. Yu, *Adv. Mater.*, 2010, **22**, 4345–4349.
377 R. E. Lee, *J. Vac. Sci. Technol.*, 1979, **16**, 164–170.
378 Q. Hao, D. Du, C. Wang, W. Li, H. Huang, J. Li, T. Qiu and P. K. Chu, *Sci. Rep.*, 2014, **4**, 6014.
379 F. De Angelis, M. Malerba, M. Patrini, E. Miele, G. Das, A. Toma, R. P. Zaccaria and E. Di Fabrizio, *Nano Lett.*, 2013, **13**, 3553–3558.
380 S. Kundan, L. Jiunn-Der and Y. Chih-Kai, *Appl. Phys. Exp.*, 2014, **7**, 092202.
381 Y. Y. Lin, J. D. Liao, Y. H. Ju, C. W. Chang and A. L. Shiau, *Nanotechnology*, 2011, **22**, 185308.
382 T. T. Gao, Z. W. Xu, F. Z. Fang, W. L. Gao, Q. Zhang and X. X. Xu, *Nanoscale Res. Lett.*, 2012, **7**, 399.
383 F. De Angelis, M. Patrini, G. Das, I. Maksymov, M. Galli, L. Businaro, L. C. Andreani and E. Di Fabrizio, *Nano Lett.*, 2008, **8**, 2321–2327.
384 H. Aouani, O. Mahboub, N. Bonod, E. Devaux, E. Popov, H. Rigneault, T. W. Ebbesen and J. Wenger, *Nano Lett.*, 2011, **11**, 637–644.
385 K. Wu, T. Rindzevicius, M. S. Schmidt, K. B. Mogensen, A. Hakonen and A. Boisen, *J. Phys. Chem. C*, 2015, **119**, 2053–2062.
386 R. Alvarez-Puebla, B. Cui, J.-P. Bravo-Vasquez, T. Veres and H. Fenniri, *J. Phys. Chem. C*, 2007, **111**, 6720–6723.
387 B. Radha, S. H. Lim, M. S. M. Saifullah and G. U. Kulkarni, *Sci. Rep.*, 2013, **3**, 1078.
388 Y. Zhong and M. M. F. Yuen, *2014 IEEE 64th Electronic Components and Technology Conference (ECTC)*, 2014, pp. 1822–1827, DOI: 10.1109/ECTC.2014.6897546.
389 M. Cottat, N. Lidgi-Guigui, I. Tijunelyte, G. Barbillon, F. Hamouda, P. Gogol, A. Aassime, J. M. Lourtioz, B. Bartenlian and M. de la Chapelle, *Nanoscale Res. Lett.*, 2014, 9.
390 T. Ding, D. O. Sigle, L. O. Herrmann, D. Wolverson and J. J. Baumberg, *ACS Appl. Mater. Interfaces*, 2014, **6**, 17358–17363.
391 J. M. Yao, A. P. Le, S. K. Gray, J. S. Moore, J. A. Rogers and R. G. Nuzzo, *Adv. Mater.*, 2010, **22**, 1102–1110.
392 A. J. Baca, T. T. Truong, L. R. Cambrea, J. M. Montgomery, S. K. Gray, D. Abdula, T. R. Banks, J. M. Yao, R. G. Nuzzo and J. A. Rogers, *Appl. Phys. Lett.*, 2009, **94**, 243109.
393 S. Kumar, S. Cherukulappurath, T. W. Johnson and S.-H. Oh, *Chem. Mater.*, 2014, **26**, 6523–6530.
394 J. S. Wi, E. S. Barnard, R. J. Wilson, M. L. Zhang, M. Tang, M. L. Brongersma and S. X. Wang, *ACS Nano*, 2011, **5**, 6449–6457.
395 D. J. Lipomi, R. V. Martinez and G. M. Whitesides, *Angew. Chem., Int. Ed.*, 2011, **50**, 8566–8583.
396 Y.-K. Baek, S. M. Yoo, T. Kang, H.-J. Jeon, K. Kim, J.-S. Lee, S. Y. Lee, B. Kim and H.-T. Jung, *Adv. Funct. Mater.*, 2010, **20**, 4273–4278.
397 N. Vogel, J. Zieleniecki and I. Koper, *Nanoscale*, 2012, **4**, 3820–3832.
398 P. Krohne-Nielsen, S. M. Novikov, J. Beermann, P. Morgen, S. I. Bozhevolnyi and O. Albrektsen, *Opt. Express*, 2012, **20**, 534–546.

**Supplement [IV]**

PEKSA, V., P. LEBRUSKOVA, H. SIPOVA, J. STEPANEK, J. BOK, M. PROCHAZKA, J. HOMOLA, **Testing gold nanostructures fabricated by hole-mask colloidal lithography as potential substrates for SERS sensors: sensitivity, signal variability, and the aspect of adsorbate deposition**. Physical Chemistry Chemical Physics, Aug 2016, 18(29), 19613-19620.

PCCP

PAPER

View Article Online
View Journal | View Issue



Cite this: *Phys. Chem. Chem. Phys.*, 2016, **18**, 19613

# Testing gold nanostructures fabricated by hole-mask colloidal lithography as potential substrates for SERS sensors: sensitivity, signal variability, and the aspect of adsorbate deposition†

Vlastimil Peksa,*[a] Petra Lebrušková,[b] Hana Šípová,[b] Josef Štěpánek,[a] Jiří Bok,[a] Jiří Homola[b] and Marek Procházka*[a]

Received 25th April 2016,
Accepted 20th June 2016

DOI: 10.1039/c6cp02752k

www.rsc.org/pccp

Gold nanoplasmonic substrates with high sensitivity and spectral reproducibility are key components of molecular sensors based on surface-enhanced Raman scattering (SERS). In this work, we used a confocal Raman microscope and several types of gold nanostructures (arrays of nanodiscs, nanocones and nanodisc dimers) prepared by hole-mask colloidal lithography (HCL) to determine the sources of variability in SERS measurements. We demonstrate that significant variations in the SERS signal can originate from the method of deposition of analyte molecules onto a SERS substrate. While the method based on incubation of SERS substrates in a solution containing the analyte yields a SERS signal with low variability, the droplet deposition method produces a SERS signal with rather high variability. Variability of the SERS signal of a single nanoparticle was determined from the statistical analysis of the SERS signal in short-range Raman maps recorded using different sized laser spots produced by means of different objectives. We show that the number of nanoparticles located within the laser spot can be a source of substantial SERS signal variability, especially for high-magnification objectives. We demonstrate that SERS substrates prepared by HCL exhibit high SERS enhancement and excellent homogeneity (about 20% relative standard deviation from short-range maps). The nanocone arrays are shown to provide the highest SERS enhancement, the lowest relative level of fluorescence background, and also slightly better homogeneity when compared with arrays of nanodisc dimers or single nanodiscs.

## Introduction

Surface-enhanced Raman scattering (SERS) is a sensitive spectroscopic method exploiting the high enhancement (by a factor above $10^6$) of Raman scattering (RS) of molecules adsorbed onto noble metal nanostructures.[1] The main enhancement mechanism – the electromagnetic mechanism – is based on the resonant excitation of localized surface plasmons on the metal nanostructure. In SERS, the most commonly used metals are silver and gold that enable the excitation of surface plasmons in the visible spectral region.[2] Gold is more suitable for applications in bioassays and biosensors due to its chemical inertness, biocompatibility and ease of functionalization.

Although recent advances have ushered in a wide variety of bioanalytical and medical applications for SERS,[3–5] insufficient and inconsistent performance of employed SERS-active substrates still hampers the routine use of SERS for quantitative analysis. In order to further expand the applicability of SERS in analytical sciences, highly-efficient, reliable and reproducible metal nanostructured substrates are desired. The ideal SERS-active substrates for biosensing should: (i) provide a great enhancement of the Raman signal, (ii) be uniform, so that the SERS signal does not vary significantly over the substrate, (iii) provide good spectral stability and reproducibility, and (iv) be clean enough from stray signals.[6] High uniformity and reproducibility of SERS substrates are particularly important in quantitative analysis, while high enhancement is preferred for trace analysis.[7] The sensitivity and spectral reproducibility are directly related to the morphology of the nanostructure (namely size, shape, and density, presence of highly enhancing hot-spots, uniformity and homogeneity). Since the SERS systems

[a] *Charles University in Prague, Faculty of Mathematics and Physics, Institute of Physics, Ke Karlovu 5, 12 16, Prague 2, Czech Republic. E-mail: peksav@karlov.mff.cuni.cz, prochaz@karlov.mff.cuni.cz*

[b] *Institute of Photonics and Electronics, Academy of Sciences of the Czech Republic, Prague, Chaberská 57, Prague 8, Czech Republic*

† Electronic supplementary information (ESI) available: Schematic representation of fabrication of the Au nanostructures, details and results of additional mapping of the SERS signal, details of computer simulation, and the fit of measured RSD values for different objectives. See DOI: 10.1039/c6cp02752k

are usually optimized for a specific experimental set-up, SERS substrate and molecule under study (analyte),[8] other sources of signal variations are often ignored, albeit the possibility of their interference with the evaluation of quality of a SERS substrate itself. They can be related to experimental conditions and set-up (such as laser power fluctuation and focus of the used objective), or to the method of analyte deposition. Moreover, the intrinsic fluorescence of plasmonic nanostructures which substantially reduces the signal-to-noise ratio,[9,10] analyte photodecomposition or interferences from other types of molecules and contaminants can also hamper the SERS analysis. The intrinsic fluorescence and contaminants' effects on the resulting signal can be determined by mapping of the supposedly clean substrates, while the photodecomposition can be assessed by measurements with decreased laser power.

A variety of high-throughput methods have been employed to fabricate SERS substrates.[8,11–15] These include nanoparticle immobilization,[16,17] nanoimprinting,[18] templating,[19] and nanosphere or nanocolloidal lithography.[20–23] The hole-mask colloidal lithography (HCL) is particularly attractive due to its high fabrication speed, simplicity and flexibility in the size and shape of the produced nanostructures (single nanodiscs, nanocones, nanodisc dimers *etc.*)[21] Nanostructures produced by means of HCL are homogenous on a millimetre scale and provide good SERS enhancement. Recently, the optimized gold nanodimers on a gold mirror were shown to provide an enhancement factor as high as $10^{11}$ and enable the detection of *trans*-1,2-bis(4-pyridyl)-ethylene at levels as low as $5.5 \times 10^{-13}$ M.[24]

In this work SERS substrates produced by HCL were used to identify the sources of variability of SERS measurements. These sources can be related to the substrate (contribution of individual nanoparticles), experimental set-up (focusing errors, size of the laser spot, *etc.*), or experimental procedures (deposition of analyte on the substrate). In SERS spectroscopy on nanostructured substrates, two methods of analyte deposition are commonly used: (i) a small drop of analyte is deposited on the metal substrate with a pipette and the droplet is let to evaporate in an ambient atmosphere and (ii) the substrate is incubated in a solution containing the analyte for a certain period of time and then removed and dried.[25] In this work, these methods are compared in terms of intensity and reproducibility of the SERS signal obtained. Furthermore, we perform SERS mapping measurements of various nanostructures prepared with HCL and investigate their SERS intensity distributions. We use three distribution moments, mean, variance and skewness, to characterize the SERS substrates in terms of enhancing properties, homogeneity and the presence of hot-spots.

# Experimental

### Fabrication of SERS substrates

The arrays of nanodiscs, nanocones and nanodisc dimers were fabricated by means of HCL,[21] the bottom-up technique based on the self-assembly of colloidal sulphonated polystyrene particles (PPs). For fabrication steps, see Fig. S1, ESI.† Glass substrates were cleaned using an ozone-cleaner UVO-Cleaner® 42-220 (Jelight Company Inc.) for 10 min, rinsed with ethanol and purified water (Milli-Q®, EMD Millipore) and dried under a stream of nitrogen. A layer of poly(methylmethacrylate) (PMMA from MicroChem Corp.) was spin-coated on the substrate, and baked on a hot plate for 10 min at a temperature of 106 °C. A positively charged overlayer was prepared by immersing the PMMA-coated samples in 0.2% water solution of polydiallyldimethyl ammonium (PDDA) for 30 s followed by rinsing in purified water and drying with nitrogen. PPs (110 nm in diameter, 0.2% solution in purified water) were dispersed over the surface. A 25 nm-thick gold film was deposited on the substrate by e-beam evaporation under vacuum. The PPs were removed by tape-stripping, leaving an array of nanoholes in the gold film. The PMMA at the bottom of the nanoholes was removed by etching in oxygen plasma (5 min for nanodiscs and nanocones and 10 min for nanodisc dimers), creating a perforated evaporation mask. The structure was coated with a 2 nm thick layer of titanium to improve the adhesion of gold nanostructures to the substrate. A layer of gold of thickness of 50 and 260 nm was deposited on the substrate to create arrays of nanodiscs and nanocones, respectively. To form an array of nanodisc dimers, a sequential deposition of 25 nm thick layer of gold was performed at two different angles. Finally, PMMA was removed by sonication in acetone. AFM images (Fig. 1) show a layout of the prepared nanostructures and their lateral profiles. Mean surface densities of nanodiscs, nanocones and nanodisc dimers on glass substrates were determined to be $11.1 \pm 0.9$, $9.6 \pm 0.9$ and $10.0 \pm 0.2$ particles per $\mu m^2$, respectively (calculated from 4–14 scans of different 4 $\mu m^2$ areas across the substrate).

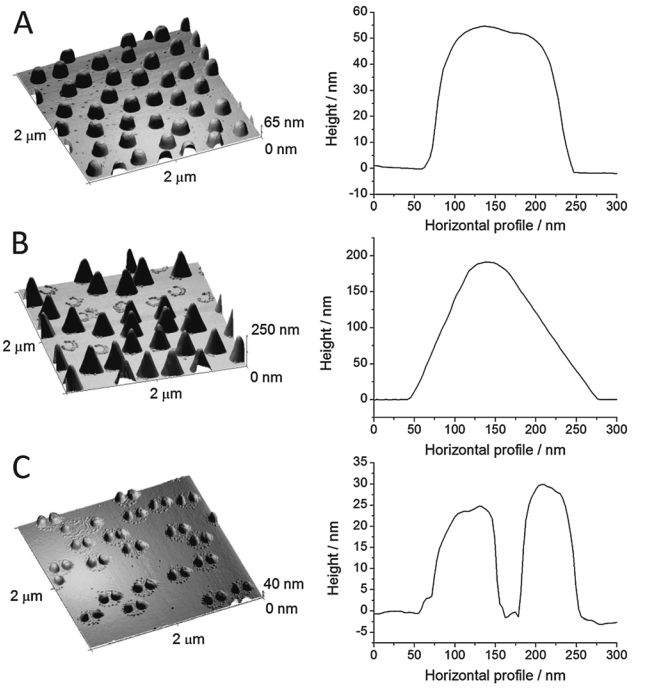


Fig. 1 AFM scans and lateral profiles of the gold nanodiscs (A), nanocones (B) and nanodisc dimers (C) fabricated on glass substrates *via* HCL.

 

### Deposition of MB

Methylene blue (MB), which was used as a model analyte, was purchased from Sigma-Aldrich and dissolved in either ethanol or deionised water in $1 \times 10^{-6}$ M concentration. The MB was deposited on the nanostructured substrates *via* (i) immersion in the solution or (ii) droplet deposition. In (i) the substrate was immersed in an aqueous solution of MB for one hour and then dried by a stream of air. In (ii) a 5 μl droplet of either aqueous or ethanolic solution of MB was deposited on the substrate and left to evaporate in an ambient atmosphere. For comparison of the three deposition methods, $5 \times 5$ mm pieces cut from a single glass slide with gold nanodiscs were used.

### SERS measurements and data processing

SERS measurements were performed using a Raman microscope LabRam HR 800 (Horiba Jobin-Yvon) with an integrated CCD detector. A 632.8 nm He–Ne laser of 100 μW laser power was used for excitation of the sample. Most of the measurements were performed using a 50× air objective (laser spot diameter is about 1.4 μm), some measurements also using 10× and 100× air objectives (3.1 μm and 0.86 μm laser spot diameters). Spectra from a particular laser spot position were collected in 1 s acquisition time and 10 accumulations. The background signal was subtracted using a method based on singular value decomposition (SVD), described by Palacký *et al.*[26] The integral intensity of the peaks was calculated as the area of Lorentz curves fitted to the experimental data using a midpoint integration method in OriginPro software.

The integral intensity of the 1620 $cm^{-1}$ MB peak was used to compare the SERS intensity across the substrates. To determine the homogeneity of the SERS enhancement within one substrate, 3 square maps (49 spots spaced 10 μm apart) were measured. The maps were placed in vertices of the equilateral triangle with sides of 1 mm. Focusing was done before each mapping measurement using the maximal signal intensity. The distribution of the SERS signal was characterized by its mean, relative standard deviation (RSD), and skewness calculated according to the formula

$$S = \frac{n}{(n-1)(n-2)} \sum \left( \frac{x_i - \bar{x}}{\sigma} \right)^3 \quad (1)$$

where $n$ is the number of values, $\bar{x}$ is the mean of the distribution and $\sigma$ is the standard deviation of the distribution. The skewness reflected the asymmetry of the distribution due to the presence of strongly enhancing hot-spots or defects on the substrate.

## Results and discussion

### SERS signal variability caused by the analyte deposition method

Fig. 2 (right) shows microscopy images of a glass substrate with nanodiscs and a comparison of three different deposition methods for analyte deposition. MB was deposited on the substrate by: (A) incubation in an aqueous solution of MB, or droplet deposition and drying of (B) aqueous or (C) ethanolic solution of MB. The microscopy images show a clear difference between the three deposition methods. When the incubation method was used, no MB patterns were visible on the substrate with an optical microscope. In contrast, the deposition using aqueous drop produced drying patterns with MB accumulated at the edges of the former drop, similarly to the coffee ring effect.[27,28] When ethanol was used as a solvent instead of water, the drying pattern still appeared, but it was significantly less pronounced. This observation very well agrees with SERS mapping measurements. Fig. 2 (left) displays the integrated intensity of the 1620 $cm^{-1}$ peak of MB in three distinct areas of each substrate. The lowest variability of the SERS signal was achieved using the incubation method (19% RSD). The highest variability of SERS intensities was observed on the substrate, on which the MB was deposited using water droplet (53% RSD), where the SERS signal was significantly enhanced in some areas of the drying pattern due to MB accumulation. Ethanol droplet deposition showed slightly increased variance compared to the incubated sample (27% RSD), which was most likely caused by subtle drying patterns visible on the microscopic images. The average SERS intensity was approximately 3 or 5 times higher for the ethanol or aqueous droplet deposition, respectively, than for the incubation method. It is most likely caused by the fact that the amount of the analyte adsorbed from the solution is smaller than the analyte amount deposited on the surface in the droplet.

The analyte deposition *via* incubation in solution is therefore much more suitable for SERS measurements than the droplet deposition, because the latter leads to the formation of drying patterns and significantly increases the variations in the SERS signal. The droplet deposition is not well suited for the determination of SERS signal intensity either, as it may provide unrealistically high values.

### SERS intensity and fluorescence background

MB was deposited on three different nanostructures (arrays of gold discs, cones and disc dimers) fabricated on glass and the SERS signal was mapped using the procedure described in the Experimental section. Fig. 3 shows averaged SERS spectra obtained from a single map prior to the background subtraction. The shape of the Raman spectrum corresponds very well to MB SERS spectra measured on other SERS-active surfaces.[29] The highest SERS signal of MB was measured on a substrate with nanocones, followed by nanodisc dimers and individual discs.

Although there was a correlation between the observed SERS intensity and the level of background fluorescence, the quantitative analysis of averaged spectra revealed that there was no direct proportionality between the fluorescence background and the SERS intensity. While the ratio of the SERS intensities obtained with the arrays of nanocones, nanodisc dimers and nanodiscs was 3.3 : 1.5 : 1, respectively, the ratio of the fluorescence background levels was 3.1 : 2.6 : 1. Therefore, the nanocones provided not only the highest SERS intensity, but also the best ratio between the SERS intensity and the fluorescence background. A higher SERS signal was observed on nanodisc dimers than on single nanodiscs, but SERS spectra of

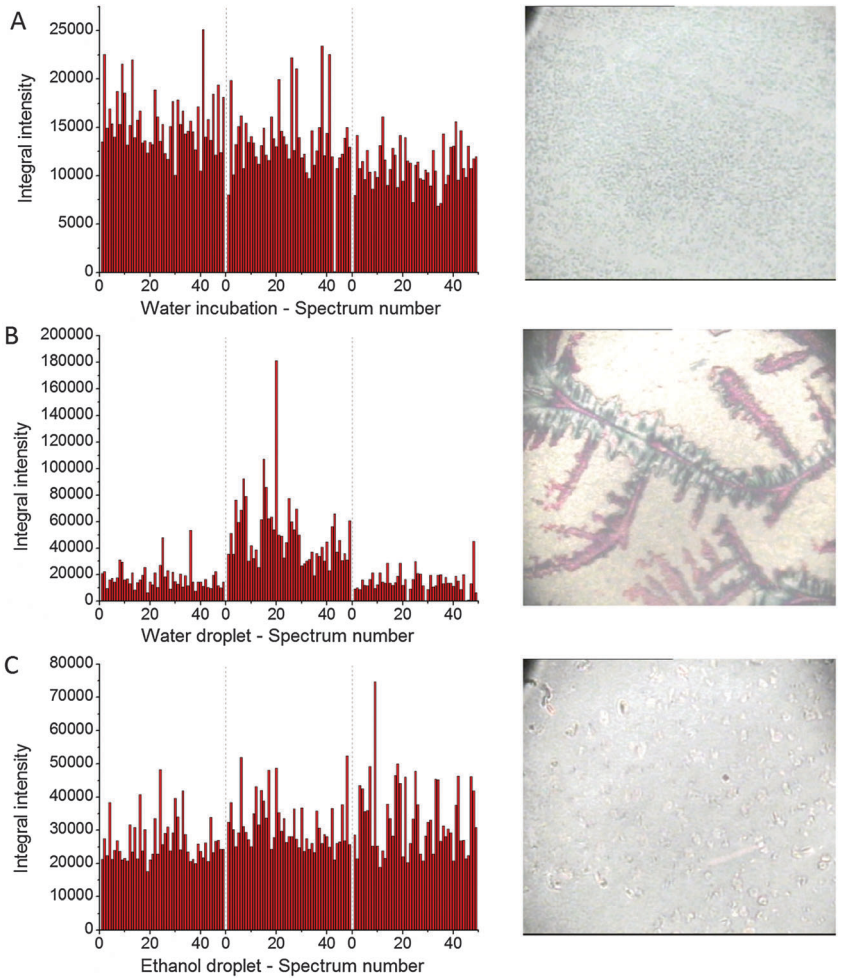


Fig. 2 Left – Variation of the baseline-corrected integrated intensity of the 1620 $cm^{-1}$ peak of MB deposited by different methods (A – incubation in aqueous solution, B – $H_2O$ droplet drying, C – ethanolic droplet drying) over three different mapping areas on the nanodisc substrate. Right – Optical microscopy images of the substrates (100× magnification).

nanodisc dimers also exhibited higher fluorescence background. Mapping of clean substrates was performed under the same conditions as SERS measurements, and with laser power reduced to 10% and 1%, respectively. No stray peaks were observed. It was observed that the fluorescence background was independent of the deposited analyte, even freshly prepared and cleaned substrates exhibited it. Therefore it can be assumed it to be the intrinsic fluorescence of the gold structures themselves.

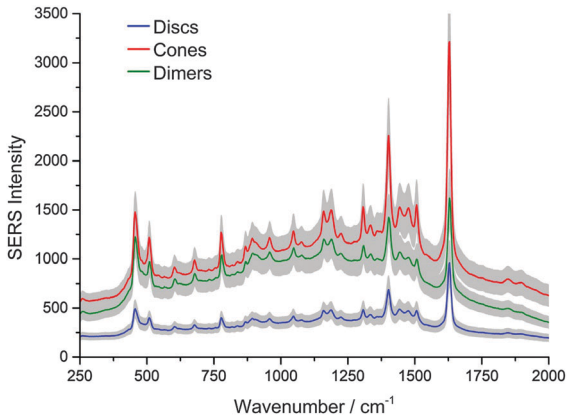


Fig. 3 Mean baseline-uncorrected SERS spectra of $1 \times 10^{-6}$ M MB from 49-point maps on nanodiscs, nanocones and nanodisc dimers produced by HCL. Grey area represents variations of the SERS intensity within standard deviation.

Fig. 4 shows the SERS signal intensity in three 49-point maps measured on different types of substrates. The skewness of distribution of SERS intensity can be used to determine the presence of highly enhancing spots on the nanostructures. As it follows from Fig. 4, a positive skew was observed for the nanostructures that provided a higher SERS signal, *i.e.*, nanocones and nanodimers. The highly-enhancing spots on cones are assumed to be located at their tips. In dimers, the enhancement is believed to be associated with the presence of hot-spots between the nanodiscs.

### Variation of the SERS signal in short-range maps

There was only a small difference between the RSD of the 3 maps measured on the same substrate. Also the RSD values

 

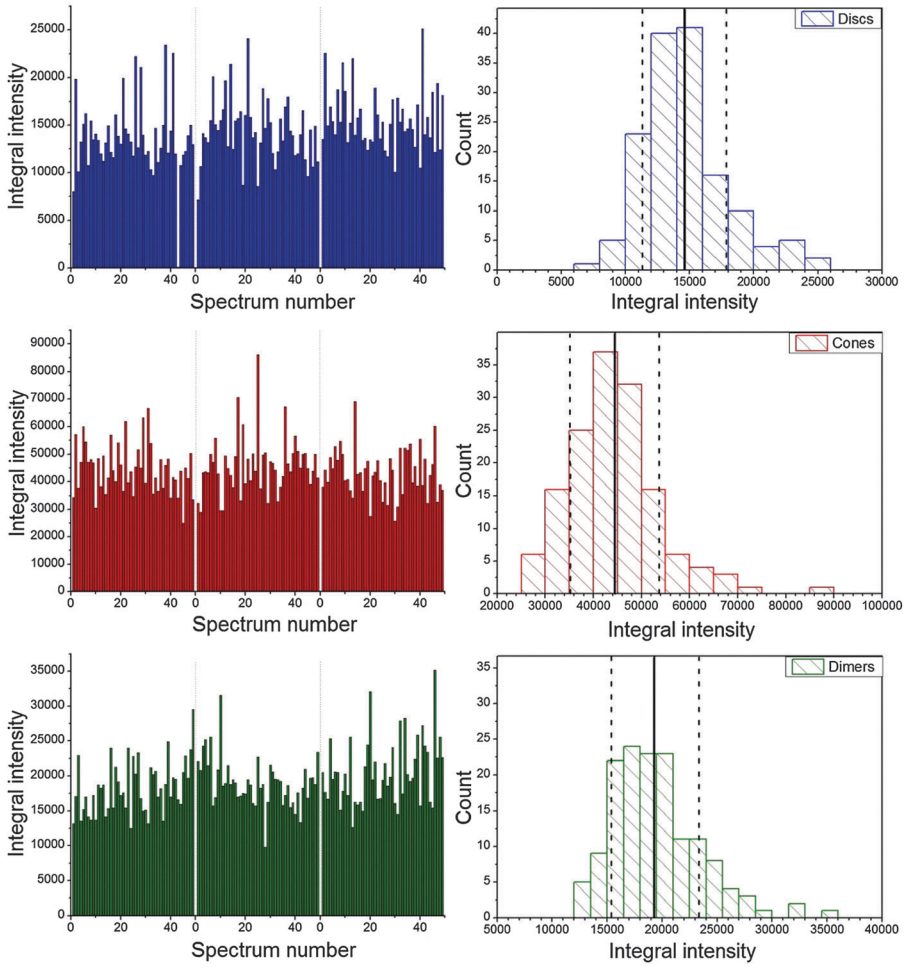


Fig. 4 SERS signal observed using different types of gold nanostructured substrates. Left – Baseline-corrected integral intensity of the 1620 $cm^{-1}$ MB peak measured in three 7 × 7-point maps. Right – Histograms of the integral intensity, its mean value (solid line) and $2\sigma$ interval (dashed lines).

of various types of nanostructures were similar: 19% RSD for nanodiscs and 20% for both nanocones and nanodisc dimers (see Table 1). A further increase in the number of measured points or maps did not improve the RSD (see Fig. S2, ESI†). To determine the origin of the signal variations, we performed a detailed analysis based on the consideration of potential sources of this variability.

The most important parameter of the investigated SERS substrate is the variation of the SERS signal from individual nanoparticles ($RSD_i$). It not only reflects the variation of the SERS enhancement factor, but also a different number of adsorbed molecules on each nanoparticle and different orientations of the molecules with respect to the nanoparticle surface. In the SERS measurements, $RSD_i$ is manifested as $RSD_N$, which is an average of $RSD_i$ of the $N$ nanoparticles present in the laser spot:

$$RSD_N = RSD_i/\sqrt{N} \quad (2)$$

Table 1 Experimental and theoretical evaluation of RSD of SERS intensity on three different types of nanostructures

| Nanostructures | Density[a] ($\mu m^{-2}$) | $RSD_{dens}$[a] (%) | Objective | RSD[b] (%) | Skewness[b] | $RSD_{numb}$[c] (%) | $RSD_i$[d] (%) |
|---|---|---|---|---|---|---|---|
| Nanodiscs | 11.1 | 8 | 50× | 19 | 0.41 | 6, 13 | 62; 40 |
| Nanocones | 9.6 | 9 | 10× | 12 | | 1.5, 4 | |
| | | | 50× | 20 | 0.75 | 7; 11 | 51; 45[e] |
| | | | 100× | 29 | | 17, 20 | |
| Nanodisc dimers | 10.0 | 2 | 50× | 20 | 0.77 | 7; 15[f] | 69; 46 |

[a] Average surface density of nanoparticles determined by AFM and its RSD. [b] RSD and skewness of the measured SERS intensity obtained from 7 × 7-point maps. 10 μm distance between neighbouring spots. [c] Numerically determined RSD due to the variable number of nanoparticles in the laser spot. Values for uniform (first number) and random (second number) distribution of nanoparticles are given. [d] Variation of the SERS signal from a single nanoparticle calculated according to eqn (2) and (3). The first number corresponds to $RSD_{numb}$ calculated for uniformly distributed nanoparticles and the second one to that of the random distribution. [e] $RSD_i$ values for nanocones obtained by the least squares fit (see the ESI for details). [f] $RSD_{numb}$ values for nanodisc dimers estimated considering the nanoparticle density and the area of the nanoparticle base (see the ESI for details).

Before assessing the $RSD_i$, other sources of the SERS signal variations should be taken into account. The first source of noise is associated with variations in the density of nanoparticles across the surface of a substrate. These variations ($RSD_{dens}$) were determined using the AFM method and are collected in Table 1. The second source of noise may be due to imperfections of the measurement process, including the instability of the measurement system, spectrometer noise effects and inaccuracies in the calculation of the integral intensity of the Raman band. We found that in our experiments, the RSD ($RSD_{ap}$) was about 3–6% (determined from repeated measurements of the MB signal in the same spot; data not shown). The third source of the signal variability is variations in the number of nanoparticles present within the laser spot. This effect was investigated by computer simulations, in which a 20 × 20 μm area was covered with circles of diameter corresponding to the base of the nanoparticles. Two distributions of the nanoparticles were computed – the random distribution of non-overlapping circles and the regular distribution of circles with a fixed spacing. We assume that the distribution of the nanoparticles on real HCL samples lies between those extreme layouts. A circle representing the laser spot was then randomly placed at various positions inside the square and the number of particle centres within the laser spot circle was calculated (see ESI† for details). The obtained RSD values ($RSD_{numb}$) are shown in Table 1.

Assuming that all these main sources of variability of the SERS signal are independent, the measured SERS signal variation (RSD) can be obtained as follows:

$$\mathrm{RSD}(d_f) = \sqrt{\mathrm{RSD_{dens}}^2 + \mathrm{RSD_{numb}}(d_f)^2 + \mathrm{RSD}_N(d_f)^2 + \mathrm{RSD_{ap}}^2} \quad (3)$$

where $d_f$ is the laser spot diameter.

To confirm this result, we performed mapping measurements on a substrate with nanocones using a 100× objective ($d_f$ = 0.86 μm), a 50× objective ($d_f$ = 1.4 μm) and a 10× objective ($d_f$ = 3.09 μm). The RSD values of the SERS signal were determined to be 29%, 20% and 12%, respectively (Table 1). $RSD_i$ and $RSD_{ap}$ were then calculated from the least squares fit (Fig. S3, ESI†), using $RSD_{numb}$ values for uniformly and randomly distributed nanoparticles. The fit provided the $RSD_i$ value of 45–51% and the $RSD_{ap}$ value was 5–6%, which agrees well with our previous estimate.

For nanodiscs and nanodisc dimers we calculated the estimates of $RSD_i$ from eqn (2) and (3) using the value of $RSD_{ap}$ = 6% (Table 1). In the case of nanodisc dimers the computer simulation of $RSD_{numb}$ was not performed because of the rather complicated ground projection of the nanoparticle unit. Nevertheless, on the basis of the results obtained for nanodiscs and nanocones, we can realistically estimate the $RSD_{numb}$ limits.

The results we obtained demonstrate that the SERS variation from a single nanoparticle is the dominant effect causing the variability of the SERS signal. Lower, but still significant variations in the SERS signal may be caused by variations in the number of nanoparticles in the laser spot. In both cases the signal variability can be decreased when the laser spot diameter is increased and/or the measurements are carried out for several laser spot positions and averaged.

### Precision of focusing and intensity standard

To determine the variability of SERS measurements caused by differences in focusing, we measured the 3 maps (7 × 7-points), while adjusting the focus before each of the mapping measurement by maximizing the SERS signal. The average SERS signals of the 1 mm distant maps showed relatively low variations: RSD of 8.7% for nanodiscs, 3.0% for nanocones, and 6.1% for nanodisc dimers. It is possible that other effects may also contribute to these numbers, such as long-range variability of the substrate properties and the limited number of values used for RSD determination. We can therefore estimate that errors caused by the variability of focusing are less than 6%.

HCL enables the fabrication of nanostructures on substrates composed of various materials. Materials such as silicon and sapphire are known to have distinct Raman signals that can be used as internal intensity standard to correct for focusing errors and fluctuations in the laser light intensity, because although the absolute intensity of Raman peaks can easily vary between different measurements, the ratio of two peaks under the same experimental conditions remains the same, thus enabling the normalization of the spectra.[7] We have therefore fabricated

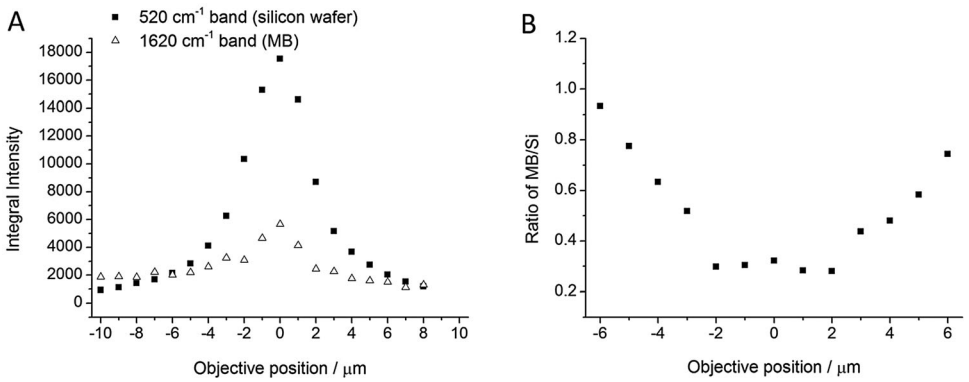


Fig. 5 A – Dependence of the SERS signal and the Raman signal from the silicon wafer on the relative objective position. B – Ratio of the intensities.

 

nanodiscs on a silicon wafer using the HCL method and monitored the sharp Raman peak of silicon at 520 $cm^{-1}$. Mapping measurements showed very low variation in the intensity of the peak ($\sim$3%). Moreover, a lower background fluorescence signal was measured in comparison with that obtained using glass substrates.

Fig. 5 shows the dependence of Raman signal intensity of the silicon band and SERS intensity of MB on the relative position of the objective during the depth scan. It can be seen that both dependencies show similar trends and the silicon band displays lower variability than the SERS signal of MB. It can be concluded that the silicon band at 520 $cm^{-1}$ can be used to find the correct focus, which can be very useful when the SERS signal of the analyte is low. The ratio of the band intensities of MB 1620 $cm^{-1}$ to silicon 520 $cm^{-1}$ is shown in Fig. 5B. It suggests that the Raman signal from the substrate can be used to normalize the SERS signal from the analyte and hence correct for the errors in focusing as part of data processing. However, this normalization can be used only if a relative distance of the objective from the right focus was within 2 micrometres (the plateau in Fig. 5B), where the Raman and SERS intensities are proportional.

## Conclusions

In this work, we explored the properties of selected SERS substrates based on gold plasmonic nanostructures produced by HCL and investigated various sources of variability of the SERS signal. We found that the most important variability of the SERS signal can be introduced by an inappropriate method for analyte deposition on the SERS substrate. We showed that drop deposition results in the formation of irregular drying patterns and high spatial variability of the SERS signal. In contrast, incubation of the SERS substrate in analyte solution has been found to provide very low variation in the SERS signal and therefore appears to be a good candidate for quantitative SERS measurements. We performed short-range mapping measurements of the nanostructured substrates and demonstrated that variations in the SERS signal from a single nanoparticle present another important contribution to the total signal variability. Variations in the number of nanoparticles in the laser spot were identified as the second largest source of variations. In contrast, the inaccuracies in the laser beam focusing were found to be of much smaller influence than the two above-mentioned effects. We also showed that increasing the laser spot diameter and/or signal averaging over several laser spot positions may help improve the reproducibility of SERS measurements. Furthermore, we demonstrated that the nanostructures we prepared using the HCL method (arrays of nanodiscs, nanocones, or nanodisc dimers) yield SERS signals with high intensity and low spatial variability. The nanocones were found to provide significantly higher SERS signal than nanodiscs and nanodisc dimers. Moreover, the nanocones exhibited the lowest variability of the SERS signal from an individual nanoparticle (our estimate of RSD was between 45 and 51%) and the lowest relative level of fluorescence background. A significant skewness in the distribution of SERS intensities from short-range maps was observed for nanodisc dimers and nanocones. While in the former case this was attributed to the presence of hot-spots, in the case of nanocones, it was most likely related to the varying sharpness of the nanocone tips.

## Author contributions

The manuscript was written through contributions from all authors. All authors have given approval to the final version of the manuscript.

## Funding sources

This work was supported by grant No. P205/12/G118 from the Czech Science Foundation and SVV-2016-260323 from the Charles University in Prague.

## Conflicts of interest

The authors declare no competing financial interest.

## Acknowledgements

The funding from the research grants P205/12/G118 from the Czech Science Foundation and SVV-2016-260323 from the Charles University in Prague is gratefully acknowledged.

## References

1 M. Fleischmann, P. J. Hendra and A. J. McQuillan, *Chem. Phys. Lett.*, 1974, **26**, 163.
2 E. C. Le Ru and P. G. Etchegoin, *Principles of Surface-Enhanced Raman Spectroscopy and Related Plasmonic Effects*, Elsevier, Amsterdam, 2009.
3 S. Schlücker, SERS Microscopy: Nanoparticle Probes and Biomedical Applications, in *Surface Enhanced Raman Spectroscopy: Analytical, Biophysical and Life Science Applications*, ed. S. Schlücker, Wiley-VCH Verlag GmbH & Co. KGaA, 2011, p. 263.
4 K. C. Bantz, A. F. Meyer, N. J. Wittenberg, H. Im, O. Kurtulus, S. H. Lee, N. C. Lindquist, S. H. Oh and C. L. Haynes, *Phys. Chem. Chem. Phys.*, 2011, **13**, 11551.
5 M. Procházka, *Surface-enhanced Raman spectroscopy, Bio-analytical*, Biomolecular and Medical Applications, Springer International Publishing Switzerland, 2016.
6 M. J. Natan, *Faraday Discuss.*, 2006, **132**, 321.
7 S. E. J. Bell and A. Stewart, Quantitative SERS Methods, in *Surface Enhanced Raman Spectroscopy: Analytical, Biophysical and Life Science Applications*, ed. S. Schlücker, Wiley-VCH Verlag GmbH & Co. KGaA, Weinheim, 2011, p. 71.
8 X. M. Lin, Y. Cui, Y. H. Xu, B. Ren and Z. Q. Tian, *Anal. Bioanal. Chem.*, 2009, **394**, 1729.

9 J. Zhu, L. Q. Huang, Y. C. Wang and Y. M. Lu, *Physica E*, 2004, **25**, 114.
10 A. Bouhelier, R. Bachelot, G. Lerondel, S. Kostcheev, P. Royer and G. P. Wiederrecht, *Phys. Rev. Lett.*, 2005, **95**, 4.
11 M. J. Banholzer, J. E. Millstone, L. D. Qin and C. A. Mirkin, *Chem. Soc. Rev.*, 2008, **37**, 885.
12 M. K. Fan, G. F. S. Andrade and A. G. Brolo, *Anal. Chim. Acta*, 2011, **693**, 7.
13 M. Jahn, S. Patze, I. J. Hidi, R. Knipper, A. I. Radu, A. Muhlig, S. Yuksel, V. Peksa, K. Weber, T. Mayerhofer, D. Cialla-May and J. Popp, *Analyst*, 2016, **141**, 756.
14 D. L. Liu, C. C. Li, F. Zhou, T. Zhang, H. H. Zhang, X. Y. Li, G. T. Duan, W. P. Cai and Y. Li, *Sci. Rep.*, 2015, **5**, 9.
15 H. H. Zhang, M. Liu, F. Zhou, D. L. Liu, G. Q. Liu, G. T. Duan, W. P. Cai and Y. Li, *Small*, 2015, **11**, 844.
16 K. C. Grabar, R. G. Freeman, M. B. Hommer and M. J. Natan, *Anal. Chem.*, 1995, **67**, 735.
17 N. Hajduková, M. Procházka, P. Molnár and J. Štěpánek, *Vib. Spectrosc.*, 2008, **48**, 142.
18 Z. Y. Li, W. M. Tong, W. F. Stickle, D. L. Neiman, R. S. Williams, L. L. Hunter, A. A. Talin, D. Li and S. R. J. Brueck, *Langmuir*, 2007, **23**, 5135.
19 G. M. Zhang, J. Zhang, G. Y. Xie, Z. F. Liu and H. B. Shao, *Small*, 2006, **2**, 1440.
20 P. L. Stiles, J. A. Dieringer, N. C. Shah and R. P. Van Duyne, *Annual Review of Analytical Chemistry*, Annual Reviews, Palo Alto, 2008, vol. 1, p. 601.
21 H. Fredriksson, Y. Alaverdyan, A. Dmitriev, C. Langhammer, D. S. Sutherland, M. Zäch and B. Kasemo, *Adv. Mater.*, 2007, **19**, 4297.
22 Y. Li, G. T. Duan, G. Q. Liu and W. P. Cai, *Chem. Soc. Rev.*, 2013, **42**, 3614.
23 Y. Li, N. Koshizaki and W. P. Cai, *Coord. Chem. Rev.*, 2011, **255**, 357.
24 A. Hakonen, M. Svedendahl, R. Ogier, Z. J. Yang, K. Lodewijks, R. Verre, T. Shegai, P. O. Andersson and M. Kall, *Nanoscale*, 2015, **7**, 9405.
25 H. H. Zhang, F. Zhou, M. Liu, D. L. Liu, D. D. Men, W. P. Cai, G. T. Duan and Y. Li, *Adv. Mater. Interfaces*, 2015, **2**, 1500031.
26 J. Palacký, P. Mojzeš and J. Bok, *J. Raman Spectrosc.*, 2011, **42**, 1528.
27 E. Kočišová and M. Procházka, *J. Raman Spectrosc.*, 2011, **42**, 1606.
28 Y. Xie, Y. Jiang and D. Ben-Amotz, *Anal. Biochem.*, 2005, **343**, 223.
29 G. N. Xiao and S. Q. Man, *Chem. Phys. Lett.*, 2007, **447**, 305.

 

**Supplement [V]**

STOLCOVA, L., PEKSA, V., PROSKA, J., PROCHÁZKA, M., **Gold film over very small (107 nm) spheres as efficient substrate for sensitive and reproducible surface-enhanced Raman scattering (SERS) detection of biologically important molecules**. Submitted to Journals of Raman Spectroscopy.

# Gold film over very small (107 nm) spheres as efficient substrate for sensitive and reproducible surface-enhanced Raman scattering (SERS) detection of biologically important molecules

*Lucie Štolcová,*[a] *Vlastimil Peksa,*[b] *Jan Proška*[a] *and Marek Procházka*[b,*]

[a] *Technical University in Prague, Faculty of Nuclear Sciences and Physical Engineering, Břehová 7, 115 19 Prague 1, Czech Republic.*
[b] *Charles University, Faculty of Mathematics and Physics, Institute of Physics, Ke Karlovu 5, 121 16 Prague 2, Czech Republic.*

*CORRESPONDING AUTHOR: M. Procházka, prochaz@karlov.mff.cuni.cz

KEYWORDS: SERS, AuFON, reproducibility, biomolecules, alkaloids

**Abstract**

Gold plasmonic nanostructures with high sensitivity and spectral reproducibility are key components of molecular sensors based on surface-enhanced Raman scattering (SERS). In this paper, we report a "bottom-up" fabrication of gold "film over nanosphere" (FON) substrates for SERS sensing based on very small (107 nm in diameter) polystyrene (PS) spheres coated with 20 nm of gold. To obtain close-packed spheres in a large scale area, the self-assembly at the water-air interface was found to be very efficient. Sensitivity and reproducibility of the AuFON substrates were tested using various molecular probes: 5,10,15,20-tetrakis(1-methyl-4-pyridyl)porphyrin (TMPyP), *p*-aminothiophenol (*p*-ATP) and benzocaine. Relative standard deviation (RSD) of SERS signal was found to be less than 20% confirming excellent spectral reproducibility especially using a 100× objective. Then, we demonstrated sensitive SERS detection of other biologically important molecules adsorbed on our AuFON substrates: thiolated-polyA, protoporphyrin IX and two alkaloids (nicotine and strychnine). We were able to detect both alkaloids at $10^{-6}$ M (in order of 100 ng.mL$^{-1}$) concentrations. Therefore, we concluded that the AuFONs deposited on PS spheres of 107 nm in diameter provided both excellent spectral reproducibility and sensitivity. Their implementation into the SERS-active system will enable to bring about new quantitative and analytical SERS applications.

## 1. Introduction

Surface-enhanced Raman scattering (SERS) spectroscopy is a sensitive and selective vibrational technique for molecular detection and identification. It profits from enormous enhancement (by factor above $10^5$) of Raman scattering of molecules on or near to certain metallic nanostructures.[1] The nanostructure, referred as SERS-active substrate, is usually made from noble metals such as gold and silver. This ensures that the resonance excitation of surface plasmons localized on the metal and consequently SERS enhancement is obtained in a

visible spectral region.[2] Nowadays, numerous applications of SERS spectroscopy including analytical, biomolecular and medical can be found in literature.[3-7]

The employed SERS-active substrate plays a key role in any SERS experiment. The spectral sensitivity and reproducibility of SERS-active substrates represents a major preoccupation in developing routine SERS quantitative analysis. Such an approach expects a use of highly-efficient, reliable and reproducible SERS-active substrates. An ideal SERS-active substrate for such purpose should fulfil four basic requirements.[8,9] First, it should be sensitive, so provide a sufficient enhancement of Raman scattering. Second, it should be uniform enough, so that the SERS signal does not vary significantly (typically less than 20 %) over the substrate. It requires a relatively ordered arrangement of the nanostructures on the substrate. Third, it should provide good spectral stability and reproducibility even after a long shelf time (typically weeks). The signal deviation should again be less than 20% for different batches of substrates. Last, the substrate should be clean enough so that it can be applied to study some weak adsorbates or even unknown samples. Ease and cost of preparation should be taken into account for routine use.[10]

The sensitivity and spectral reproducibility of SERS-active substrates are directly related to the morphology of the nanostructures (namely size, shape, spacing; presence of highly enhancing hot-spots; uniformity and homogeneity). High reproducibility and homogeneity of SERS enhancement over the whole surface can be intrinsically ensured at solid regular periodic surfaces. In the past years, a great advance has been made both in fabricating such nanostructures and designing their optimal shape and size using computer simulations of their interactions with incident light.[7,9-15] A variety of "bottom-up" methods include nanoimprinting,[16] templating,[17] and nanosphere or nanocolloidal lithography.[18–21] The metal "film over nanospheres" (FON) surface can be formed by polystyrene (PS) or silica micro- or nano-spheres self-assembled on a solid support and then sputtered with metal.[22-24] Owing to their excellent spectral reproducibility they were successfully employed in SERS sensing of small molecules such as glucose and biowarfare agents.[25] This technique is particularly advantageous because of its low cost and the possibility to create large surfaces (~ $cm^2$). The shape, size and spacing of the nanostructures can be controlled by the size of the spheres and the thickness of deposited metal.[24] Moreover, optical properties of these periodic structures determined by their characteristic dimensions can be easily tuned by the size of individual particles. It was found that a very sharp angle of intersection (i.e., very sharp crevice) between neighbouring spheres in AuFON are favourable for electromagnetic fields localization and very large SERS enhancements.[26] These geometrical circumstances can be reached by smaller PS spheres diameter and smaller Au thickness.

In this paper, we report fabrication of AuFON substrates using very small (107 nm in diameter) PS spheres on silicon. To obtain close-packed spheres, the self-assembly at the water-air interface was used. Sensitivity and reproducibility of our AuFON substrates were tested using various molecular probes: 5,10,15,20-tetrakis(1-methyl-4-pyridyl) porphyrin (TMPyP), *p*-ATP and benzocaine. Then, they were employed for sensitive SERS detection of other biologically important molecules: nucleic acid, protoporphyrin IX, nicotine and strychnine.

## 2 Materials and methods

### 2.1 Materials

Aqueous dispersions of polystyrene (PS) spheres (107 nm in diameter) were purchased from microParticles GmbH (Berlin, Germany). Nicotine, strychnine (hemisulfate salt), *p*-

aminothiophenol (*p*-ATP), 5,10,15,20-tetrakis(1-methyl-4-pyridyl)porphyrin (TMPyP), protoporphyrin IX and benzocaine were purchased from Sigma Aldrich. 10-mer thiolated polyA was synthesized by Biomers.net.

### 2.2 Preparation and characterization of AuFON substrate

Hexagonally ordered monolayers of close-packed PS spheres were prepared by self-assembly at the water-air interface as described in ref. 27. Aqueous dispersions of PS spheres (107 nm in diameter) were mixed with ethanol (1:1 v/v) and carefully deposited on a water surface using a glass pipette. The monolayer was then transferred onto clean silicon substrates (approx. 1 cm × 1 cm) and left to dry at room temperature. Finally, the monolayer was coated with 20 nm of gold in Cressington 208HR high-resolution sputter coater.
The scanning electron microscopy (SEM) images were obtained by scanning electron microscope JEOL JSM-7500F.

### 2.3 Preparation of SERS-active systems and SERS measurement

All analytes were diluted in water except for nicotine which was diluted in water solution of $10^{-2}$ M KBr. The as-prepared AuFON substrates were dipped in the solution of analyte overnight and then dried in a nitrogen flow before Raman measurements. Only SH-polyA was dropped by pipette to the AuFON substrate and left to dry.
SERS spectra were measured on the confocal Raman microspectrometer LabRAM HR800 (Horiba Jobin Yvon) with a nitrogen cooled CCD detector. An objective 100× (NA = 0.9) focused laser beam to a spot about 1-1.2 μm diameter. Two excitation lines were used: He-Ne laser (632.8 nm laser, power at the sample 0.02 mW) and diode laser (785 nm, power at the sample 0.04 mW) were used, as the substrate exhibited SERS effect for both lines. The 632.8 nm line yielded better results, however due to burning effects and strong fluorescence background, the 785 nm was necessary to be used in some cases, such as in trace detection of alkaloids. Experimental conditions (laser line, accumulation times) can be found in the captions of each Figure.

## 3 Results and discussion

### 3.1 Preparation and characterization of AuFON substrates

Up to now, the spin-coating has been employed as a fast and repeatable method to self-assemble the PS spheres during preparation of Au or Ag FON substrates for SERS.[18, 22-25] Diameter of PS spheres varied from 920 nm[18] to 220 nm.[23] In our case, we used self-assembly at the air-liquid interface[27] which appeared to be more suitable in the case of very small (107 nm in diameter) PS spheres. The self-assembled layer on the air-liquid interface was about 1 $dm^2$, from which it was transferred onto pre-cut silicon supports, sized approximately 0.5 $cm^2$ each. Figure 1 shows SEM images of typical AuFON substrate. It proves that the packing density is homogeneous on the micrometer scale. According to our knowledge, it is a first AuFON substrate formed on such small PS spheres. We used it previously for detection and quantification of azorubine dye in drinks.[28]

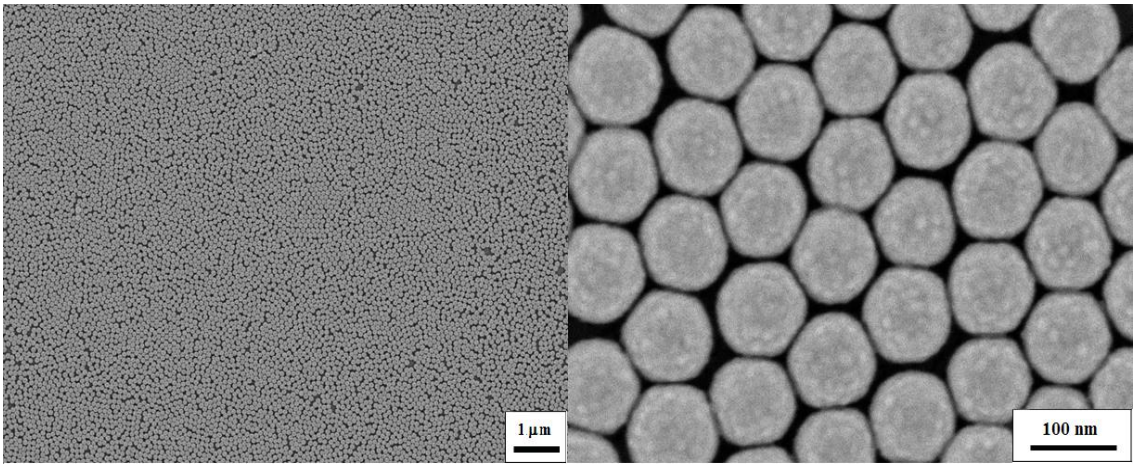


**Figure 1** SEM of AuFON substrate (PS spheres of 107 nm in diameter covered with 20 nm of gold layer).

### 3.2 SERS spectral testing: reproducibility

SERS reproducibility of SERS-active substrate is a key point in any SERS analytical application. To test our AuFON substrates we used a molecular probe TMPyP porphyrin. TMPyP is a cationic porphyrin well known to provide a strong SERS signal on Au surfaces.[29] Prior to spectral reproducibility study it was necessary to chose a suitable way to adsorb our molecular probe to AuFON. Previously, we reported that one source of variations in the SERS signal originates from the method of deposition of analyte molecules onto a SERS substrate.[20] While incubation of SERS substrates in a solution containing the analyte yielded a SERS signal with low variability, the droplet deposition method produced a SERS signal with rather high variability. For this reason, we used the incubation method to test reproducibility of our AuFON substrates.

Figure 2 shows typical SERS spectra of TMPyP probe molecule obtained for different incubation concentrations in AuFON substrate. We were able to obtain the SERS spectra of TMPyP down to $10^{-7}$ M. The SERS spectra as well as the TMPyP detection limit are very similar to those obtained from Au nanoparticles attached to silanized glass plates.[29]

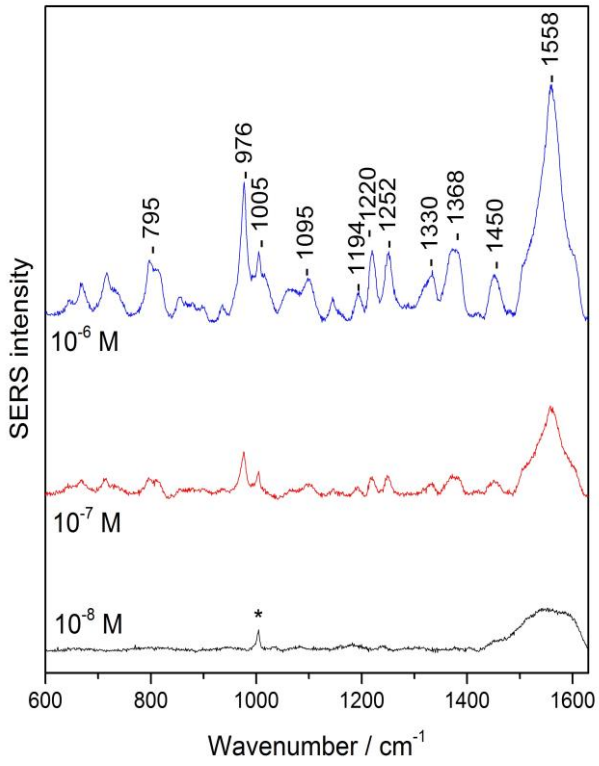


(CAN BE BLACK AND WHITE IN PRINT)

**Figure 2** SERS spectra of TMPyP obtained for different incubation concentrations in AuFON substrate. Spectra are baseline corrected and shifted in the intensity scale for clarity. Raman signal of PS spheres is marked by an asterisk. Each spectrum is an average of the 25 spectra measured from different spots on the substrate, accumulation time 6×10s, 632.8 nm excitation.

Reproducibility of our AuFON substrates was tested using TMPyP of 1 μM incubation concentration. Three spectral maps of 10×10 points with 5 μm increment were measured from different location of two AuFON substrates (A and B). Spectral intensity was determined as intensity of 1220 $cm^{-1}$ TMPyP band. Figure 3 shows the spectral maps and corresponding relative standard deviation (RSD) determined from three spectral maps of 10×10 points measured from different locations of the AuFON substrates (A, B). The average SERS intensities acquired from both substrates and from three different locations of the same substrate as well are nearly identical. In all cases, RSD of the SERS signal was less than 20% which is expected to be sufficient for quantitative SERS applications.[8] We would like to emphasize this result especially in condition of the strongly focused laser beam using a 100× objective. For instance, RSD of methylene blue SERS signal on gold nanostructures prepared by hole-mask colloidal lithography measured using a 100× objective was about 29%.[20]

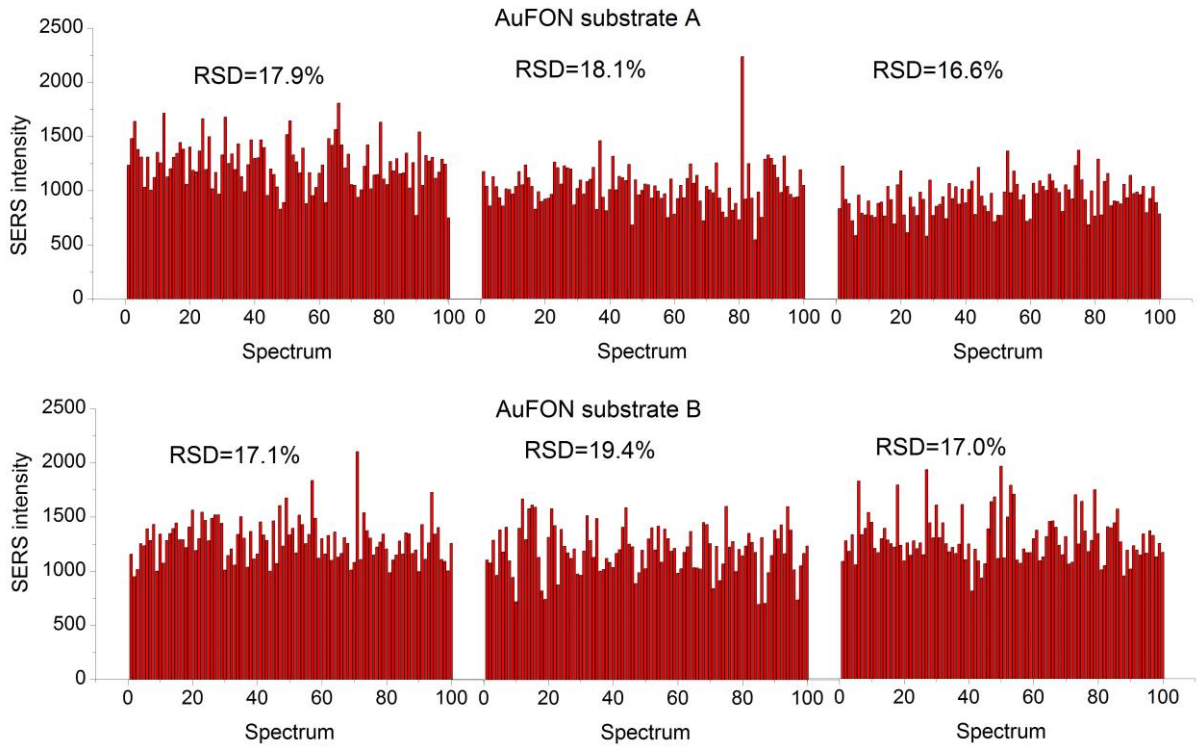


(CAN BE BLACK AND WHITE IN PRINT)

**Figure 3** Variability of SERS signal of TMPyP determined from three spectral maps of 10×10 points measured from different locations of two AuFON substrates (A, B). RSD=relative standard deviation of the SERS signal. Accumulation time for each spectrum 5×10s, 632.8 nm excitation.

### 3.3 SERS spectral testing: sensitivity

Another key point of any SERS analytical application is SERS sensitivity of a SERS-active substrate. We used two molecular probes, *p*-ATP and benzocaine, to test them on AuFONs substrates. The thiol group of *p*-ATP is known to be covalently attached to gold and therefore it is a suitable molecule for SERS testing of Au substrates. Benzocaine was chosen as a model drug molecule because it is commonly used as a marker for drugs due to its physical and chemical similarities to cocaine.

Figure 4 shows typical SERS spectra of *p*-ATP and benzocaine probe molecules obtained for different incubation concentrations in AuFON substrate. We were able to obtain the SERS spectra of *p*-ATP down to $10^{-7}$ M. This concentration is several orders of magnitude better than concentrations used previously in AuFON substrates prepared on bigger PS spheres.[24,26] In the case of benzocaine (Figure 4, right) we compared SERS spectra with normal Raman spectrum of benzocaine powder. The SERS spectral bands of benzocaine at 861, 1171, 1280, 1367, 1442, 1572 and 1602 $cm^{-1}$ correspond closely with those of benzocaine powder. We were able to obtain the SERS spectrum of benzocaine down to $10^{-6}$ M.

Therefore, we suggest that our AuFON substrates based on PS spheres of 107 nm in diameter provide excellent SERS sensitivity for quantitative and analytical SERS applications.

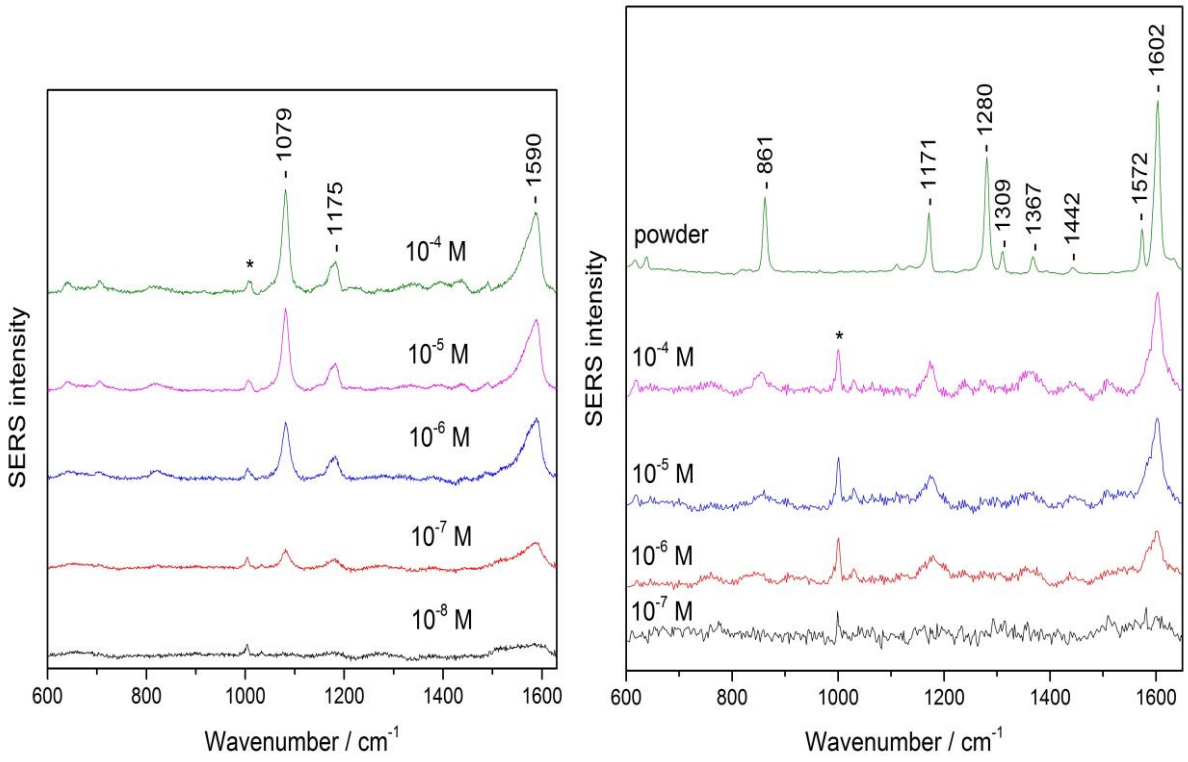


(CAN BE BLACK AND WHITE IN PRINT)

**Figure 4** SERS spectra of *p*-ATP (left) and benzocaine (right) obtained for different incubation concentrations in AuFON substrate. Spectra are baseline corrected and shifted in the intensity scale for clarity. Each spectrum is an average of the 3 spectra measured from different spots of the substrate, accumulation time 6×10s, 632.8 nm excitation. Raman signal of PS spheres is marked by an asterisk. Raman spectrum of benzocaine powder was obtained with accumulation time 6×10s and 785 nm excitation to avoid fluorescence.

### 3.4 SERS spectra of other biologically important molecules

To prove SERS analytical potential of our AuFON substrates, we tested other biologically important analytes.

Figure 5 shows SERS spectrum of 10-mer thiolated polyA oligonucleotide ($8\times10^{-5}$ M concentration in base pairs) dropped and dried on the AuFON substrate. The bands at 729, 800, 1013, 1271, 1302, 1342 $cm^{-1}$ agree with those observed in SERS spectrum of thiolated 24-mer polyA on Au nanoparticles.[30] The 676, 1095, 1573 $cm^{-1}$ bands were assigned to adenine in thiolated oligonucleotide adsorbed on Au nanshells.[31] Therefore, we conclude that our spectrum is a SERS spectrum of polyA.

Another biomolecule studied was protoporphyrin IX, a well known marker in clinical diagnosing of early stages of cancer. SERS spectrum measured from AuFON incubated in $10^{-5}$ M concentration of protoporphyrin IX is shown in Figure 5. The 675, 737, 960, 1124, 1228, 1375, 1540, 1587 and 1606 $cm^{-1}$ bands are in accord with those in SERS spectrum of protoporphyrin IX obtained from Ag nanoparticles.[32]

Finally, we tested the possibility to detect trace amounts of two alkaloids: nicotine and strychnine. Nicotine is a potent neuroactive alkaloid, the lethal dosage for adult humans is about 40 – 60 mg. Nicotine is still used as an insecticide in some countries and could be present in some food as a contaminant. Strychnine is an alkaloid with high toxicity (about 50

mg for adult human) and thus it was a widely used poison. In low dosages, it can be misused by athletes as a stimulant or a performance enhancing drug.

To find the limits of detection, we measured SERS spectra of both alkaloids adsorbed on AuFON substrate from different incubation concentrations. Figure 5 shows the SERS spectra of nicotine and strychnine obtained for the $10^{-6}$ M (in order of 100 ng.mL$^{-1}$) incubation concentrations which corresponds roughly with detection limit. The SERS spectrum of nicotine represented by bands at 1031 and 1053 cm$^{-1}$ corresponds to the SERS spectrum reported from Ag nanoparticles.[33] The SERS spectrum of strychnine is dominated by two peaks at 647 cm$^{-1}$ and 1023 cm$^{-1}$, which agree perfectly with the two most intense vibrational modes in the Raman spectrum of strychnine reported elsewhere.[34]

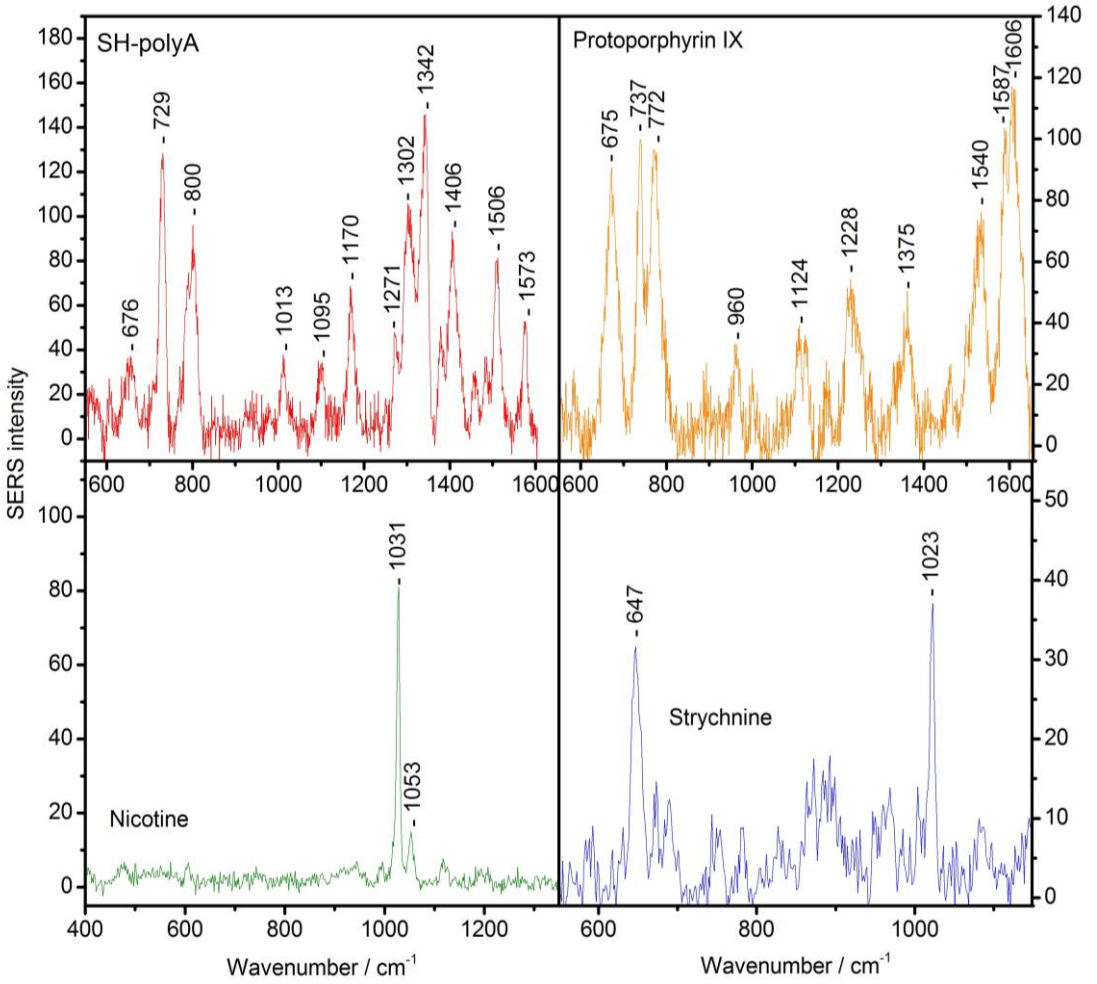


(CAN BE BLACK AND WHITE IN PRINT)

**Figure 5** SERS spectra of 10-mer thiolated polyA ($8\times10^{-5}$ M concentration in base pairs), protoporphyrin IX ($10^{-5}$ M incubation concentration), nicotine ($10^{-6}$ M incubation concentration) and strychnine ($10^{-6}$ M incubation concentration). Spectra are baseline corrected and shifted in the intensity scale for clarity. The Raman spectrum of AuFON substrate is subtracted from the SERS spectra. Experimental conditions: 632.8 nm excitation and accumulation time 6×10s (SH-polyA, protoporphyrin IX), 785 nm excitation and accumulation time 20×5s (nicotine), 785 nm excitation and accumulation time 30×5s (strychnine).

## 4 Conclusions

In this paper, we report a "bottom-up" fabrication of gold "film over nanosphere" (FON) SERS substrates using very small (107 nm in diameter) PS spheres. Hexagonally ordered monolayers of close-packed PS spheres were coated with 20 nm of gold. To obtain close-packed spheres in large scale area, the self-assembly at the water-air interface was found to be very efficient. The packing density is homogeneous on the micrometer scale which is crucial for spectral reproducibility. Sensitivity and reproducibility of AuFON substrates were tested using various molecular probes: 5,10,15,20-tetrakis(1-methyl-4-pyridyl)porphyrin (TMPyP), *p*-aminothiophenol (*p*-ATP) and benzocaine. Relative standard deviation (RSD) of SERS signal obtained from the AuFON substrates incubated in solution of analyte overnight was found to be less than 20% confirming excellent spectral reproducibility especially using a 100× objective. Moreover, we demonstrated a sensitive SERS detection of other biologically important molecules adsorbed on the AuFON substrates: thiolated-polyA, protoporphyrin IX and two alkaloids (nicotine and strychnine). We were able to detect both alkaloids at $10^{-6}$ M (in order of 100 ng.mL$^{-1}$) concentrations. Therefore, we conclude that our AuFONs substrates deposited on PS spheres of 107 nm in diameter provided both excellent spectral reproducibility and sensitivity and can be successfully applied for quantitative and analytical SERS studies.

**Acknowledgment**
This work was supported by grant No. P205/13/20110S from the Czech Science Foundation and GAUK No. 572216 from the Charles University.

**References**

1. M. Fleischmann, P. J. Hendra and A. J. McQuillan, *Chem. Phys. Lett*. **1974**, *26*, 163.
2. E. C. Le Ru and P. G. Etchegoin, *Principles of Surface-Enhanced Raman Spectroscopy and Related Plasmonic Effects*, Elsevier, Amsterdam, **2009**.
3. S. Schlücker, SERS Microscopy: Nanoparticle Probes and Biomedical Applications, in *Surface Enhanced Raman Spectroscopy: Analytical, Biophysical and Life Science Applications*, ed. S. Schlücker, Wiley-VCH Verlag GmbH & Co. KGaA, **2011**, pp. 263.
4. K. C. Bantz, A. F. Meyer, N. J. Wittenberg, H. Im, O. Kurtulus, S. H. Lee, N. C. Lindquist, S. H. Oh and C. L. Haynes, *Phys. Chem. Chem. Phys*. **2011**, *13*, 11551.
5. S. Schlücker, *Angew. Chem. Int. Ed.* **2014**, *53*, 4756.
6. W. Xie and S. Schlücker, *Phys. Chem. Chem. Phys.* **2013**, *15*, 5329.
7. M. Procházka, *Surface-enhanced Raman spectroscopy, Bioanalytical, Biomolecular and Medical Applications*, Springer International Publishing Switzerland, **2016**.
8. M. J. Natan, *Faraday Discuss*. **2006**, *132*, 321.
9. X. M. Lin, Y. Cui, Y. H. Xu, B. Ren and Z. Q. Tian, *Anal. Bioanal. Chem.* **2009**, *394*, 1729.
10. R. J. C. Brown and M. J. T. Milton, *J. Raman Spectrosc.*, **2008**, *39*, 1313.
11. M. J. Banholzer, J. E. Millstone, L. D. Qin and C. A. Mirkin, *Chem. Soc. Rev.* **2008**, *37*, 885.
12. M. K. Fan, G. F. S. Andrade and A. G. Brolo, *Anal. Chim. Acta* **2011**, *693*, 7.
13. Y. Li, G. T. Duan, G. Q. Liu and W. P. Cai, *Chem. Soc. Rev.* **2013**, *42*, 3614.
14. C. Farcau and S. Astilean, *J. Mol. Struct.* **2014**, *1073*, 102.
15. M. Jahn, S. Patze, I. J. Hidi, R. Knipper, A. I. Radu, A. Muhlig, S. Yuksel, V. Peksa, K. Weber, T. Mayerhofer, D. Cialla-May and J. Popp, *Analyst* **2016**, *141*, 756.

16. Z. Y. Li, W. M. Tong, W. F. Stickle, D. L. Neiman, R. S. Williams, L. L. Hunter, A. A. Talin, D. Li and S. R. J. Brueck, *Langmuir* **2007**, *23*, 5135.
17. G. M. Zhang, J. Zhang, G. Y. Xie, Z. F. Liu and H. B. Shao, *Small* **2006**, *2*, 1440.
18 J. C. Hulteen and R. P. Van Duyne, *J. Vac. Sci. Technol. A* **1995**, *13*, 1553.
19. H. Fredriksson, Y. Alaverdyan, A. Dmitriev, C. Langhammer, D. S. Sutherland, M. Zäch and B. Kasemo, *Adv. Mat.* **2007**, *19*, 4297.
20. V. Peksa, P. Lebrušková, H. Šípová, J. Štěpánek, J. Bok, J. Homola and M. Procházka, *Phys. Chem. Chem. Phys.* **2016**, *18*, 19613.
21. J. Zhang, Y. Li, X. Zhang and B. Yang, *Adv. Mat.* **2010**, *22*, 4249.
22. L. A. Dick, A. D. McFarland, C. L. Haynes and R. P. Van Duyne, *J. Phys. Chem. B* **2002**, *106*, 853.
23. M. Baia, L. Baia and S. Astilean, *Chem. Phys. Lett.* **2005**, *404*, 3.
24. L. Baia, M. Baia, J. Popp and S. Astilean, *J. Phys. Chem. B* **2006**, *110*, 23982.
25. C. L. Haynes, C. R. Yonzon, X. Zhang and R. P. Van Duyne, *J. Raman Spectrosc.* **2005**, *36*, 471.
26. C. Forcau and S. Astilean, *J. Phys. Chem. C* **2010,** *114*, 11717.
27. A. Kosiorek, W. Kandulski, P. Chudzinski, K. Kempa and M. Giersig, *Nano Letters* **2004**, *4*, 1359.
28. V. Peksa, M. Jahn, L. Štolcová, V. Schulz, J. Proška, M. Procházka, K. Weber, D. Cialla-May and J. Popp, *Anal. Chem.* **2015**, *87*, 2840.
29. N. Hajduková, M. Procházka, P. Molnár and J. Štěpánek, *Vib. Spectrosc.* **2008**, *48*, 142.
30. E. Papadopoulou and S. E. J. Bell, *Chem. Commun.* **2011**, *47*, 10966.
31. A. Barhoumi, D. Zhang, F. Tam and N. J. Halas, *J. Am. Chem. Soc.* **2008**, *130*, 5523.
32. M. Sládková, B. Vlčková, P. Mojzeš, M. Šlouf, C. Naudin and G. Le Bourdon, *Faraday Discuss.* **2006**, *132*, 121.
33. S. E. J. Bell and N. M. S. Sirimuthu, *Analyst* **2004**, *129*, 1032.
34. V. A. Narayanan, N. A. Stump, G. D. Del Cul and T. Vo-Dinh, *J. Raman Spectrosc.* **1999**, *30*, 435.